AFRL-VA-WP-TR-1998-3027

STRESS ANALYSIS AND STRENGTH PREDICTION OF ADHESIVELY BONDED COMPOSITE JOINTS

Naveen Rastogi
Alexander E. Bogdanovich
Som R. Soni

AdTech Systems Research, Inc.
1342 N. Fairfield Rd
Beavercreek, OH 45432

JUNE 1998

FINAL REPORT FOR PERIOD JULY 1995 – JANUARY 1998

19981109 045

Approved for public release; distribution unlimited

AIR VEHICLES DIRECTORATE
AIR FORCE RESEARCH LABORATORY
AIR FORCE MATERIEL COMMAND
WRIGHT-PATTERSON AIR FORCE BASE, OH 45433-7542

DTIC QUALITY INSPECTED 4

NOTICE

USING GOVERNMENT DRAWINGS, SPECIFICATIONS, OR OTHER DATA INCLUDED IN THIS DOCUMENT FOR ANY PURPOSE OTHER THAN GOVERNMENT PROCUREMENT DOES NOT IN ANY WAY OBLIGATE THE US GOVERENMENT. THE FACT THAT THE GOVERNMENT FORMULATED OR SUPPLIED THE DRAWINGS, SPECIFICATIONS, OR OTHER DATA DOES NOT LICENSE THE HOLDER OR ANY OTHER PERSON OR CORPORATION; OR CONVEY ANY RIGHTS OR PERMISSION TO MANUFACTURE, USE, OR SELL ANY PATENTED INVENTION THAT MAY RELATE TO THEM.

GOVERNMENT PURPOSE LICENSE RIGHTS LEGEND (SBIR PROGRAM)

Contract Number: F33615-95-C-2549
Contractor: AdTech Systems Research, Inc.

For a period of two (2) years after the delivery and acceptance of the last deliverable item under the above contract, all technical data contained in this report marked as Government Purpose License Rights data shall be subject to the restrictions contained in the definition of "Limited Rights in DFARS clause 252.227-7013 (Oct. 1988). After the two-year period, the data shall be subject to the restrictions contained in the definition of "Government Purpose License Rights" in DFARS clause 252.227.7013 (Oct. 1988). The Government assumes no liability for unauthorized use or disclosure by others. This legend, together with the indications of the portions of the data which are subject to such limitations, shall be included on any reproduction hereof which contains any portions subject to such limitations and shall be honored only as long as the data continues to meet the definition on Government purpose license rights.

This technical report has been reviewed and is accepted under the provisions of the Small Business Innovation Research Program.

ARVIND NAGAR
PROJECT ENGINEER
STRUCTURAL INTEGRITY BRANCH

John T. Ach
JOHN T. ACH
BRANCH CHIEF
STRUCTURAL INTEGRITY BRANCH

JOSEPH M. MANTER
CHIEF
STRUCTURES DIVISION

This report is published in the interest of scientific and technical information exchange and does not constitute approval or disapproval of its ideas or findings.

Do not return copies of this report unless contractual obligations or notice on a specific document requires its return.

REPORT DOCUMENTATION PAGE

Form Approved
OMB No. 0704-0188

Public reporting burden for this collection of information is estimated to average 1 hour per response, including the time for reviewing instructions, searching existing data sources, gathering and maintaining the data needed, and completing and reviewing the collection of information. Send comments regarding this burden estimate or any other aspect of this collection of information, including suggestions for reducing this burden, to Washington Headquarters Services, Directorate for Information Operations and Reports, 1215 Jefferson Davis Highway, Suite 1204, Arlington, VA 22202-4302, and to the Office of Management and Budget, Paperwork Reduction Project (0704-0188), Washington, DC 20503.

1. AGENCY USE ONLY *(Leave blank)*

2. REPORT DATE
June 1998

3. REPORT TYPE AND DATES COVERED
Final Report July 1995-January 1998

4. TITLE AND SUBTITLE
Stress Analysis and Strength Prediction of Adhesively Bonded Composite Joints

5. FUNDING NUMBERS
C - F33615-95-C-2549
PE - 65502F
PR - 3005
TA - 41
WU - 3F

6. AUTHOR(S)
Naveen Rastogi, A. E. Bogdanovich, Som R. Soni

7. PERFORMING ORGANIZATION NAME(S) AND ADDRESS(ES)
AdTech Systems Research, Inc.
1342 N. Fairfield Road
Beavercreek OH 45432-2698

8. PERFORMING ORGANIZATION REPORT NUMBER
723 Final Report
Volume II

9. SPONSORING/MONITORING AGENCY NAME(S) AND ADDRESS(ES)
Air Vehicles Directorate
Air Force Research Laboratory
Air Force Material Command
Wright-Patterson Air Force Base, OH 45433-7542
P.O.C.: Arvind Nagar, AFRL/VASE (937) 255-6104 ext 238

10. SPONSORING/MONITORING AGENCY REPORT NUMBER
AFRL-VA-WP-TR-1998-3027

11. SUPPLEMENTARY NOTES

12a. DISTRIBUTION/AVAILABILITY STATEMENT
Approved for public release; distribution unlimited

12b. DISTRIBUTION CODE

13. ABSTRACT *(Maximum 200 words)*

Report developed under SBIR contract.

The state of the art in the stress analysis and strength prediction of adhesively bonded composite joints is presented. A *generalized coordinate* finite element analysis based on rectangular, cylindrical and wedge solid elements is developed and utilized for the three-dimensional analysis of composite bonded joints. The comparison of results between 2-D and 3-D bonded joint analysis tools are made and their limitations are discussed. Further, the submodeling technique available in the commercial finite element package ABAQUS is explored to study the three-dimensional stress field in the vicinity of joint edges and debond cracks. The series of bolted joint design codes BONJO developed by Lockheed are incorporated into a PC based Bolted and Bonded Joint (BBJ) design methodology. The Bolted and Bonded Joint design tool is made more informative and user-friendly through the use of Windows 95TM based Graphic User Interfaces (GUIs) fully integrated with a material database and on-line help.

14. SUBJECT TERMS
Composite bonded joints, finite element analysis, variable-order elements, three-dimensional stresses, submodeling, debond

15. NUMBER OF PAGES
161

16. PRICE CODE

17. SECURITY CLASSIFICATION OF REPORT
Unclassified

18. SECURITY CLASSIFICATION OF THIS PAGE
Unclassified

19. SECURITY CLASSIFICATION OF ABSTRACT
Unclassified

20. LIMITATION OF ABSTRACT
SAR

NSN 7540-01-280-5500

Standard Form 298 (Rev. 2-89)
Prescribed by ANSI Std. Z39-18
298-102

TABLE OF CONTENTS

SECTION **PAGE**

1.0 INTRODUCTION 1

2.0 BACKGROUND 4

2.1 Computer Codes for Analysis of Bonded Joints 5
  2.1.1 Joint 6
  2.1.2 JTSDL/JTSTP 7
  2.1.3 BOND3/BOND4 7
  2.1.4 BONJO 7
  2.1.5 A4EI 8
  2.1.6 PGLUE 9
  2.1.7 SAVE 9

3.0 THREE-DIMENSIONAL LINEAR ELASTIC STRUCTURAL ANALYSIS USING *VARIABLE-ORDER* ELEMENTS 12

3.1 Mathematical Formulations for *Variable-Order* Elements 12
  3.1.1. Rectangular Brick Element 15
  3.1.1.1 Strain-Displacement Relations 15
  3.1.1.2 Constitutive Law 16
  3.1.1.3 Virtual Work Functional 16
  3.1.1.4 Displacement Approximations 18
  3.1.2 Cylindrical Brick Element 20
  3.1.2.1 Strain-Displacement Relations 20
  3.1.3 Solid Wedge Element 21
  3.1.3.1 External Work Due to Surface Tractions 21
  3.1.3.2 Displacement Approximations 22
  3.1.4 Singular Brick Element 23
  3.1.5 Formulation of Stiffness and Load Matrices 24
  3.1.6 Boundary Conditions for the Element 27

3.2 Numerical Examples 29
  3.2.1 Bernstein Polynomials as Displacement Functions 30
  3.2.2 Analysis of Laminated Plates Using *Variable-Order* Rectangular Solid Elements 32
  3.2.2.1 Transverse Bending of a Laminated Plate 33
  3.2.2.2 Uniaxial Extension of a Laminated Plate 36
  3.2.2.3 Restrained Thermal Expansion of a Laminated Plate 43
  3.2.3 Analysis of Cylindrical Shells Using *Variable-Order* Cylindrical Solid Elements 46
  3.2.3.1 Transverse Bending of a Laminated Cylindrical Panel 46
  3.2.3.2 An Infinite, Thick Isotropic Cylindrical Shell Under Internal Pressure 50
  3.2.3.3 Uniaxial Extension of a Laminated Cylindrical Panel 53

TABLE OF CONTENTS (Continued)

SECTION **PAGE**

4.0 ANALYSIS OF DOUBLE-LAP BONDED JOINTS 59

4.1 Analysis of Adhesively Bonded Double-Lap Joints: Comparison Between BONJO and FEM Analyses 59
- 4.1.1 Stresses at the Center Line of the Adhesive Layer 64
- 4.1.2 Stresses at the Interface Between Adhesive Layer and 0° Ply of the Upper Adherend 66
- 4.1.3 Stresses at the Interface of 0° Ply and 45° Ply in the Upper Adherend 66
- 4.1.4 Stresses at the Interface of -45° ply and 0° Ply of the Upper Adherend 70
- 4.1.5 Stresses at the Top Surface of the Upper Adherend (in 0° ply) 72
- 4.1.6 Stresses at the Interface Between Adhesive Layer and Lower Adherend 74
- 4.1.7 Stresses at the Midplane of the Joint (or Midplane of Lower Adherend) 76
- 4.1.8 Angle Ply Effects 78
- 4.1.9 Summary 86

4.2 Three-Dimensional Analysis of Perfectly Bonded Plates 89
- 4.2.1 Variation of Stresses at the Aluminum-Boron/Epoxy Interface 92
- 4.2.2 Comparison of the Stresses in the Adherends for Restrained Versus Unrestrained Cases 94
- 4.2.3 Stress Field in the Joint for Various Composite Material Upper Adherends 97
- 4.2.4 Summary 98

4.3 Thermomechanical Analysis of Adhesively Bonded Double-Lap Joints: A Combined Analytical and Experimental Study 100
- 4.3.1 Experimental Failure Loads 101
- 4.3.2 Results and Discussions 103
- 4.3.2.1 Stress Distributions in Baseline Model 2-75 104
- 4.3.2.2 Stress Distributions in Model 2-65 vs. Model 2-75 108
- 4.3.2.3 Stress Distributions in Model 1-75 vs. Model 2-75 112
- 4.3.2.4 Stress Distributions in Model 3-75 vs. Model 2-75 115
- 4.3.3 Summary 119

4.4 Software Development 120

5.0 THREE-DIMENSIONAL FINITE ELEMENT ANALYSIS OF COMPOSITE-TO-METAL AND COMPOSITE-TO-COMPOSITE BONDED JOINTS 121

5.1 Introduction 121

5.2 The Concept of Submodeling 121

TABLE OF CONTENTS (Continued)

SECTION **PAGE**

5.3 Three-Dimensional Stress Analysis of Composite-to-Metal Bonded Joint 123

5.4 Stress Analysis in the Presence of Initial Debond Crack 131

5.5 Analysis of Composite-to-Composite Adhesive Bonded Joint 132

6.0 CONCLUSIONS AND RECOMMENDATIONS 139

6.1 Summary and Conclusions 139

6.2 Recommendations for Future Work 140

7.0 REFERENCES 142

Appendix A: Off-Axis Thermoelastic Constants for a Laminae 148

Appendix B: Elements of Stiffness Matrix for a Variable-Order Rectangular Solid Element 150

Appendix C: Elements of Stiffness Matrix for a Variable-Order Cylindrical Solid Element 155

Appendix D: Elements of Stiffness Matrix for a Variable-Order Wedge Solid Element 159

List of Figures

Figure		Page
1.1	Typical adhesively bonded joints	2
3.1	A rectangular solid element in a global Cartesian (x,y,z) coordinate system	15
3.2	A cylindrical solid element in a global cylindrical (x,θ,z) coordinate system	20
3.3	A solid wedge element in a global Cartesian (x,y,z) coordinate system	21
3.4	A rectangular solid element with a crack face having stress singularities at the crack tip	24
3.5	A solid rectangular element in a non-dimensional, local Cartesian (ξ,η,ζ) coordinate system	25
3.6	A simply-supported $[0/90/0]_T$ laminate subjected to sinusoidal loading on the top surface	33
3.7	A simply-supported [0/90]s laminate subjected to uniform axial extension	36
3.8	Distributions of transverse normal stress σ_{zz} at the mid plane of a [0/90]s laminate subjected to uniform axial extension	38
3.9	Distributions of transverse normal stress σ_{zz} at the 0/90 interface of a [0/90]s laminate subjected to uniform axial extension (1x12x8 mesh with M=3)	39
3.10	Distributions of transverse normal stress σ_{zz} in the close vicinity of the free-edge at the 0/90 interface of a [0/90]s laminate subjected to uniform axial extension (1x12x8 mesh with M=3)	39
3.11	Distributions of transverse normal stress σ_{zz} in the close vicinity of the free-edge at the 0/90 interface of a [0/90]s laminate subjected to uniform axial extension (1x12x8 mesh with M=4)	40
3.12	Distributions of transverse normal stress σ_{zz} in the close vicinity of the free-edge at the 0/90 interface of a [0/90]s laminate subjected to uniform axial extension (1x20x12 mesh with M=3)	40
3.13	Distributions of transverse shear stress τ_{yz} at the 0/90 interface of a [0/90]s laminate subjected to uniform axial extension (1x20x12 mesh with M=3).	42
3.14	Distributions of transverse shear stress τ_{yz} in the close vicinity of the free-edge at the 0/90 interface of a [0/90]s laminate subjected to uniform axial extension (1x12x8 mesh with M=3)	42

List of Figures (Continued)

Figure		Page
3.15	Distribution of normal stress σ_{zz} at 0/90 interface of a [0/90]s laminate subjected to uniform thermal loading	44
3.16	Distributions of normal stress σ_{yy} at the 0/90 interface of a [0/90]s laminate subjected to uniform thermal loading	44
3.17	Distributions of transverse normal stress σ_{zz} at the 0/90 interface of a [0/90]s laminate subjected to uniform thermal loading	45
3.18	Distributions of transverse shear stress τ_{yz} at the 0/90 interface of a [0/90]s laminate subjected to uniform thermal loading	45
3.19	Distributions of transverse displacements at the 0/90 interface of a [0/90]s laminate subjected to uniform thermal loading	46
3.20	A simply-supported $[90/0/90]_T$ laminated cylindrical panel subjected to sinusoidal loading on the top surface	47
3.21	1/4th configuration of a thick, isotropic cylindrical and shell subjected to uniform internal pressure	50
3.22	A simply-supported $[0/90]_T$ laminated cylindrical panel subjected to uniform axial extension	53
3.23	Distributions of normal stress σ_{xx} at the 0/90 interface of a $[0/90]_T$ laminated cylindrical panel subjected to uniform axial extension	54
3.24	Distributions of normal stress $\sigma_{\theta\theta}$ at the 0/90 interface of a $[0/90]_T$ laminated cylindrical panel subjected to uniform axial extension	55
3.25	Distributions of transverse normal stress σ_{zz} at the 0/90 interface of a $[0/90]_T$ laminated cylindrical panel subjected to uniform axial extension	55
3.26	Distributions of transverse shear stress $\tau_{\theta z}$ at the 0/90 interface of a $[0/90]_T$ laminated cylindrical panel subjected to uniform axial extension	56
3.27	Distributions of transverse displacements at the 0/90 interface of a $[0/90]_T$ laminated cylindrical panel subjected to uniform axial extension	56
3.28	Distributions of transverse normal stress σ_{zz} inside the 90° layer ($z/h = 0.4$) of a $[0/90]_T$ laminated cylindrical panel subjected to uniform axial extension	57
4.1	A double-lap adhesively bonded joint configuration	59
4.2	1/8th configuration of the double-lap adhesively bonded joint	60

List of Figures (Continued)

Figure		Page
4.3	Finite element mesh configuration	61
4.4	Finite element mesh configuration	62
4.5	Double-lap bonded joint configuration analyzed by BONJO code	63
4.6	Distributions of shear stress τ_{xz} in the adhesive layer	65
4.7	Distributions of normal stress σ_z in the adhesive layer	66
4.8	Distributions of normal stress σ_x in the 0° ply of the upper adherend at the adhesive layer-upper adherend interface	67
4.9	Distributions of normal stress σ_z in the 0° ply of the upper adherend at the adhesive layer-upper adherend interface	68
4.10	Distributions of shear stress τ_{xz} in the 0° ply of the upper adherend at the adhesive layer-upper adherend interface	68
4.11	Distributions of normal stress σ_z in the 0° ply at the 0°/45° interface of the upper adherend	69
4.12	Distributions of normal stress sz in the 0°/45° interface of the upper adherend	69
4.13	Distributions of shear stress τ_{xz} in the 0° ply at the 0°/45° interface of the upper adherend	70
4.14	Distributions of normal stress σ_z in the -45°/0° interface of the upper adherend	71
4.15	Distributions of normal stress σ_z in the -45° ply at the -45°/0° interface of the upper adherend	71
4.16	Distributions of shear stress τ_{xz} in the -45° ply at the -45°/0° interface of the upper adherend	72
4.17	Distributions of normal stress σ_x in 0° ply of the upper adherend at the top surface	73
4.18	Distributions of normal stress σ_z in 0° ply of the upper adherend at the top surface	73

List of Figures (Continued)

Figure		Page
4.19	Distributions of shear stress τ_{xz} in 0° ply of the upper adherend at the top surface	74
4.20	Distributions of normal stress σ_x in the lower adherend at the adhesive layer-lower adherend interface	75
4.21	Distributions of normal stress σ_z in the lower adherend at the adhesive layer-lower adherend interface	75
4.22	Distributions of shear stress τ_{xz} in the lower adherend at the adhesive layer-lower adherend interface	76
4.23	Distributions of normal stress σ_x at the midplane of the lower adherend	77
4.24	Distributions of normal stress σ_z at the midplane of the lower adherend	77
4.25	Distributions of shear stress τ_{xz} at the midplane of the lower adherend	78
4.26	Distributions of normal stress σ_z in the adhesive layer	79
4.27	Distributions of shear stress τ_{xz} in the adhesive layer	80
4.28	Distributions of normal stress σ_x at the midplane of the lower adherend	80
4.29	Distributions of normal stress σ_x at the midplane of the upper adherend	81
4.30	Distributions of normal stress σ_z in the adhesive layer	82
4.31	Distributions of shear stress τ_{xz} in the adhesive layer	82
4.32	Distributions of normal stress σ_x at the midplane of the lower adherend	83
4.33	Distributions of normal stress σ_x in the 0° ply at the 0°/90° interface of the upper adherend	83
4.34	Distributions of normal stress σ_x in the 90° ply at the 0°/90° interface of the upper adherend	84
4.35	Distributions of normal stress σ_x in the 45°/0° interface of the upper adherend	85

List of Figures (Continued)

Figure **Page**

4.36 Distributions of normal stress σ_x in the 0° ply at the 45°/0° interface of the upper adherend 86

4.37 Distributions of normal stress σ_x in the 25°/0° interface of the upper adherend 87

4.38 Distributions of normal stress σ_x in the 0° ply at the 25°/0° interface of the upper adherend 88

4.39 Distributions of normal stress σ_x in the 65°/0° interface of the upper adherend 88

4.40 Distributions of normal stress σ_x in the 0° ply at the 65°/0° interface of the upper adherend 89

4.41 A symmetric, perfectly bonded double-lap joint configuration 89

4.42 1/8th configuration of the perfectly bonded double-lap joint modeled for analysis 91

4.43 Distributions of normal stress σ_{xx} at the aluminum-boron/epoxy interface at $y/b=0$ 93

4.44 Distributions of normal stress σ_{zz} at the aluminum-boron/epoxy interface at $y/b = 0$ 93

4.45 Distributions of transverse shear stress τ_{xz} at the aluminum-boron/epoxy interface at $y/b = 0$ 94

4.46 Distributions of normal stress σ_{xx} in the aluminum adherend at the aluminum-boron/epoxy interface at $y/b = 0$. 95

4.47 Distributions of normal stress σ_{yy} in the aluminum adherend at the aluminum-boron/epoxy interface at $y/b = 0$ 96

4.48 Distributions of normal stress σ_{zz} in the aluminum adherend at the aluminum-boron/epoxy interface at $y/b = 0$ 96

4.49 Distributions of transverse shear stress τ_{xz} in the aluminum adherend at the aluminum-boron/epoxy interface at $y/b = 0$ 97

4.50 Distribution of normal stress σ_{xx} in the aluminum adherend at the aluminum-composite interface at $y/b = 0$ 98

List of Figures (Continued)

Figure		Page
4.51	Distributions of transverse shear stress τ_{xz} in the aluminum adherend at the aluminum-composite interface at y/b = 0	99
4.52	Distributions of normal stress σ_{xx} in the composite adherend at the aluminum-composite interface at y/b = 0	99
4.53	Distributions of transverse shear stress τ_{xz} in the composite adherend at the aluminum-composite interface at y/b = 0	100
4.54	An adhesively bonded, symmetric double-lap joint	100
4.55	Double-lap bonded joint configuration analyzed by BONJO	101
4.56	Distributions of normal stress σ_{xx} in the parent laminate at the adhesive-parent laminate interface at y/b = 0	105
4.57	Distributions of normal stress σ_{yy} in the parent laminate at the adhesive-parent laminate interface at y/b = 0	105
4.58	Distributions of normal stress σ_{zz} in the parent laminate at the adhesive-parent laminate interface at y/b = 0	106
4.59	Distributions of transverse shear stress τ_{xz} in the parent laminate at the adhesive-parent laminate interface at y/b = 0	106
4.60	Distributions of normal (peel) stress σ_{zz} in the adhesive at the adhesive centerline at y/b = 0	107
4.61	Distributions of transverse shear stress τ_{xz} in the adhesive at the adhesive centerline at y/b = 0	107
4.62	Distributions of normal stress σ_{xx} in the parent laminate at the adhesive-parent laminate interface at y/b = 0	109
4.63	Distributions of normal stress σ_{yy} in the parent laminate at the adhesive-parent laminate interface at y/b = 0	109
4.64	Distributions of normal stress σ_{zz} in the parent laminate at the adhesive-parent laminate interface at y/b = 0	110
4.65	Distributions of transverse shear stress τ_{xz} in the parent laminate at the adhesive-parent laminate interface at y/b = 0	110

List of Figures (Continued)

Figure		Page
4.66	Distributions of normal (peel) stress σ_{zz} in the adhesive at the adhesive centerline at y/b = 0	111
4.67	Distributions of transverse shear stress τ_{xz} in the adhesive at the adhesive centerline at y/b = 0	111
4.68	Distributions of normal stress σ_{xx} in the parent laminate at the adhesive-parent laminate interface at y/b = 0	112
4.69	Distributions of normal stress σ_{yy} in the parent laminate at the adhesive-parent laminate interface at y/b = 0	113
4.70	Distributions of normal stress σ_{zz} in the parent laminate at the adhesive-parent laminate interface at y/b = 0	113
4.71	Distribution of transverse shear stress τ_{xz} in the parent laminate at the adhesive-parent laminate interface at y/b = 0	114
4.72	Distributions of normal (peel) stress σ_{zz} in the adhesive at the adhesive centerline at y/b = 0	114
4.73	Distributions of transverse shear stress τ_{xz} in the adhesive at the adhesive centerline at y/b = 0	115
4.74	Distributions of normal stress σ_{xx} in the parent laminate at the adhesive-parent laminate interface at y/b = 0	116
4.75	Distributions of normal stress σ_{yy} in the parent laminate at the adhesive-parent laminate interface at y/b = 0	116
4.76	Distributions of normal stress σ_{zz} in the parent laminate at the adhesive-parent laminate interface at y/b = 0	117
4.77	Distributions of transverse shear stress τ_{xz} in the parent laminate at the adhesive-parent laminate interface at y/b = 0	117
4.78	Distributions of normal (peel) stress $\sigma_{zz/}$ in the adhesive at the adhesive centerline at y/b = 0	118
4.79	Distributions of transverse shear stress τ_{xz} in the adhesive at the adhesive centerline at y/b = 0	118

List of Figures (Continued)

Figure		Page
5.1	Schematic of a double-lap joint (a) and its 1/8th part (b) solved	122
5.2	Schematic of the global and local regions considered in the analysis	122
5.3	Variations of σ_x/σ_0, σ_z/σ_0 and τ_{xz} / σ_0 in Gr/Ep (a,c,e) and Al (b,d,f) adherends in local region 1at $y/b = 1$, $z/h = 0.5$	129
5.4	Variations of σ_x/σ_0 (a), σ_z/σ_0 (b) and τ_{xz} / σ_0 (c) in the width direction for Gr/Ep and Al adherends in local region 1 at $y/b - 1$, $z/h = 0.5$	130
5.5	Initial debond crack at the end of the overlap zone	132
5.6	Variations of σ_x/σ_0, σ_z/σ_0 and τ_{xz} / σ_0 in Gr/Ep (a,c,e) and Al (b,d,f) adherends at $y/b = 1$, $z/h = 0.5$ without crack and with initial debond crack of two different lengths	133
5.7	Schematic of a composite-to-composite adhesive bonded joint (a) and its 1/8th part (b) considered in the analysis	134
5.8	A view of global and local regions in the planes x-y (a) and x-z (b)	135
5.9	Variations of σ_x/σ_0, σ_z/σ_0 and τ_{xz} / σ_0 in the adhesive layer (a,c,e) and middle adherend (b,d,f) along the interface at $y/b = 1$, $z/h - 0.3214$	137
5.10	Variations of σ_x/σ_0, σ_z/σ_0 and τ_{xz} / σ_0 in the adhesive layer (a,c,e) and upper adherend (b,d,f) along the interface at $y/b = 1$, $z/h = 0.3571$	138

List of Tables

Table		Page
2.1	Computer Codes for Analysis of Bonded Joints	6
3.1	Comparison between the results obtained from (a) the present 3-D analysis performed with one variable-order rectangular solid element each in x- and y- directions and one variable-order rectangular solid element per layer in the z-direction, and (b) those obtained by Pagano [1970] for a $[0/90/0]_T$ simply supported, laminated plate (a=b=4h) subjected to sinusoidal loading on the top surface	35
3.2	Comparison between the results obtained for various a/h ratios (a) from the present 3-D analysis performed with one variable-order (M=6) rectangular solid element each in x- and y- directions and one variable-order (M=6) rectangular solid element per layer in the z-direction, and (b) by Pagano [1970] for a $[0/90/0]_T$ simply supported, laminated plate (a=b) subjected to sinusoidal loading on the top surface	36
3.3	Comparison between the results obtained for various R/h ratios (a) from the present 3-D analysis performed with one variable-order (M=6) cylindrical brick element each in x- and θ- directions and one variable order (M=6) cylindrical brick element per layer in the z-direction, and (b) by Ren [1989] for a $[90/0/90]_T$ simply supported, finite length (a/R=5), laminate cylindrical panel subjected to sinusoidal loading on the top surface	49
3.4	Comparison between the results obtained from (a) the present 3-D analysis performed using a single variable-order cylindrical solid element, (b) the analysis performed using I-DEAS[70], and (c) the Strength of Materials (S.O.M.) plane-stress solution given in the text by Srinath[71] for an infinite length, thick isotropic cylindrical shell subjected to internal pressure loading	52
3.5	Comparison between the results obtained from (a) the present 3-D analysis performed using one variable-order cylindrical solid element each in the x- and θ- directions and two or more variable-order cylindrical solid element in the z-direction, and (b) the Strength of Material (S.O.M.) plane stress solution given in the text by Srinath71 for an infinite length, thick isotropic cylindrical shell subjected to internal pressure loading	52
4.1	Material properties for the adherends and adhesive	64
4.2	Thermoelastic properties of the adherends	90
4.3	Average failure loads for double-lap bonded joint specimens	102
5.1	Element meshes used in global analysis	124
5.2	Normalized displacements at x = 0.5a, y = 0.8b, z = 0.5h computed with the element meshes of Table 5.1	125
5.3	Various x-direction meshes used in Submodel 1 analysis	126

List of Tables (Continued)

Table **Page**

5.4 Stresses in Al and Gr/Ep adherends at x = 0.5a, y = b, z = 0.5h computed with the element meshes of Table 5.3 126

5.5 Element meshes in the y-direction used in Submodel 1 analysis 127

5.6 Stresses in Al and Gr/Ep adherends at x = 0.5a, y = b, z = 0.5h computed with the element meshes of Table 5.5 127

5.7 Element meshes used in Submodel 2 analysis 127

5.8 Stresses in Al and Gr/Ep adherends computed in Submodel 2 analysis 128

1.0 INTRODUCTION

Advanced composites have been identified as candidate material systems for a variety of aeropropulsion, aerostructure, space structure, and airframe components. A number of these applications involve joints between similar and dissimilar material systems. Some of these are mechanical joints such as bolted and riveted connections. Others are fabricated by adhesive bonding, welding, brazing, and a variety of other methods. Adhesive bonding has always been a very desirable method for joining the composite components to achieve maximum structural efficiency and improve the structural integrity. Bonded joints not only have better strength-to-weight ratio but they also avoid the use of thousands of fasteners and the fastener holes in the structure. Figure 1.1 shows various types of bonded joints commonly used in the assembly of aerospace structures.

Apart from the mechanical loads such as tension/compression, bending and shear, the aerospace structures are subjected to aerodynamic and radiation heating resulting in thermal loads. For example, in space structures the cold space coupled with radiant solar heating can lead to a wide range of operating temperatures which are of the order of 160°C to 120°C. A bonded joint is also subjected to cyclic thermal loading due to the variation in the operating temperature of the aircraft. For example, at the cruise altitude the fuselage of a transport aircraft cools down to approximately -55°C thereby subjecting the bonded joint or bonded repaired structure to cyclic thermal stresses during each flight. Yet another source of thermal stresses in bonded structures is due to the fact that bonding usually requires curing of the adhesive at temperatures higher than the room temperature.

When two adherends are made of dissimilar materials having different coefficients of thermal expansions, the cool down phase of the curing process induces residual stresses in the jointed materials even in an unrestrained structure. Such situations commonly exist when one adherend is made of metallic material and the other is a laminated composite plate. Thus, the analysis of adhesively bonded joints where bonding between two dissimilar materials with different thermal expansion coefficients is involved or where the structure is constrained against its free expansion (even if the two jointed materials are identical), requires due consideration of the thermal stresses.

An understanding of the load transfer mechanism and the location(s) of severely stressed regions is of utmost importance for designing a reliable bonded joint. An accurate prediction of static strength of the joint or its service life under sustained thermomechanical loading is also dependent upon how accurately the stress distributions are predicted by an analysis approach. In addition, the analytical model/approach employed for the stress analysis of bonded joints should be computationally efficient as well as viable for its further use into a fracture mechanics based strength and life prediction methodology. Thus, the importance of an accurate stress analysis of bonded joints needs no further discussion. This work is primarily focused on the various aspects of the stress analysis in bonded joints subjected to thermomechanical loads.

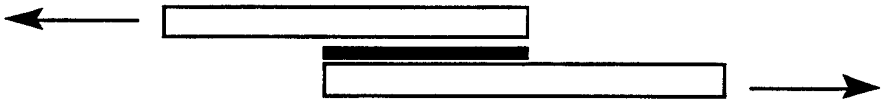

Single Lap

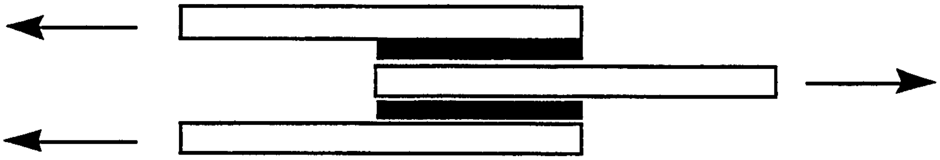

Double Lap

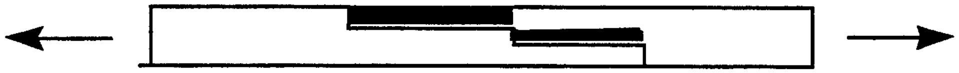

Stepped Lap

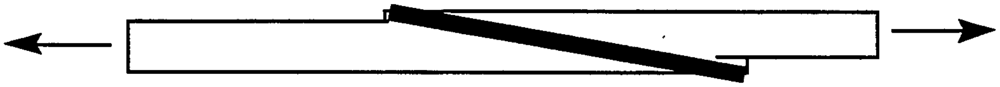

Scarf

Fig. 1.1 Typical adhesively bonded joints.

During the SBIR Phase-II activity an extensive survey of the existing state of the art in the analysis and design of adhesively bonded joints is performed. Some of the computer codes for the analysis of adhesively bonded joints, developed as part of the earlier efforts by Air Force and Navy, are obtained and made operational on IBM RISC 6000 and PC.

The most versatile and best code among them is selected for further studies and software development. In addition, a versatile three-dimensional, *generalized coordinate* finite element analysis based on *variable-order* (similar to *p*-type) solid elements is also developed and applied to analyze some double-lap bonded joint configurations subjected to thermomechanical loading. Using this analysis the effects of change in the design parameters such as bond length, bond thickness and adhesive curing temperature on the failure loads of a double-lap adhesively bonded joint are studied through a combined analytical and experimental work. Finally, three-dimensional stresses in the composite-to-metal and composite-to-composite double-lap bonded joints are obtained using a submodeling technique available in the commercial finite element analysis package ABAQUS. Subsequently, the stress field in the presence of an initial debond was also studied using ABAQUS.

2.0 BACKGROUND

The design and analysis of the bonded joints require analytical tools for accurate determination of the stress distributions in the adherends and the adhesive. In the last half century engineers and researchers have developed a number of analysis tools to analyze adhesively bonded joints. These analytical methods are based on continuum mechanics, plane strain/stress closed form solutions, 2-D and 3-D finite element analyses solutions. The classical paper published by Goland and Reissner[1] in 1944 is perhaps the most cited work in the analysis of adhesively bonded joints. In their work Goland and Reissner analyzed a single lap joint for two limiting cases, i.e., (i) where the adhesive layer is so thin that its effect on flexibility of joints can be neglected, and (ii) where the joint flexibility is mainly due to the adhesive layer (as is the case of most thin-walled bonded aerospace structures). During the analysis they assumed that (i) the axial stress in the adhesive layer can be neglected, and (ii) normal and transverse shear stresses in the adhesive layer do not vary across the thickness of the adhesive. Since the publication of Goland and Reissner's work more than half a century ago, these basic assumptions have been employed by numerous authors to extend the work in the area of analysis and/or design of bonded joints. In his extensive work on bonded joints, Hart-Smith[2-6, 40-43, 50] has outlined various aspects of efficient bonded joint design in composite structures that an airframe designer should consider while designing bonded joints between components in the aircraft structures. Hart-Smith also made many useful studies to analyze the load transfer mechanism in the adhesive bonded joint(s) and outlined some practical ways to minimize the transverse shear and peel stresses in the adhesive layer. The extensive work done by Hart-Smith in the last three decades gives a deep insight into the practical joint design considerations in primary aircraft structure components viz., fuselage, wing, horizontal and vertical tails, and control surfaces, etc.. Vinson[7] carried out extensive analytical and experimental work in the area of adhesively bonded joints involving polymer composite adherends. Vinson and his colleagues[8-12] developed analytical tools to analyze adhesively bonded joints by including into the analysis the effects of transverse shear deformation, transverse normal strain, temperature and moisture variations. Adams and his colleagues[13-15] also contributed immensely to improve the understanding of adhesive bonded joints in engineering applications. The text by Adams and Wake[16] presents a comprehensive treatise on the design and production of adhesively bonded joints used as primary load carrying members. The mechanics and chemistry of designing a sound bonded joints are discussed, and standard methods of testing adhesives are outlined.

An excellent review of the work performed prior to 1969 in the area of adhesively bonded joints is presented by Kutscha[17] and Kutscha and Hofer[18]. Schliekelmann[19]edited an AGARD lecture series on adhesive bonded joints in 1979. This lecture series contains work on analysis and design, failure response, processing and testing of adhesively bonded joints by the leading researchers/engineers of that time. An excellent bibliography on adhesive bonded joints is also included in Ref. [19]. In 1988 Mall, et al.[20] and

Johnson[21] compiled and edited some of the work on the advancement of adhesively bonded joints technology. Vinson[7] reviewed the state of the art of analysis and design of adhesive bonded joints in 1989. Apart from the literature mentioned above, there is plenty of open literature on the analysis and design, preparation, processing and testing of adhesively bonded composite joints. Closed-form analytical solutions of adhesively bonded joints were obtained by Delale, et al.,[22] Groth,[23] Liu,[24] Pahoja,[25] and Srinivas.[26] Adams and Peppiatt,[13] Amijima, et al.,[27-28] Roy and Reddy,[29] Sable and Sharifi,[30] Humpherys and Herakovich,[31] Barthelemy, et al.,[32] and Barker and Hatt,[33] all performed finite element based analysis of bonded joints. In addition to the efforts of Hart-Smith, Vinson and Adams, the work on design and/or analysis of bonded joints was also extended by Chamis and Murthy,[34] Shyprykevich,[35] Findlater,[36] Kelly, et al.,[37] and Tsai and Morton.[38]

2.1 COMPUTER CODES FOR ANALYSIS OF BONDED JOINTS

For the past three decades the researchers and engineers have been involved in the development of various analytical techniques to analyze bonded composite joints. Efforts by the various groups have resulted in some useful computer programs that can be utilized by the aerospace engineers and designers engaged in bonded joint design work. An updated list of composite bonded joint programs developed as of 1994 was compiled by Negaard[39] and published by Aerospace Structures Information and Analysis Center (ASIAC). These programs are listed in Table 2.1. The state-of-stress accounted for in the strength/stress analysis, and name of the agency responsible for developing these computer programs is also stated therein. Table 2.1 also lists the *generalized coordinate* finite element analysis program Structural Analysis using Variable-order Elements (SAVE), developed as part of the current SBIR Phase-II activity. This program has been applied to analyze some double-lap bonded joint configurations subjected to thermomechanical loading. The solution approach employed in each of these codes, and their capabilities and/or limitations are discussed briefly in the following paragraphs.

Table 2.1 Computer codes for analysis of bonded joints.

Sl. No.	Analysis Code	Agency/Developer (Year)	State-of-stress	Applications
1.	JOINT	A. F. /McDonnell D. (1978)	1-D	Single lap, double lap, scarf and step lap joints
2.	JTSDL/ JTSTP	A. F. / SwRI (1972)	2-D	Single lap, double lap and step lap joints
3.	BOND3/ BOND4	A. F. /U. of Delaware. (1974)	2-D	Single lap joints
4.	BONJO I	A. F. /Lockheed (1972)	2-D	Single and double lap joints
5.	A4EI	A. F. /McDonnell D. (1982)	1-D	Stepped lap and doubler joint repair
6.	PGLUE	Navy/McDonnell D. (1987)	2-D	Bonded joint repair
7.	SAVE	Air Force/AdTech (1996-)	2-D/3-D	2-D/3-D generalized coordinate FE structural analysis using variable-order elements.

2.1.1 JOINT

This is an " Interactive Composite Joint Design" program developed by Hart-Smith, et al.[40-43] for the analyses of bolted and bonded composite joints. In the case of bonded composite joints, the following four types of joints can be analyzed (see Fig. 1.1):

(i) unsupported/supported single lap
(ii) double lap
(iii) stepped lap
(iv) scarf

The in-plane loads are assumed to act in the adherends, with no lateral applied loads. The analysis can also account for the initial stresses induced by the bonding of metals to composites. The adherend materials have linear elastic behavior, while adhesive is modeled as an elastic-plastic material to account for its considerable nonlinear deformation prior to failure. For a given in-plane loading, optimum overlap, adhesive strengths and adherend strengths are calculated. The analysis approach is based on the solution to differential equations from the classical continuum mechanics. Some solutions are explicit, while others are exact, but implicit, and require an iterative solution. Experimentally determined material stress-strain curves are used to cover the possible failure modes of adhesive shear, adhesive peel, and adherend in-plane and interlaminar failures. The analysis capabilities of this approach are limited by the fact that it utilizes a lot of test data for the adhesive and the jointed plates to compute the joint strengths. Thus, each change of material system requires a complete repetition of all testing.

2.1.2 JTSDL/JTSTP

This is a nonlinear design/analytical method developed for the analysis of bonded single, double, and step-lap joints by Grimes, et al.[44] The analysis is based on the elastic continuum method and utilizes the Ramberg-Osgood[45] three parameter stress-strain curves for the adhesive and adherends. A state of plane strain is assumed and the effects of interlaminar shear stress and transverse normal strain are neglected in the analysis. The adhesive shear and peel (normal) stresses are assumed to be constant through the adhesive thickness. The joint behavior may be predicted throughout the elastic and inelastic range to failure. Maximum stress theory is used to predict failure for both adhesive and metallic adherends, and maximum strain theory is used to predict failures of laminated adherends. At the predicted failure load, the stresses in adhesive and adherends can be obtained along the overlap length. For a laminated, composite adherend ply-by-ply stress distributions can be obtained. The approach is limited in its application due to the non inclusion of the effects of transverse shear and normal stresses into the analysis. The work of Sharpe and Muha[46] also emphasized this limitation of JTSDL code by showing that the boundary condition on the transverse shear stress at the free-edge is violated by this analysis code.

2.1.3 BOND3/BOND4

The computer codes BOND3 and BOND4 were developed by Renton and Vinson[47-48] to analyze a single lap bonded joint with similar and/or dissimilar adherends of either isotropic or anisotropic materials. This linear elastic analysis is based on the assumption of plane strain and considers applied axial tensile loads and thermal strains. The adhesive layer is modeled after Goland-Reissner assumptions. The computer code is based on a closed form solution obtained for stresses and deformations in adhesive joint and adherends and incorporates transverse shear deformations and normal strain. Thus, the shear stress is zero at each end of the overlap, and reaches its maximum a short distance away from the edge and diminishes somewhat further in the interior of the single lap joint. The distribution of shear and peel stresses in adhesive and axial, transverse shear and normal stresses in each ply of the composite adherends can be obtained as an output from the computer code. Sharpe and Muha[46] found that the shear stress distribution predicted by the BOND4 code compared well with their experimental observations for a single lap bonded joint with identical adherends.

2.1.4 BONJO

A comprehensive linear analysis method and the associated computer program (BONJO Series) was developed by Dickson, et al.[49] for the purpose of analyzing bonded joints in composite structures. Three separate computer programs were developed to analyze the bonded joints in composite structures. They are

1. BONJOIG,
2. BONJOIS,

3. and BONJO.

BONJOIG analyzes any general single lap (different adherends) or double lap bonded joint configuration by assuming a linear elastic stress-strain behavior of adhesive. BONJOIS analyzes only single lap bonded joint configuration in which the two adherends are identical. BONJOIS also assumes a linear elastic stress-strain behavior of adhesive. BONJO approximates the adhesive material behavior by means of a bilinear elastic-perfectly plastic stress-strain relationship, and is an extension of BONJOIG program.

An analytical closed-form solution is obtained for single lap and double lap bonded joints (see Fig. 1.1) with laminated composite material adherends. A narrow uniaxially loaded joint configuration is assumed so that a state of plane stress exists. The mathematical model for the adhesive is based on Goland and Reissner's[1] assumptions i.e., axial stress in the adhesive and through-the-thickness variations of adhesive normal stress and shear stress are neglected during the analysis. The effects of transverse shear deformations and normal strain have been taken into account in analyzing the adherends. This effect is important for an accurate prediction of peak shear stresses in the adhesive because of the relatively low transverse shear stiffness and normal stiffness (through the thickness of the laminate) of most fibrous composites. The work is further extended to include joints with ideally elastic-plastic adhesive stress-strain behavior. Sharpe and Muha[46] made a comparison of adhesive shear and normal stresses obtained from computer codes BONJO, BOND4, JTSDL and NASTRAN for a single lap bonded joint with identical adherends, and found that the stress values predicted by BONJO and BOND4 were nearly the same. They also pointed out that the stresses obtained from the closed form solution BONJO compared fairly well with the experimental observations for a single lap bonded joint with identical adherends.

2.1.5 A4EI

This program was developed by Hart-Smith[50] to analyze adhesive-bonded stepped-lap joints and doublers (see Fig. 1.1). The computer program A4EI is particularly useful in optimizing the proportions of stepped lap joints, as between metallic edge members and composite laminates. It can also be used to analyze bonded joint repairs. Both the analysis and experimental observations have pointed out that the strength of the metal-to-composite stepped-lap joints can be particularly sensitive to poor detailing of the end step of the metal plate as well as the gross mismatch of adherend stiffness. The A4EI program performs a nonlinear analysis of the stepped-lap joints, and accounts for elastic, elasto-plastic, and bilinear adhesive behaviors. The analysis approach is based on the solution to differential equations from the classical continuum mechanics. The analytical solutions are obtained for the stepped-lap bonded joints that include the effect of the type load such as tension, compression, or in-plane shear; and residual thermal stresses due to curing; optimization of joint proportions; the changes in critical failure mode with temperature and/or loading; and the load distribution around the flaws.

2.1.6 PGLUE

The computer code PGLUE was developed by Fogarty and Saff[51] in 1987. The objective of this program is to provide stress and deflection analysis of repairs made with adhesively bonded patches. The computer program PGLUE requires geometry, material properties, and the loading conditions as input, and gives stresses, strains and deflections at various points in the three medium (skin, patch, and adhesive) as output. This program performs a three-dimensional analysis of the bonded repairs and thus, offers significant advantages over the two-dimensional analysis program such as A4EI. PGLUE requires significantly less empirical data than A4EI, and uses only the standard material data and the adhesive stress-strain curve to provide a solution. The major features of this program are given below:

1. A quasi-three dimensional analysis of bonded repairs is performed.
2. Biaxial and shear loadings can be applied.
3. Bilinear as well as elastic/perfectly plastic behavior of the adhesive can be accommodated.
4. Tapered patch repairs with variable thickness can be analyzed.
5. Plastic zone size can be calculated in two in-plane dimensions.

The PGLUE code is based on the quasi-3-D finite element analysis using a linear eight-node hexahedron element. An elastic-plastic analysis of the adhesive is also incorporated into the code to determine load levels at which small scale yielding occurs. The assumption of small scale yielding implies only small modifications to the elastic strain field and adhesive material stress-strain curve to simulate bondline yielding. This resulted in determination of the location and extent of bondline yielding with reasonably small computational time. However, Fogarty and Saff found that this quick design feature limited the accuracy of the plastic analysis and predicted the size of the plastic zone to within 50 percent of the plastic zone size computed by the computer program A4EI.

2.1.7 SAVE

SAVE is a novel, *generalized coordinate* finite element program developed in-house as part of the SBIR Phase II activity. The SAVE program can be utilized to model and analyze various adhesively bonded joint configurations as shown in Fig. 1.1. The computational algorithm of the SAVE program is based on *variable-order* rectangular, cylindrical and wedge solid elements, and does not involve any coordinate interpolation. Thus, only the structural problems having geometry which is exactly discretized as an assemblage of any of the *variable-order* solid element shapes such as rectangular, cylindrical and wedge or their combination thereof, can be analyzed by this analysis technique. However, compared to standard FE formulations based on nodal variables, the *generalized coordinate* finite element formulations presented here provides higher numerical accuracy in the solution of the structural problems having geometry which can be exactly discretized by the selected element shape. Further, through the use of higher-order polynomials in the elemental displacement field approximations, *variable-order* solid elements provide higher accuracy in the solution with substantially lower degrees of freedom in the computational model. The analytical solution obtained by using these elements satisfies the transverse stress continuity at the material interface(s) and the traction-free static boundary conditions in the structure with much higher accuracy. An accurate stress analysis of the structure is a prerequisite to subsequently develop any credible damage evolution and failure prediction methodology.

Conceptually, a *variable-order* element is a higher-order element employing a *complete* set of Mth order polynomials to approximate the elemental displacement field. (In finite element analysis the use of complete polynomials are most desirable[7].) A *variable-order* element allows one to add higher-order polynomial terms in its displacement approximations, albeit, not *hierarchically*. The order M of a *variable-order* element describes the highest degree of the polynomials used to approximate the displacement field of an element in its entire domain. For example, $M = 2$ results in the element displacement(s) being approximated by quadratic polynomial functions. Similarly, $M = 3$ signifies a cubic variation of the displacement field in the entire domain of the element, and so on. In this respect the *variable-order* elements seem very similar to the *p*-type finite elements; however, most of the *p*-type elements do not use a *complete* set of polynomials, and permit only *hierarchic* addition of higher-order polynomial terms.

The principle of virtual work is employed to obtain the stiffness matrices and load vectors for various solid elements subjected to hygrothermomechanical loads. Explicit expressions for the coefficients of stiffness matrices for *variable-order* rectangular, cylindrical and wedge solid elements are derived for the case when the elemental displacement field is approximated by the triple series. The mathematical formulations for these elements are presented in Section 3.

The computational algorithm for SAVE program employs Bernstein polynomials to approximate the elemental displacement field of the *variable-order* rectangular and cylindrical solid elements in the three coordinate directions. It follows much of the standard finite element procedure such as computation of element stiffness and load matrices, assembly of global stiffness and load matrices for the complete structure by enforcing the displacement continuity between the elements, reduction in the total number of the unknown *generalized coordinates* (or displacement coefficients) after accounting for the global boundary constraints on the structure, subsequent restructuring of the global stiffness and load matrices, and solution of the resulting linear system of equations. Once the solution to the unknown *generalized coordinates* is obtained, the displacements, stresses and strains in the structure are then computed. The computer program called SAVE is written in FORTRAN, and is currently implemented on a Cray C90 high performance computer to run large-scale structural analysis.

Several numerical examples were analyzed to demonstrate the accuracy and effectiveness of the *variable-order* solid elements in structural analysis. Some benchmark problems comparing the solutions obtained from the present analysis using *variable-order* rectangular and cylindrical solid elements with those given in the open literature are presented in the next section. In the SAVE computer program the accuracy of solution can be improved either by increasing the order M of the *variable-order* element or by using more *variable-order* elements in the discrete representation of the structure or by using a combination of both. This aspect of the *variable-order elements* is also amply demonstrated by analyzing some benchmark problems (see Section 3) in multiple ways. Some of the major advantages of the displacement-based analysis using *variable-order* rectangular and cylindrical solid elements (SAVE) are listed below:

(i) The continuity of stresses at the interface(s) of the elements of the same material or of different materials is achieved with a very high accuracy without enforcing it *a priori*.

(ii) The static (or natural) boundary conditions at the external surfaces are satisfied with a very high accuracy without enforcing them *a priori*.

(iii) In most cases, the analysis using *variable-order* elements requires less degrees of freedom to solve the problem and achieve same or even higher accuracy of the solution.

(iv) The flexibility of selecting a higher-order approximation function for the displacement field replaces the need of working with the higher-order theories.

However, it is found that there is always an optimum level of order M of the *variable-order* elements beyond which there is not much significant improvement in the accuracy of the solution. Thus, it is preferable to achieve an optimum combination of the order M and the number of *variable-order* elements to analyze a given structural problem. The extension of the *generalized coordinate* finite element analysis program SAVE for the two-dimensional analysis of structures using *variable-order* quadrilateral, triangular, plane stress/plane strain, plate and shell elements is straightforward.

3.0 THREE-DIMENSIONAL LINEAR ELASTIC STRUCTURAL ANALYSIS USING *VARIABLE-ORDER* ELEMENTS

In this section, first, the mathematical formulations for the displacement-based *variable-order* rectangular (hexahedron), cylindrical, wedge and singular 3-D solid (brick) elements are presented. Then these elements are utilized to perform a linear elastic, thermomechanical analysis of some benchmark structural problems. The mathematical formulations presented here are applicable to the analysis of structures exhibiting a wide spectrum of material behavior such as isotropic, orthotropic or monoclinic. Each *variable-order* solid element can have unique material properties defining its material behavior. It is envisaged that the family of *variable-order* rectangular, cylindrical, wedge and singular 3-D solid elements will find its most glamorous application in the analysis of advanced composite material structures having material and geometrical discontinuities where the higher-order displacement approximations would be able to represent the structural response more accurately.

3.1 MATHEMATICAL FORMULATIONS FOR *VARIABLE-ORDER* ELEMENTS

The last four decades have seen the emergence of finite element analysis as the most powerful tool to solve complex engineering problems. Vast improvements in the computational resources, both in terms of storage capacity and processing speed of the computer, has fueled the rapid development of more complex finite elements to efficiently model specific problems and improve accuracy of the solution. In their text Bathe and Wilson[52] described numerous ways to classify the finite element formulations even when restricting oneself to the solution of structural mechanics problems based on the variational principles. For example, a finite element formulation can be displacement-based, stress-based, mixed, or hybrid, etc. The displacement-based finite element formulation is the most widely used because of its simplicity, generality, and good numerical properties.[52] Moreover, the convergence criterion for the displacement-based finite element formulations are precisely established as compared to the other formulations. Each of these formulations have been applied by many researchers to develop a wide variety of beam, plate, shell, plane stress, plane strain, axisymmetric and general three-dimensional elements. In this work only the displacement-based finite element formulations are considered; however, the extension of this work to other types of finite element formulations such as stress-based, mixed, or hybrid can also be undertaken.

The principle of virtual work forms the basis of the displacement-based finite element formulations. The structure is represented as an assemblage of finite number of elements. The displacement field of each element is approximated in the form of a function whose unknown coefficients are treated as *generalized coordinates*. Bathe and Wilson[52] termed this kind of finite element formulation as the *generalized coordinate finite element formulation.* However, most of the standard/commercial finite element analysis models express the *generalized coordinates* in terms of the element nodal point displacements. Polynomials are commonly employed to approximate the element displacement field. The element stiffness and load matrices are formulated, and the global stiffness and load vectors for the complete structure are obtained by assembling the element stiffness and load matrices. Depending upon the type of formulation used either the *generalized coordinates* or the nodal displacements are the unknowns in the numerical analysis. Once the solution for the unknowns is obtained, the displacements, stresses and strains in the structure can be computed.

In the finite element analysis the accuracy of solution depends mainly on the number of elements used, and the nature of assumed displacement functions within the elements. In particular, the accuracy of the analysis can be increased either by using more elements in the representation of the structure or by adding higher-order terms in the assumed displacement functions or by using a combination of both. The first method of improving the accuracy of the solution is known as the *h*-version of finite element analysis. The most common technique to improve the displacement approximations of an element is to *hierarchically* add higher-order terms. This method of improving the accuracy of the solution is known as the *p*-version of finite element analysis.[53-55] Incorporating the advantages of both the *h*- and the *p*- versions is the *h-p* version of the finite element[56,57] that simultaneously utilizes more elements to represent the structure and also add, *hierarchically,* the higher-order terms in the displacement approximations. When the refinements in the mesh and the displacement approximations are performed in an adaptive manner, the resulting finite element technique is known as an *adaptive h-p* version. The work by Zeinkiewicz, et al.,[53,56] Babuska, et al.,[54,57] and Szabo[55] provide a deep insight into *h*- and *p*- , and *h-p* versions of the finite element analysis.

Another commonly used technique to increase the accuracy of the solution is to add the intermediate node(s) to the side(s) of the element. Bathe and Wilson[52] called such an element a *variable-number-nodes element.* While using the *variable-number-nodes element,* it is not always necessary to add the intermediate nodes to more than one side of the element at once. There is a flexibility to choose the side(s) and the number of intermediate node(s) to be added to an element. The most notable feature of the *variable-number-nodes element* is that any addition of intermediate node(s) essentially results in the addition of a higher-order polynomial term(s) in the displacement approximations, albeit, not *hierarchically.* (It may be emphasized here that in this work the term *hierarchically* is used as defined by Zeinkiewicz, et al.[53] That is why this type of FE technique may not exactly fall into the *p*-version of the finite element analysis which is solely used in the context of the *hierarchic* addition of higher-order polynomial terms in the displacement approximations. Thus, without the loss of generality, a *variable-number-nodes element* can be termed as a higher-order finite element. Now, let's consider the formulation of a *variable-number-nodes element* in terms of the *generalized coordinates* instead of the nodal displacements. Any addition of a higher-order polynomial term would now result in an additional *generalized coordinate* (or unknown coefficient) in the assumed displacement approximations of the element. It is proposed to express such an element simply as a *variable-order element.* Thus, a *variable-order element* is a *generalized coordinate finite element* which allows one to add higher-order polynomial terms in the displacement (or even stress) approximations, albeit, not *hierarchically.* The order of the *variable-order* element, denoted as M, describes the degree of polynomial used to approximate the displacement field in the entire domain of an element. For example, $M = 2$ results in the element displacement(s) approximated by quadratic polynomial functions. Similarly, $M = 3$ provides a cubic variation of the displacement field in the entire domain of the element.

Based on the mathematical formulations presented here a computational algorithm in FORTRAN language has been developed for the 3-D *variable-order* rectangular and cylindrical solid elements. The extension of the computational algorithm to incorporate the 3-D wedge and singular solid elements is currently in progress. The computational algorithm follows much of the standard finite element procedure such as computation of element and load stiffness matrices, assembly of global stiffness and load matrices for the complete structure by enforcing the displacement continuity between the elements, reduction in the total number of the unknown *generalized coordinates* (or displacement coefficients) after accounting for the global boundary constraints on the structure, subsequent restructuring of the global stiffness and load matrices, and solution of the resulting linear system of equations. Once the solution to the unknown *generalized coordinates* is obtained, the displacements, stresses and strains in the structure are then computed. In the computational algorithm presented, the accuracy of the solution can be improved either by increasing the order M of the *variable-order* element or by using more *variable-order* elements in the representation of the structure or by using a combination of both. The accuracy and the effectiveness of the *variable-order elements* in analyzing complex structures will be demonstrated in the subsequent works where several numerical examples will be presented comparing the solution obtained from the present analysis with those given in the open literature for some benchmark problems.

The following sections contain the mathematical formulations for the 3-D *variable-order* rectangular, cylindrical, wedge and singular brick elements. First, the mathematical formulations for a *variable-order* rectangular brick element are presented. Most of the formulations described for the *variable-order* rectangular brick element can also be utilized to formulate the stiffness and load matrices of the *variable-order* rectangular wedge and singular brick elements. The major differences among these three elements occur in terms of their assumed displacement field. Subsequently, the mathematical formulations for a *variable-order* cylindrical brick element are presented. The major differences between the mathematical formulations of rectangular and cylindrical brick elements occur due to the definition of the reference coordinate system for quantities such as displacements, strains and stresses and the strain-displacement relations.

3.1.1 Rectangular brick element

3.1.1.1 Strain-displacement relations

Figure 3.1 shows a rectangular brick element in the Cartesian (*x*, *y*, *z*) coordinate system. The generalized displacement vector of the brick element shown in Fig. 3.1 is given by

$$\bar{u} = [u, v, w]^T \tag{1}$$

where $u = u(x,y,z)$, $v = v(x,y,z)$ and $w = w(x,y,z)$.
Let the generalized strain vector for the brick element be

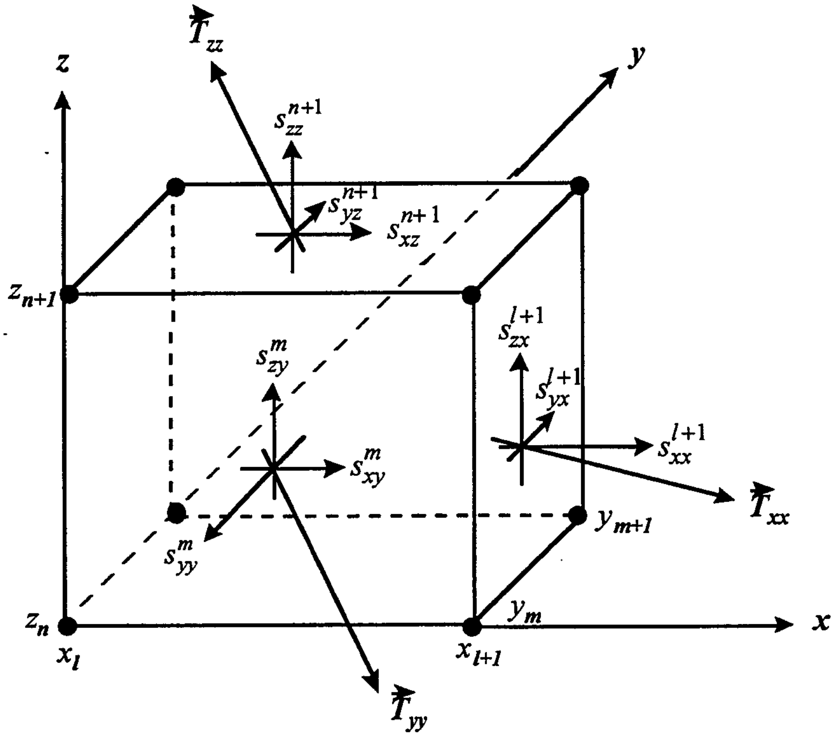

z
$\bar{T}_{zz}$
s_{zz}^{n+1}
y
s_{yz}^{n+1}
s_{xz}^{n+1}
z_{n+1}
s_{zx}^{l+1}
s_{zy}^{m}
s_{yx}^{l+1}
s_{xx}^{l+1}
s_{xy}^{m}
$\bar{T}_{xx}$
y_{m+1}
s_{yy}^{m}
z_n
y_m
x
x_l
x_{l+1}
$\bar{T}_{yy}$

$$x_{l+1} - x_l = a;\ y_{m+1} - y_m = b;\ z_{n+1} - z_n = h.$$

Fig. 3.1 A rectangular solid element in a global Cartesian (*x*, *y*, *z*) coordinate system.

$$\bar{\varepsilon} = [\varepsilon_{xx}, \varepsilon_{yy}, \varepsilon_{zz}, \gamma_{yz}, \gamma_{xz}, \gamma_{xy}]^T \tag{2}$$

Assuming small displacements and displacement gradients, the three-dimensional strain-displacement relations for the brick element are written as:

$$\varepsilon_{xx} = \frac{\partial u}{\partial x}, \ \varepsilon_{yy} = \frac{\partial v}{\partial y}, \ \varepsilon_{zz} = \frac{\partial w}{\partial z}, \gamma_{yz} = \frac{\partial v}{\partial z} + \frac{\partial w}{\partial y}, \ \gamma_{xz} = \frac{\partial u}{\partial z} + \frac{\partial w}{\partial x},$$

$$\gamma_{xy} = \frac{\partial u}{\partial y} + \frac{\partial v}{\partial x} \tag{3}$$

3.1.1.2 Constitutive law

Let the generalized stress vector for the rectangular brick element be given by

$$\vec{\sigma} = [\sigma_{xx}, \sigma_{yy}, \sigma_{zz}, \tau_{yz}, \tau_{xz}, \tau_{xy}]^T \tag{4}$$

Also, let ΔT and Δm represent the distribution of change in temperature and moisture content, respectively, of the elemental brick from some datum values. The term distribution in the previous statement means that the change in the temperature or the moisture content need not be constant in the brick element, and $\Delta T = \Delta T(x,y,z)$ and $\Delta m = \Delta m(x,y,z)$. The constitutive law for the brick element including hygrothermal effects can be written as

$$\vec{\sigma} = \{Q\}\vec{\varepsilon} - \vec{R}^{\alpha}\Delta T - \vec{R}^{\beta}\Delta m \tag{5}$$

where

$$\{Q\} = \begin{bmatrix} Q_{11} & Q_{12} & Q_{13} & 0 & 0 & Q_{16} \\ Q_{12} & Q_{22} & Q_{23} & 0 & 0 & Q_{26} \\ Q_{13} & Q_{23} & Q_{33} & 0 & 0 & Q_{36} \\ 0 & 0 & 0 & Q_{44} & Q_{45} & 0 \\ 0 & 0 & 0 & Q_{45} & Q_{55} & 0 \\ Q_{16} & Q_{26} & Q_{36} & 0 & 0 & Q_{66} \end{bmatrix} \tag{6}$$

and

$$\vec{R}^i = [R_1^i, R_2^i, R_3^i, 0, 0, R_6^i]^T, \qquad i = \alpha, \beta. \tag{7}$$

The stiffness coefficients Q_{ij} in Eq. (6), and the coefficients R_j^i in Eq. (7) are given in Appendix A.

3.1.1.3 Virtual work functional

The statement of virtual work for the brick element is written as

$$\delta W^{\text{int}} = \delta W^{ext} \tag{8}$$

where the internal virtual work for the brick element is

$$\delta W^{\text{int}} = \iiint_V \delta\bar{\varepsilon}^T \bar{\sigma}\, dV\,, \tag{9}$$

and the virtual work due to external forces acting on the element is

$$\delta W^{ext} = \iint_{S_i} \vec{T}_i \cdot \delta\vec{u}_i\, dS + \iiint_V \vec{B} \cdot \delta\vec{u}\, dV\,, \qquad i = 1,2...6\,. \tag{10}$$

In Eq. (10) S_i represents the surface area of the ith face of the elemental brick and V is the volume of the brick element shown in Fig. 3.1. Also, in Eq. (10) $\vec{T}_i$ is external surface traction vector acting on the ith face of the brick element, $\delta\vec{u}_i$ is virtual displacement vector of the ith face of the brick element, and $\vec{B}$ is body force vector in the domain (or volume) V. Substituting Eq. (5) in Eq. (9), neglecting the contribution of body forces in the external virtual work of the brick element given by Eq. (10) and rearranging the terms, the virtual work statement (Eq. (8)) for the brick element subjected to external surface tractions and hygrothermal loads can be written in the following functional form as

$$\iiint_V \delta\bar{\varepsilon}^T \{Q\} \bar{\varepsilon}\, dV = \iint_{S_i} \vec{T}_i \cdot \delta\vec{u}_i dS + \iiint_V \delta\bar{\varepsilon}^T \bar{R}^{\alpha} \Delta T dV + \iiint_V \delta\bar{\varepsilon}^T \bar{R}^{\beta} \Delta m dV \tag{11}$$

The typical external surface tractions acting on the rectangular brick element are shown in Fig. 3.1. They are

$$\begin{aligned}
&s_{xx}^{l}, s_{yx}^{l}, s_{zx}^{l} \text{ at } x = x_l,\; s_{xx}^{l+1}, s_{yx}^{l+1}, s_{zx}^{l+1} \text{ at } x = x_{l+1}\\
&s_{xy}^{m}, s_{yy}^{m}, s_{zy}^{m} \text{ at } y = y_m,\; s_{xy}^{m+1}, s_{yy}^{m+1}, s_{zy}^{m+1} \text{ at } y = y_{m+1}\\
&s_{xz}^{n}, s_{yz}^{n}, s_{zz}^{n} \text{ at } z = z_n,\; s_{xz}^{n+1}, s_{yz}^{n+1}, s_{zz}^{n+1} \text{ at } z = z_{n+1}
\end{aligned} \tag{12}$$

The traction vector $\vec{T}_i$ acting on the ith face of the brick element can be written in terms of the surface tractions acting on that face. For example, the surface traction vectors acting on the faces $x = x_l$ and $x = x_{l+1}$ of the brick element are given by

$$\vec{T}_1 = s_{xx}^{l}(y,z)\vec{\upsilon}^{x1} + s_{yx}^{l}(y,z)\vec{\upsilon}^{y1} + s_{zx}^{l}(y,z)\vec{\upsilon}^{z1} \text{ at } x = x_l \text{ (denoted as face 1), and} \tag{13}$$

$$\vec{T}_2 = s_{xx}^{l+1}(y,z)\vec{\upsilon}^{x2} + s_{yx}^{l+1}(y,z)\vec{\upsilon}^{y2} + s_{zx}^{l+1}(y,z)\vec{\upsilon}^{z2} \quad \text{at} \quad x = x_{l+1} \quad \text{(denoted as face 2),}$$

respectively.

Similarly, the virtual displacement vectors for the faces $x = x_l$ and $x = x_{l+1}$ of the brick element are given by

$$\delta\vec{u}_1 = \delta u(x_l,y,z)\vec{\upsilon}^{x1} + \delta v(x_l,y,z)\vec{\upsilon}^{y1} + \delta w(x_l,y,z)\vec{\upsilon}^{z1} \quad \text{at } x = x_l \text{, and} \qquad (14)$$
$$\delta\vec{u}_2 = \delta u(x_{l+1},y,z)\vec{\upsilon}^{x2} + \delta v(x_{l+1},y,z)\vec{\upsilon}^{y2} + \delta w(x_{l+1},y,z)\vec{\upsilon}^{z2} \quad \text{at } x = x_{l+1}.$$

In the Eqs. (14) and (15) the $\vec{\upsilon}^{xi}, \vec{\upsilon}^{yi}, \vec{\upsilon}^{zi}$ are the direction cosines w.r.t. to *x*-, *y*-, and *z*-coordinate axes for the *i*th face of the brick. Similar expressions for the traction vectors and the virtual displacement vectors for other four faces can also be written. Thus, by using the definitions of traction vectors at the six faces of the brick element in terms of the applied surface tractions given by Eqs. (12) and (13), and also by formulating the virtual displacement vectors for each of the brick faces as described above (see Eqs. (14)), the external virtual work term in Eq. (11) for the brick element is expressed as

$$\begin{aligned}
&\iint_{S_i} \vec{T}_i \cdot \delta\vec{u}_i dS \\
&= \iint_{S_l} \left[s_{xx}^{l}(y,z)\delta u(x_l,y,z) + s_{yx}^{l}(y,z)\delta v(x_l,y,z) + s_{zx}^{l}(y,z)\delta w(x_l,y,z) \right] dydz \\
&+ \iint_{S_{l+1}} \left[s_{xx}^{l+1}(y,z)\delta u(x_{l+1},y,z) + s_{yx}^{l+1}(y,z)\delta v(x_{l+1},y,z) + s_{zx}^{l+1}(y,z)\delta w(x_{l+1},y,z) \right] dydz \\
&+ \iint_{S_m} \left[s_{xy}^{m}(x,z)\delta u(x,y_m,z) + s_{yy}^{m}(x,z)\delta v(x,y_m,z) + s_{zy}^{m}(x,z)\delta w(x,y_m,z) \right] dxdz \qquad (15) \\
&+ \iint_{S_{m+1}} \left[s_{xy}^{m+1}(x,z)\delta u(x,y_{m+1},z) + s_{yy}^{m+1}(x,z)\delta v(x,y_{m+1},z) + s_{zy}^{m+1}(x,z)\delta w(x,y_{m+1},z) \right] dxdz \\
&+ \iint_{S_n} \left[s_{xz}^{n}(x,y)\delta u(x,y,z_n) + s_{yz}^{n}(x,y)\delta v(x,y,z_n) + s_{zz}^{n}(x,y)\delta w(x,y,z_n) \right] dxdy \\
&+ \iint_{S_{n+1}} \left[s_{xz}^{n+1}(x,y)\delta u(x,y,z_{n+1}) + s_{yz}^{n+1}(x,y)\delta v(x,y,z_{n+1}) + s_{zz}^{n+1}(x,y)\delta w(x,y,z_{n+1}) \right] dxdy
\end{aligned}$$

The Eq. (11) in conjunction with Eq. (15) provides the complete statement for virtual work for the elemental brick.

3.1.1.4 Displacement approximations

Let the actual displacement field for the rectangular brick element shown in Fig. 3.1 be represented in the variable separable form by the triple series as

$$u(x,y,z)=\sum_{i=1}^{I}\sum_{j=1}^{J}\sum_{k=1}^{K}U_m F_i^u(x)G_j^u(y)H_k^u(z) \tag{16}$$

$$v(x,y,z)=\sum_{i=1}^{I}\sum_{j=1}^{J}\sum_{k=1}^{K}V_m F_i^v(x)G_j^v(y)H_k^v(z) \tag{17}$$

$$w(x,y,z)=\sum_{i=1}^{I}\sum_{j=1}^{J}\sum_{k=1}^{K}W_m F_i^w(x)G_j^w(y)H_k^w(z) \tag{18}$$

where $m=i+I*(j-1)+I*J*(k-1)$.

In Eqs. (16) $F_i^u(x)$, $G_j^u(y)$ and $H_k^u(z)$ are the displacement approximation functions for the *u*-displacement field for the rectangular brick element in the *x*-, *y*-, and *z*- directions, respectively. Similarly, in Eqs. (17) $F_i^v(x)$, $G_j^v(y)$ and $H_k^v(z)$ are the displacement approximation functions for the v-displacement field, and in Eqs. (18) $F_i^w(x)$, $G_j^w(y)$ and $H_k^w(z)$ are the displacement approximation functions for the *w*-displacement field for the brick element in the *x*-, *y*-, and *z*- directions, respectively. Also, in Eqs. (16)-(18) *I*, *J* and *K* are the upper summation indices for the terms retained in the displacement approximations in the *x*-, *y*-, and *z*- directions, respectively. It may be noted that the largest value of the upper summation indices *I*, *J* or *K* determine the order of the *variable-order* solid element. For the special case of $I=J=K=M$ the order of the *variable-order* rectangular solid element is represented by the value of *M*. Equations. (16)-(18) represent a general form in which various polynomial approximations such as Lagrange, Legendre, Bernstein, B-splines, etc., or trigonometric functions or their combinations thereof can be used to approximate the displacement field for the rectangular brick element.

The test space of the virtual displacement field of the brick element is taken as the same space used for the actual displacement field. This results in a symmetric stiffness matrix for the element. Thus, the virtual displacements for the brick element are written as

$$\delta u(x,y,z)\in\{\delta U_n F_p^u(x)G_q^u(y)H_r^u(z)\} \tag{19}$$

$$\delta v(x,y,z)\in\{\delta V_n F_p^v(x)G_q^v(y)H_r^v(z)\} \tag{20}$$

$$\delta w(x,y,z)\in\{\delta W_n F_p^w(x)G_q^w(y)H_r^w(z)\} \tag{21}$$

where $p\in\{1,2,\dots,I\}, q\in\{1,2,\dots,J\}$, $r\in\{1,2,\dots,K\}$ and $n=p+I*(q-1)+I*J*(r-1)$.

3.1.2 Cylindrical brick element

Figure 3.2 shows a cylindrical brick element in the Cylindrical (x, θ, z) coordinate system. Replacing coordinate variable y by θ in Eqs. (1), (2) and (4)-(21) for the rectangular brick element results in the generalized displacement vector, constitutive law, virtual work functional, and the actual and virtual displacement fields for the cylindrical brick element. Further, in Eq. (15) the term dy is now replaced by $(R+z)\, d\theta$, where R is taken as the radius of curvature of the lower surface of the cylindrical brick element (see Fig. 3.2). The strain-displacement relations for the cylindrical brick element are given below.

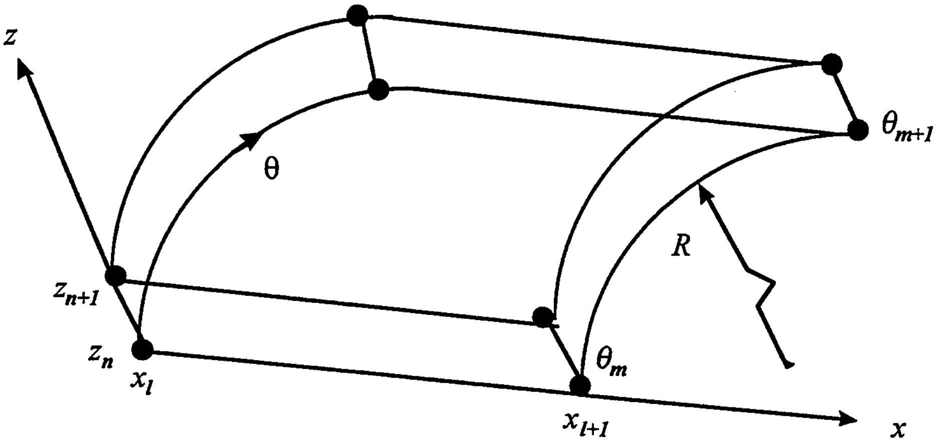

$$x_{l+1} - x_l = a;\ \theta_{m+1} - \theta_m = \Theta;\ z_{n+1} - z_n = h.$$

Fig. 3.2 A cylindrical solid element in a global Cylindrical (x, θ, z) coordinate system.

3.1.2.1 Strain-displacement relations

Based on the discussion given above, the generalized strain vector for the cylindrical brick element is written as

$$\bar{\varepsilon} = [\varepsilon_{xx}, \varepsilon_{\theta\theta}, \varepsilon_{zz}, \gamma_{\theta z}, \gamma_{xz}, \gamma_{x\theta}]^T \tag{22}$$

Assuming small displacements and displacement gradients, the three-dimensional strain-displacement relations for the cylindrical brick element are

$$\varepsilon_{xx}=\frac{\partial u}{\partial x},\qquad \varepsilon_{\theta\theta}=\frac{1}{(R+z)}\left(\frac{\partial v}{\partial\theta}+w\right),\qquad \varepsilon_{zz}=\frac{\partial w}{\partial z},\qquad \gamma_{\theta z}=\frac{\partial v}{\partial z}+\frac{1}{(R+z)}\left(\frac{\partial w}{\partial\theta}-v\right),$$

$$\gamma_{xz}=\frac{\partial u}{\partial z}+\frac{\partial w}{\partial x},\ \gamma_{x\theta}=\frac{1}{(R+z)}\frac{\partial u}{\partial\theta}+\frac{\partial v}{\partial x}. \tag{23}$$

3.1.3 Solid wedge element

Figure 3.3 shows a solid wedge element in the Cartesian (*x*, *y*, *z*) coordinate system. Equations (1)-(11) describing the displacement field, strain-displacement relations, Hooke's law and principle of virtual work for the rectangular brick element are also applicable to the solid wedge element. Other details for the solid wedge element are described in the following paragraphs.

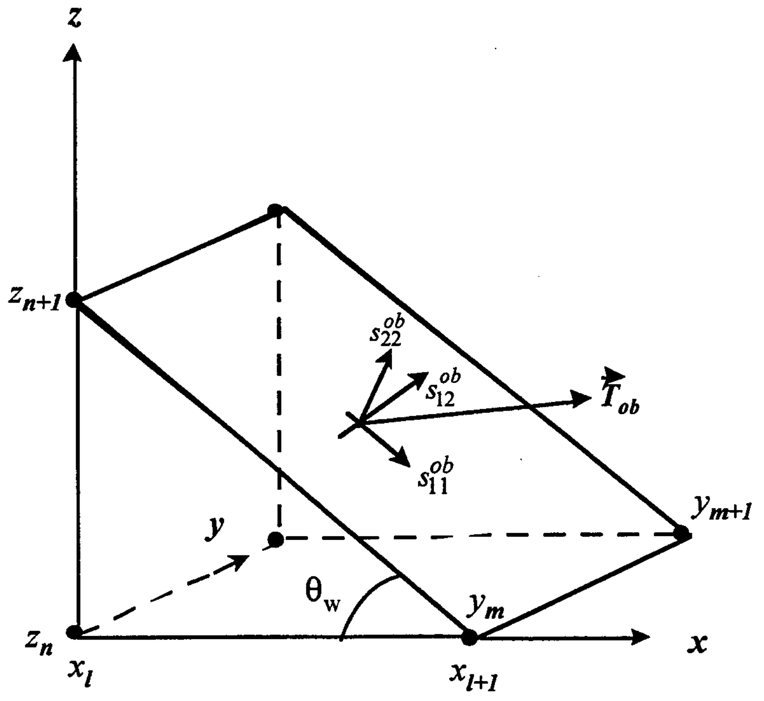

$$x_{l+1}-x_l=a;\ y_{m+1}-y_m=b;\ z_{n+1}-z_n=h.$$

Fig. 3.3 A solid wedge element in a global Cartesian (*x*, *y*, *z*) coordinate system.

3.1.3.1 External work due to surface tractions

The solid wedge element has five faces instead of six as compared to the rectangular brick element described earlier. As shown in Fig. 3.3 the five wedge surfaces (or faces) are $x=x_l,\ z=z_n,\ y=y_m,\ y=y_{m+1}$ and the inclined face where all the three coordinates may vary. However, at the inclined face the two variables *x* and *z* are related to each other by the expression

$$z = x \tan\theta_w, \tag{24}$$

where $\theta_w = \tan^{-1}\left(\dfrac{z_{n+1} - z_n}{x_{l+1} - x_l}\right)$ is the wedge angle as shown in Fig. 3.3. In Eq. (11) the external work term for the wedge element due to the applied surface tractions is given by

$$\begin{aligned}
&\iint\limits_{S_i} \vec{T}_i \cdot \delta\vec{u}_i dS \\
&= \iint\limits_{S_l} \left[s_{xx}^l(y,z)\delta u(x_l,y,z) + s_{yx}^l(y,z)\delta v(x_l,y,z) + s_{zx}^l(y,z)\delta w(x_l,y,z) \right] dydz \\
&+ \iint\limits_{S_m} \left[s_{xy}^m(x,z)\delta u(x,y_m,z) + s_{yy}^m(x,z)\delta v(x,y_m,z) + s_{zy}^m(x,z)\delta w(x,y_m,z) \right] dxdz \\
&+ \iint\limits_{S_{m+1}} \left[s_{xy}^{m+1}(x,z)\delta u(x,y_{m+1},z) + s_{yy}^{m+1}(x,z)\delta v(x,y_{m+1},z) + s_{zy}^{m+1}(x,z)\delta w(x,y_{m+1},z) \right] dxdz \\
&+ \iint\limits_{S_n} \left[s_{xz}^n(x,y)\delta u(x,y,z_n) + s_{yz}^n(x,y)\delta v(x,y,z_n) + s_{zz}^n(x,y)\delta w(x,y,z_n) \right] dxdy \\
&+ \iint\limits_{S_{ob}} \vec{T}_{ob} \cdot \delta\vec{u}_{ob} \sec\theta_w dxdy
\end{aligned} \tag{25}$$

In Eq. (25) quantities $\vec{T}_{ob}$, $\delta\vec{u}_{ob}$ and S_{ob} represent the traction vector, virtual displacement vector and surface area of the oblique (or inclined) surface, respectively. Thus, Eq. (11) in conjunction with Eq. (25) provides the complete statement for virtual work for the solid wedge element.

3.1.3.2 Displacement approximations

As mentioned earlier, the displacement field for the wedge element has a different form than the one used to approximate the rectangular brick element. The actual displacement field for a solid wedge element (see Fig. 3.3) is assumed in the triple series as

$$u(x,y,z) = \sum_{i=1}^{I}\sum_{j=1}^{J}\sum_{k=1}^{K} U_m F_{ik}^u(x,z) H_j^u(y) \tag{26}$$

$$v(x,y,z) = \sum_{i=1}^{I}\sum_{j=1}^{J}\sum_{k=1}^{K} V_m F_{ik}^v(x,z) H_j^v(y) \tag{27}$$

$$w(x,y,z) = \sum_{i=1}^{I}\sum_{j=1}^{J}\sum_{k=1}^{K} W_m F_{ik}^w(x,z) H_j^w(y) \tag{28}$$

where $m = i + I*(j-1) + I*J*(k-1), I - i - k + 1 \geq 0$.

Note the coupling of the displacement approximation functions between x- and z-coordinate directions. This is also obvious from Eq. (24) also where x- and z- coordinates are dependent on each other. Due to the inherent coupling of the displacements, and therefore strains and stresses, in the two coordinate directions, it is felt that the wedge elements might be more suitable to analyze composite laminates with angle-plies. (It may be noted that the wedge element described here can also have coupling in the *x-y* or the *y-z* planes by a simple exchange of the coordinate variables in Eqs. (26)-(28) for the displacements.)

The test space for the virtual displacement field of the wedge element is taken as the same space used for the actual displacement field. Thus, the virtual displacements for the solid wedge element are written as

$$\delta u(x,y,z) \in \{\delta U_n F^u_{pr}(x,z) H^u_q(y)\} \tag{29}$$

$$\delta v(x,y,z) \in \{\delta V_n F^v_{pr}(x,z) H^v_q(y)\} \tag{30}$$

$$\delta w(x,y,z) \in \{\delta W_n F^w_{pr}(x,z) H^w_q(y)\} \tag{31}$$

where $p \in \{1,2,\dots,I\}, q \in \{1,2,\dots,J\}$, $r \in \{1,2,\dots,K\}$ and
$n = p + I*(q-1) + I*J*(r-1)$, $I - p - r + 1 \geq 0$.

3.1.4 Singular brick element

Figure 3.4 shows a rectangular brick element with a crack face (denoted as singular brick element) in Cartesian (*x, y, z*) coordinate system. The mathematical formulations presented earlier (see Eqs. (1)-(21)) for the rectangular brick element are also applicable for the singular brick element. However, for the singular brick element the displacement field is approximated such that the strains and therefore, the stresses at the crack tip are singular in nature. It may be noted that the development of a singular cylindrical brick element from a singular rectangular brick element involves essentially the same changes as described earlier in the section on the mathematical formulations for the cylindrical brick element. This topic will be discussed in detail in the subsequent works where numerical examples and the displacement approximations for singular brick elements will be presented.

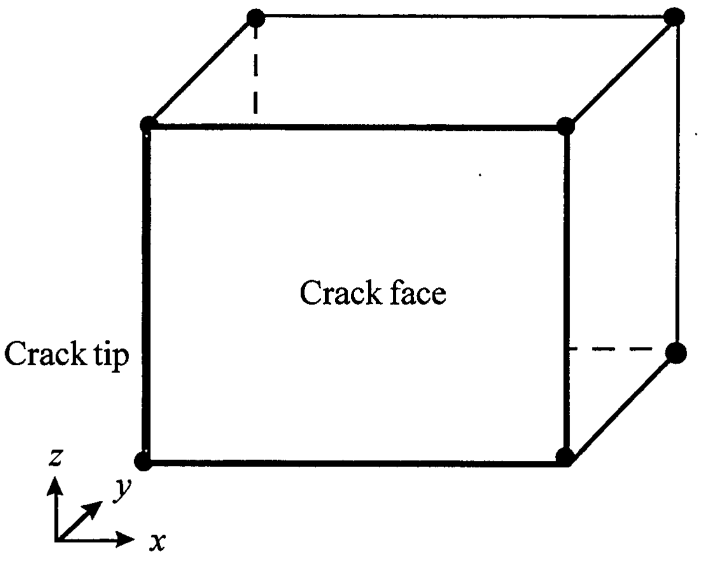

Fig. 3.4 A rectangular solid element with a crack face having stress singularities at the crack tip.

3.1.5 Formulation of stiffness and load matrices

The displacement-based finite element analysis can be regarded as an *extended* Ritz analysis.[52] Thus, the convergence properties and numerical advantages associated with the Ritz method are also applicable to the finite element method. In the Ritz analysis the displacement approximations (e.g., $F_i^u(x)$, $G_j^u(y)$ and $H_k^u(z)$, etc., in Eqs. (16)-(18)) are required to satisfy any enforced kinematic constraints (also known as the essential boundary conditions) on the element. Further, the displacement approximation functions are assumed to be linearly independent in each coordinate direction, and also represent the general and the particular solutions of the structural problem under consideration. Thus, the set of linearly independent displacement approximation functions given in Eqs. (16)-(18) form the *basis* or the *fundamental system* of solutions for the solid element subjected to arbitrary kinematic and static boundary conditions and external loads. These displacement approximation functions are also called the *displacement basis functions*. The procedure for obtaining the stiffness matrix and load vector of a typical rectangular brick element is outlined next. Unless otherwise noted, most of the discussion given here applies to other *variable-order* elements as well. A similar procedure can be adopted to obtain the stiffness and load matrices of other *variable-order* elements.

It is conventional to obtain the stiffness matrix and load vector of an element in a non-dimensional, local coordinate system. This ensures that an element is representative of a typical element located anywhere in the structure. Figure 3.5 shows a rectangular element in Cartesian (ξ,η,ζ) non-dimensional, local coordinate system, where $\xi=\left(\frac{x-x_l}{a}\right)$, $\eta=\left(\frac{y-y_m}{b}\right)$ and $\zeta=\left(\frac{z-z_n}{h}\right)$. All other 3-D solid elements can be similarly represented in a non-dimensional, local coordinate system. The Eqs. (3) for strain-displacement relations in conjunction with the actual and virtual displacements approximations given by Eqs. (16)-(18) and Eqs. (19)-(21), respectively, are substituted into the virtual work functional given by Eq. (11). Then, the integration over the brick volume is performed.

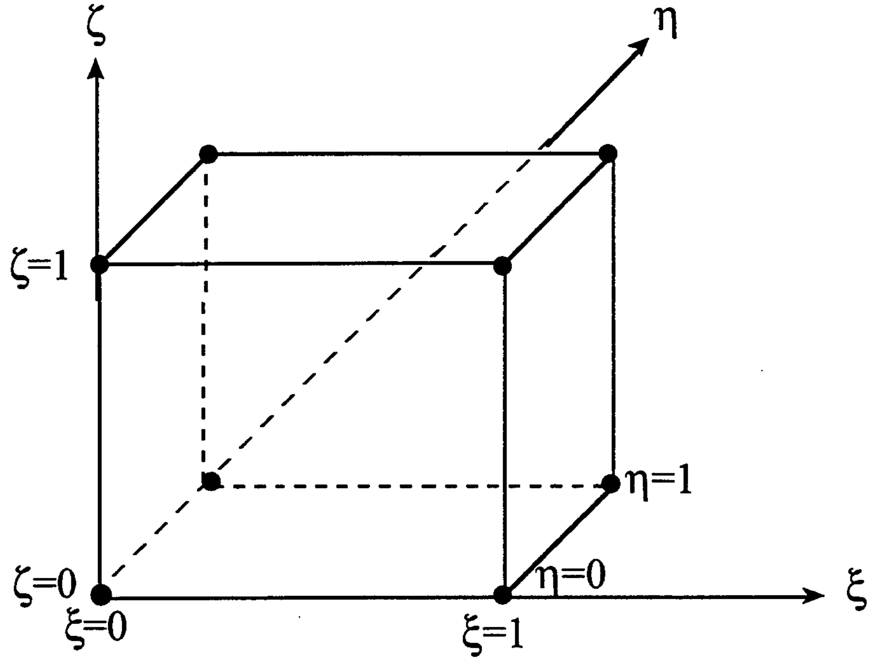

Fig. 3.5 A solid rectangular element in a non-dimensional, local Cartesian (ξ, η, ζ) coordinate system.

This process results in a $3*(I+1)*(J+1)*(K+1)$ system of linear simultaneous equations which can be written in the compact form as

$$\bar{\bar{A}}_{nm}\vec{x}_m = \vec{B}_n^s + \vec{B}_n^\alpha + \vec{B}_n^\beta \tag{32}$$

Equation (32) represents the general form of linear simultaneous equations for the *variable-order* element subjected to mechanical and hygrothermal loads. In Eq. (32) $\vec{x}_m$ is the vector of unknown displacement coefficients (or *generalized coordinates*) , and is given by

$$\vec{x}_m = [\vec{x}_u, \vec{x}_v, \vec{x}_w] \tag{33}$$

where

$\vec{x}_u = [U_1, U_2, ..., U_M]$, $\vec{x}_v = [V_1, V_2, ..., V_M]$, $\vec{x}_w = [W_1, W_2, ..., W_M]$,

and $M = (I+1) * (J+1) * (K+1)$. It may be noted that the *variable-order* wedge element would have less unknown displacement coefficients (or *generalized coordinates*) as compared to the other three *variable-order* elements.

The matrix $\overline{\overline{A}}_{nm}$ in Eq. (32) is the stiffness matrix. The stiffness matrix $\overline{\overline{A}}_{nm}$ is square, symmetric and positive definite. It may be noted that each row in the stiffness matrix $\overline{\overline{A}}_{nm}$ corresponds to a specific term in the virtual displacement field approximation, and each column in the stiffness matrix $\overline{\overline{A}}_{nm}$ corresponds to a specific term in the actual displacement field approximation of the brick element. The coefficients A_{ij} of the stiffness matrix are dependent on the geometry and material properties of the element. Explicit forms of these coefficients are given in Appendix B, C and D for the 3-D rectangular, cylindrical and wedge solid elements, respectively. For most types of assumed displacement basis functions, the integrals given in the Appendices B, C and D can be very accurately evaluated either analytically or using an appropriate numerical integration scheme. The coefficients A_{ij} described in Appendix B, C and D are used to compute the *unrestrained* stiffness matrix $\overline{\overline{A}}_{nm}$ for the 3-D rectangular, cylindrical and wedge solid elements, respectively.

The first term on the right-hand side of Eq. (32) is the force vector obtained from the external virtual work terms (Eq. (15)) due to the applied surface tractions. The elements B_n^s, $n = 1,2,..3*(I+1)*(J+1)*(K+1)$ of the force vector $\vec{B}_n^s$ are dependent upon the magnitude and distribution of applied surface tractions at the element faces. As is evident from Eq. (15), first the applied surface tractions at a particular face are multiplied by the assumed virtual displacement field evaluated at that surface. Then, the resulting product is integrated over the surface area to obtain the contributions of these surface tractions to the external virtual work vector $\vec{B}_n^s$ for the brick element. Depending upon the distributions of the applied surface tractions and assumed virtual displacement field, the evaluation of the integrals of external virtual work terms in Eq. (15) can be either very simple and performed analytically, or can be extremely complex and may require a numerical integration scheme. The elements of the vector $\vec{B}_n^\alpha$ are obtained from the second term on the right-hand side of the virtual work functional, Eq. (11), and represent the contribution of the applied temperature distributions in the element. Similarly, the vector $\vec{B}_n^\beta$ is obtained from the third term on the right-hand side of Eq. (11), and is contribution due to the change in moisture content of the element. Once again, as is evident from Eq. (11), the integrals of terms appearing in the vectors $\vec{B}_n^\alpha$ and $\vec{B}_n^\beta$ can be either simple or complex to evaluate depending upon the distributions of the temperature and moisture content and the assumed virtual displacement field for the element. For uniform applied surface tractions on the face or for a uniform change in temperature or moisture content of the brick element, the integrals of the terms appearing in the force vector $\vec{B}_n^s$ or the vectors $\vec{B}_n^\alpha$ and $\vec{B}_n^\beta$ are simply the integrals of the assumed displacement functions or their first derivatives in the *x*-, *y*- and *z*-directions. In view of the above discussion, the explicit general forms of the terms appearing in the force vectors $\vec{B}_n^s$, $\vec{B}_n^\alpha$ and $\vec{B}_n^\beta$ are not considered very useful, and hence, are not described here. However, these terms will be described when presenting the specific numerical examples.

3.1.6 Boundary conditions for the element

The kinematic (or essential) and static (or natural) boundary conditions for the rectangular brick element subjected to applied surface tractions as shown in Fig. 3.1 are derived here. (A similar procedure can be used to obtain the kinematic and static boundary conditions for other elements as well.) Using Eq. (8) in conjunction with Eqs. (9) and (10), the statement of virtual work for the rectangular brick element can be written as

$$\iiint_V \delta\bar{\varepsilon}^T \bar{\sigma}\, dV = \iint_{S_i} \vec{T}_i \cdot \delta\vec{u}_i\, dS + \iiint_V \vec{B} \cdot \delta\vec{u}\, dV\,, \quad i = 1,2..6\,. \tag{34}$$

Using Eqs. (2) and (4) for the generalized strain and stress vectors, substituting the strain-displacement relations, Eqs. (3), and integrating by parts, the Eq. (34) in conjunction with Eq. (15) results in three equations of equilibrium and a boundary integral term. The three well-known equations of equilibrium are

$$\begin{aligned}
\delta u&: \quad \frac{\partial\sigma_{xx}}{\partial x} + \frac{\partial\sigma_{yx}}{\partial y} + \frac{\partial\sigma_{zx}}{\partial z} + B_1 = 0 \\
\delta v&: \quad \frac{\partial\sigma_{xy}}{\partial x} + \frac{\partial\sigma_{yy}}{\partial y} + \frac{\partial\sigma_{zy}}{\partial z} + B_2 = 0 \\
\delta w&: \quad \frac{\partial\sigma_{xz}}{\partial x} + \frac{\partial\sigma_{yz}}{\partial y} + \frac{\partial\sigma_{zz}}{\partial z} + B_3 = 0
\end{aligned} \tag{35}$$

The condition that the boundary integral term must vanish at the external surfaces results in six sets of kinematic and static boundary conditions for the six faces of the brick element. It may be noted that the virtual displacements are continuous single-valued functions of the spatial coordinates, and vanish on the surfaces on which the displacements are prescribed. The kinematic (or essential) and static (or natural) boundary conditions for the elemental brick are given below:

At the face $x = x_l$:

prescribe u or $\sigma_{xx} = s_{xx}^{l}$ but not both

prescribe v or $\sigma_{yx} = s_{yx}^{l}$ but not both (36)

prescribe w or $\sigma_{zx} = s_{zx}^{l}$ but not both

At the face $x = x_{l+1}$:

prescribe u or $\sigma_{xx} = s_{xx}^{l+1}$ but not both

prescribe v or $\sigma_{yx} = s_{yx}^{l+1}$ but not both (37)

prescribe w or $\sigma_{zx} = s_{zx}^{l+1}$ but not both

At the face $y = y_m$:

prescribe u or $\sigma_{xy} = s_{xy}^{m}$ but not both

prescribe v or $\sigma_{yy} = s_{yy}^{m}$ but not both (38)

prescribe w or $\sigma_{zy} = s_{zy}^{m}$ but not both

At the face $y = y_{m+1}$:

prescribe u or $\sigma_{xy} = s_{xy}^{m+1}$ but not both

prescribe v or $\sigma_{yy} = s_{yy}^{m+1}$ but not both (39)

prescribe w or $\sigma_{zy} = s_{zy}^{m+1}$ but not both

At the face $z = z_n$:

prescribe u or $\sigma_{xz} = s_{xz}^{n}$ but not both

prescribe v or $\sigma_{yz} = s_{yz}^{n}$ but not both (40)

prescribe w or $\sigma_{zz} = s_{zz}^{n}$ but not both

At the face $z = z_{n+1}$:

prescribe u or $\sigma_{xz} = s_{xz}^{n+1}$ but not both

prescribe v or $\sigma_{yz} = s_{yz}^{n+1}$ but not both (41)

prescribe w or $\sigma_{zz} = s_{zz}^{n+1}$ but not both

In the boundary conditions given by Eqs. (36)-(41) the spatial coordinates are omitted for the sake of convenient representation. Thus, in Eqs. (36)-(41), it is implicit that the displacements, stresses and applied tractions are evaluated at spatial coordinates of the face on which they are prescribed. In the variational analysis the equations of equilibrium given by Eqs. (35) and the static (or natural) boundary conditions listed in Eqs. (36)-(41) are satisfied in the weak sense. In other words they are satisfied in the integral sense in the domain, and not point-wise. Whenever the kinematic boundary conditions at the external surfaces of the brick element are prescribed the system of equations for the brick element, Eq. (32), is modified. This is due to the fact that the virtual displacements vanish on the external surfaces on which the displacements are prescribed. The modified stiffness matrix is called the *restrained* stiffness matrix of the element.

Equations (1)-(41) form the basis of the three-dimensional, linear elastic analysis of the structures using *variable-order* rectangular, cylindrical, wedge and singular solid elements. The stiffness matrix and the load vectors for a variety of displacement approximation functions such as Chebyshev, Lagrange, Legendre, and B-splines, Bernstein polynomials, trigonometric functions, etc., or their combinations thereof can now be obtained.

3.2 NUMERICAL EXAMPLES

Based on the mathematical formulations presented in Section 3.1 a computational algorithm in FORTRAN has been developed for three-dimensional analysis of structures using *variable-order* rectangular and cylindrical solid elements. The Bernstein polynomials are employed to approximate the elemental displacement field of *variable-order* rectangular and cylindrical solid elements in the three coordinate directions. The computer program called SAVE is currently implemented on the Cray high performance computer to run large-scale structural analysis.

Several benchmark examples were analyzed using the SAVE program. Here, results are presented for a select few by comparing the solution obtained from the present analysis using *variable-order* rectangular and cylindrical solid elements with those given in the open literature. In the SAVE computer program the accuracy of the solution can be improved either by increasing the order *M* of the *variable-order* element or by using more *variable-order* elements in the discrete representation of the structure or by using a combination of both. This aspect of the *variable-order elements* is also amply demonstrated by analyzing some benchmark problems in multiple ways.

In the following subsections, first, a brief discussion is provided on the Bernstein polynomials employed as displacement approximations for the structural analysis. Next several numerical examples are presented demonstrating the accuracy and effectiveness of the *variable-order* rectangular and cylindrical solid elements in the thermomechanical analysis of structures composed of isotropic and orthotropic materials. The advantages and limitations of the *variable-order* rectangular and cylindrical solid elements are also discussed.

3.2.1 Bernstein polynomials as displacement functions

In general, the Bernstein polynomials belong to the family of Bezier curves.[58] The use of Bernstein polynomials (or Bezier functions) in solving the structural mechanics problems seems to be fairly recent. Perhaps, Singh[59] was the first author to use Bezier polynomials in the structural analysis problems. Singh studied the free-vibration of shells of revolution using Bezier polynomials as displacement approximations. Kumar and Singh[60] employed quintic Bezier (Bernstein) polynomials to approximate the circumferential displacement field in the free vibration analysis of non-circular cylindrical shells. For the purpose of analysis Kumar and Singh[60] divided the cylindrical shell surface into a finite number of segments and enforced C^0, C^1, and C^2 continuities on Bernstein polynomials so as to achieve the continuity of displacements, slopes and curvatures, respectively, between different segments of the cylindrical shell surface. A detail discussion on the methodology to achieve various orders of continuity using Bernstein (Bezier) polynomials is given in Ref. [60]. Kumar and Singh[60] also pointed out that Bezier functions offer easy incorporation of the boundary conditions and provide higher accuracy of the solution with lesser number of unknowns.

Bogdanovich, Pastore and Deepak[61] and Bogdanovich and Deepak[62] employed Bernstein polynomials in the thickness direction to study the three-dimensional state-of-stress in the laminated composite plates using various analytical approaches based on the energy principles. In these works simply-supported, laminated composite plates subjected to transverse bending loads were analyzed. The double Fourier Series was used to approximate the displacements and/or stresses in the inplane directions. The Bernstein polynomials were used to approximate the displacements and/or stresses in the thickness coordinate direction. The problem was essentially reduced to a one-dimensional problem requiring discretization of the structure in the thickness direction only. Bogdanovich, et al.[61,62] presented numerical results by varying the degree of Bernstein polynomials in the thickness directions and achieving the convergence of numerical results as well as the required continuity of stresses across the interfaces of various layers of the laminated structure.

Bogdanovich and Rastogi[63] employed Bernstein polynomials to approximate the displacement field in all three coordinate directions and studied the three-dimensional state-of-stress in bonded composite plates. In this work the general idea of a 3-D brick-type rectangular mosaic parallelepiped aimed at the stress analysis of inhomogeneous materials and structures, proposed in Bogdanovich,[64] was utilized to analyze bonded composite plates subjected to uniaxial extension. Bogdanovich and Rastogi[63] employed three-dimensional formulations based on the principle of minimum potential energy, and presented numerical results for the case when the displacement field in each rectangular brick was approximated by cubic Bernstein polynomials in all three directions.

In the mathematical formulations presented in Section 3.1 for the *variable-order* rectangular and cylindrical solid elements, the elemental displacement field in a non-dimensional (ξ,η,ζ) coordinate system is approximated in the triple series as (Eq. (B-5); Appendix B)

$$\vec{u}(\xi,\eta,\zeta) = \sum_{i=1}^{I}\sum_{j=1}^{J}\sum_{k=1}^{K}\vec{U}_m F_i\ (\xi) G_j(\eta) H_k(\zeta) \tag{42}$$

where $m = i + I*(j-1) + I*J*(k-1)$ and $\vec{u} = [u,v,w]^T$.

Since the displacement-based finite element analysis can be regarded as an *extended* Ritz analysis,[52] the convergence properties and numerical advantages associated with the Ritz method are also applicable to the finite element method. In the finite element analysis the monotonic convergence of the numerical solution is achieved if the elements are complete and compatible.[52] The requirement of completeness means that the displacement functions $F_i\ (\xi)$, $G_j(\eta)$ and $H_k(\zeta)$ in Eq. (42) must be able to represent the rigid body displacements and constant strain states of the element. The compatibility requirement is fulfilled when these displacement functions are continuous within the elements and across the element boundaries. Thus, no gap occurs between the element boundaries when the assembly is performed. The rate of convergence depends upon the type of polynomial functions used in the displacement approximation, and generally, the use of complete polynomials are most desirable.[65] When the displacement functions $F_i\ (\xi)$, $G_j(\eta)$ and $H_k(\zeta)$ in Eq. (42) are assumed as Bernstein polynomials, all the requirements of completeness and compatibility are identically fulfilled.

The Bernstein polynomials, denoted as $B_i^I(t)$, are expressed as[58]

$$B_i^I(t) = \binom{I}{i} t^i (1-t)^{I-i}\ ,\ i = 0,\ldots,I \tag{43}$$

Further, Bernstein polynomials form a *partition of unity*[58], i.e.,

$$\sum_{i=0}^{I} B_i^I(t) \equiv 1 \tag{44}$$

This property of Bernstein polynomials is extremely important and simplifies the application of various kinematic boundary conditions. Incidentally, Eq. (44) is also identical to the condition imposed on shape functions to satisfy the completeness requirement[52] in the finite element analysis. Thus, approximating the displacement functions $F_i(\xi)$, $G_j(\eta)$ and $H_k(\zeta)$ in Eq. (42) by Bernstein polynomials $B_i^I(t)$ given by Eq. (43) identically fulfills the requirements of completeness as described earlier. It may be noted that in fact this completeness requirement is satisfied for any arbitrary degree of Bernstein polynomials (i.e., irrespective of the value of the summation index I in Eqs. (43) and (44)).

In the displacement-based three-dimensional analysis using solid elements the compatibility requirement is automatically fulfilled when the interelement continuity of the three displacements, u, v, and w, is enforced.[52] The property of Bernstein polynomials that $B_0^I(0)=1$, $B_I^I(1)=1$ and $B_i^I(0)=B_i^I(1)=0$, $i=1,\ldots,I-1$ makes it fairly easy to enforce the interelement continuity of the displacements during the assemblage of the elements. Thus, Bernstein polynomials are used to approximate the displacement field of the *variable-order* rectangular and cylindrical solid elements.

The development of computational algorithm for the SAVE computer program is currently based on the assumption that (i) the same type of displacement functions are used to approximate all three components (u, v and w) of the displacement field given in Eq. (42), and (ii) the same order of Bernstein polynomials are used in all the three coordinate directions to approximate a displacement component, i.e., $I=J=K$.

3.2.2 Analysis of laminated plates using *variable-order* rectangular solid elements

In this section the following three problems are analyzed using *variable-order* rectangular solid elements:

(i) A simply-supported $[0/90/0]_T$ laminated plate subjected to sinusoidal loading on the top surface. The numerical results as obtained from the present analysis are compared with those obtained by Pagano[66] using exact three-dimensional elasticity formulations.

(ii) A $[0/90]_S$ laminated plate subjected to uniaxial extension. A comparison of the interlaminar stress solution as obtained from the present analysis is made with that obtained by Pagano.[67]

(iii) A $[0/90]_S$ laminated plate subjected to thermal loads.

In all the three numerical examples studied the layers are assumed to be of equal thickness.

3.2.2.1 Transverse bending of a laminated plate

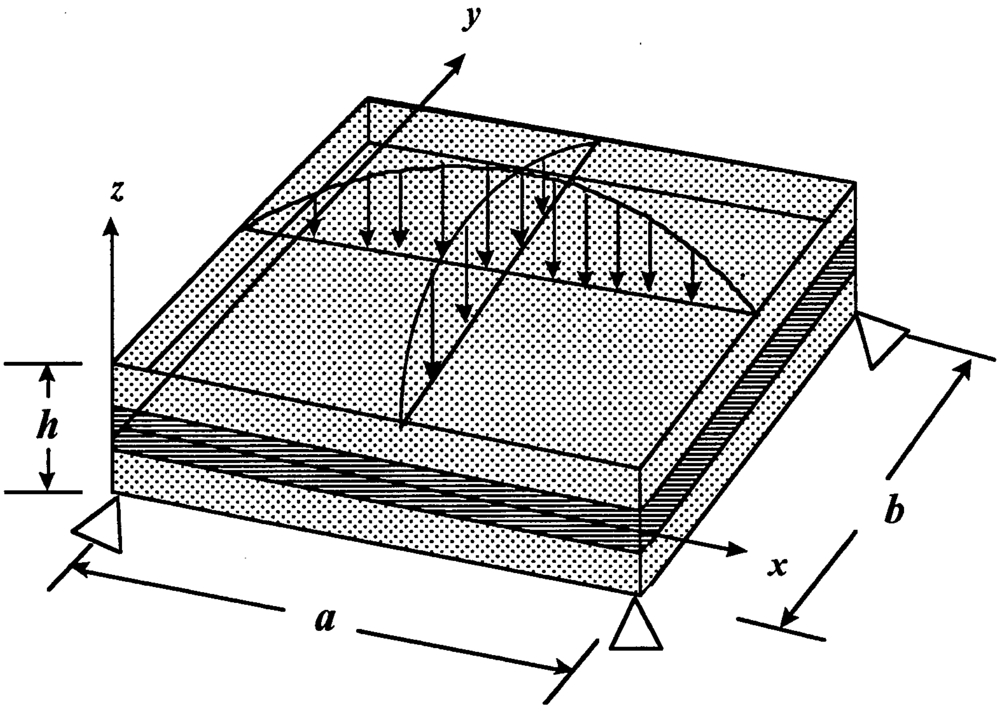

Fig. 3.6 A simply-supported $[0/90/0]_T$ laminate subjected to sinusoidal loading on the top surface.

A simply-supported $[0/90/0]_T$ laminated plate subjected to sinusoidal loading on the top surface (see Fig. 3.6) is analyzed using one *variable-order* rectangular solid element in x- and y-direction each and one *variable-order* rectangular solid element per layer in the z-direction. Henceforth, this discretization of the laminated plate would be denoted as 1x1x3 mesh. The benchmark solution to this problem was presented by Pagano.[66] The origin of the right-handed coordinate system is chosen at the corner of the middle surface of the plate, i.e., $0 \le x \le a$, $0 \le y \le b$ and $-\frac{h}{2} \le z \le \frac{h}{2}$ (see Fig. 3.6). The simply-supported laminated plate is subjected to the following global kinematic boundary conditions:

$$u(x,0,z) = u(x,b,z) = 0\,;\; v(0,y,z) = v(a,y,z) = 0\,; \text{and}$$
$$w(0,y,z) = w(a,y,z) = w(x,0,z) = w(x,b,z) = 0\,. \qquad (45)$$

As is shown in Fig. 3.6 the laminated plate is subjected to external sinusoidal load on the top surface of the 0^0 ply. In other words only the *variable-order* rectangular solid element representing the 0^0 ply is subjected to an applied surface traction given by

$$s_{zz}^{n+1}(x,y) = q_0 Sin(\frac{\pi x}{a}) Sin(\frac{\pi y}{b}) \tag{46}$$

Thus, in Eq. (15) the only nonzero external force is $s_{zz}^{n+1}(x,y)$ applied at $z = z_{n+1} = \frac{h}{2}$ on the surface S_{n+1}, and for this numerical example Eq. (15) for the *variable-order* rectangular solid element representing the 0^0 ply reduces to

$$\iint_{S_i} \bar{T}_i \cdot \delta\bar{u}_i dS = \int_0^b \int_0^a q_0 Sin(\frac{\pi x}{a}) Sin(\frac{\pi y}{b}) \delta w(x,y,\frac{h}{2}) dx dy \tag{47}$$

Thus, in Eq. (32) the force vectors $\vec{B}_n^{\alpha} = \vec{B}_n^{\beta} = 0$ for all the elements, and the force vector $\vec{B}_n^{s}$ would receive non-zero contributions only from the *variable-order* rectangular solid element representing the 0^0 ply. These non-zero terms are computed from Eq. (47) above. For the purpose of analysis a square laminate is assumed i.e., $a = b$ in Fig. 1. The material properties for the lamina are taken from Ref. [66] as

$$E_1 = 25 \text{ Msi}, E_2 = E_3 = 1.0 \text{ Msi}, G_{12} = G_{13} = 0.5 \text{ Msi}, G_{23} = 0.2 \text{ Msi},$$
$$\upsilon_{12} = \upsilon_{13} = \upsilon_{23} = 0.25 \tag{48}$$

The results obtained from the present 3-D analysis using the *variable-order* rectangular solid elements are compared with those obtained by Pagano[66] using closed-form solution approach. These are presented in Tables 3.1 and 3.2. The normalized stresses used in Tables 3.1 and 3.2 are described below:

$$\overline{\sigma_{xx}} = \sigma_{xx} / (q_0 s^2), \quad \overline{\sigma_{yy}} = \sigma_{yy} / (q_0 s^2), \quad \overline{\sigma_{zz}} = \sigma_{zz} / q_0,$$
$$\overline{\tau_{xy}} = \tau_{xy} / (q_0 s^2), \quad \overline{\tau_{xz}} = \tau_{xz} / (q_0 s), \quad \overline{\tau_{yz}} = \tau_{yz} / (q_0 s), \tag{49}$$

where $s = a / h$. Table 3.1 shows the improvement in the accuracy of the solution as the order of the *variable-order* rectangular solid elements is increased from $M = 3$ to $M = 6$. For $M = 3$ the displacement field in the *variable-order* rectangular solid element is approximated by cubic Bernstein polynomials, i.e., $I = J = K = 3$ in Eq. (42). Similarly, for $M = 6$ the displacement field in the *variable-order* rectangular solid element is approximated by the sixth degree Bernstein polynomials ($I = J = K = 6$ in Eq. (42)). During the analysis the mesh design was kept fixed at 1x1x3. The solution obtained from the present analysis using *variable-order* rectangular solid element with $M = 6$ shows excellent agreement with the exact solution of Pagano (see Table 3.1). Note the numerically small values of quantity $\overline{\sigma_{zz}}$ at the unloaded surface, i.e., at $z = -\frac{h}{2}$. In order to satisfy the traction free static boundary condition at the surface $z=-\frac{h}{2}$, the stress component σ_{zz} (= s_{zz}^{n}) should be identically zero at this surface. In the present analysis, this static boundary condition is *not* enforced *a priori*. Rather, at the converged solution this condition is satisfied in the week sense. Similarly, from Table 3.1 it can be seen that the quantity $\overline{\sigma_{zz}}$ attains a unit value at the loaded surface, $z=\frac{h}{2}$, for the converged solution corresponding to $M = 6$. Thus, the converged solution provides a very high accuracy for this boundary condition, $\sigma_{zz} = s_{zz}^{n+1}$ at $z=\frac{h}{2}$, without it being enforced *a priori* in the solution. Some more numerical results obtained for various *a/h* ratios using *variable-order* rectangular solid elements with $M = 6$ and with the mesh design 1x1x3 are presented in Table 3.2. It can be seen that the results obtained from the present 3-D analysis using *variable-order* rectangular solid elements ($M = 6$) are practically identical to the results obtained by Pagano[66] for various *a/h* ratios.

Table 3.1. Comparison between the results obtained from (a) the present 3-D analysis performed with one variable-order rectangular solid element each in x- and y- directions and one variable-order rectangular solid element per layer in the z-direction, and (b) those obtained by Pagano [1970] for a $[0/90/0]_T$ simply supported, laminated plate ($a = b = 4h$) subjected to sinusoidal loading on the top surface (see Fig. 3.6).

QUANTITY	$M = 3$	$M = 4$	$M = 5$	$M = 6$	Pagano [1970]
$\overline{\sigma_{zz}}(\frac{a}{2},\frac{b}{2},-\frac{h}{2})$	0.00930	0.00223	0.00051	0.00004	0.0
$\overline{\sigma_{zz}}(\frac{a}{2},\frac{b}{2},\frac{h}{2})$	0.9266	0.9967	0.9983	0.9999	1.0
$\overline{\sigma_{xx}}(\frac{a}{2},\frac{b}{2},\frac{h}{2})$	0.699	0.740	0.798	0.801	0.801
$\overline{\sigma_{xx}}(\frac{a}{2},\frac{b}{2},-\frac{h}{2})$	-.659	-0.786	-0.752	-0.754	-0.755
$\overline{\sigma_{yy}}(\frac{a}{2},\frac{b}{2},\frac{h}{6})$	0.471	0.523	0.532	0.534	0.534
$\overline{\sigma_{yy}}(\frac{a}{2},\frac{b}{2},-\frac{h}{6})$	-0.491	-0.545	-0.534	-0.556	-0.556
$\overline{\tau_{xy}}(0,0,\frac{h}{2})$	-0.0662	-0.0506	-0.0506	-0.0511	-0.0511
$\overline{\tau_{xy}}(0,0,-\frac{h}{2})$	0.0652	0.0501	0.0500	0.0505	0.0505
$\overline{\tau_{xz}}(0,\frac{b}{2},0)$	0.291	0.254	0.254	0.256	0.256
$\overline{\tau_{yz}}(\frac{a}{2},0,0)$	0.3166	0.2160	0.2127	0.2172	0.2172

Table 3.2. Comparison between the results obtained for various a/h ratios (a) from the present 3-D analysis performed with one variable-order (M = 6) rectangular solid element each in x- and y- directions and one variable-order (M = 6) rectangular solid element per layer in the z-direction, and (b) by Pagano [1970] for a $[0/90/0]_T$ simply supported, laminated plate (a = b) subjected to sinusoidal loading on the top surface (see Fig. 3.6).

QUANTITY	$a/h = 2$	$a/h = 4$	$a/h = 10$	$a/h = 50$	$a/h = 100$
$\overline{\sigma_{xx}}(\frac{a}{2},\frac{b}{2},\frac{h}{2})$	(a) 1.436 (b) 1.436	(a) 0.801 (b) 0.801	(a) 0.590 (b) 0.590	(a) 0.541 (b) 0.541	(a) 0.539 (b) 0.539
$\overline{\sigma_{xx}}(\frac{a}{2},\frac{b}{2},-\frac{h}{2})$	(a) -0.937 (b) -0.938	(a) -0.754 (b) -0.755	(a) -0.590 (b) -0.590	(a) -0.541 (b) -0.541	(a) -0.539 (b) -0.539
$\overline{\sigma_{yy}}(\frac{a}{2},\frac{b}{2},\frac{h}{6})$	(a) 0.668 (b) 0.669	(a) 0.534 (b) 0.534	(a) 0.284 (b) 0.285	(a) 0.184 (b) 0.185	(a) 0.181 (b) 0.181
$\overline{\sigma_{yy}}(\frac{a}{2},\frac{b}{2},-\frac{h}{6})$	(a) -0.742 (b) -0.742	(a) -0.556 (b) -0.556	(a) -0.288 (b) -0.288	(a) -0.185 (b) -0.185	(a) -0.181 (b) -0.181
$\overline{\tau_{xy}}(0,0,\frac{h}{2})$	(a) -0.0859 (b) -0.0859	(a) -0.0511 (b) -0.0511	(a) -0.0288 (b) -0.0289	(a) -0.0216 (b) -0.0216	(a) -0.0214 (b) -0.0213
$\overline{\tau_{xy}}(0,0,-\frac{h}{2})$	(a) 0.0702 (b) 0.0702	(a) 0.0505 (b) 0.0505	(a) 0.0290 (b) 0.0289	(a) 0.0216 (b) 0.0216	(a) 0.0214 (b) 0.0213
$\overline{\tau_{xz}}(0,\frac{b}{2},0)$	(a) 0.164 (b) 0.164	(a) 0.256 (b) 0.256	(a) 0.357 (b) 0.357	(a) 0.393 (b) 0.393	(a) 0.395 (b) 0.395
$\overline{\tau_{yz}}(\frac{a}{2},0,0)$	(a) 0.2591 (b) 0.2591	(a) 0.2172 (b) 0.2172	(a) 0.1228 (b) 0.1228	(a) 0.0842 (b) 0.0842	(a) 0.0828 (b) 0.0828

3.2.2.2 Uniaxial extension of a laminated plate

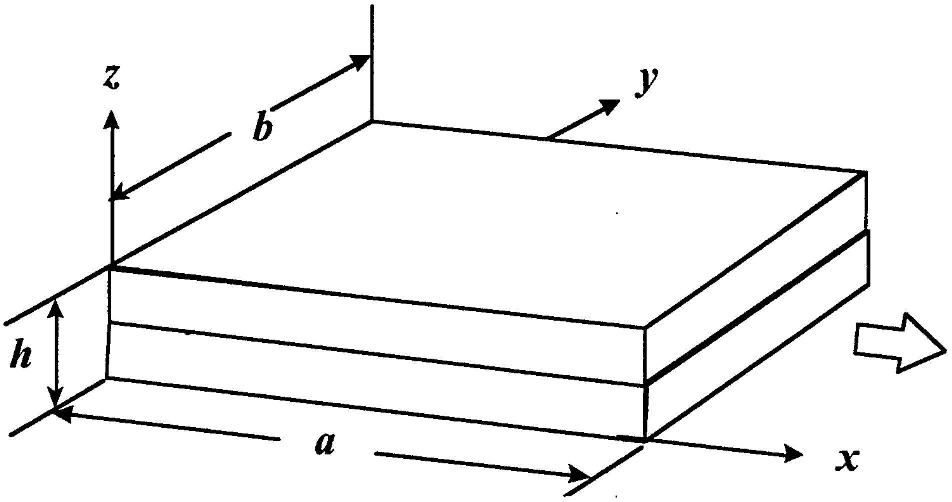

Fig. 3.7 $[0/90]_S$ laminate subjected to uniform axial extension.

This example problem involves the analysis of interlaminar stresses in a $[0/90]_S$ laminated plate subjected to uniaxial extension (see Fig. 3.7) using *variable-order* rectangular solid elements. The solution to this classical problem was presented by Pagano[67] in 1974. Later on Pagano and Soni[69] also solved this problem using a global-local variational model. The focus of this example problem is to study the continuity of interlaminar stresses at the 0/90 interface of the $[0/90]_S$ laminated plate subjected to uniaxial extension. For this purpose a series of systematic analyses were performed so as to achieve an accurate and converged numerical solution. The analyses were performed either by increasing the number of *variable-order* rectangular solid elements in the mesh while keeping the order M of the *variable-order* rectangular solid elements constant or by increasing the order M of the *variable-order* rectangular solid elements without changing the number of *variable-order* rectangular solid elements in the mesh. Here the final results are presented for the following three analyses performed using

(i) 1x12x8 mesh (i.e., one *variable-order* rectangular solid element in the x-direction, 12 *variable-order* rectangular solid element in the y-direction and 8 *variable-order* rectangular solid element in the z-direction) with $M = 3$ (d.o.f = 9,002),
(ii) same mesh design as in (i) above but with $M = 4$ (d.o.f = 20,0611), and
(iii) 1x20x12 mesh (i.e., one *variable-order* rectangular solid element in the x-direction, 20 *variable-order* rectangular solid element in the y-direction and 12 *variable-order* rectangular solid element in the z-direction) with $M = 3$ (d.o.f = 22,178).

Due to the symmetry of the geometrical and material properties and the applied loading, only 1/8th of the configuration of the $[0/90]_S$ laminated plate ($a = b = 4h$; see Fig. 3.7) need be analyzed. The uniform extension of the laminated plate is achieved by applying a uniform axial displacement at the ends $x = a$. For the purpose of analyses the following lamina elastic constants are taken from References [67,68].

$$E_1 = 20 \text{ Msi}, E_2 = E_3 = 2.1 \text{ Msi}, G_{12} = G_{13} = G_{23} = 0.85 \text{ Msi}, \upsilon_{12} = \upsilon_{13} = \upsilon_{23} = 0.21 \quad (50)$$

The distributions of interlaminar stresses as obtained from the three analyses are plotted along the y-direction at $x/a = 0.5$. All the stress components are normalized by the applied axial strain. The distributions of the transverse normal stress σ_{zz} as obtained from the three analyses at the mid surface of the $[0/90]_S$ laminate in the 90° layer are shown in Fig. 3.8. As shown in Fig. 3.8 the distributions of the transverse normal stress σ_{zz} as obtained from the three analyses are essentially the same. The normalized peak value of

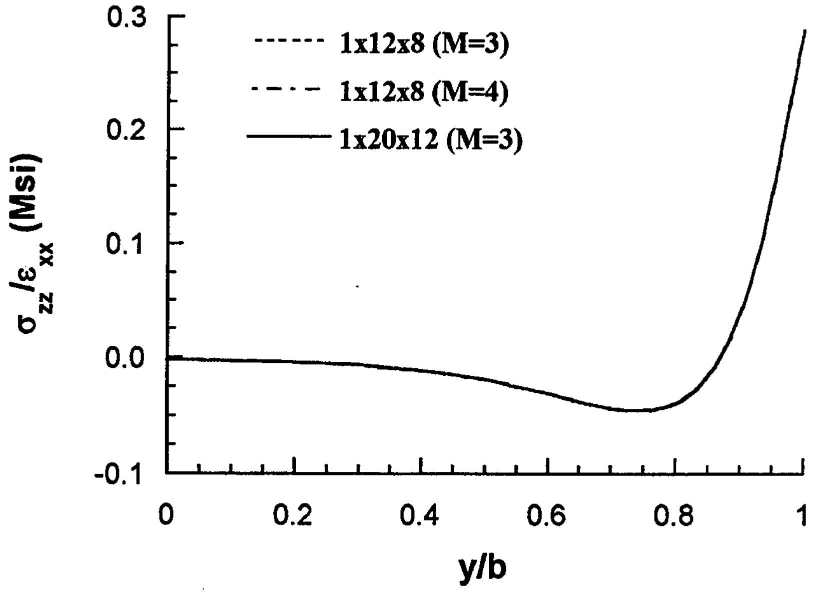

Fig. 3.8 Distributions of transverse normal stress σ_{zz} at the mid plane of a $[0/90]_S$ laminate subjected to uniform axial extension.

0.3 Msi for this stress component, which occurs at the free edge $y/b = 1$, compares very well with those obtained by Pagano[67] and Pagano and Soni[68].

Next the attention is turned to the interface of 0/90 layers where achieving the continuity of the transverse normal stress σ_{zz} and the transverse shear stress τ_{yz} is of special significance. The distributions of the normalized transverse normal stress component σ_{zz} as obtained from the three analyses at the interface of the 0/90 layers are shown in Figs. 3.9-3.12. The first look at Fig. 3.9 suggests that the continuity of the transverse normal stress component σ_{zz} is satisfied extremely well all along the y-direction for the analysis performed using 1x12x8 mesh with M = 3. (Similar results were obtained from the other two analyses as well, but are not presented here to save space.) However, a closer look at the distributions of the transverse normal stress component σ_{zz} in the 0° and 90° layers at the interface of 0/90 layers in the vicinity of the free edge, $0.95 \le y/b \le 1.0$, show that somewhere in the vicinity of $y/b \approx 0.98$ the two curves representing the stress values in the 0° and 90° plies start to separate with some oscillations encroaching into the solution (see Fig. 3.10). A similar conclusion can be drawn regarding the distributions of the transverse normal stress component σ_{zz} in the 0° and 90° layers at the interface of 0/90 layers in the vicinity of the free edge as obtained from the analysis performed using 1x12x8 mesh with M = 4 (see Fig. 3.11), except that the two curves now start to separate around $y/b \approx 0.988$. While there is more than

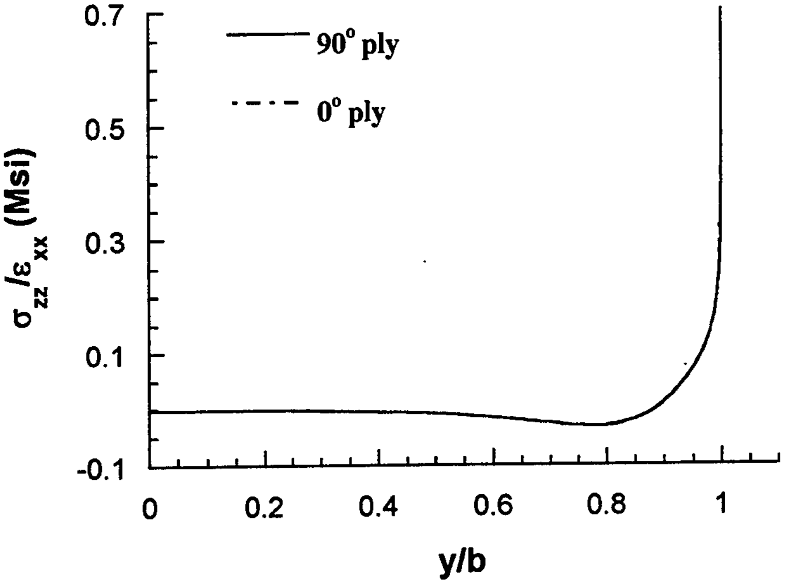

Fig. 3.9 Distributions of transverse normal stress σ_{zz} at the 0/90 interface of a $[0/90]_S$ laminate subjected to uniform axial extension (1x12x8 mesh with $M = 3$).

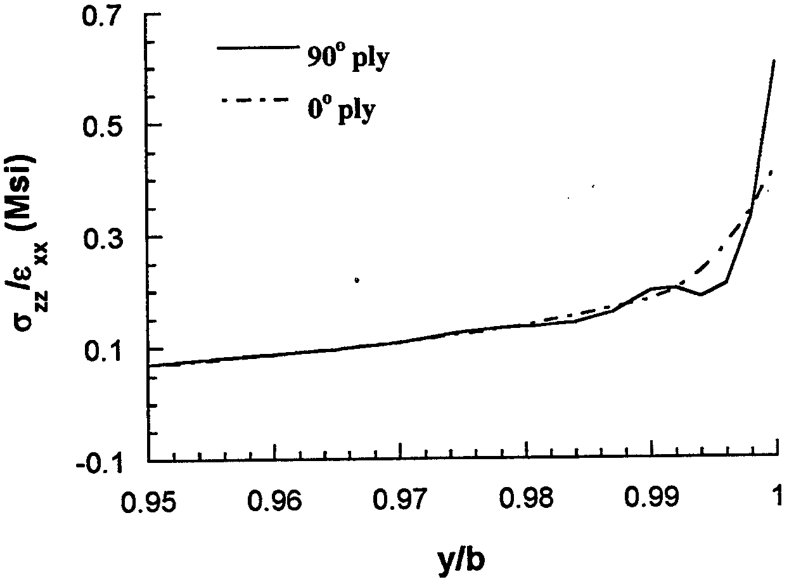

Fig. 3.10 Distributions of transverse normal stress σ_{zz} in the close vicinity of the free-edge at the 0/90 interface of a $[0/90]_S$ laminate subjected to uniform axial extension (1x12x8 mesh with $M = 3$).

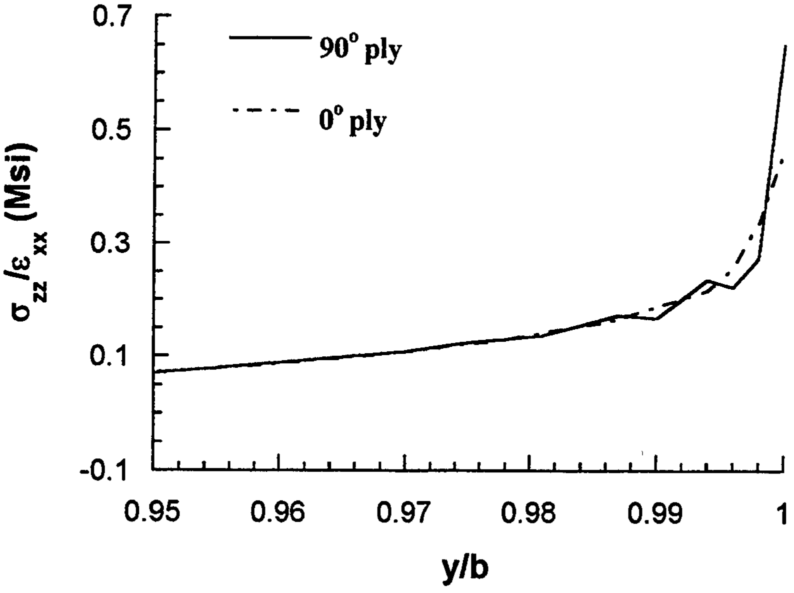

Fig. 3.11 Distributions of transverse normal stress σ_{zz} in the close vicinity of the free-edge at the 0/90 interface of a $[0/90]_S$ laminate subjected to uniform axial extension (1x12x8 mesh with $M = 4$).

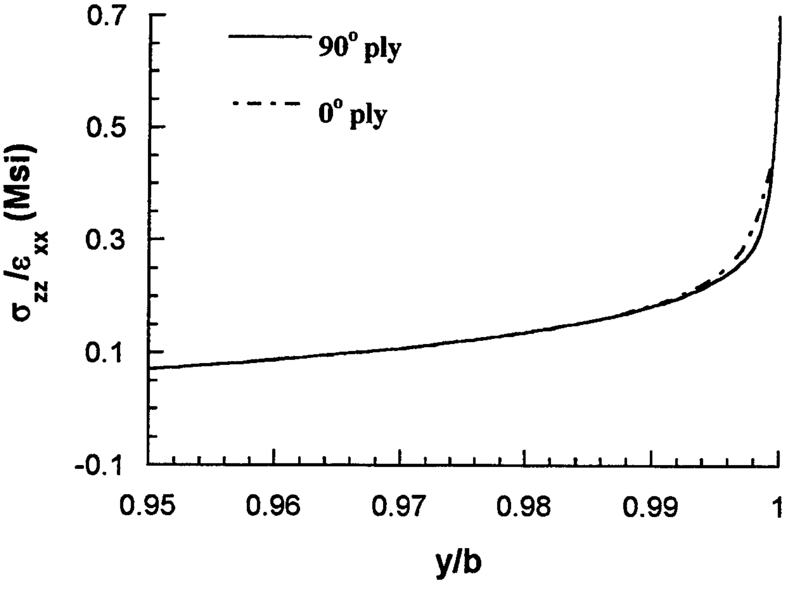

Fig. 3.12 Distributions of transverse normal stress σ_{zz} in the close vicinity of the free-edge at the 0/90 interface of a $[0/90]_S$ laminate subjected to uniform axial extension (1x20x12 mesh with $M = 3$).

twofold increase in the degrees of freedom between the two analysis, there does not seem to be a whole lot of improvement in the solution of the problem. Next, Fig. 3.12 shows the distributions of the transverse normal stress component σ_{zz} in the 0° and 90° layers at the interface of 0/90 layers in the vicinity of the free edge, $0.95 \leq y/b \leq 1.0$, for the analysis performed with 1x20x12 mesh with M = 3. As is shown in Fig. 3.12 the continuity of the transverse normal stress component σ_{zz} is satisfied extremely well in this analysis, even in the extreme vicinity of the free edge $y/b = 1$. The two curves tend to separate only around $y/b \approx 0.994$ and all the oscillations observed in the earlier solutions have gone. Here, it is extremely important to mention that the numerical values of the transverse normal stress component σ_{zz} used to create the plots in Figs. 3.9-3.12 (and for all the other plots presented in this work) are the *true* values as obtained from the different *variable-order* rectangular solid elements meeting at a material point in the discretized structure. In other words these values are not averaged in any way from the two or more adjacent elements as is normally done in many standard FE programs. Thus, the results presented here are all the more accurate.

Similar observations are also made regarding the distributions of the transverse shear stress component τ_{yz} from the three analyses in the vicinity of the free edge. Only the distributions of the transverse shear stress component τ_{yz} as obtained from the third analysis (1x20x12 mesh with $M = 3$) are presented here as shown in Figs. 3.13-3.14. As shown in Figs. 3.13 and 3.14 the continuity of the transverse shear stress component τ_{yz} at the 0/90 interface is satisfied extremely well all along the y-direction except in the extreme vicinity of the free edge, $0.98 \leq y/b \leq 1.0$. It has been observed that in the vicinity of the free edge, the continuity of transverse shear stresses is more difficult to satisfy as compared to the continuity of the transverse normal stress σ_{zz} at the interface of different layers (or materials).

The results presented above emphasize the importance of achieving a balance between the order M and the number of the *variable-order* elements to be used to analyze a given structural problem so as to achieve the desired accuracy in the converged solution. This also justifies the need to use transition elements as described earlier. The *variable-order* transition elements can be used to greatly reduce the degrees of freedom in the problem by modeling the regions of high stress gradients with the elements having order M higher than that used for the elements in regions where stress response is fairly uniform, simultaneously using transition elements in the intermediate regions connecting two different order elements. Further, it is also shown that in a displacement-based analysis using the *variable-order* rectangular solid elements, the continuity of stresses at the interface of the elements of the same material or even of the different materials is achieved with a very high accuracy without enforcing it *a priori*.

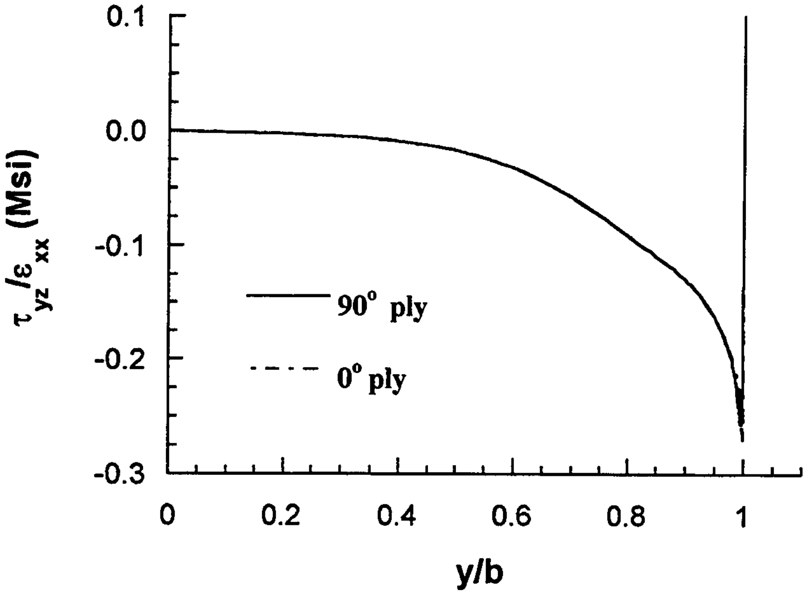

Fig. 3.13 Distributions of transverse shear stress τ_{yz} at the 0/90 interface of a [0/90]$_S$ laminate subjected to uniform axial extension (1x20x12 mesh with $M = 3$).

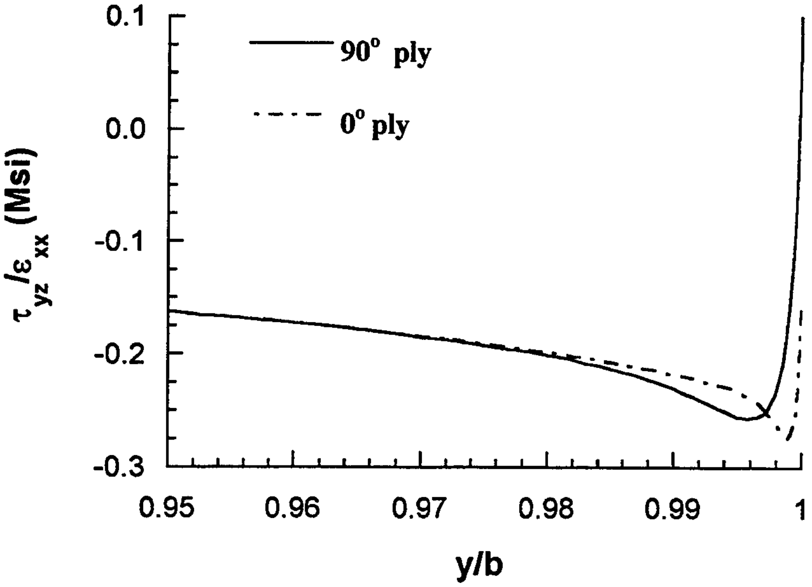

Fig. 3.14 Distributions of transverse shear stress τ_{yz} in the close vicinity of the free-edge at the 0/90 interface of a [0/90]$_S$ laminate subjected to uniform axial extension (1x12x8 mesh with $M = 3$).

3.2.2.3 Restrained thermal expansion of a laminated plate

Next a $[0/90]_S$ laminated plate ($a/b = 5$, $b/h = 10$; see Fig. 3.7 for notations) subjected to uniform thermal load $\Delta T = -100^0$C and restrained against expansion in axial direction is analyzed using the *variable-order* rectangular solid elements. A 1x20x12 mesh with $M = 3$ (d.o.f = 22,178) is used to model and analyze the 1/8th configuration of the structure. For this numerical example the force vectors $\bar{B}_n^s = \bar{B}_n^\beta = 0$ in Eq. (32) for all the elements, and the force vector $\bar{B}_n^\alpha$ would receive non-zero contributions from all the 240 *variable-order* rectangular solid elements. For the purpose of analysis the three-dimensional thermomechanical properties of the lamina material are taken as $E_1 = 20$ Msi, $E_2 = E_3 = 1.5$ Msi, $G_{12} = G_{13} = 0.8$ Msi, $G_{23} = 0.48$ Msi, $\upsilon_{12} = \upsilon_{13} = 0.3$, $\upsilon_{23} = 0.55$, $\alpha_1 = 0.4\text{e-}6$ /°C, $\alpha_2 = \alpha_3 = 15.0\text{e-}6$ /°C.

The distributions of non-zero stresses and displacements as obtained from the present analysis at $x/a = 0.5$ at the 0/90 interface in the 0^0 and 90^0 layers are shown in Figs. 3.15-3.19. As is shown in Fig. 3.15 the distributions of the normal stress σ_{xx} in the 0^0 and 90^0 layers are fairly uniform along the *y*-direction except in the vicinity of the free edge $y/b = 1$ where this stress component shows a steep rise in the magnitude with high stress gradients. The distributions of the other in-plane normal stress component σ_{yy} in the 0^0 and 90^0 layers along the *y*-direction are shown in Fig. 3.16. The normal stress component σ_{yy} should attain a zero value at the free edge so as to satisfy the traction-free static boundary condition at the edge $y/b = 1$. However, as is the case with most FE based numerical analyses, the solution from the present analysis also fails to exactly satisfy this static boundary condition at the free edge at material interface. Figures 3.17 and 3.18 depict excellent continuity of transverse normal stress σ_{zz} and transverse shear stress τ_{yz}, respectively, achieved from the present analysis at the 0/90 interface. The distributions of the normalized displacements *v* and *w* along *y*-direction are shown in Fig. 3.19. The transverse normal displacement *w* shows a steep change in its magnitude in the vicinity of the edge $y/b = 1$.

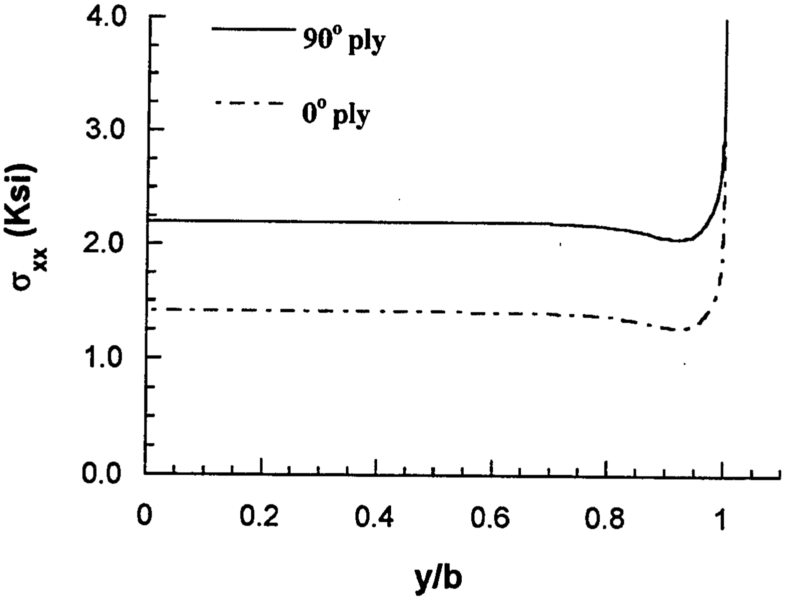

Fig. 3.15 Distributions of normal stress σ_{xx} at the 0/90 interface of a $[0/90]_S$ laminate subjected to uniform thermal loading.

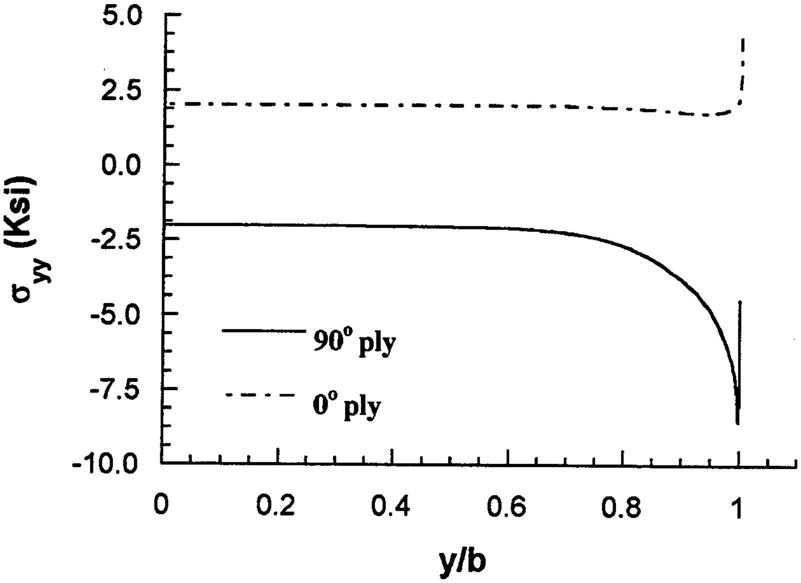

Fig. 3.16 Distributions of normal stress σ_{yy} at the 0/90 interface of a $[0/90]_S$ laminate subjected to uniform thermal loading.

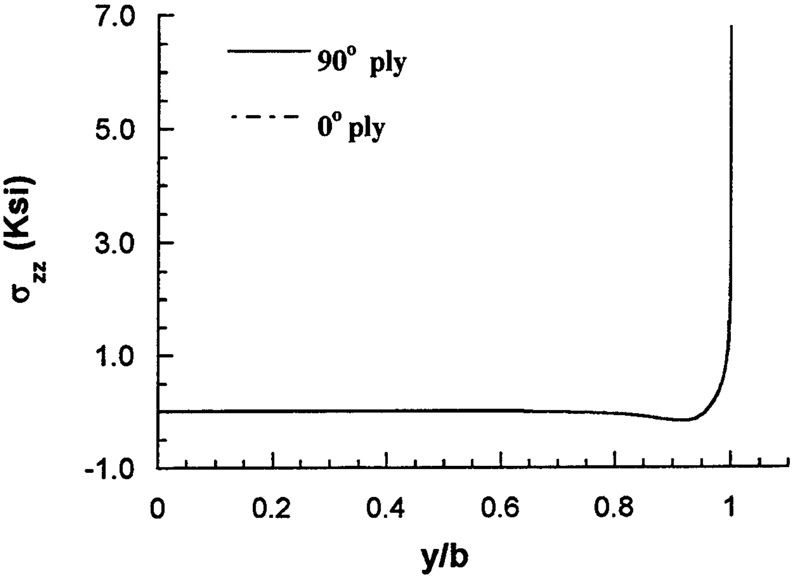

Fig. 3.17 Distributions of transverse normal stress σ_{zz} at the 0/90 interface of a $[0/90]_S$ laminate subjected to uniform thermal loading.

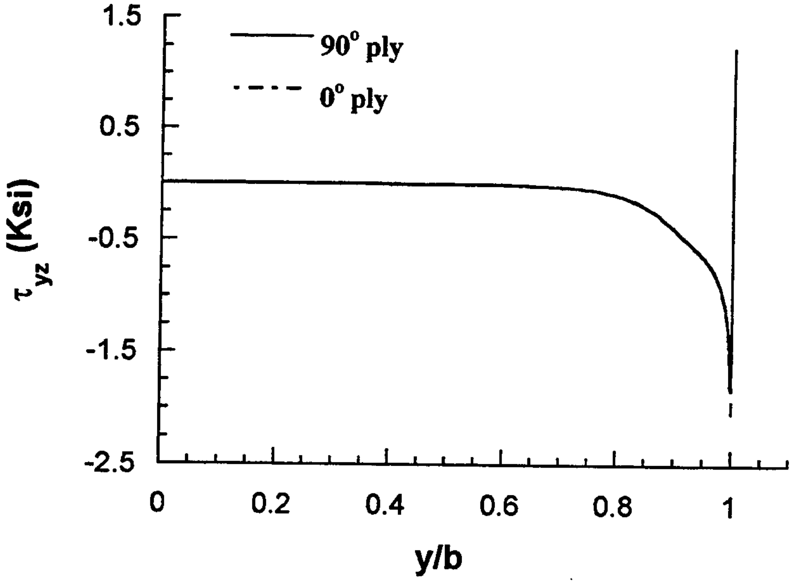

Fig. 3.18. Distributions of transverse shear stress τ_{yz} at the 0/90 interface of a $[0/90]_S$ laminate subjected to uniform thermal loading.

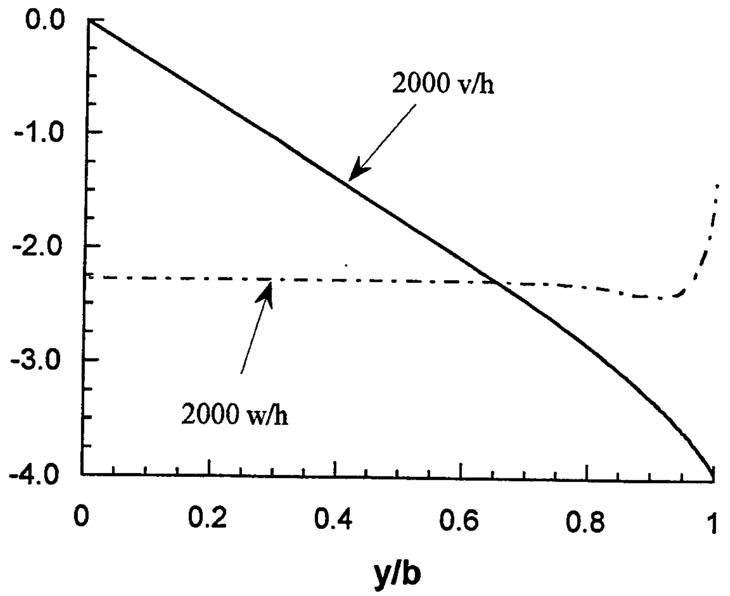

Fig. 3.19 Distributions of transverse displacements at the 0/90 interface of a $[0/90]_S$ laminate subjected to uniform thermal loading.

3.2.3 Analysis of cylindrical shells using *variable-order* cylindrical solid elements

In this section the following three problems are analyzed using *variable-order* cylindrical solid elements:

(i) A simply-supported $[90/0/90]_T$ laminated cylindrical panel subjected to sinusoidal loading on the top surface. The numerical results as obtained from the present analysis are compared with those obtained by Ren[69].

(ii) An infinitely long, thick, isotropic circular cylinder subjected to internal pressure. The numerical results obtained from the present analysis are compared with those given in the verification manual of the commercial software package I-DEAS[70] and also with the plane-stress Strength of Materials (S.O.M.) solution.[71]

(iii) A $[0/90]_T$ laminated cylindrical panel subjected to longitudinal extension.

In the numerical examples (i) and (iii) the orthotropic layers are assumed to be of equal thickness.

3.2.3.1 Transverse bending of a laminated cylindrical panel

A simply-supported $[90/0/90]_T$ laminated cylindrical panel subjected to sinusoidal loading on the top surface (see Fig. 3.20) is analyzed using one *variable-order* cylindrical solid element in *x*-and *y*-direction each and one *variable-order* cylindrical solid element per layer in the z-direction. The benchmark solution to this problem was presented by Ren.[69] As shown in Fig. 3.20 the origin of the right-handed coordinate system is located at the corner of the middle surface of the cylindrical panel, i.e., $0 \le x \le a$, $0 \le \theta \le \Theta$ and

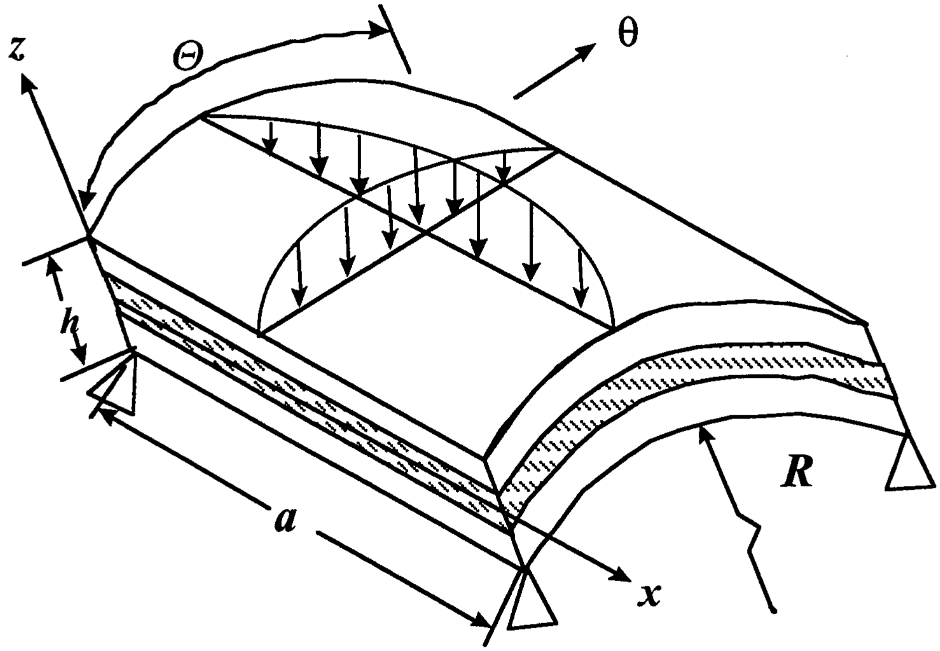

Fig. 3.20 A simply-supported $[90/0/90]_T$ laminated cylindrical panel subjected to sinusoidal loading on the top surface.

$-\frac{h}{2} \le z \le \frac{h}{2}$. The simply-supported cylindrical panel shown in Fig. 3.20 is subjected to the following kinematic boundary conditions:

$$u(x,0,z) = u(x,\Theta,z) = 0;\ v(0,\theta,z) = v(a,\theta,z) = 0;\ \text{and}$$
$$w(0,\theta,z) = w(a,\theta,z) = w(x,0,z) = w(x,\Theta,z) = 0. \tag{51}$$

The laminated cylindrical panel is subjected to an external sinusoidal load on the top surface of the 0^0 ply. Thus, the *variable-order* cylindrical solid element representing the 0^0 ply is subjected to an applied surface traction given by

$$s_{zz}^{n+1}(x,\theta) = q_0 Sin(\frac{\pi x}{a}) Sin(\frac{\pi\theta}{\Theta}) \tag{52}$$

Thus, in Eq. (15) the only nonzero external force is $s_{zz}^{n+1}(x,\theta)$ applied at $z = z_{n+1} = \frac{h}{2}$ on the surface S_{n+1}, and for this numerical example Eq. (15) for the *variable-order* cylindrical solid element representing the 0^0 ply reduces to

$$\iint_{S_i} \vec{T}_i \cdot \delta\vec{u}_i dS = \int_0^a \int_0^\Theta q_0 Sin(\frac{\pi x}{a}) Sin(\frac{\pi \theta}{\Theta}) \delta w(x,\theta,\frac{h}{2})(R+h) d\theta dx \qquad (53)$$

Further, in Eq. (32) the force vectors $\vec{B}_n^{\alpha} = \vec{B}_n^{\beta} = 0$ for all the elements, and only the force vector $\vec{B}_n^{s}$ for the *variable-order* cylindrical solid element representing the 0^0 ply will contain non-zero terms computed from Eq. (53) above. The geometrical parameters for the laminated panel are *a/R = 5* and $\Theta = \pi / 3$ radians (see Fig. 3.20). The lamina material properties are the same as given in Eq. (48).

Table 3.3 shows the results obtained from the present 3-D analysis using *variable-order* cylindrical solid elements and those obtained by Ren[69] for various *R/h* ratios. The normalized quantities used in Table 3.3 are described below:

$$\overline{\sigma_{xx}} = \sigma_{xx} / (q_0 s^2), \qquad \overline{\sigma_{\theta\theta}} = \sigma_{\theta\theta} / (q_0 s^2), \qquad \overline{\tau_{x\theta}} = \tau_{x\theta} / (q_0 s^2),$$
$$\overline{\tau_{xz}} = \tau_{xz} / (q_0 s), \qquad \overline{\tau_{\theta z}} = \tau_{\theta z} / (q_0 s), \qquad \overline{w} = 100 w E_3 / (q_0 h s^4), \qquad (54)$$

where $s = R / h$. The *variable-order* cylindrical solid elements with order $M = 6$ provided a converged solution satisfying the static boundary conditions σ_{zz} (= s_{zz}^n) at $z = -\frac{h}{2}$ and $\sigma_{zz} = s_{zz}^{n+1}$ at $z = \frac{h}{2}$. Thus, only the numerical results corresponding to $M = 6$ are presented here. As shown in Table 3.3 the results obtained from the present analysis are practically identical to the results obtained by Ren[69] for various *R/h* ratios except for the case when *R/h = 50.* The accuracy of the solution seems to get slightly reduced when very thin $(h / R << 1)$ cylindrical solid elements are used in the analysis. This aspect of the analysis using *variable-order* cylindrical solid elements needs further attention and will be subjected to more rigorous examination during future studies.

Table 3.3. Comparison between the results obtained for various R/h ratios (a) from the present 3-D analysis performed with one variable-order (M = 6) cylindrical brick element each in x- and θ- directions and one variable-order (M = 6) cylindrical brick element per layer in the z-direction, and (b) by Ren [1989] for a [90/0/90]$_T$ simply supported, finite length (a/R = 5), laminated cylindrical panel subjected to sinusoidal loading on the top surface (see Fig. 3.20).

QUANTITY	$R/h = 2$	$R/h = 4$	$R/h = 10$	$R/h = 20$	$R/h = 50$
$\overline{\sigma_{\theta\theta}}(\frac{a}{2},\frac{\theta}{2},\frac{h}{2})$	(a) 2.638 (b) 2.637	(a) 1.252 (b) 1.252	(a) 0.957 (b) 0.957	(a) 0.860 (b) 0.860	(a) 0.750 (b) 0.753
$\overline{\sigma_{\theta\theta}}(\frac{a}{2},\frac{\theta}{2},-\frac{h}{2})$	(a) -3.944 (b) -3.951	(a) -1.558 (b) -1.562	(a) -1.055 (b) -1.058	(a) -0.895 (b) -0.899	(a) -0.751 (b) -0.760
$\overline{\sigma_{xx}}(\frac{a}{2},\frac{\theta}{2},\frac{h}{2})$	(a) 0.1135 (b) 0.1135	(a) 0.0306 (b) 0.0306	(a) 0.0170 (b) 0.0170	(a) 0.0141 (b) 0.0141	(a) 0.0152 (b) 0.0153
$\overline{\sigma_{xx}}(\frac{a}{2},\frac{\theta}{2},-\frac{h}{2})$	(a) -0.0489 (b) -0.0489	(a) -0.0170 (b) -0.0170	(a) -0.0099 (b) -0.0099	(a) -0.0068 (b) -0.0069	(a) -0.0020 (b) -0.0021
$\overline{\tau_{x\theta}}(0,0,\frac{h}{2})$	(a) -0.0350 (b) -0.0350	(a) -0.00959 (b) -0.00959	(a) -0.00310 (b) -0.00310	(a) 0.00099 (b) 0.00099	(a) 0.00939 (b) 0.00943
$\overline{\tau_{x\theta}}(0,0,-\frac{h}{2})$	(a) 0.07499 (b) 0.07499	(a) 0.02564 (b) 0.02565	(a) 0.01530 (b) 0.01531	(a) 0.01455 (b) 0.01457	(a) 0.02030 (b) 0.02040
$\overline{\tau_{xz}}(0,\frac{\theta}{2},-\frac{h}{4})$	(a) 0.04574 (b) 0.04575	(a) 0.01671 (b) 0.01672	(a) 0.01063 (b) 0.01064	(a) 0.01032 (b) 0.01034	(a) 0.01427 (b) 0.01436
$\overline{\tau_{\theta z}}(\frac{a}{2},0,-\frac{h}{4})$	(a) 0.552 (b) 0.552	(a) 0.532 (b) 0.533	(a) 0.509 (b) 0.510	(a) 0.483 (b) 0.486	(a) 0.411 (b) 0.426
$\overline{w}(\frac{a}{2},\frac{\theta}{2},0)$	(a) 16.723 (b) 16.728	(a) 3.692 (b) 3.694	(a) 1.576 (b) 1.577	(a) 1.015 (b) 1.017	(a) 0.770 (b) 0.774

3.2.3.2 An infinite, thick isotropic cylindrical shell under internal pressure

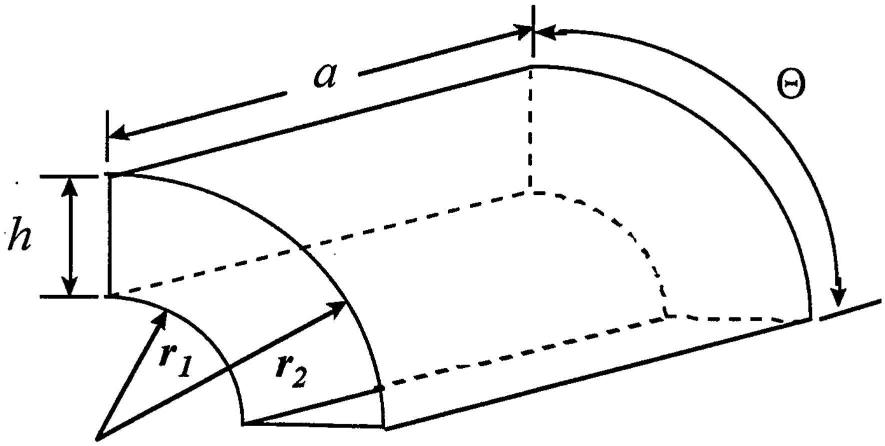

Fig. 3.21 1/4th configuration of a thick, isotropic cylindrical shell subjected to uniform internal pressure.

In this example an infinite, thick isotropic cylindrical shell subjected to internal pressure loading is analyzed using *variable-order* cylindrical solid elements. This problem is taken from the verification manual[70] of commercial FE package I-DEAS.™ The plane-stress Strength of Materials (S.O.M.) solution to this problem is also obtained from the equations given in the text by Srinath.[71] Due to the symmetry of geometrical and material properties and applied loading only 1/4th configuration of the cylindrical shell is modeled in the present analysis as shown in Fig. 3.21. The appropriate symmetric kinematic boundary conditions are imposed in the x- and θ-directions. The geometrical parameters of the 1/4th configuration of the thick cylindrical shell are $r_1 = 0.1$ m, $r_2 = 0.2$ m, $a = 1.0$ m and $\Theta = \pi/2$ radians. The material properties of the cylinder are taken as E = 200 MPa and $\upsilon = 0.3$. The cylindrical panel is subjected to a uniform pressure load of 60 MPa (= $q0$) on the inner- surface. Thus, the *variable-order* cylindrical solid element representing the inner most surface of the cylindrical shell is subjected to an applied surface traction given by

$$s_{zz}^{n}(x,\theta) = q_0 \qquad (55)$$

Thus, in Eq. (15) the only nonzero external force is $s_{zz}^{n}(x,\theta)$ applied at $z = z_n = 0$ on the surface S_n, and for this numerical example Eq. (15) for the *variable-order* cylindrical solid element representing the innermost surface of the cylindrical shell reduces to

$$\iint_{S_i} \bar{T}_i \cdot \delta\bar{u}_i dS = \int_0^{a}\int_0^{\Theta} q_0 \delta w(x,\theta,0) R d\theta dx \qquad (56)$$

Further, in Eq. (32) the force vectors $\bar{B}_n^{\alpha} = \bar{B}_n^{\beta} = 0$ for all the elements, and only the force vector $\bar{B}_n^s$ for the *variable-order* cylindrical solid element representing the innermost surface of the cylindrical shell will contain non-zero terms computed from Eq. (56) above.

The numerical results for this example are obtained using three different computational models. The first model uses only one *variable-order* cylindrical solid element to represent the structure shown in Fig. 3.21; the second model uses two identical *variable-order* cylindrical solid elements through the thickness (1x1x2 mesh); and the third model uses eight *variable-order* cylindrical solid elements through the thickness (1x1x8 mesh with non-uniform *z*-refinement). The numerical results obtained from the analysis performed using the first computational model with the order of the *variable-order* cylindrical solid element systematically increased from $M = 2$ to $M = 8$ are presented in Table 3.4. Further, the numerical results obtained from the analyses performed using (i) the second model with the order of the *variable-order* cylindrical solid element increased systematically from $M = 2$ to $M = 5$, and (ii) the third model with the order of the *variable-order* cylindrical solid element taken as $M = 2$ are presented in Table 3.5. For comparison the results given in the verification manual[70] of commercial FE package I-DEAS^{TM} and the plane-stress S.O.M. solution[71] are also provided in Tables 3.4 and 3.5. In Tables 3.4 and 3.5 the stresses are normalized by the applied pressure load ($q0$) and the displacements are normalized by the shell thickness ($h = r_1 - r_2$). As shown in Table 3.4, the numerical results indicate an improvement in the accuracy of the solution as the order of the *variable-order* cylindrical solid element is increased from $M = 2$ to $M = 8$. However, beyond a certain optimum level of the order of *variable-order* elements (e.g., $M = 6$ for this problem) there is not much significant improvement in the accuracy of the solution. Instead, as indicated by the numerical results presented in Table 3.5, it is advantageous to increase the number of *variable-order* cylindrical solid elements in the analysis while keeping the order M of *variable-order* elements the same. For example, compare the solutions obtained for $M = 2$ and $M = 4$ from the first and second models, respectively (see Tables 3.4 and 3.5). The numerical results obtained from the third model seem to provide the converged solution with the least number of d.o.f. in the analysis (see Table 3.5). However, the non-uniform refinement of the mesh in the *z*-direction that provided the converged solution, was achieved after a number of trial and errors. Thus, sometimes it is computationally efficient (in terms of time) to simply increase the order *M* of the *variable-order* elements using a uniform mesh design. From the numerical results presented in Tables 3.4 and 3.5 it can be observed that, as compared to I-DEAS[70], the present analysis provides a highly accurate solution with much lower degrees of freedom in the model. The infinite, thick isotropic cylindrical shell described above was also analyzed subjected to external pressure using *variable-order* cylindrical solid elements. The third model

Table 3.4. Comparison between the results obtained from (a) the present 3-D analysis performed using a single variable-order cylindrical solid element, (b) the analysis performed using I-DEAS[70], and (c) the Strength of Materials (S.O.M.) plane-stress solution given in the text by Srinath[71] for an infinite length, thick isotropic cylindrical shell subjected to internal pressure loading (see Fig. 3.21).

QUANTITY	$M=2$	$M=4$	$M=6$	$M=8$	I-DEAS[70]	S.O.M Solution[71]
$\bar{\sigma}_{zz}(r = 0.1m)$	-0.590	-0.974	-0.999	-1.001	-0.967	-1.0
$\bar{\sigma}_{\theta\theta}(r = 0.1m)$	1.802	1.655	1.644	1.644	1.633	1.667
$\bar{w}(r = 0.1m)$	5.8e-4	5.8e-4	5.8e-4	5.8e-4	5.8e-4	5.9e-4
$\bar{\tau}_{\max}(r = 0.1m)$	1.196	1.315	1.322	1.323	1.3	1.333
$\bar{\sigma}_{zz}(r = 0.2m)$	0.170	0.007	0.003	0.002	0.0	0.0
$\bar{\sigma}_{\theta\theta}(r = 0.2m)$	0.725	0.659	0.655	0.655	0.667	0.667
$\bar{w}(r = 0.2m)$	3.9e-4	3.9e-4	3.9e-4	3.9e-4	4.0e-4	4.0e-4
$\bar{\tau}_{\max}(r = 0.2m)$	0.278	0.326	0.326	0.327	0.333	0.333
D.O.F	54	300	882	1944	1953-5733	-

Table 3.5. Comparison between the results obtained from (a) the present 3-D analysis performed using one variable-order cylindrical solid element each in the x- and θ-directions and two or more variable-order cylindrical solid element in the z-direction, and (b) the Strength of Materials (S.O.M.) plane stress solution given in the text by Srinath[71] for an infinite length, thick isotropic cylindrical shell subjected to internal pressure loading (see Fig. 3.21).

QUANTITY	$M=2$ (1x1x2)	$M=3$ (1x1x2)	$M=4$ (1x1x2)	$M=5$ (1x1x2)	$M=2$ (1x1x8)	S.O.M Solution[71]
$\bar{\sigma}_{zz}(r = 0.1m)$	-0.838	-0.974	-0.996	-1.0	-1.0	-1.0
$\bar{\sigma}_{\theta\theta}(r = 0.1m)$	1.734	1.678	1.668	1.667	1.667	1.667
$\bar{w}(r = 0.1m)$	5.9e-4	5.9e-4	5.9e-4	5.9e-4	5.9e-4	5.9e-4
$\bar{\tau}_{\max}(r = 0.1m)$	1.286	1.326	1.332	1.333	1.333	1.333
$\bar{\sigma}_{zz}(r = 0.2m)$	0.027	0.003	0.0	0.0	0.0	0.0
$\bar{\sigma}_{\theta\theta}(r = 0.2m)$	0.678	0.665	0.667	0.667	0.667	0.667
$\bar{w}(r = 0.2m)$	4.0e-4	4.0e-4	4.0e-4	4.0e-4	4.0e-4	4.0e-4
$\bar{\tau}_{\max}(r = 0.2m)$	0.326	0.331	0.333	0.333	0.333	0.333
D.O.F	90	252	540	990	306	-

(1x1x8, $M = 2$, d.o.f = 306) was used for the purpose of this analysis. The same high accuracy of the numerical results was achieved in this study as well. Further, using the present analysis the numerical results for the plane-strain S. O. M. solution[71] were also duplicated with high accuracy by solving the problem of thick isotropic cylindrical shell under axial restraints, subjected to internal and/or external pressure loads.

3.2.3.3 Uniaxial extension of a laminated cylindrical panel

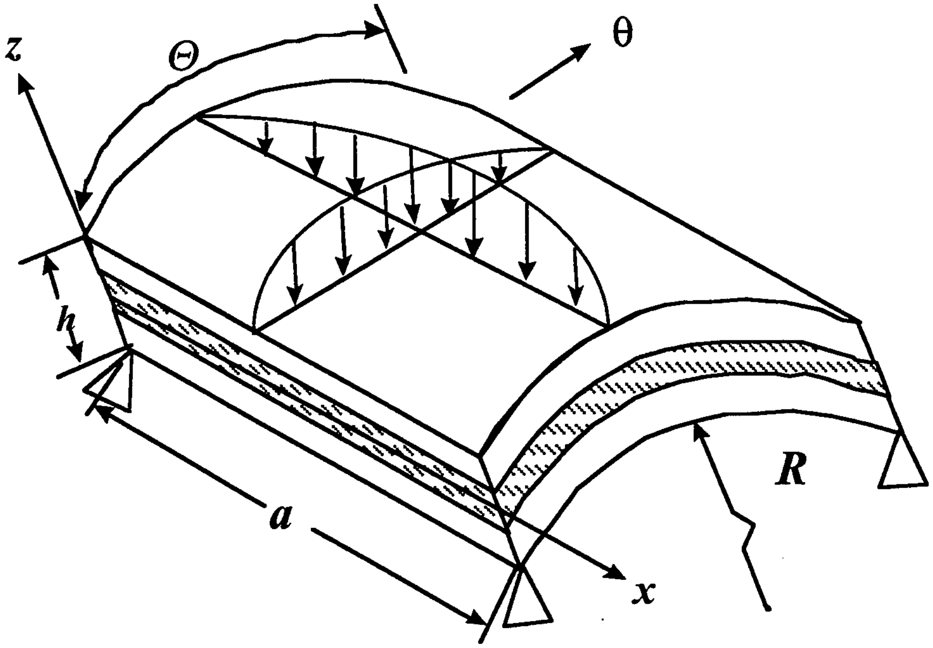

Fig. 3.22 A $[0/90]_T$ laminated cylindrical panel subjected to uniform axial extension.

Next a $[0/90]_T$ laminated cylindrical panel subjected to uniform axial extension is analyzed using the *variable-order* cylindrical solid elements. A 1x20x12 mesh with $M = 3$ (d.o.f = 22,422) is used to model and analyze the 1/4th configuration of the cylindrical panel ($a/R = 0.4$, $a/h = 4$ and $\Theta = 0.4$ radians; refer to Fig. 3.22 for notations). The three-dimensional material properties of the lamina are given by Eq. (50).

The distributions of the non-zero stresses as obtained from the present analysis at $x/a = 0.5$ at the 0/90 interface in the 0^0 and 90^0 layers are shown in Figs. 3.23-3.26. All the stress components are normalized by the applied axial strain. As shown in Fig. 3.23 the distributions of the normal stress σ_{xx} in the 0^0 and 90^0 layers are uniform along the θ-direction. The distributions of the other in-plane normal stress component $\sigma_{\theta\theta}$ in the 0^0 and 90^0 layers along the θ-direction are shown in Fig. 3.24. The normal stress component

$\sigma_{\theta\theta}$ should attain a zero value at the free edge so as to satisfy the traction-free static boundary condition at the edge $\theta/\Theta = 1$. However, as is the case with most of the discrete numerical analyses, the solution from the present analysis also fails to exactly satisfy this static boundary condition at the free edge at material interface. However, in the present analysis this traction-free edge static boundary condition is satisfied with high accuracy as one moves away from the interface region. As shown in Figs. 3.25 and 3.26 the distributions of the interlaminar stresses at the 0/90 interface depict the excellent continuity of transverse normal stress σ_{zz} and transverse shear stress $\tau_{\theta z}$, respectively, achieved in the present analysis. The free-edge (or boundary layer) effects are equally significant in the laminated cylindrical panels as well. The distributions of the normalized displacements v and w along the θ-direction are shown in Fig. 3.27. As shown in Fig. 3.28 the transverse normal displacement w undergoes change in sign as well as magnitude as one moves from the mid plane ($\theta/\Theta = 0$) towards the free edge ($\theta/\Theta = 1$).

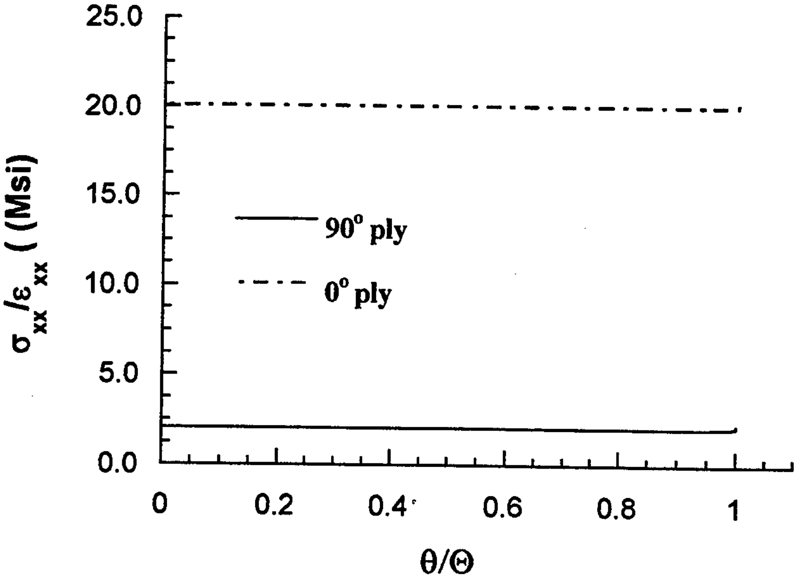

Fig. 3.23 Distributions of normal stress σ_{xx} at the 0/90 interface of a $[0/90]_T$ laminated cylindrical panel subjected to uniform axial extension.

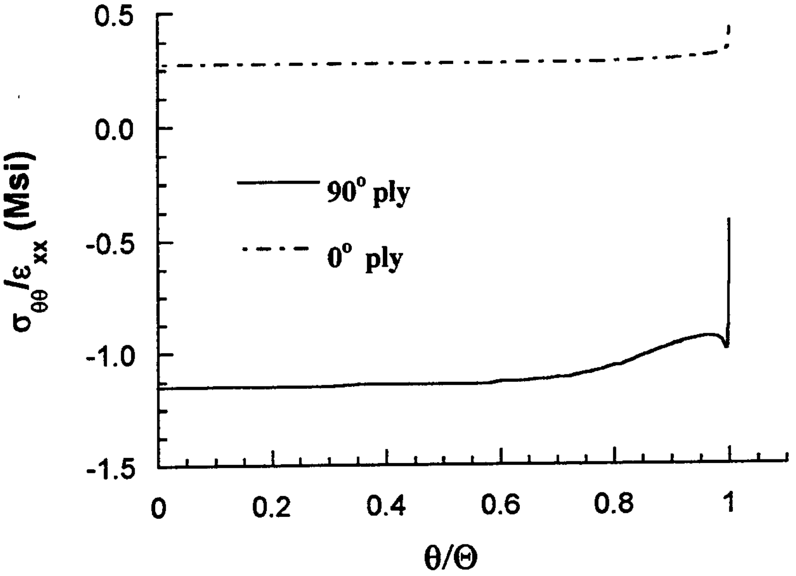

Fig. 3.24. Distributions of normal stress $\sigma_{\theta\theta}$ at the 0/90 interface of a $[0/90]_T$ laminated cylindrical panel subjected to uniform axial extension.

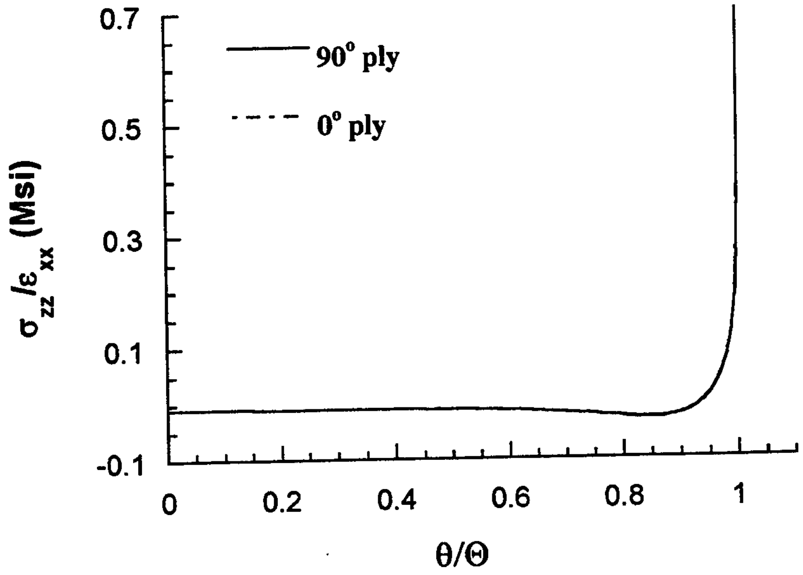

Fig. 3.25 Distributions of transverse normal stress σ_{zz} at the 0/90 interface of a $[0/90]_T$ laminated cylindrical panel subjected to uniform axial extension.

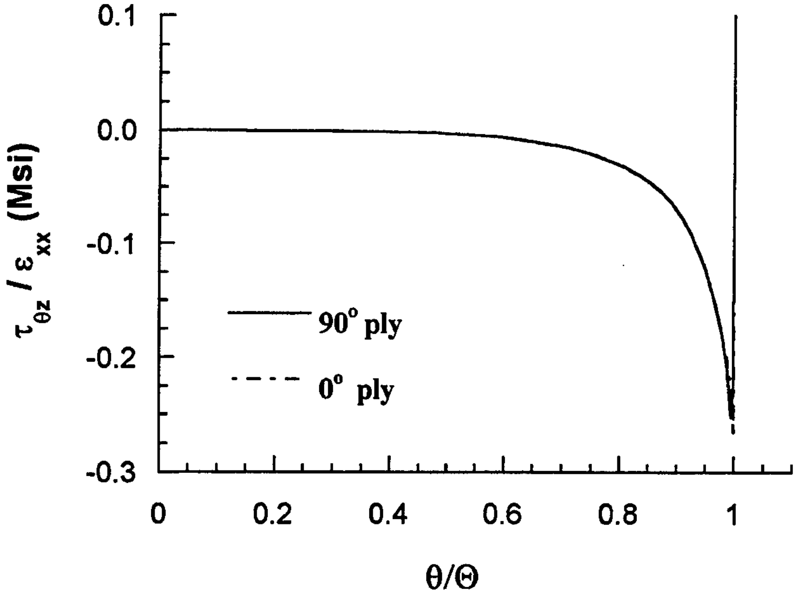

Fig. 3.26 Distributions of transverse shear stress $\tau_{\theta z}$ at the 0/90 interface of a $[0/90]_T$ laminated cylindrical panel subjected to uniform axial extension.

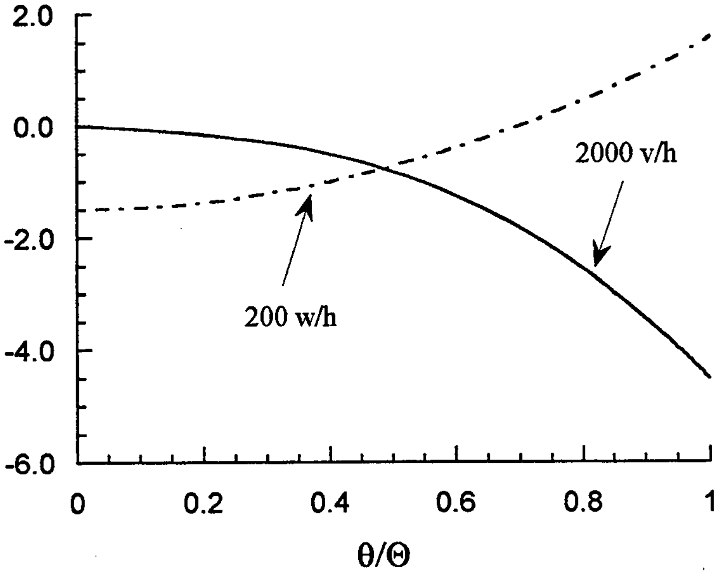

Fig. 3.27 Distributions of transverse displacements at the 0/90 interface of a $[0/90]_T$ laminated cylindrical panel subjected to uniform axial extension.

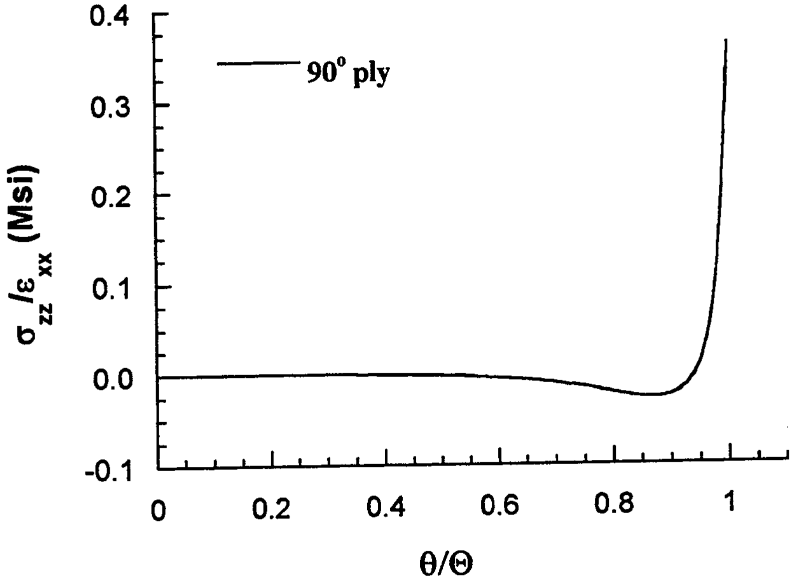

Fig. 3.28 Distributions of transverse normal stress σ_{zz} inside the 90^0 layer (*z/h* = 0.4) of a $[0/90]_T$ laminated cylindrical panel subjected to uniform axial extension.

The distribution of the transverse normal stress σ_{zz} inside the 90^0 layer (*z/h* = 0.4; see Fig. 3.22) is shown in Fig. 3.28. As shown in Fig. 3.28 this stress component reaches a normalized peak value of about 0.375 Msi at the free edge $\theta/\Theta = 1$. Further, the magnitudes of transverse normal stress σ_{zz} and transverse shear stress $\tau_{\theta z}$ obtained from the present analysis are found to be numerically very small (zero) in the 90° layer at the bottom surface (*z/h* = 0) of the $[0/90]_T$ laminate, thus, satisfying the traction-free static boundary conditions at that surface. Once again the results presented here show that in a displacement-based analysis using the *variable-order* cylindrical solid elements, the continuity of stresses at the interface of the elements of the same material or even of the different materials is achieved with a very high accuracy without enforcing it *a priori.*

The numerical examples presented so far demonstrate the high accuracy of the solution achieved by *variable-order* rectangular and cylindrical solid elements. Based on the results presented in this work for the displacement-based analyses using *variable-order* rectangular and cylindrical solid elements, the following conclusions are drawn:

(i) The continuity of stresses at the interface(s) of the elements of the same material or of different materials is achieved with a very high accuracy without enforcing it *a priori.*

(ii) The static boundary conditions at the external surfaces are satisfied with a very high accuracy.

(iii) In most cases the analysis using *variable-order* elements requires less degrees of freedom to solve the problem and achieve same or even higher accuracy of the solution.

(iv) There is always an optimum level of order M of the *variable-order* elements beyond which there is not much significant improvement in the accuracy of the solution. Thus, it is preferable to achieve an optimum combination of the order M and the number of *variable-order* elements to analyze a given structural problem.

The extension of computational algorithm to include the singular 3-D *variable-order* solid elements (rectangular and cylindrical) for application in the linear fracture mechanics problems, and the *variable-order* wedge element for analyzing more general configurations is currently in progress. Furthermore, *variable-order* rectangular and cylindrical solid *transition elements* are also developed which can be effectively utilized to assemble two *variable-order* elements of different order, say $M = 2$ and $M = 4$. This will not only make the analysis of complex structural problems elegant by providing the user the flexibility of refining the order of the *variable-order* elements in the region of high stress gradients (or the region of their interest) but also make the SAVE computer program computationally efficient. It is envisaged that the *variable-order* elements will find its most glamorous application in the analysis of advanced composite material structures having material and geometrical discontinuities where the higher-order displacement approximations would be able to represent the structural response more accurately.

4.0 ANALYSIS OF DOUBLE-LAP BONDED JOINTS

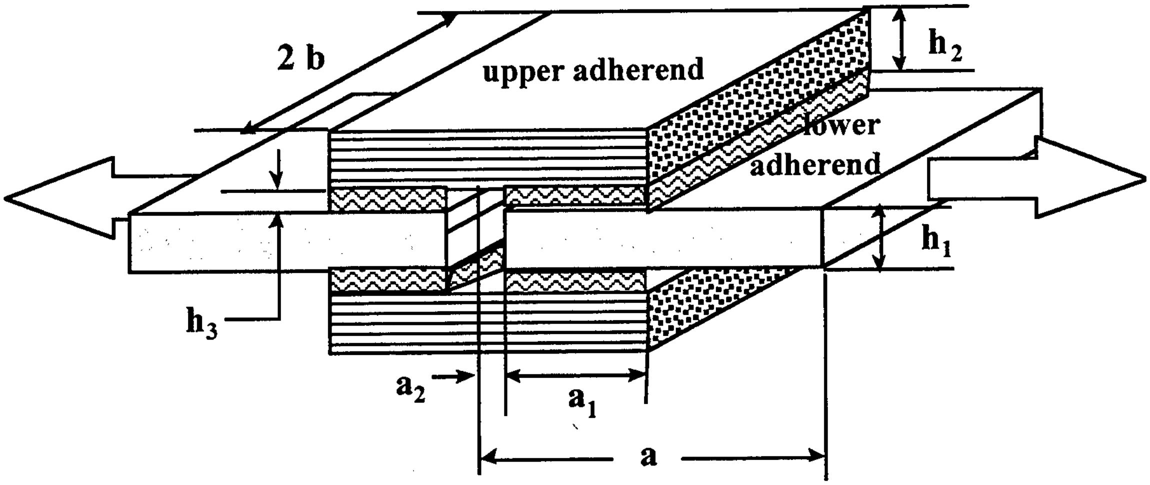

Figure 4.1 A double-lap adhesively bonded joint configuration.

A typical double-lap bonded joint configuration shown in Fig. 4.1 is analyzed using a quasi-2D closed-form solution BONJO,[49] a finite element based commercial software ABAQUS[72] and a generalized coordinate finite element computer program SAVE developed in-house (see Section 3 for details). Metallic and composite adherends were considered during these analyses. Section 4.1 provides a comparison between the results obtained from BONJO and 2-D/3-D analyses using the commercial FE software ABAQUS™ for a double-lap adhesively bonded joint having graphite/epoxy and titanium adherends. Angle-ply effects are also discussed therein. Section 4.2 gives the details of the 3-D thermomechanical analysis performed using the generalized coordinate finite element computer program SAVE for a perfectly bonded double-lap joint having four different composite upper adherends and aluminum lower adherends. In this section the effects of restrained curing are also discussed. The effects of change in the design parameters such as bond length, bond thickness and adhesive curing temperature on the failure loads of a double-lap adhesively bonded joint are studied through a combined analytical and experimental work in Section 4.3.

4.1 ANALYSIS OF ADHESIVELY BONDED DOUBLE-LAP JOINTS: COMPARISON BETWEEN BONJO AND FEM ANALYSES

In this section, a plane stress solution to the adhesively double lap joint configuration (see Fig. 4.1) under uniaxial load is obtained from BONJO[49] computer code and compared with 2-D/3-D FE analysis solution obtained using commercial package ABAQUS.[72] The 2-D plane stress analysis using a 4-node bilinear plane stress element (CPS4), and 3-D finite element analyses using ABAQUS 8-node solid element (C3D8) and ABAQUS 27-node (C3D27), respectively, are performed for the same joint configuration. Due to the symmetry of the joint with respect to *x*-, *y*- and *z*-directions, only 1/8th of the joint configuration as shown in Fig. 4.2 is analyzed by the 3-D finite element analysis. Three different mesh configurations are used to model double-lap joint for the 2-D stress analysis as is shown in Fig. 4.3. The coarsest mesh is labeled Mesh-1, and has 1,042 elements and 2,282 degrees of freedom. The intermediate mesh, denoted as Mesh 2, has 1,839 elements and 3,970 d.o.f.. The finest mesh, called Mesh 3, has 3,286 elements and 6,912 degrees of freedom. Two different mesh configurations are used to model double-lap joint for the 3-D stress analysis as shown in Fig. 4.4. The meshes shown in Fig. 4.4 represent part of the detailed meshes for the symmetric quarter section of the double-lap joint configuration

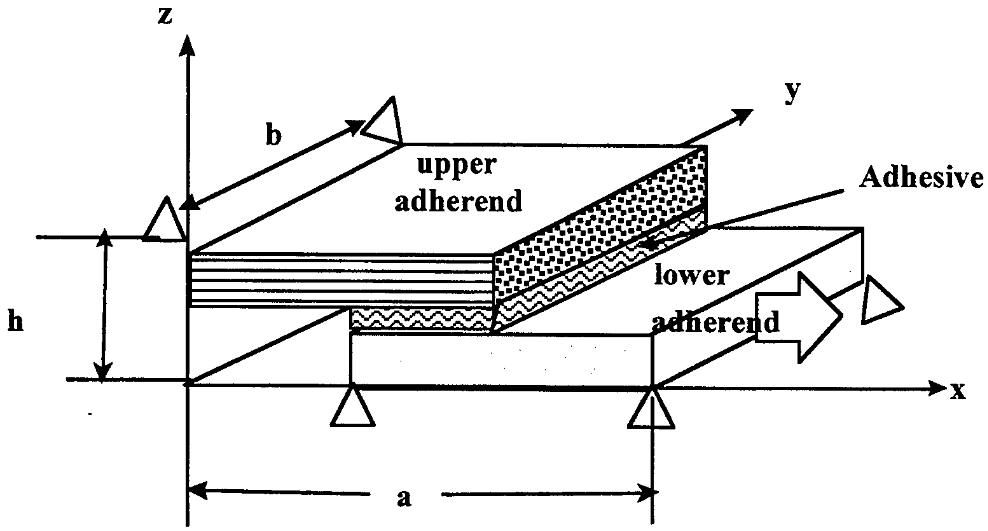

△ : Represents symmetry condition for the edge.

Fig. 4.2 1/8th configuration of the double-lap adhesively bonded joint.

analyzed in Fig. 4.2. The 3-D finite element model has 3,304 elements and 13,830 degrees of freedom for the 8-node element mesh and 1,360 elements and 39,447 degrees of freedom for the 27-node element mesh. The BONJO series codes analyze only the overlapped portion of joint, i.e., the configuration comprising of only the portions of the adherends which are bonded to the either side of the adhesive layer. This is illustrated in Fig. 4.5 for an adhesively bonded double-lap joint.

The upper adherend is a seven -ply $[0/45/-45/0/-45/45/0]_T$ graphite/epoxy 5206 composite laminate, the lower adherend is a 7075-T6 Titanium splice plate, and the adhesive layer is AF-126-2. The joint dimensions are given based on the 1/8th geometry of the joint (see Figs. 4.1 and 4.2. The ply thickness in upper adherend is 0.007 inches (i.e., $h_2 = 0.049$ in.). The thickness of the titanium plate is $h_1 = 0.25$ inches, and the thickness of adhesive layer is $h_3 = 0.01$ inches. The joint dimensions are: $a = 5.5$ in., $a_1 = 1.25$ in., and $a_2 = 0.5$ in.. The width of the adherends '2b' is 1.5 inches. A uniform tensile stress

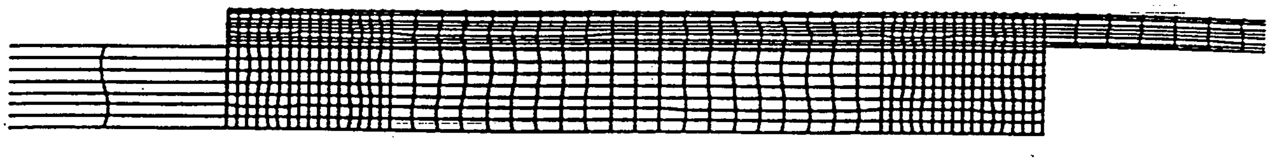

Mesh 1, No of elements 1042, DOF 2282

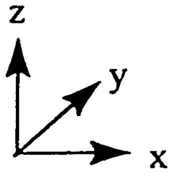

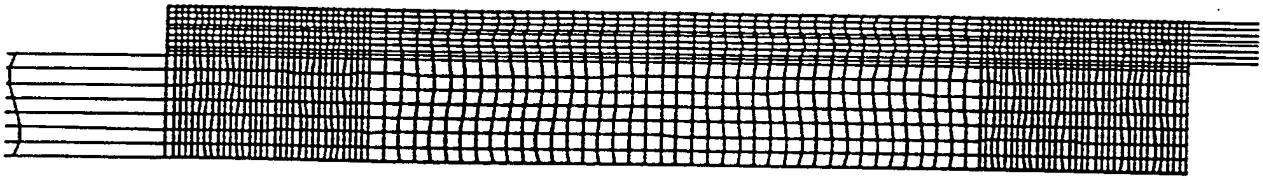

Mesh 2, No of elements 1839, DOF 3970

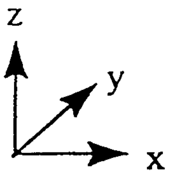

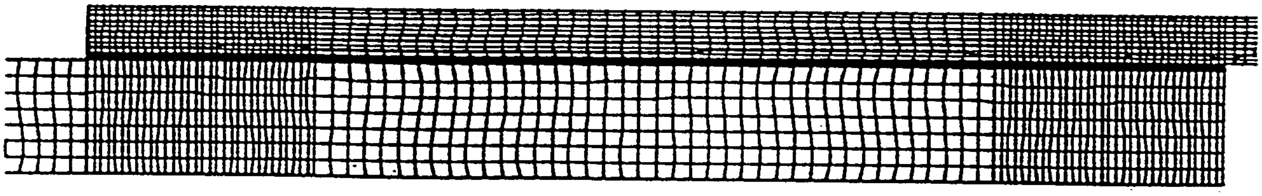

Mesh 3, No of elements 3286, DOF 6912

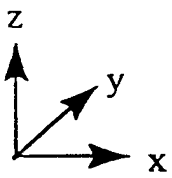

Figure 4.3. Finite element mesh configuration

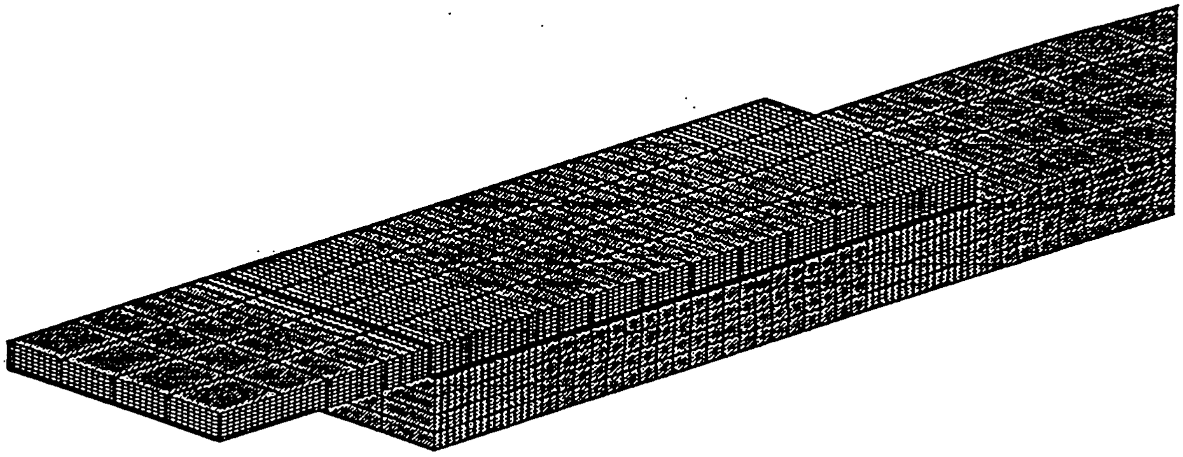

Mesh 1, No of elements 3304,DOF 13830

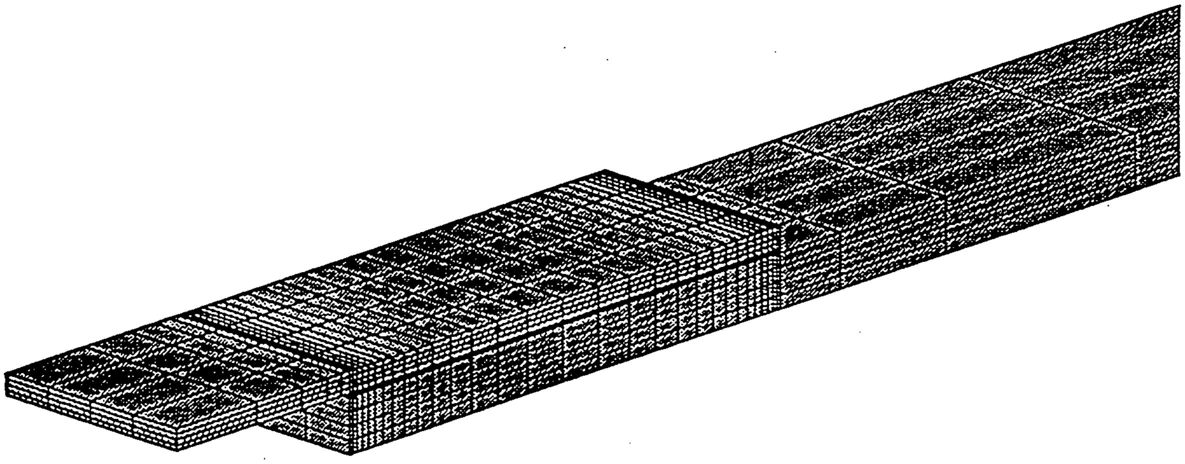

Mesh 2, No of elements 1360,DOF 39447

Figure 4.4. Finite element mesh configuration

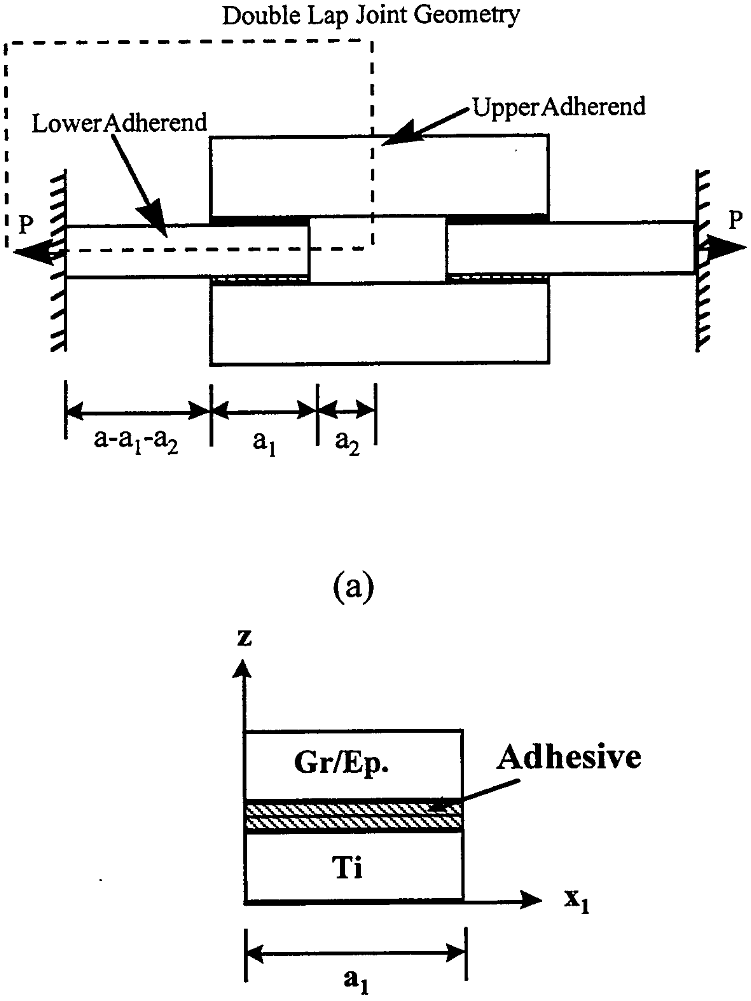
Double Lap Joint Geometry
Lower Adherend
Upper Adherend
P
P
a-a$_1$-a$_2$
a$_1$
a$_2$
z
Gr/Ep.
Adhesive
Ti
x$_1$
a$_1$

(a)

(b)

Figure 4.5 Double-lap bonded joint configuration analyzed by BONJO code.

'σ_0' of 2000 psi is applied at the ends of the Titanium plate. The material properties for the adherends and the adhesive are given in Table 4.2.

Table 4.1 Material properties for the adherends and adhesive.

	Upper Adherend	Lower Adherend	Adhesive
E1	.22e+8 PSI	.103e+8 PSI	.455e+6 PSI
E2	.19e+7 PSI	.103e+8 PSI	.455e+6 PSI
E3	.19e+7 PSI	.103e+8 PSI	.455e+6 PSI
G12	.72e+6 PSI	.390e+7 PSI	.175e+6 PSI
G13	.72e+6 PSI	.390e+7 PSI	.175e+6 PSI
G23	.57e+6 PSI	.390e+7 PSI	.175e+6 PSI
ν12	.33	.33	.3
ν13	.33	.33	.3
ν23	.33	.33	.3

The distributions of axial stress σ_x, normal stress σ_z, and transverse shear stress τ_{xz} in the upper and lower adherends, and adhesive are obtained from the closed form analysis BONJO and FE analysis ABAQUS. Only the results obtained from ABAQUS using 27-node brick element are plotted versus BONJO results for clarity of graphs. The results obtained from 2-D FE analysis using finest mesh (Mesh 3, see Fig 4.3), and 3-D analysis using 8-node and 27-node brick element were found to compare well with each other.

The distributions of the stress components along the bondline (i.e., along $0 < x_1 < a_1$; see Fig. 4.5 or along $a_2 < x < a_1 + a_2$; see Fig. 4.2) are plotted and compared from the closed form solution BONJO and 3-D FE analysis at various locations in the joint. All the stress components are normalized by the applied stress σ_0. It may be noted here that in the FE model the locations $x_1 = a_1$ in the upper adherend and $x_1 = 0$ in the lower adherend are not the free edges (refer to Fig. 4.5). However, in the BONJO solution approach, the locations $x_1 = a_1$ in the upper adherend and $x_1 = 0$ in the lower adherend are modeled as free edges where the shear force, and hence, the transverse shear stress component τ_{xz} are zero.

4.1.1 Stresses at the center line of the adhesive layer

The distributions of adhesive shear stress τ_{xz} and normal stress σ_z at the centerline of the adhesive as obtained from various analyses are shown in Fig. 4.6 and 4.7, respectively. It can be seen from Fig. 4.6 that the magnitudes of adhesive shear stress τ_{xz} predicted by the two approaches compare very well in the regions slightly away from the edges $x_1/a_1 = 0$ and $x_1/a_1 = 1$. As shown in Fig. 4.6, the adhesive shear stress τ_{xz} from the closed from solution BONJO attains a zero value at the $x_1/a_1 = 0$ and $x_1/a_1 = 1$ thereby satisfying the traction free boundary conditions at these edges. As is expected, the FE solution does not exactly satisfies the traction free edge conditions at $x_1/a_1 = 0$ and $x_1/a_1 = 1$. In finite element analysis the value of adhesive shear stress τ_{xz} has been found to approach zero with the refinement in the FE mesh. However, it is questionable if shear stress τ_{xz} would converge to zero with further mesh refinement. As shown in Fig. 4.7, the values of adhesive normal stress σ_z predicted by different models along the bond line compare very well in the regions slightly away from the free edges $x_1/a_1 = 0$ and $x_1/a_1 = 1$. At the edges $x_1/a_1 = 0$ and $x_1/a_1 = 1$, the values of adhesive normal stress σ_z predicted by closed form solution BONJO are lower in magnitude than those predicted by the FE analysis.

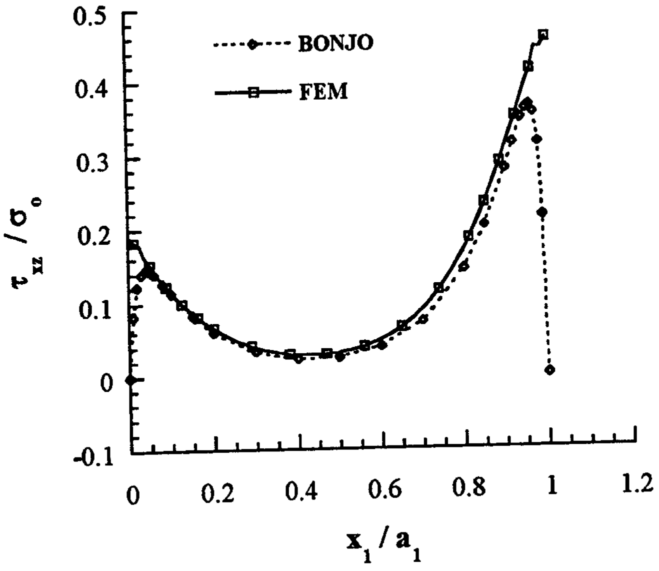

Fig. 4.6 Distributions of shear stress τ_{xz} in the adhesive layer.

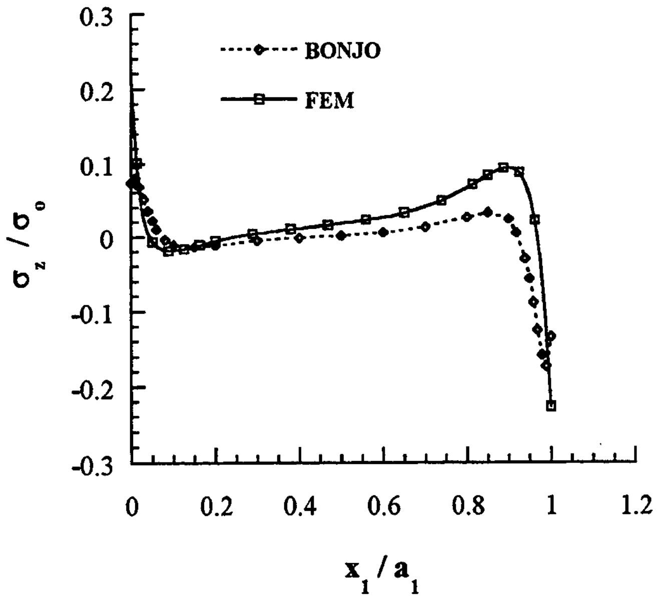

Fig.4.7 Distributions of normal stress σ_z in the adhesive layer.

4.1.2 Stresses at the interface between adhesive layer and 0° ply of the upper adherend

The distributions of axial stress σ_x, normal stresses σ_z, and shear stress τ_{xz} in the 0° ply of the upper adherend at the adhesive/upper adherend interface along the bondline are shown in Figs. 4.8, 4.9 and 4.10, respectively. The values of these stress components as predicted by the different models compare very well in the regions slightly away from the edges $x_l/a_l = 0$ and $x_l/a_l = 1$. As shown in Fig. 4.8, the value of ply axial stress σ_x predicted by the closed form solution BONJO at the edge $x_l/a_l = 1$ is higher in magnitude than those predicted by the FE analysis. At the edges $x_l/a_l = 0$ and $x_l/a_l = 1$, the values of ply normal stress σ_z predicted by the closed form solution BONJO are lower in magnitude than those predicted by the FE solution (see Fig. 4.9). The shear stress component τ_{xz} obtained from the closed from solution BONJO attains a zero value at $x_l/a_l = 0$ and $x_l/a_l = 1$ thereby satisfying the traction free boundary conditions at these edges, as shown in Fig. 4.10. Note that in BONJOIG solution $x_l/a_l = 1$ is modeled as a freeedge.

4.1.3 Stresses at the interface of 0° ply and 45° ply in the upper adherend

The distributions of axial stress σ_x, normal stresses σ_z, and shear stress τ_{xz} in the 0° ply of the upper adherend at the interface of 0° ply and 45° ply along the bondline are shown in Figs. 4.11, 4.12 and 4.13, respectively. The values of these stress components as predicted by the different models compare very well in the regions slightly away from the edges $x_1/a_1 = 0$ and $x_1/a_1 = 1$. As shown in Fig. 4.11, the value of ply axial stress σ_x predicted by closed form solution BONJO at the edge $x_1/a_1 = 1$ is higher in magnitude than those predicted by the FE model. At the edges $x_1/a_1 = 0$ and $x_1/a_1 = 1$, the values of ply normal stress σ_z predicted by the closed form solution BONJO are higher in magnitude than those predicted by the FEM solution (see Fig. 4.12). The shear stress component τ_{xz} obtained from the closed form solution BONJO attains a zero value at the $x_1/a_1 = 0$ $x_1/a_1 = 1$ thereby satisfying the traction free boundary conditions at these edges, as shown in Fig. 4.13. In the finite element analysis the value of the shear stress component τ_{xz} tends towards zero at the $x_1/a_1 = 0$ edge. The edge $x_1/a_1 = 1$ is *not* a free edge in FEM analysis.

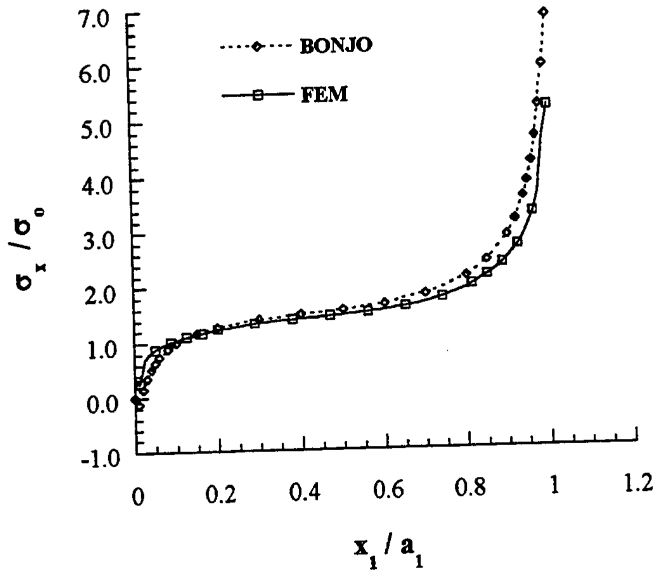

Fig. 4.8 Distributions of normal stress σ_x in the 0° ply of the upper adherend at the adhesive layer-upper adherend interface.

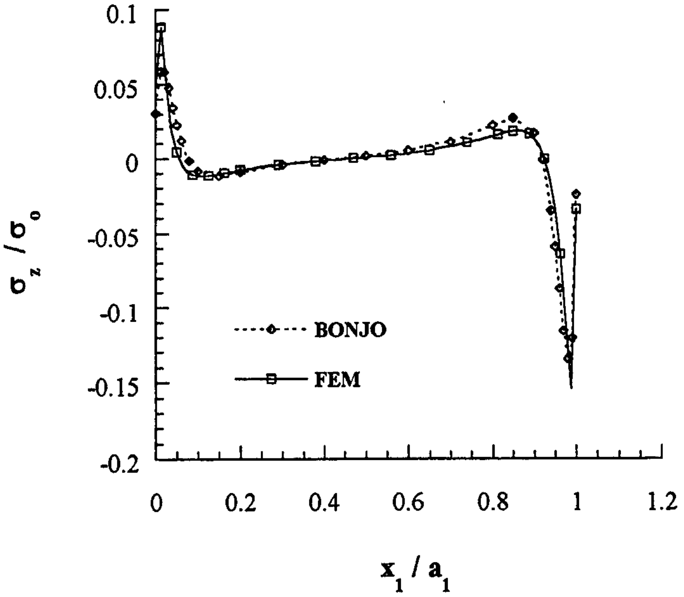

Fig. 4.9 Distributions of normal stress σ_z in the 0° ply of the upper adherend at the adhesive layer-upper adherend interface.

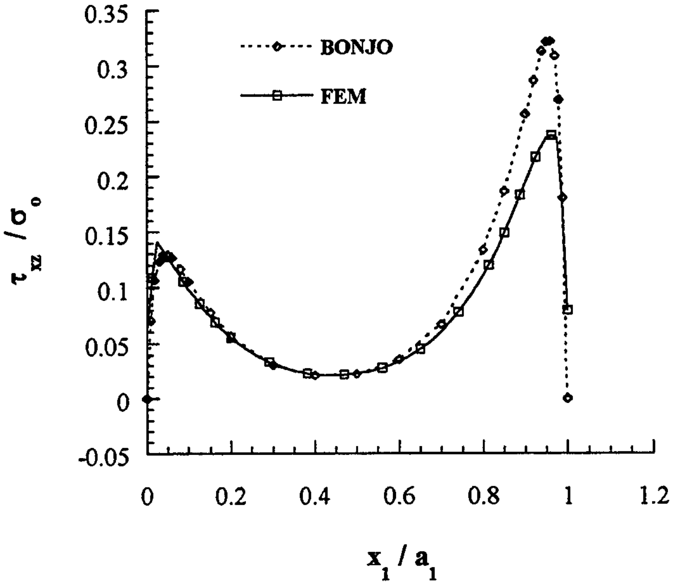

Fig. 4.10 Distributions of shear stress τ_{xz} in the 0° ply of the upper adherend at the adhesive layer-upper adherend interface.

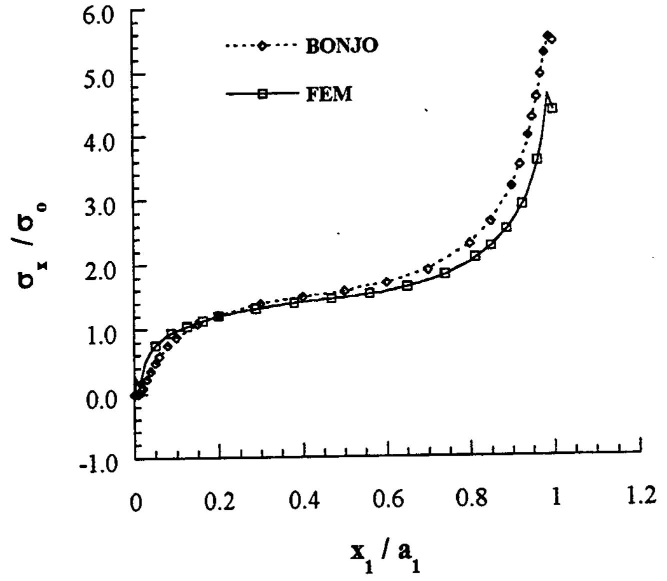

Fig. 4.11 Distributions of normal stress σ_x in the 0° ply at the 0°/45° interface of the upper adherend.

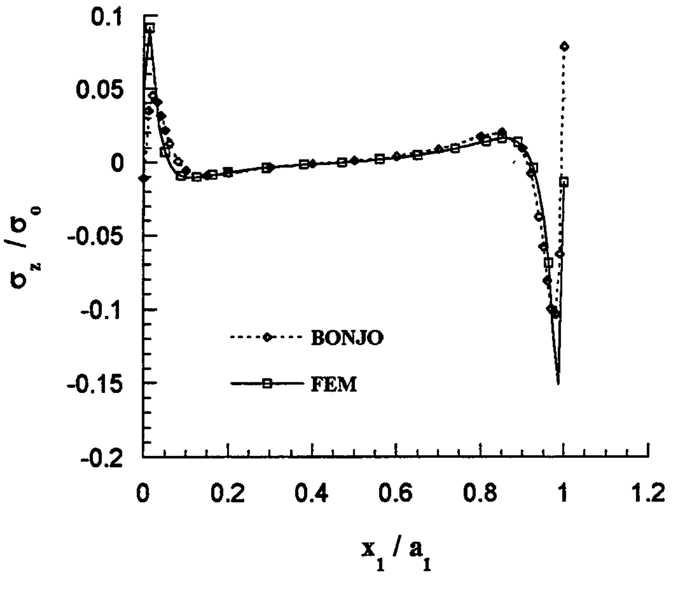

Fig. 4.12 Distributions of normal stress σ_z in the 0° ply at the 0°/45° interface of the upper adherend.

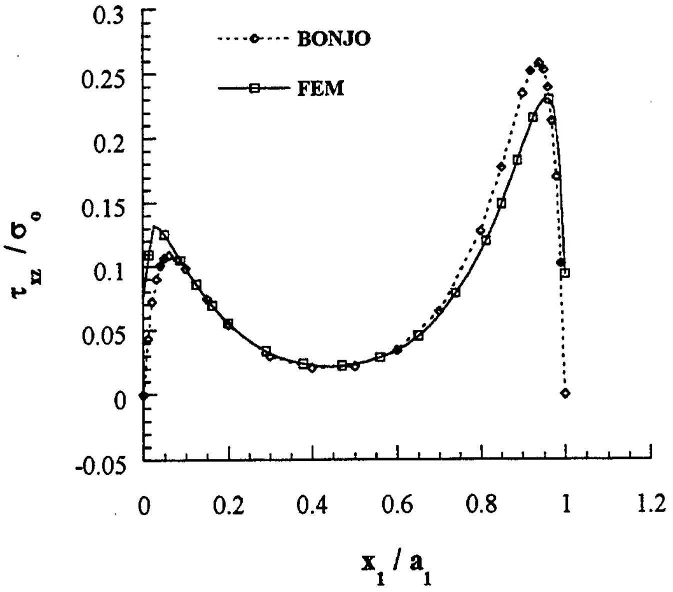

Fig. 4.13 Distributions of shear stress τ_{xz} in the 0° ply at the 0°/45° interface of the upper adherend.

4.1.4. Stresses at the interface of -45° ply and 0° ply of the upper adherend

The distributions of axial stress σ_x, normal stresses σ_z, and shear stress τ_{xz} in the -45° ply of the upper adherend at the interface of -45° ply and 0° ply along the bondline are shown in Figs. 4.14, 4.15, and 4.16, respectively. The values of the normal stresses σ_z and shear stress τ_{xz} in the -45° ply as predicted by the different models compare very well in the regions slightly away from the edges $x_l/a_l = 0$ and $x_l/a_l = 1$. As shown in Fig. 4.14, the values of axial stress component σ_x predicted by the closed form solution BONJO and the FEM analysis do not agree well. At the free edge $x_l/a_l = 0$ the values of ply normal stress σ_z predicted by the closed form solution BONJO are lower in magnitude than those predicted by the FE model (see Fig. 4.15). However, the reverse is true at the $x_l/a_l = 1$ edge. The shear stress component τ_{xz} in -45° ply as obtained from the closed form solution BONJO attains a zero value at the $x_l/a_l = 0$ and $x_l/a_l = 1$ thereby satisfying the traction free boundary conditions at these edges, as shown in Fig. 4.16.

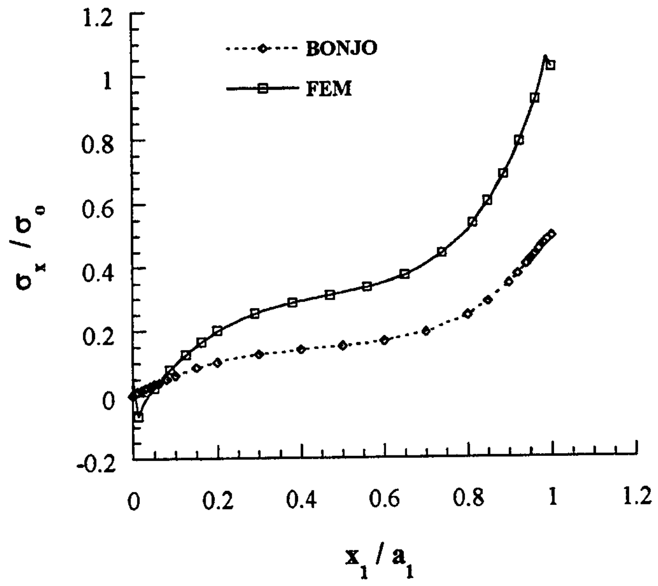

Fig. 4.14 Distributions of normal stress σ_x in the -45° ply at the -45°/0° interface of the upper adherend.

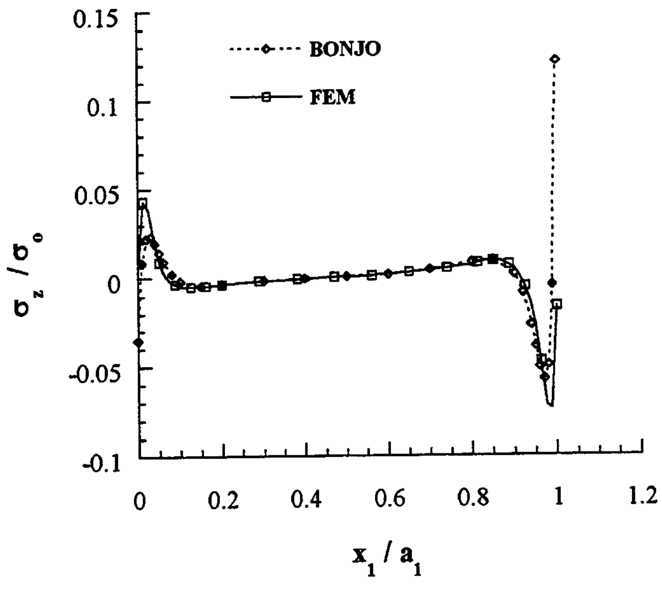

Fig. 4.15 Distributions of normal stress σ_z in the -45° ply at the -45°/0° interface of the upper adherend.

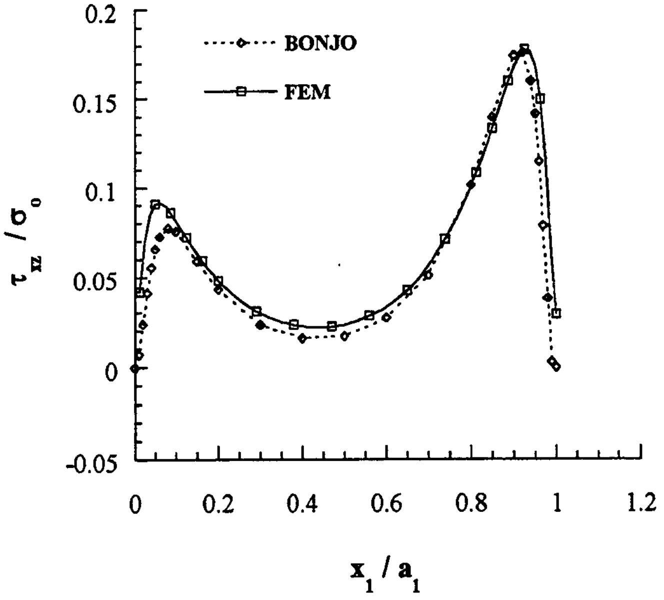

Fig. 4.16 Distributions of shear stress τ_{xz} in the -45° ply at the -45°/0° interface of the upper adherend.

4.1.5 Stresses at the top surface of the upper adherend (in 0° ply)

The distributions of axial stress σ_x, normal stresses σ_z, and shear stress τ_{xz} in the 0° ply of the upper adherend at the top surface along the bondline are shown in Figs. 4.17, 4.18 and 4.19, respectively. As shown in Fig. 4.17, the values of ply axial stress σ_x predicted by closed form solution BONJO at the edge $x = 1.25$ is higher in magnitude than those predicted by the different FE models. The normal stresses σ_z and the shear stress component τ_{xz} in 0° ply obtained from the closed form solution BONJO attains a zero value along the bondline thereby satisfying the traction free boundary conditions at the top surface, as shown in Figs. 4.18 and 4.19, respectively. In the finite element analysis the values of normal stresses σ_z and shear stress component τ_{xz} at the top are numerically small as well.

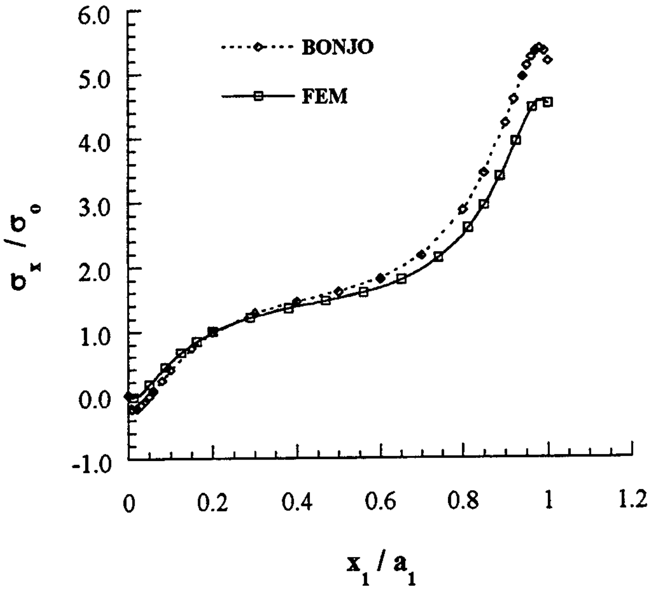

Fig. 4.17 Distributions of normal stress σ_x in 0° ply of the upper adherend at the top surface.

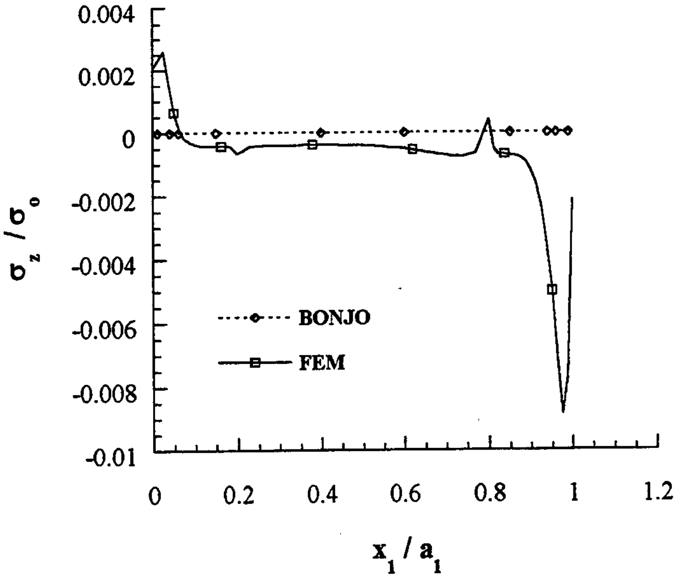

Fig. 4.18 Distributions of normal stress σ_z in 0° ply of the upper adherend at the top surface.

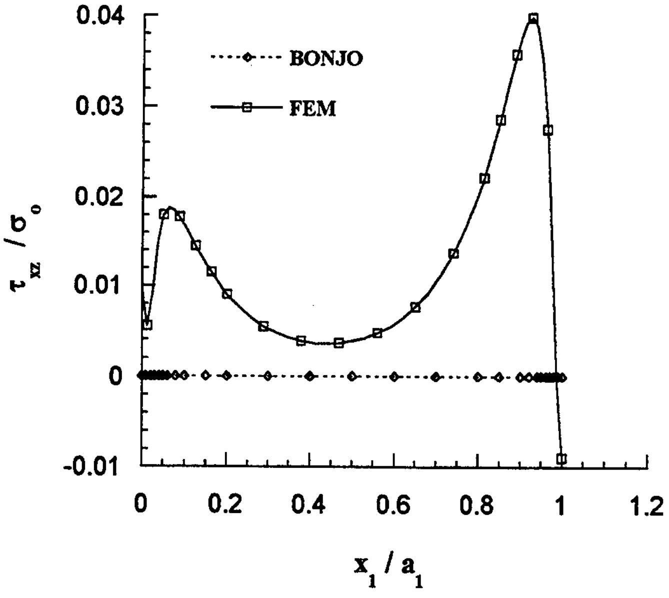

Fig. 4.19 Distributions of shear stress τ_{xz} in 0° ply of the upper adherend at the top surface.

4.1.6 Stresses at the interface between adhesive layer and lower adherend

The distributions of axial stress σ_x, normal stresses σ_z, and shear stress τ_{xz} in the Titanium plate at the interface of adhesive/lower adherend along the bondline are shown in Figs. 4.20, 4.21, and 4.22, respectively. The values of these stress components as predicted by the different models compare very well in the regions slightly away from the edges $x_1/a_1 = 0$ and $x_1/a_1 = 1$. As shown in Fig. 4.20, the value of axial stress σ_x predicted by closed form solution BONJO at the edge $x_1/a_1 = 0$ is lower in magnitude than those predicted by the FE model. At the edges $x_1/a_1 = 0$ and $x_1/a_1 = 1$, the values of normal stress σ_z predicted by the closed form solution BONJO are lower in magnitude than those predicted by the different FE models (see Fig. 4.21). The shear stress component τ_{xz} obtained from the closed form solution BONJO attains a zero value at the $x_1/a_1 = 0$ and $x_1/a_1 = 1$ thereby satisfying the traction free boundary conditions at these edges, as shown in Fig. 4.22. Once again it is emphasized that in BONJO solution $x_1/a_1 = 0$ edge is modeled as a free edge, while in the FE model the location $x_1/a_1 = 0$ in the lower adherend is not a free edge.

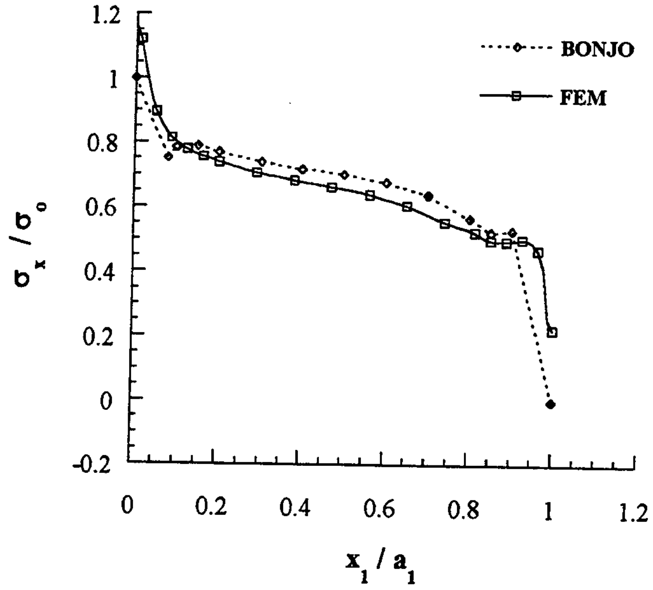

Fig. 4.20 Distributions of normal stress σ_x in the lower adherend at the adhesive layer-lower adherend interface.

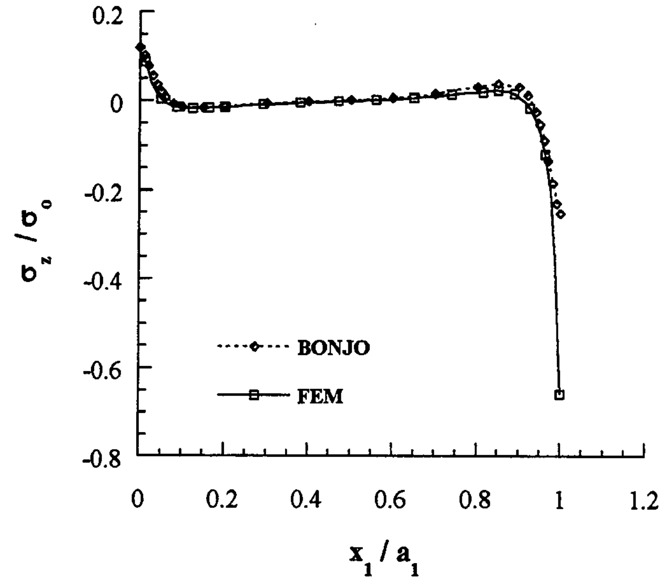

Fig. 4.21 Distributions of normal stress σ_z in the lower adherend at the adhesive layer-lower adherend interface.

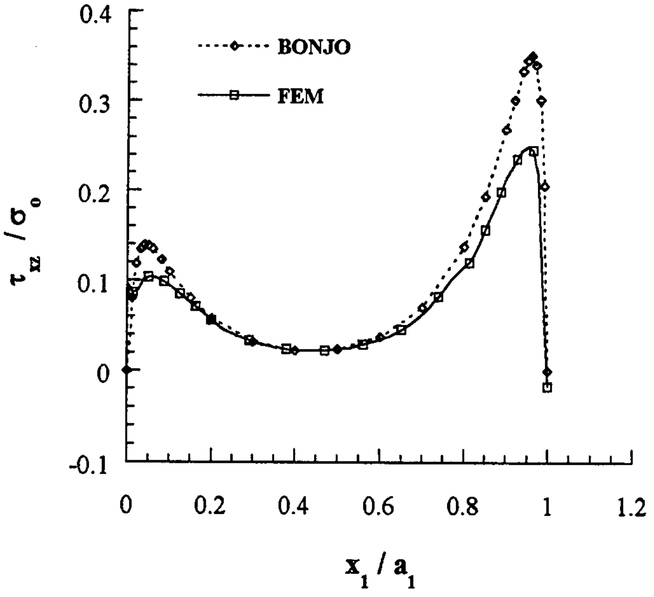

Fig. 4.22 Distributions of shear stress τ_{xz} in the lower adherend at the adhesive layer-lower adherend interface.

4.1.7 Stresses at the midplane of the joint (or midplane of lower adherend)

The distributions of axial stress σ_x, normal stresses σ_z, and shear stress τ_{xz} in the Titanium plate at the midplane of the lower adherend (or joint) along the bondline are shown in Figs. 4.23, 4.24, and 4.25, respectively. The values of these stress components as predicted by the different models compare very well in the regions slightly away from the edges $x_1/a_1 = 0$ and $x_1/a_1 = 1$. As shown in Fig. 4.23, the value of axial stress σ_x predicted by closed form solution BONJO at the free edge $x_1/a_1 = 0$ is slightly higher in magnitude than those predicted by the FE analysis. At the edges $x_1/a_1 = 0$ and $x_1/a_1 = 1$, the values of normal stress σ_z predicted by the closed form solution BONJO are much higher in magnitude than those predicted by the FE model (see Fig. 4.24). The shear stress component τ_{xz} attains numerically small values along the bondline at the midplane of the joint as obtained from the two solution approaches thereby satisfying the symmetry conditions at the mid surface of the joint, as shown in Fig. 4.25.

The highlights of the comparison study between BONJO and FE analyses are summarized below:

1. The distributions of axial stress σ_x, normal stress σ_z, and transverse shear stress τ_{xz} in the upper and lower adherends, and the distributions of normal stress σ_z, and transverse shear stress τ_{xz} in the adhesive layer are obtained from the closed form analysis BONJO

and 3-D FE analysis ABAQUS. The numerical values of these stress components as predicted by the two analyses compare very well in the bond regions slightly away from the edges.

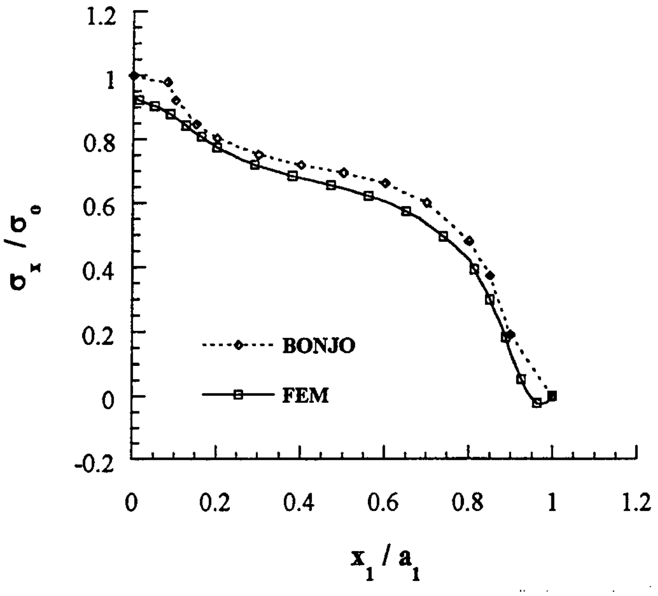

Fig. 4.23 Distributions of normal stress σ_x at the midplane of the lower adherend.

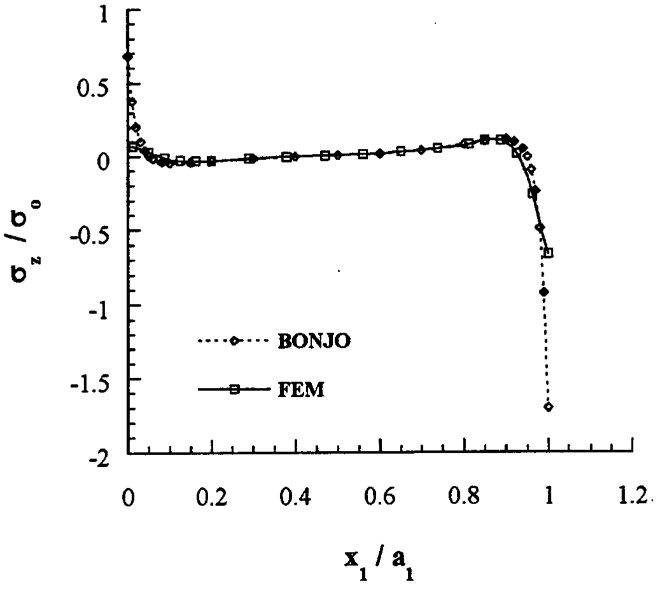

Fig. 4.24 Distributions of normal stress σ_z at the midplane of the lower adherend.

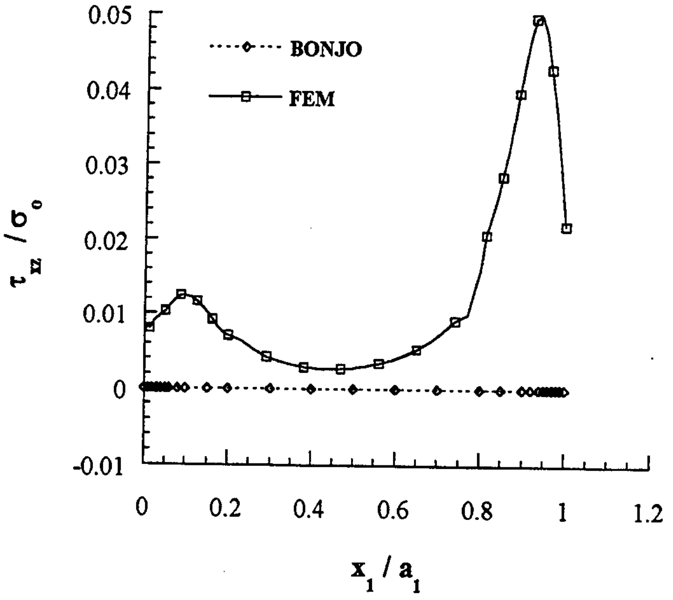

Fig. 4.25 Distributions of shear stress τ_{xz} at the midplane of the lower adherend.

2. The shear stress component τ_{xz} obtained from the closed form solution BONJO attains a zero value at the $x_1/a_1 = 0$ and $x_1/a_1 = 1$ edges of the joint thereby satisfying the traction-free boundary conditions at these edges. In the finite element analysis the value of the shear stress component τ_{xz} numerically approach zero at the $x_1/a_1 = 0$ or $x_1/a_1 = 1$ edge (depending upon whether it is an upper adherend or a lower adherend) with the refinement in the FE mesh.
3. At the edges $x_1/a_1 = 0$ and $x_1/a_1 = 1$, the values of normal stress σ_z predicted by the closed form solution BONJO do not agree well with those predicted by the FE model. A possible explanation of this could be the fact that the normal stress component σ_z is exhibiting a singular behavior at these edges thereby attaining different numerical values in the two solution approaches.
4. At the edge $x_1/a_1 = 0$, the numerical values of axial normal stress σ_x predicted by the closed form solution BONJO have only slight differences with those predicted by the different FE models. An exception to this is the axial stress component σ_x in 45° plies of the upper adherend where the closed form solution results do not agree well with those obtained from the FE analysis all along the bondline.

4.1.8 Angle ply effects

In this section a detailed comparison of the distributions of stresses as obtained from the BONJO and FE analyses is performed by varying the orientation of the angle-plies in the upper adherend of the double-lap joint. In particular, the distribution of axial normal stress component σ_x in angle-plies is subjected to a closed scrutiny. In the absence of any bench mark solution to the double-lap joint problem being analyzed, a systematic comparison is made between closed form solution BONJO[49] and finite element solution using commercial package ABAQUS[54]. During this investigation some interesting results were obtained which are discussed in the following paragraphs.

As first step the complexity of the analysis due to the presence of angle plies was avoided by replacing ±45° plies by 0° plies in the stacking sequence of the upper adherend. Thus, the double lap configuration of Fig. 4.2 (or Fig. 4.5) was analyzed with a seven-ply unidirectional graphite/epoxy 5206 upper adherend. All the other joint details were left unchanged. The distributions of axial stress σ_x, normal stress σ_z, and transverse shear stress τ_{xz} in the upper and lower adherends were obtained from the closed form analysis BONJO and 3-D FE analyses. The distributions of normal stress σ_z and transverse shear stress τ_{xz} in the adhesive layer were also obtained as a result of these analyses. The distributions of all the stress components at various locations as obtained from the two solution approaches were found to compare well with each other. The distributions of stresses σ_z and τ_{xz} in the adhesive layer, normal stress σ_x at the midplane of the joint in lower adherend, and at the midplane of the upper adherend are shown in Figs. 4.26, 4.27 4.28 and 4.29, respectively, to support this claim. In general, it is found that the points 1 through 3 summarized at the end of the sub-section 4.1.7 are valid for this numerical example also. Notice that the distributions of normal stress component σ_x shown in Fig. 4.29 at the interface (in mathematical sense) of the two 0° layers compare very well from the two analyses.

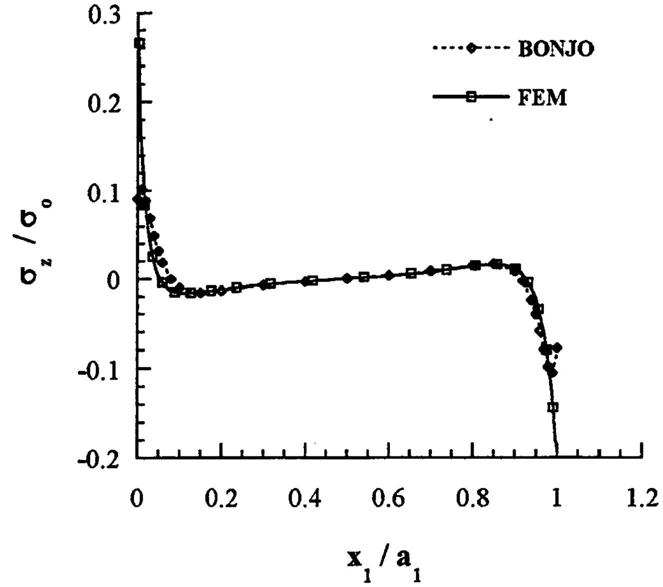

Fig. 4.26 Distributions of normal stress σ_z in the adhesive layer.

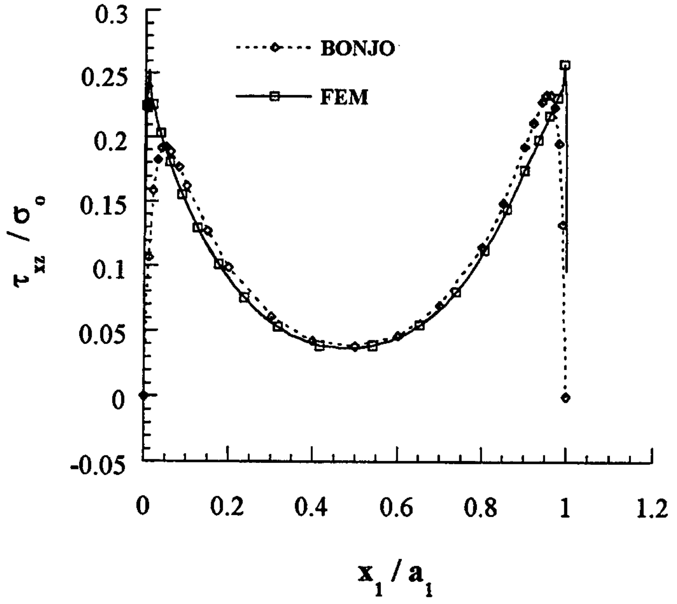

Fig. 4.27 Distributions of shear stress τ_{xz} in the adhesive layer.

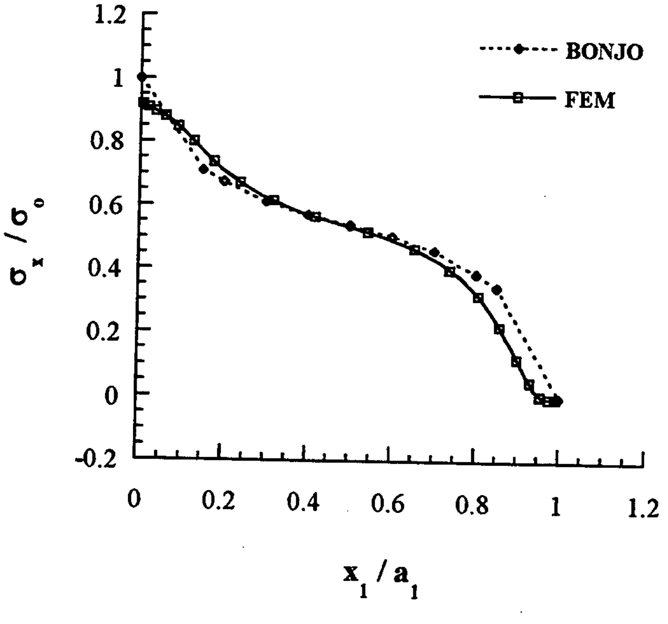

Fig. 4.28 Distributions of normal stress σ_x at the midplane of the lower adherend.

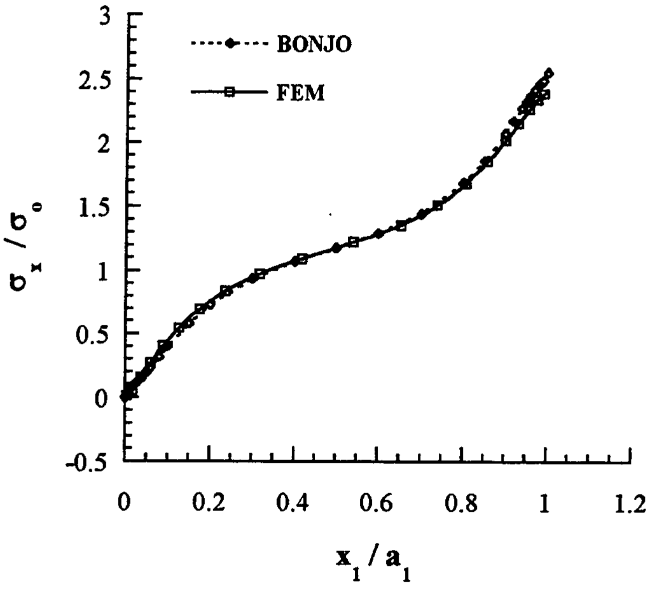

Fig. 4.29 Distributions of normal stress σ_x at the midplane of the upper adherend.

Next, the ± 45° plies were replaced by 90° plies in the stacking sequence of the upper adherend. The double lap configuration of Fig. 4.2 was now analyzed with a seven-ply $[0/90/90/0/90/90/0]_T$ graphite/epoxy 5206 composite laminate as the upper adherend. All the other joint details remained the same. In general, the observations made during the analysis of the numerical example of the first step are found to be valid for this numerical example as well. The distributions of all the stress components at various locations as obtained from the two solution approaches were found to compare well with each other. The distributions of stresses σ_z and τ_{xz} in the adhesive layer, normal stress σ_x at the midplane of the joint in lower adherend, and at the interface of 0°/90° plies of the upper adherend in 0° and 90° plies are shown in Figs. 4.30, 4.31, 4.32, 4.33, and 4.34 respectively, to support this claim. It may be noted that the distributions of normal stress component σ_x shown in Fig. 4.34 in the 90° at the interface of the 0°/90° layers compare very well from the two analyses.

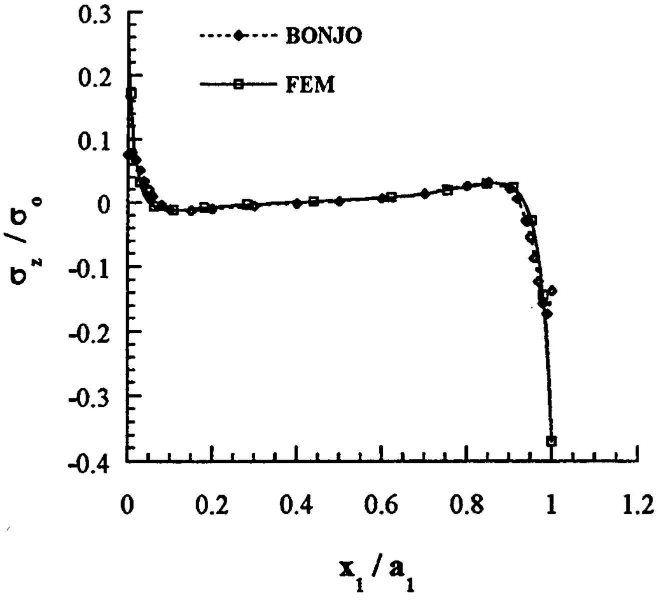

Fig. 4.30 Distributions of normal stress σ_z in the adhesive layer.

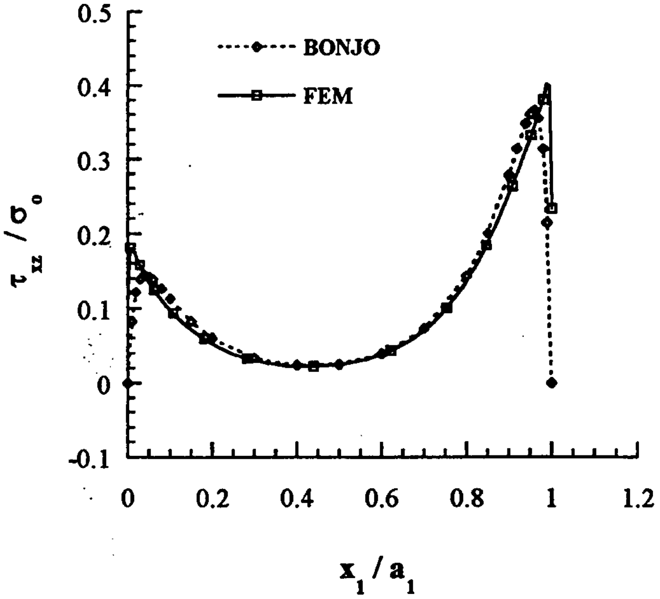

Fig. 4.31 Distributions of shear stress τ_{xz} in the adhesive layer.

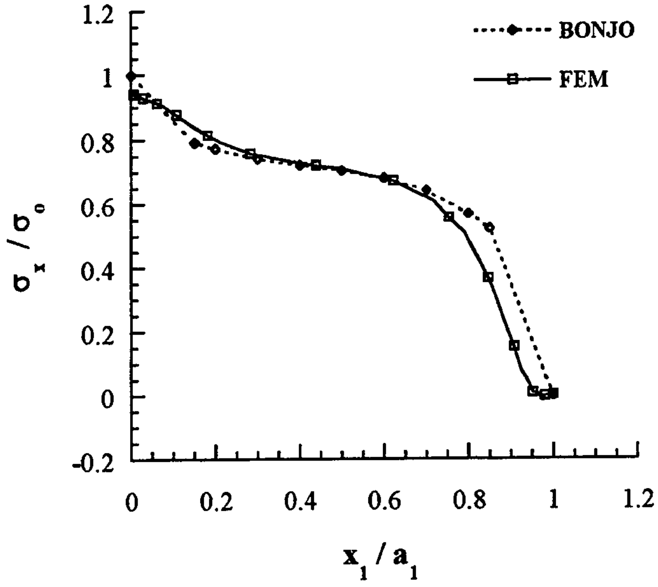

Fig. 4.32 Distributions of normal stress σ_x at the midplane of the lower adherend.

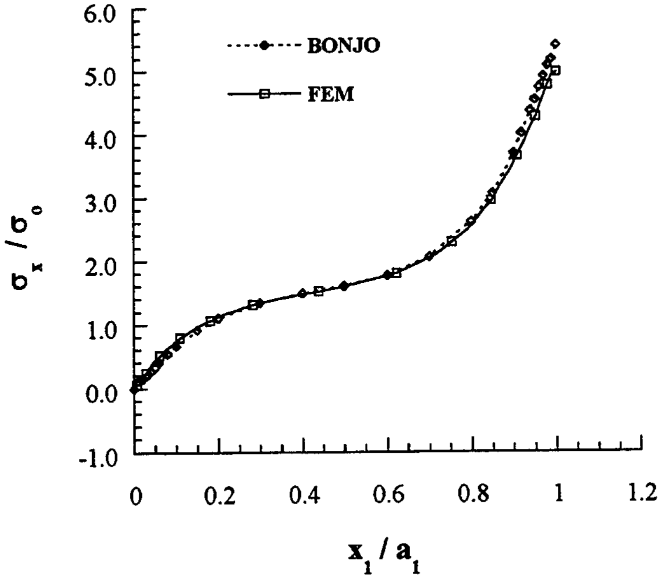

Fig. 4.33 Distributions of normal stress σ_x in the 0^0 ply at the $0^0/90^\circ$ interface of the upper adherend.

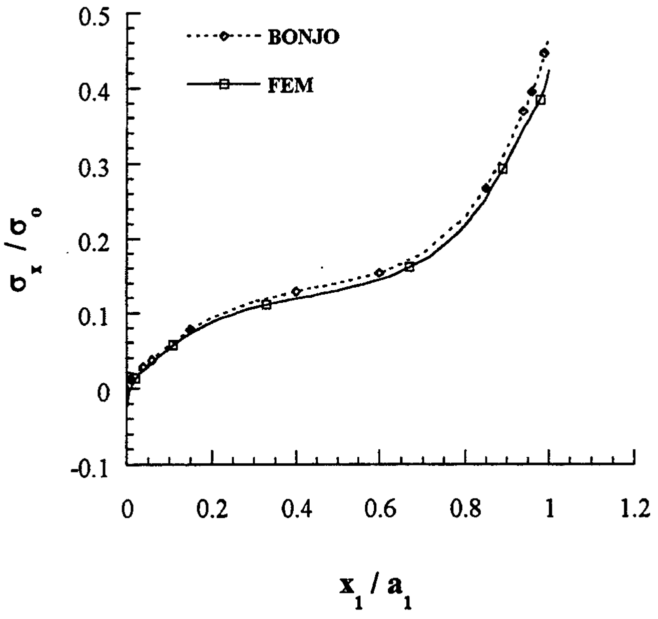

Fig. 4.34 Distributions of normal stress σ_x in the 90^0 ply at the $0^0/90^o$ interface of the upper adherend.

The numerical examples studied so far have shown that for unidirectional and cross-ply laminates the BONJO codes and FEM results compare very well in the regions slightly away from the joint corners. However, the distributions of axial stress component σ_x in 45° plies do not agree well from the BONJO and FEM analyses. A detailed study of the solution approach[49] employed by BONJO codes revealed that the stretching-shearing coupling effects introduced by the presence of angle-plies have been neglected during the analysis in the stress-strain law for the axial stress component σ_x for the lamina. (See equation (58) of Ref.[49] which has been derived based on *combined* assumption of plane stress and plane strain thereby neglecting the shear strain term ε_{xy}.) This assumption does not seem to effect the overall solution in the present example of double lap bonded joint where the stress distributions in the adhesive, lower adherends and 0° plies of upper adherends compare well from the two solutions. This can be attributed to the fact that the upper adherend is a *balanced* laminate, and in laminated plate theory the terms A_{16}, A_{26}, etc., do not contribute in the expressions for stress and moment resultants for a balanced symmetric laminate. However, the effects of these terms and shear strain should be included for a computation of lamina stresses in the angle plies. Renton and Vinson[47-48] also made similar observations during the development of codes BOND3 and BOND4.

The aforementioned statements were verified by *purposefully* neglecting the effects of terms A_{16}, A_{26}, etc., during the FEM analysis. This was achieved by setting the compliance S_{16}, S_{26}, S_{36}, and S_{45} in the strain-stress relation of the element to zero in the ABAQUS code. The double lap bonded joint with 45° plies in the upper adherend was analyzed. The distributions of axial stress component σ_x in the 45° ply at the 45°/0° interface are shown in Fig. 4.35. Notice the effect of neglecting the stretching-shearing coupling in the FEM analysis; now the FEM results with coupling terms set to zero compare very well with the BONJO solution. As shown in Fig. 4.36, the distributions of axial stress component σ_x in the 0° ply at the 45°/0° interface obtained by setting the coupling terms to zero in FEM analysis compare better with BONJO solution.

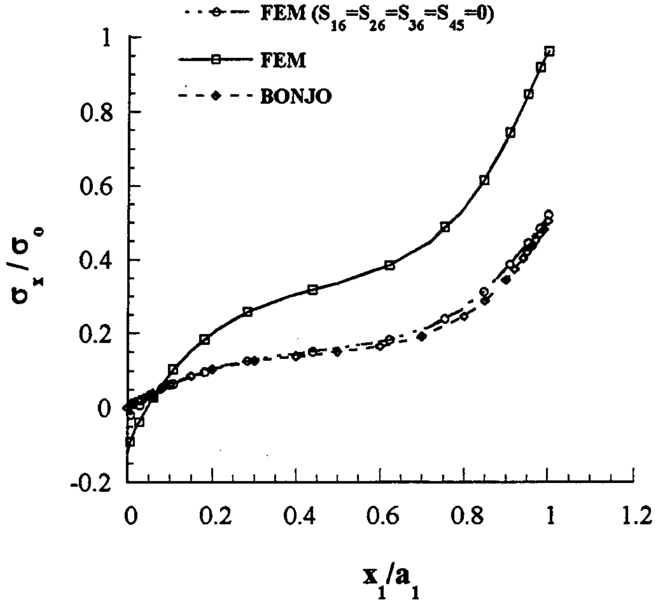

Fig. 4.35 Distributions of normal stress σ_x in the 45° ply at the 45°/0° interface of the upper adherend.

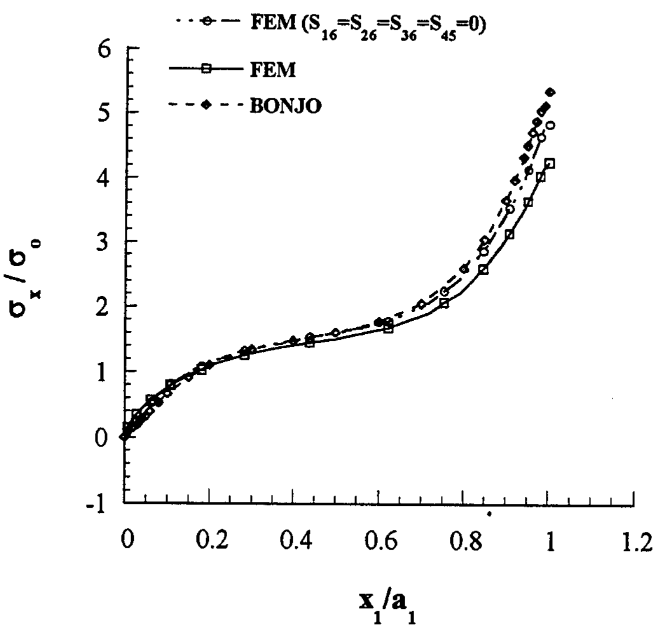

Fig. 4.36 Distributions of normal stress σ_x in the 0^0 ply at the $45^0/0^o$ interface of the upper adherend.

For the further study of the angle-ply effects in detail, the results for the double-lap joint problem with two more stacking configurations for the upper adherend viz., seven-ply $[0/25/-25/0/-25/25/0]_T$ and seven-ply $[0/65/-65/0/-65/65/0]_T$ graphite/epoxy 5206 composite, were compared from the two analyses. All other problem parameters were unchanged. The distributions of axial stress component σ_x in the 25° ply and 0° at the 25°/0° interface for the two cases are shown in Figs. 4.37 and 4.38, respectively. As shown in Figs. 4.37 and 4.38, the distributions of axial stress component σ_x in the 25° ply and 0° ply at the 25°/0° interface obtained by setting the coupling terms to zero in FEM analysis compare very well with the BONJO solution. The distributions of axial stress component σ_x in the 65° ply and 0° at the 65°/0° interface for the two cases are shown in Figs. 4.39 and 4.40, respectively. As shown in Fig. 4.39, the distributions of axial stress component σ_x in the 65° ply at the 65°/0° interface obtained by setting the coupling terms to zero in FEM analysis compare very well with the BONJO solution. The FEM results with coupling terms set to zero for axial stress component σ_x in the 0° ply at the 65°/0° interface show an excellent comparison with the BONJO solution.

4.1.9 Summary

A double lap adhesively bonded joint configuration shown in Fig. 4.1 was analyzed using closed form solution BONJO and the commercial finite element analysis package ABAQUS™. The results obtained from this study lead to the conclusion that the

BONJO solution approach provides reasonably accurate stress distributions in the adhesive and adherends when the adherends are either unidirectional, cross-ply or balanced laminates. However, in the case of balanced laminates the axial stress in the angle plies may not be correctly predicted by the BONJO solution approach due to the neglect of extension-shear coupling effects in the lamina constitutive law. In such cases the BONJO solution approach should be used with caution and one's own engineering judgment.

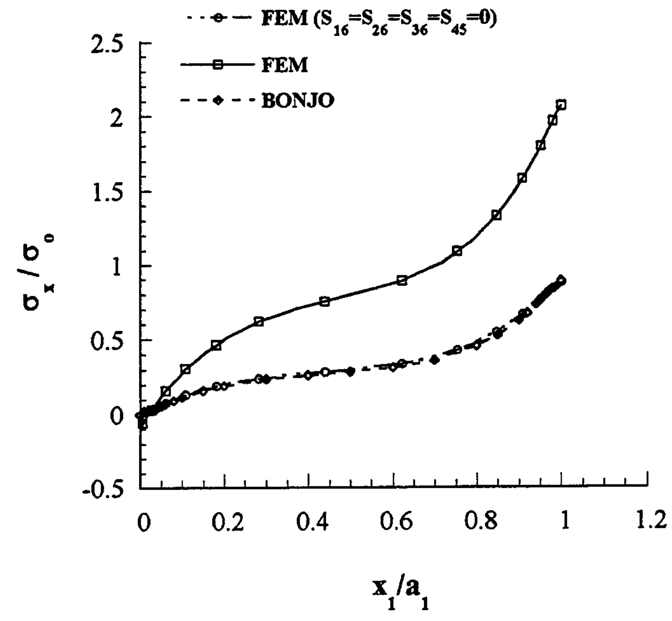

Fig. 4.37 Distributions of normal stress σ_x in the 25^0 ply at the $25^0/0^o$ interface of the upper adherend.

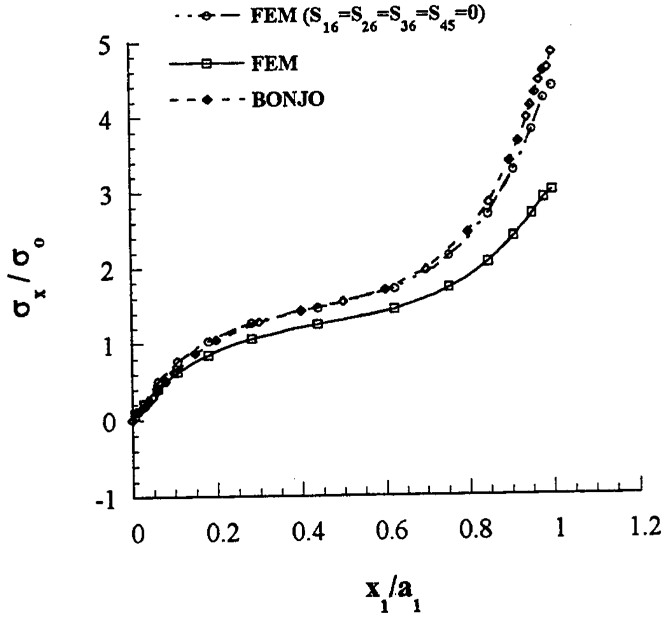

Fig. 4.38 Distributions of normal stress σ_x in the 0^0 ply at the $25^0/0^o$ interface of the upper adherend.

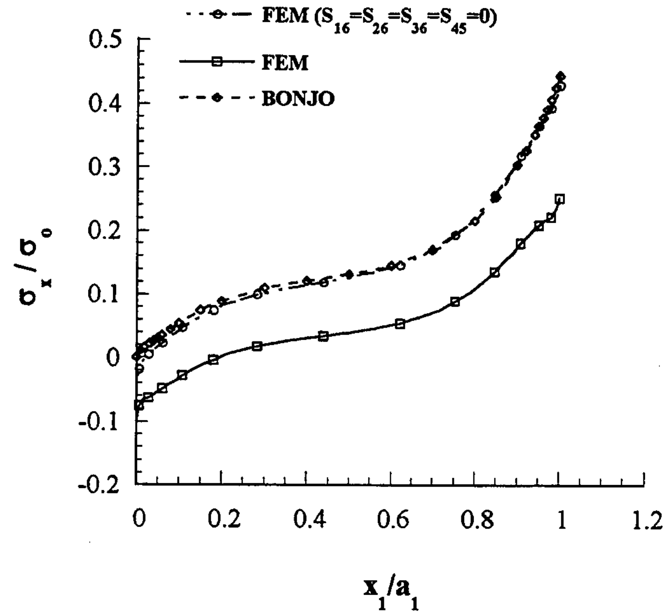

Fig. 4.39 Distributions of normal stress σ_x in the 65^0 ply at the $65^0/0^o$ interface of the upper adherend.

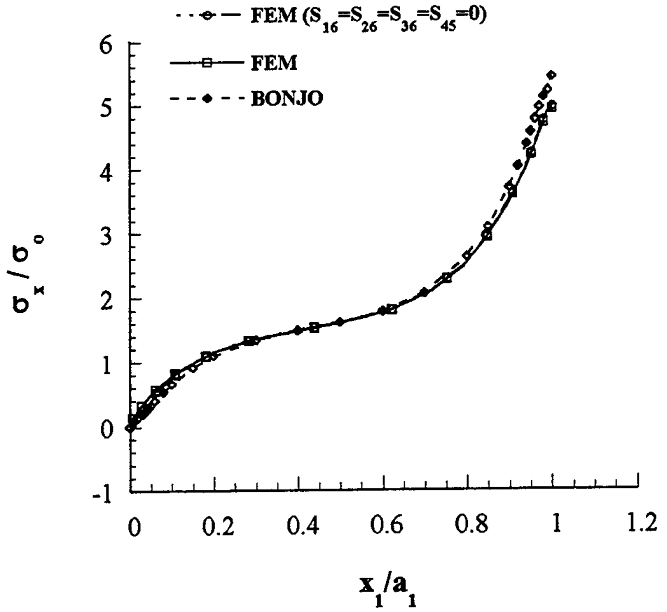

Fig. 4.40 Distributions of normal stress σ_x in the 0^0 ply at the $65^0/0^o$ interface of the upper adherend.

4.2 THREE-DIMENSIONAL ANALYSIS OF PERFECTLY BONDED PLATES

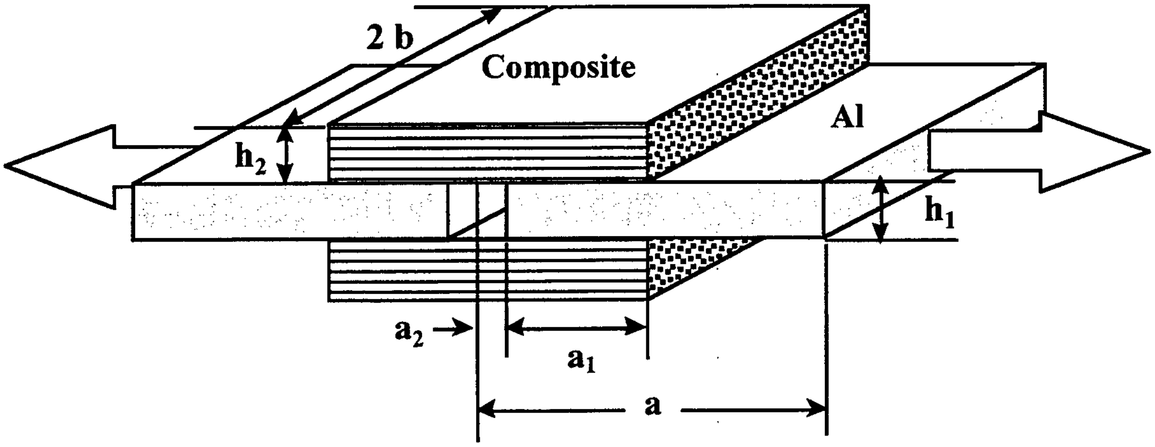

Fig. 4.41 A symmetric, perfectly bonded double-lap joint configuration

In this section the structural analysis program SAVE is utilized to model and analyze a perfectly bonded, symmetric, double-lap joint configuration as shown in Fig. 4.41. Due to the symmetry of the joint (see Fig. 4.41) only 1/8th configuration of the perfectly bonded, symmetric, double-lap joint is analyzed as shown in Fig. 4.42. The upper adherend is a unidirectional composite laminate and the lower adherend is an aluminum plate. The geometric parameters used in the analysis are: $a/a_1 = a/a_2 = a/b = 4$, $a/h_2 = 20$ and $a/h_1 = a/h = 10$, where $h = h_2 + h_1/2$. Four types of composite material systems used to model the upper adherends are boron/epoxy, graphite/epoxy, glass/epoxy, and GLARE^{TM}. The thermoelastic properties of these materials are given in Table 4.2.

Table 4.2: Thermoelastic properties of the adherends.

	Aluminum	Boron/epoxy	Graphite/epoxy	Glass/epoxy	GLARE^{TM}
E_{11}, GPa (Msi)	73.8 (10.7)	208.3 (30.2)	164.6 (23.86)	38.6 (5.6)	65.6 (9.51)
E_{22}, GPa (Msi)	73.8 (10.7)	25.4 (3.68)	9.83 (1.43)	8.28 (1.2)	50.7 (7.35)
E_{33}, GPa (Msi)	73.8 (10.7)	25.4 (3.68)	9.83 (1.43)	8.28 (1.2)	50.7 (7.35)
G_{12}, GPa (Msi)	29.5 (4.28)	7.24 (1.05)	6.78 (0.98)	4.14 (0.6)	19.5 (2.83)
G_{13}, GPa (Msi)	29.5 (4.28)	7.24 (1.05)	6.78 (0.98)	4.14 (0.6)	19.5 (2.83)
G_{23}, GPa (Msi)	29.5 (4.28)	7.24 (1.05)	3.66 (0.53)	3.31 (0.48)	19.5 (2.83)
υ_{12}	0.25	0.18	0.24	0.26	0.33
υ_{13}	0.25	0.18	0.24	0.26	0.33
υ_{23}	0.25	0.17	0.34	0.26	0.33
α_1x 10^6 / °C (°F)	23.6 (13.1)	4.5 (2.5)	0.02 (0.01)	8.6 (4.8)	17.9 (9.95)
α_2 x 10^6 / °C (°F)	23.6 (13.1)	23.0 (12.8)	22.5 (12.5)	22.1 (12.3)	24.2 (13.4)
α_3 x 10^6 / °C (°F)	23.6 (13.1)	23.0 (12.8)	22.5 (12.5)	22.1 (12.3)	24.2 (13.4)

There are a total of 234 *variable-order* rectangular solid elements in the computational model of the analyzed configuration shown in Fig. 4.42, out of which 126 elements are used to model the aluminum plate and 108 elements are used to model the composite laminate. The normalized coordinates of the boundaries of the elements in the three coordinate directions are listed below (refer to Fig. 4.42):

x/a: 0.0, 0.23, 0.245, 0.25, 0.26, 0.28, 0.3, 0.4, 0.45, 0.47, 0.48, 0.485, 0.49, 0.494, 0.497, 0.498, 0.499, 0.4995, 0.5, 0.5025, 0.51, 0.52, 0.55, 0.75, 1.0;

y/b: 0.0, 0.96, 1.0; and

z/h: 0.0, 0.4, 0.45, 0.5, 0.55, 0.6, 1.0.

The three-dimensional displacement field in each rectangular solid element is approximated by cubic Bernstein polynomials ($M = 3$). This resulted in 22,362 unknown *generalized coordinates* (or d.o.f.) in the analysis. It took approximately 6100 seconds of CPU time and 240 MW of memory to solve this problem on Cray C90 available at the ASC MSRC (Aeronautical Systems Center Major Shared Resource Center) HPC (High Performance Computing) facility at the Wright-Patterson Air Force Base, Dayton, Ohio.

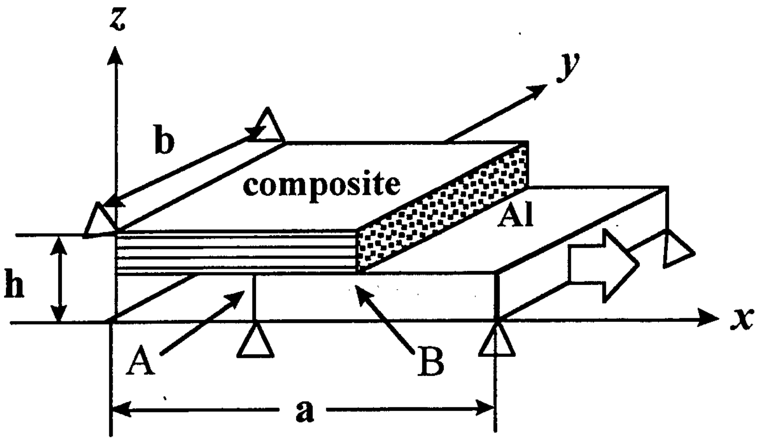

△ : Represents symmetry condition for the edge.

Fig. 4.42 1/8th configuration of the perfectly bonded double-lap joint modeled for analysis.

Numerical results are presented for the two cases: (i) when the double-lap joint is allowed to expand (or contract) freely in all the directions, and (ii) when the free expansion of the joint in the x- and y-directions is restrained. In the first case, only the symmetry boundary conditions $u=0$ at $x/a=0$, $v=0$ at $y/b=0$ and $w=0$ at $z/h=0$ are imposed on the analyzed configuration shown in Fig. 4.42. (u,v and w are the displacement components of the element in the x-, y- and z-directions, respectively; see Appendix A.) In the second case, the boundary conditions $u=0$ at $x/a=1$ and $v=0$ at $y/b=1$ are also imposed in addition to the symmetry boundary conditions described above. Furthermore, four types of composite material systems are used to model the unidirectional composite upper adherends for the case of free-expansion analysis; while one material system viz., boron/epoxy composite, is used to study the effects of restrained expansion (or contraction) in the second analysis.

The variation of stresses in the lower and upper adherends along the x-direction at $y/b=0$ and $z/h=05$ for the joint configuration shown in Fig. 4.42 subjected to a uniform temperature difference ΔT of -111.11°C (-200°F) is presented in this section. This kind of thermal loading can result either during the adhesive curing process or because of the variation in the operating temperature of the aircraft. The magnitudes of the transverse shear stress components τ_{xy} and τ_{yz} obtained from the analyses were found to be negligibly small, and hence are not presented here.

In the following paragraphs, first, the nature of the stress field for the case of free (unrestrained) expansion of the joint with aluminum lower adherend and boron/epoxy upper adherend is discussed in detail. Then, the variation of stresses in the joint at the interface of the aluminum lower adherend and the boron/epoxy upper adherend is compared for the cases of unrestrained and restrained expansions. Finally, the stress distributions in the upper adherend for four different composite materials are discussed for the case of the unrestrained expansion of the joint.

4.2.1 Variation of stresses at the aluminum-boron/epoxy interface

The variation of stresses at the interface of the aluminum-boron/epoxy interface are shown in Figs. 4.43-4.45. As shown in Fig. 4.43, cooling of the joint by -111.11°C induces a tensile axial stress in the aluminum plate and a compressive axial stress in the boron/epoxy laminate in the overlap (or bond) region ($0.25 < x / a < 0.5$) of the joint. The coefficient of thermal expansion of the aluminum in the x-direction is about five times higher, and its Young's modulus is about three times lower than that of the boron/epoxy (see Table 4.2). Thus, more compliant aluminum plate would tend to undergo much higher deformation in the axial direction as compared to the boron/epoxy laminate. In the present case of negative temperature difference, the aluminum plate would tend to shrink more than the boron/epoxy laminate in the x-direction. However, the stiffer boron/epoxy laminate would offer resistance to this high shrinking of the aluminum plate. Since the deformation of the two adherends have to be compatible in the interface region, the aluminum plate would have to expand and the boron/epoxy laminate would have to contract thereby inducing tensile axial stress in the aluminum plate and a compressive axial stress in the boron/epoxy laminate as shown in Fig. 4.43. The axial stress σ_{xx} is tensile in nature at the joint corner **A** and compressive at joint corner **B**. Further, the magnitude of the axial stress component σ_{xx} in the aluminum plate away from the bond region is small as shown in Fig. 4.43.

The distribution of transverse normal stress component σ_{zz} in the aluminum and boron/epoxy adherends is shown in Fig. 4.44. As shown in Fig. 4.44 the magnitude of the transverse stress component σ_{zz} is negligibly small in the aluminum and boron/epoxy adherends in the overlap region. Further, the transverse normal stress σ_{zz} is tensile in nature at the joint corner **A** and compressive at joint corner **B**. Thus, the joint corner **A** is more susceptible to debonding as compared to the joint corner **B**. The transverse normal stress component σ_{zz} attains numerically zero value in the aluminum plate at the joint corner **B** and in the boron/epoxy laminate at the joint corner **A** thereby satisfying the stress-free boundary conditions at these edges.

The distribution of transverse shear stress component τ_{xz} in the aluminum and boron/epoxy adherends is shown in Fig. 4.45 and is kind of anti-symmetric in nature. As shown in Fig. 4.45 the magnitude of the transverse shear stress component τ_{xz} is comparable to the magnitude of axial stress component σ_{xx} in the aluminum and boron/epoxy adherends in the overlap region. Further, the transverse shear stress component τ_{xz} attains numerically zero value in the aluminum plate at the joint corner **B** and in the boron/epoxy laminate at the joint corner **A** thereby satisfying the stress-free boundary conditions at these edges.

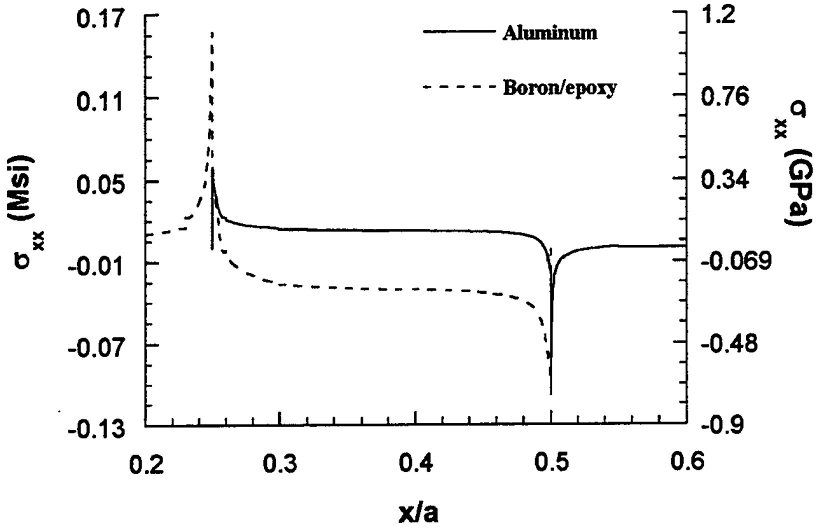

Fig. 4.43 Distributions of normal stress σ_{xx} at the aluminum-boron/epoxy interface at $y/b = 0$.

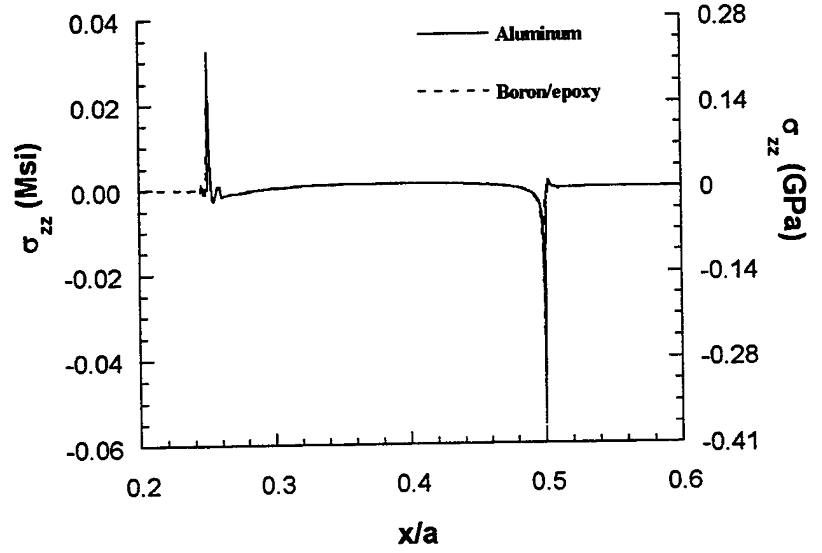

Fig. 4.44 Distributions of normal stress σ_{zz} at the aluminum-boron/epoxy interface at $y/b = 0$.

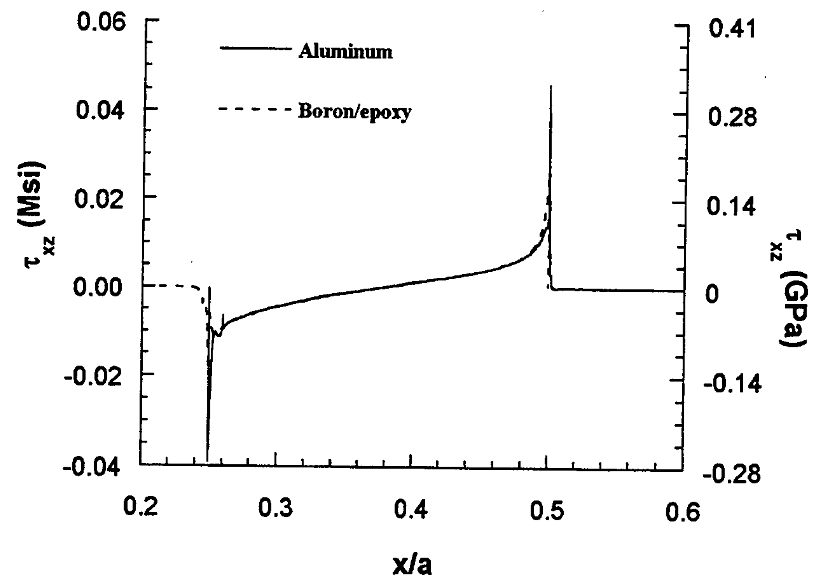

Fig. 4.45 Distributions of transverse shear stress τ_{xz} at the aluminum-boron/epoxy interface at $y/b = 0$.

One may notice slight oscillations in the numerical solution of the stresses in the vicinity of the joint corner **A** as compared to the joint corner **B.** This is due to the fact that the computational elements are more refined in the vicinity of the joint corner **B** in comparison to the joint corner **A.** It may also be noted that in the present analysis the stresses are *not* averaged from the two adjacent elements as is done in many standard FE packages. Instead the *true* values of the stress components as computed from the two elements at their common boundary are used to create all the plots shown. Further, it does not seem necessary to enforce the stress continuity at the boundary of the two *homogeneous* elements (or elements with same material properties) because the stresses are practically continuous along these boundaries as shown in Figs. 4.43-4.45. This is particularly so in the vicinity of the joint corner **B** where more computational elements are taken. It is further pointed out that the continuity of the transverse normal and shear stresses along the interface of the two adherends is also achieved with a very high accuracy as shown in Figs. 4.44 and 4.45, respectively.

4.2.2 Comparison of the stresses in the adherends for restrained versus unrestrained cases

The distributions of stresses in the aluminum plate at the aluminum-boron/epoxy interface for the cases of unrestrained and restrained expansion of the double-lap joint are shown in Figs. 4.46-4.49. In general, the magnitude of the inplane stress components σ_{xx} and σ_{yy} increased manyfold after constraints on the joint against its free expansion are imposed (see Figs. 4.46 and 4.47). Such restraint of the metallic skin and joints commonly occurs in the vicinity of stringers, frames and spars, etc., in primary aerospace structures. Further, as shown in Fig. 4.48 the transverse normal stress component σ_{zz} in the aluminum changes sign from compression to tension at the joint corner **B** thereby making the joint corner **B** also a critical region for debonding along with the joint corner **A**. Another noticeable change occurs in the distribution of transverse shear stress component τ_{xz} which is no more anti-symmetric in nature (see Fig. 4.49). Further, the magnitude of τ_{xz} is also higher at the joint corner **A** for the restrained problem as compared to the unrestrained problem. Similar observations were also made in respect of the stress field in the boron/epoxy adherend when comparing the restrained and unrestrained situations. However, the distributions of stresses in the boron/epoxy laminate at the aluminum-boron/epoxy interface comparing the unrestrained and restrained expansions of the double-lap joint are not shown here due to the lack of space. The overall effect of restrained expansion is to enhance the severity of the stresses in the overlap region of the double-lap bonded joint subjected to thermal loading.

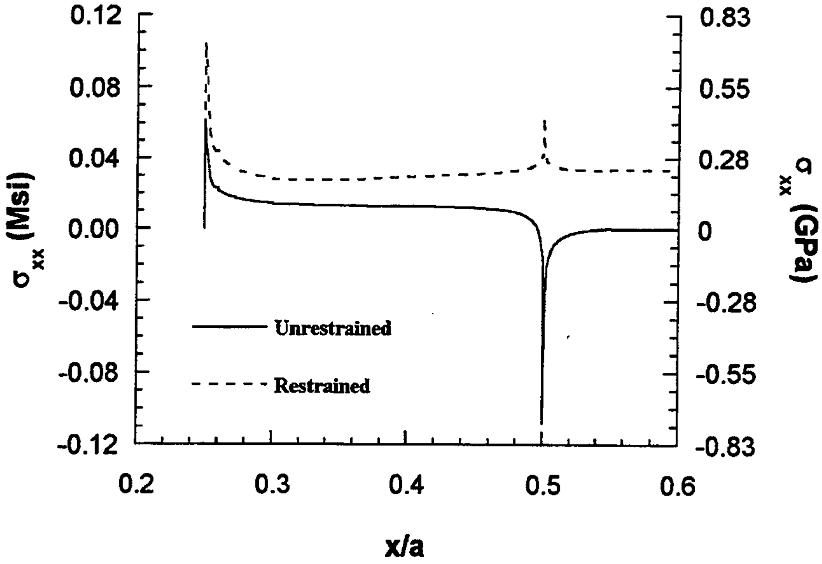

Fig. 4.46 Distributions of normal stress σ_{xx} in the aluminum adherend at the aluminum-boron/epoxy interface at *y/b* = 0.

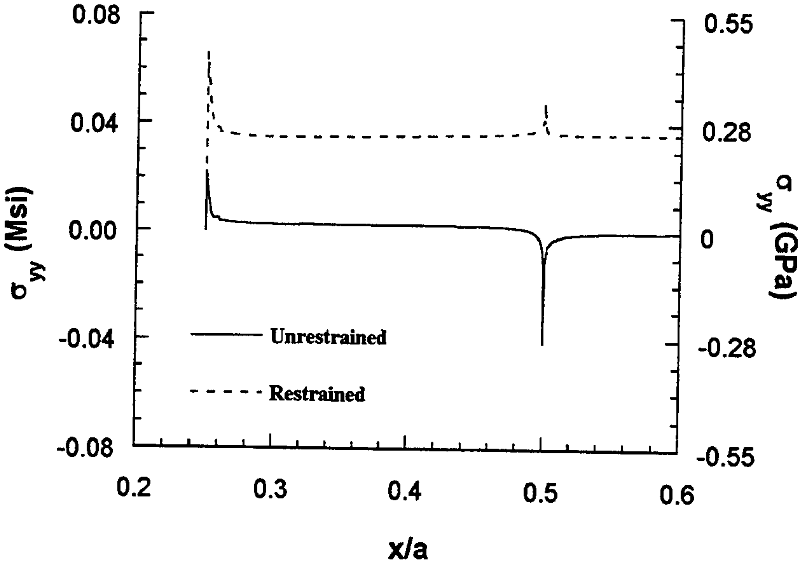

Fig. 4.47 Distributions of normal stress σ_{yy} in the aluminum adherend at the aluminum-boron/epoxy interface at *y/b* = 0.

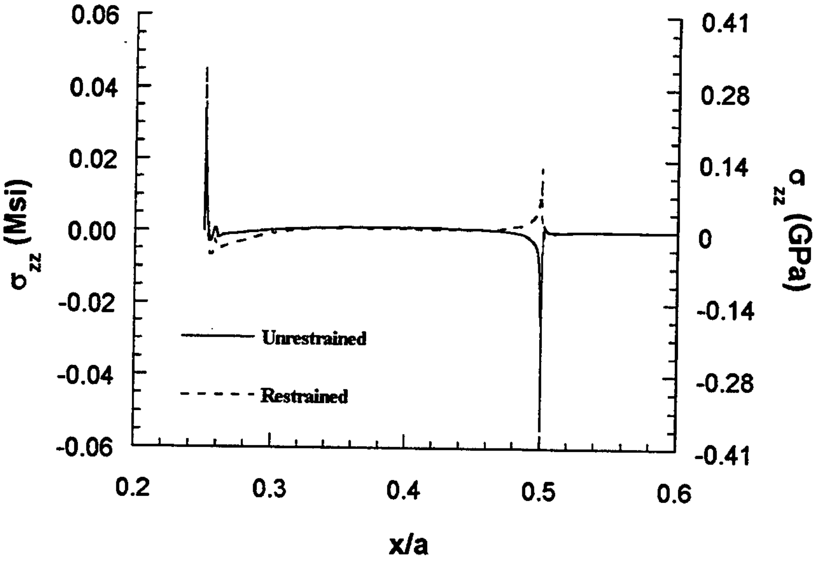

Fig. 4.48 Distributions of normal stress σ_{zz} in the aluminum adherend at the aluminum-boron/epoxy interface at *y/b* = 0.

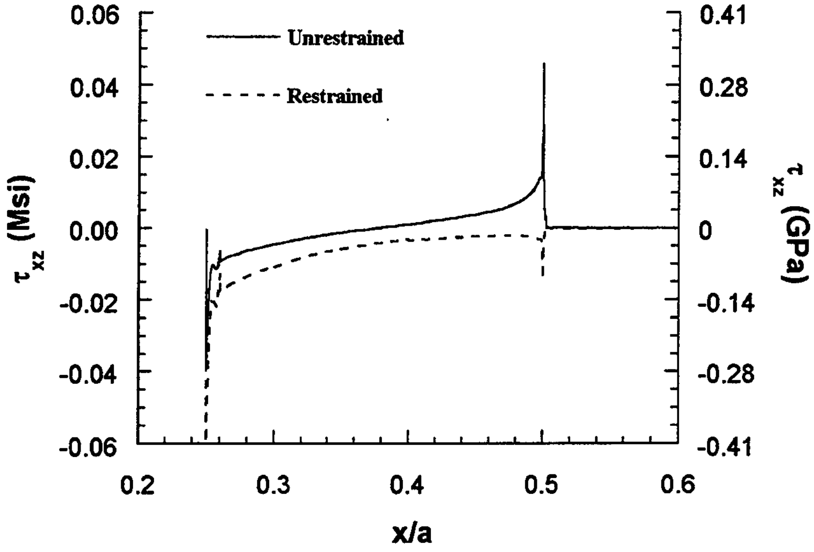

Fig. 4.49 Distributions of transverse shear stress τ_{xz} in the aluminum adherend at the aluminum-boron/epoxy interface at *y/b* = 0.

4.2.3 Stress field in the joint for various composite material upper adherends

The distributions of axial stress σ_{xx} and transverse shear stress τ_{xz} in the aluminum plate at the aluminum-composite upper adherend interface for the case of unrestrained expansion (or contraction) of the symmetric double-lap joint for four different composite material upper adherends are shown in Figs. 4.50 and 4.51, respectively. Similarly, the distributions of axial stress σ_{xx} and transverse shear stress τ_{xz} in the composite upper adherends at the aluminum-composite adherend interface for four different composite material upper adherends are shown in Figs. 4.52 and 4.53, respectively. In general the magnitudes of the stress components σ_{xx} and τ_{xz} in the aluminum plate are lower when the upper adherends are made up of glass/epoxy or GLARE^{TM} material as compared to those when they are made up of boron/epoxy or graphite/epoxy material. The severity of thermal stresses in the aluminum plate is highest in the case of graphite/epoxy and lowest in the case of GLARE^{TM} as the upper adherends (see Figs. 4.50 and 4.51). Similar trends are observed for the stresses in the composite adherends where graphite/epoxy has the highest magnitude of thermal stresses and GLARE^{TM} the lowest (see Figs. 4.52 and 4.53). In fact the use of GLARE^{TM} as upper adherend provides negligibly small magnitude of stresses in both the adherends.

4.2.4 Summary

A three-dimensional analysis based on *variable-order* solid elements (SAVE) is used to analyze a perfectly bonded, symmetric, double-lap joint subjected to uniform temperature loading. The joint configuration considers an aluminum adherend in combination with four different unidirectional laminated composite adherends. When the free expansion of the joint was permitted, the aluminum plate had much higher magnitude of the thermal stresses for the cases when the upper adherends were either boron/epoxy or graphite/epoxy composite laminates as compared to those cases when the upper adherends were either glass/epoxy or the GLARE^{TM}. When the joint was restrained against its free expansion in the inplane coordinate directions the magnitudes of the inplane stress components σ_{xx} and σ_{yy} in the aluminum and the boron/epoxy adherends increased manyfold. However, the magnitude of transverse shear stress τ_{xz} increased at the joint corner **A** and decreased at the joint corner **B**. Further, the transverse normal stress σ_{zz} was found to change sign from compression to tension at the joint corner **B** thereby making both joint corners critical regions for initiation of debonding and subsequent failure of the joint.

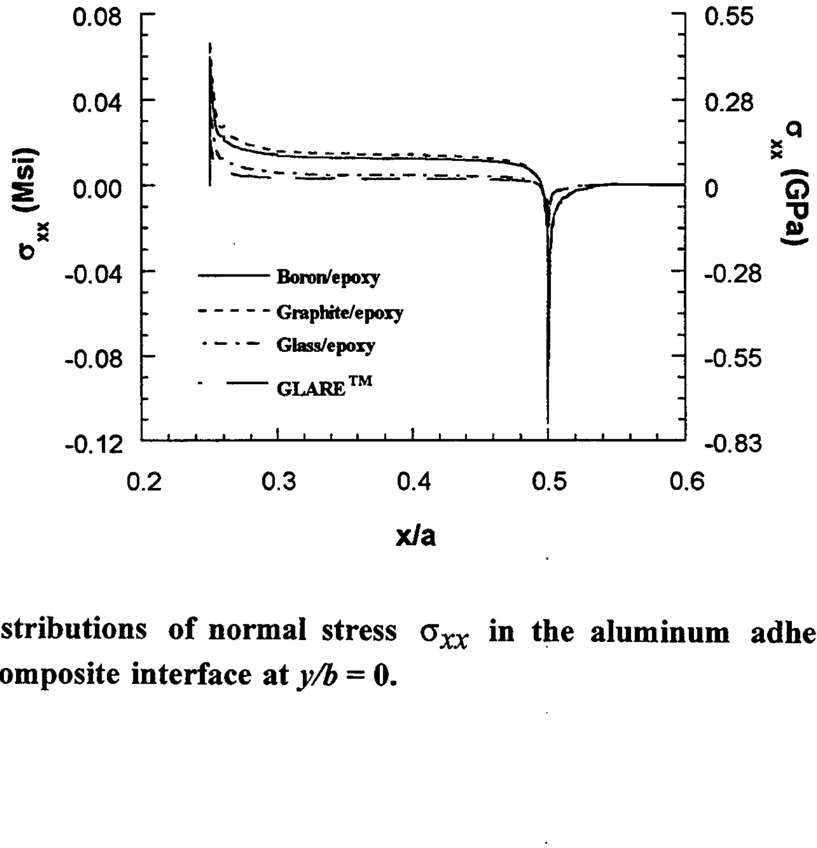

Fig. 4.50 Distributions of normal stress σ_{xx} in the aluminum adherend at the aluminum-composite interface at $y/b = 0$.

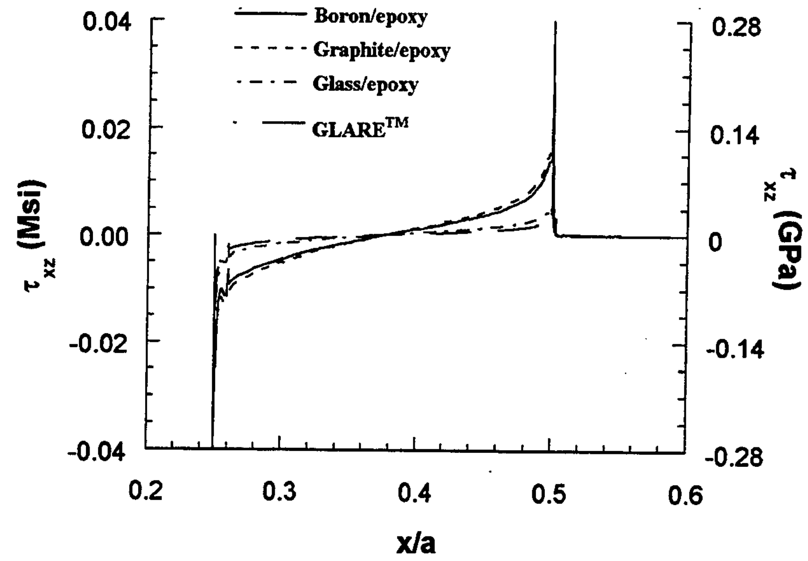

Fig. 4.51 Distributions of transverse shear stress τ_{xz} in the aluminum adherend at the aluminum-composite interface at *y/b* = 0.

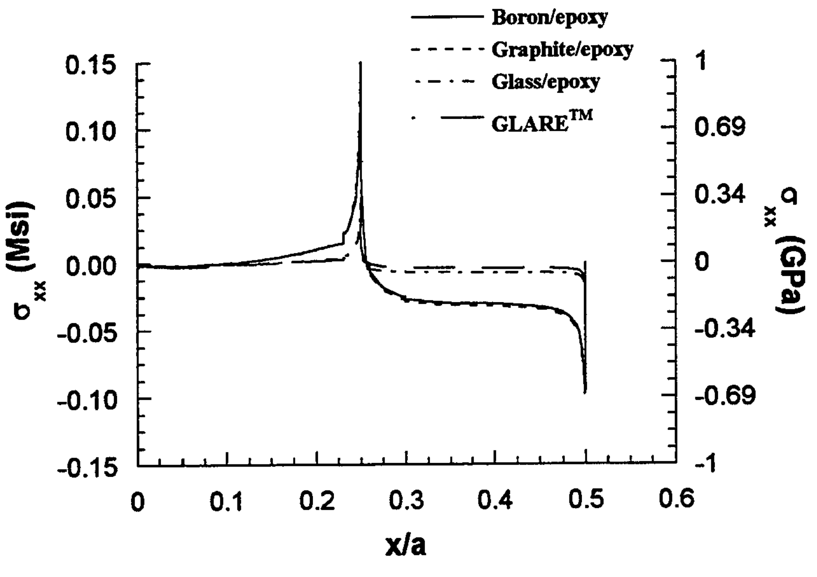

Fig. 4.52 Distributions of normal stress σ_{xx} in the composite adherend at the aluminum-composite interface at *y/b* = 0.

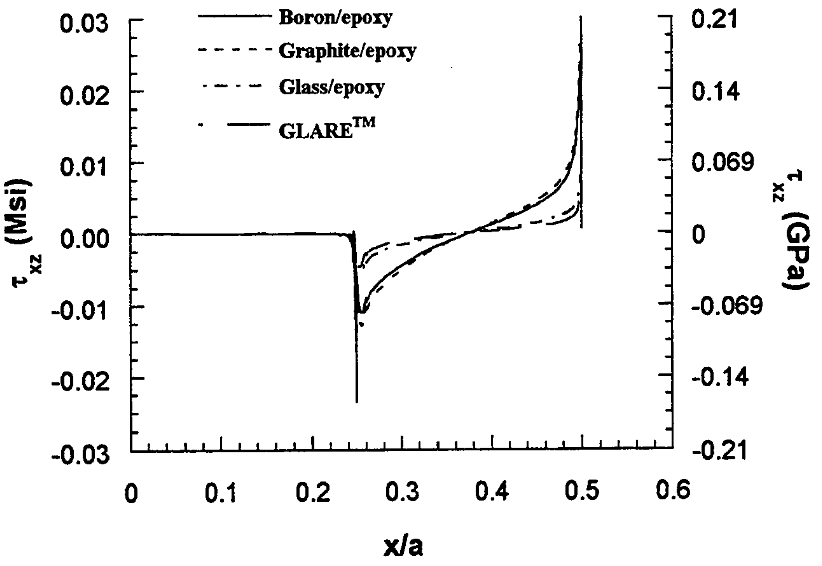

Fig. 4.53 Distributions of transverse shear stress τ_{xz} in the composite adherend at the aluminum- composite interface at *y/b* = 0.

4.3 THERMOMECHANICAL ANALYSIS OF ADHESIVELY BONDED DOUBLE-LAP JOINTS: A COMBINED ANALYTICAL AND EXPERIMENTAL STUDY

In this section, the effects of change in the design parameters such as bond length, bond thickness and adhesive curing temperature on the failure loads of a double-lap adhesively bonded joint are studied through a combined analytical and experimental work. The design parameters such as bond length, bond thickness and adhesive curing temperature, etc., affect the failure strength of adhesively bonded joints, and are important for optimum design considerations as well.

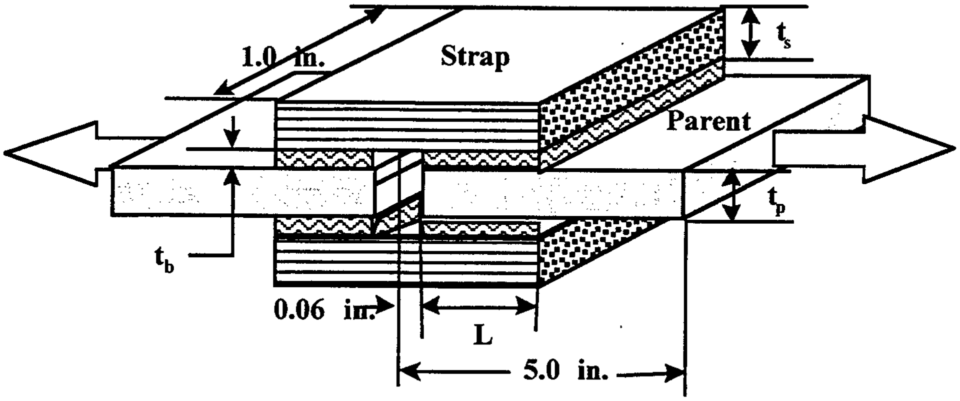

Fig. 4.54 An adhesively bonded, symmetric double-lap joint

The failure loads for two sets each of the bond length, bond thickness and curing temperature were obtained experimentally for two sets of parent-strap lay-up combination by McDonnell Douglas Aircraft Corporation for an adhesively bonded double-lap joint tested under axial extension as shown in Fig. 4.54. The experimental observations are corroborated with the analytical studies performed by using a closed-form, qusai-2D analysis program BONJO[49] and generalized coordinate finite element analysis program SAVE. The stress distributions in the adhesive and the parent material as obtained from the two analyses are discussed in conjunction with the experimental observations. A brief discussion of BONJO and SAVE analysis programs is provided in Sub-sections 2.1.4 and 2.1.7, respectively. However, as mentioned earlier BONJO computer code analyzes only the overlapped portion of joint, i.e., the configuration comprising of only the portions of the adherends which are bonded to the either side of the adhesive layer (see Fig. 4.55).

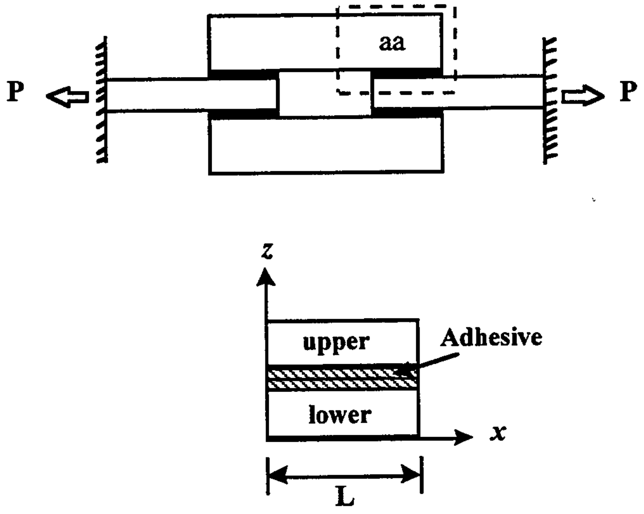

Detail ‘aa’

Figure 4.55 Double-lap bonded joint configuration analyzed by BONJO.

4.3.1 Experimental failure loads

A number of double-lap bonded joint specimens (see Fig. 4.54) were tested by McDonnell Douglas Corporation. Mr. Bob Funke, McDonnell Douglas Aircraft Corporation, St. Louis, MO 63166 provided the experimental data on double-lap bonded joints. Various joint parameters such as bond length, bond thickness and the adhesive curing temperatures were varied during this testing program. The average failure loads obtained for the bonded joint specimens at two different curing temperatures are presented in Table 4.3. Each specimen is allocated a model number. Further, the cure temperature is combined with the model number to represent the test specimen at a particular cure temperature. For example, Model 1-75 represents the Model 1 cured at 75°F. Thus, from here onwards the specimens will be referred to as per these notations.

Table 4.3. Average failure loads for double-lap bonded joint specimens (Data supplied by McDonnell Douglas Corporation, St. Louis, MO.).

Model	**Bond Length L (in)**	**Adhesive Thickness t_b (in)**	**Parent Layup**	**Parent Thickness t_p (in)**	**Strap Layup**	**Strap Thickness t_s (in)**	**Avg. Failure Load (lb/in) - 65° F dry**	**Avg. Failure Load (lb/in) 75° F dry**
1	0.5	0.006	C	0.1872	1	0.0936	4300	5240
2	1.5	0.006	C	0.1872	1	0.0936	5630	7848
3	1.5	0.018	C	0.1872	1	0.0936	n/a	n/a
4	0.5	0.006	B	0.0624	2	0.0312	3560	5220
5	1.5	0.006	B	0.0624	2	0.0312	4180	5430
6	1.5	0.018	B	0.0624	2	0.0312	3220	4960

The following observations are made from the experimental data provided in Table 4.2:

1. Model 2-65 with a lower curing temperature has failure load which is 28% lower than Model 2-75.
2. Model 1-75 with smaller bond length has failure load which is about 33% lower than Model 2-75.
3. Model 3-75 with larger bond thickness would have failure load lower than Model 2-75. (This observation is reasonable if one compares the failure loads for Models 5-75 and 6-75.)

Thus, it is observed that a lower curing temperature, a smaller bond length and an increase in the bond thickness results in a lower joint failure load.

The correlation of experimental observations outlined above with the analytical studies is the goal here. For this purpose Model 2-75 with $L = 1.5$ inches, $t_b = 0.006$ inches cured at 75° F is considered as the baseline model (see Table 4.3). The Model 1-75 with $L = 0.5$ inches, $t_b = 0.006$ inches cured at 75° F represents the effect of change in the bond length when compared with the Model 2-75. Similarly, Model 3-75 with $L = 1.5$ inches, $t_b = 0.018$ inches cured at 75° F represents the effect of change in the bond thickness when compared to the model 2-75. Further, Model 2-65 with $L = 1.5$ inches, $t_b = 0.006$ inches cured at -65°F represents the effect of change in the curing temperature as compared to the Model 2-75.

There are two reasons for selecting Model 2 as a baseline model for the analysis instead of Model 5. The first reason is that the effect of changes in bond length and curing temperature on the ultimate failure loads is more pronounced for the models with parent lay-up C and strap lap-up 2 (Models 1, 2 and 3) as compared to the models with parent lay-up B and strap lap-up 1 (Models 4, 5 and 6). The other reason is that the potential of three-dimensional analysis is better realized when the adherends are thicker as in the case of models with parent C and strap 2 (Models 1, 2 and 3) as compared to the joint models with parent B and strap 1 (Models 4, 5 and 6).

4.3.2 Results and discussions

The four models denoted by 2-75, 2-65, 1-75 and 3-75 are analyzed using BONJO and SAVE computer programs. A typical double-lap bonded joint configuration shown in Fig. 4.54 has been analyzed. Due to the symmetry of the joint with respect to the *x*-, *y*- and the *z*-directions, only 1/8th of the joint configuration (see Fig. 4.2) is analyzed by the SAVE program using a variable-order rectangular solid element with order (M = 4). Thus, the three-dimensional displacement field in each element is approximated by *fourth degree* Bernstein polynomials in all three coordinate directions. There are 19, 947 d.o.f. in the analytical model of the double-lap joint.

The material for parent and strap is Graphite/epoxy. The adhesive material is FM300. The parent (or lower adherend) is a 36-ply $[(\pm45)/(0/90)_2/(90/0)_2/(\pm45)_2/(0/90)_2]_s$ balanced symmetric laminate (lay-up C). The strap (or upper adherend) is a 18-ply unidirectional composite laminate (lay-up 2). For the purpose of analysis the parent adherend is modeled as $[SL1/SL2]_s$ where the sub-laminate SL1 = ($\pm$45), and the sub-laminate SL2 = $[(0/90)_2/(90/0)_2/(\pm45)_2/(0/90)_2]$. The effective (or smeared) thermoelastic properties of the sub-laminates SL1 and SL2 are obtained based on the work by Johnson and Rastogi[73]. Each of these sub-laminates is then discretely modeled with the smeared thermoelastic properties. A uniform axial displacement is applied at the face x = 5.0 inches (see Fig. 4.54). Thermal stresses due to adhesive curing are also accounted for in the analysis. In the following paragraphs, first, the stress distributions in the baseline Model 2-75 as obtained from the two analyses BONJO and SAVE are compared. Next, the three-dimensional stress fields obtained from the SAVE analysis for Models 2-65, 1-75 and 3-75 are compared with those obtained for the baseline Model 2-75.

The stress distributions for the four models described earlier are presented along the bondline of the joint (i.e., along the *x*-direction) at the two locations along the thickness coordinate (see Figs. 4.2 and 4.55). These locations are (i) the adhesive and parent laminate interface, and (ii) the adhesive centerline. During the experimental study the failure was observed to initiate either at the interface of the first ply of the parent laminate and the adhesive or at the interface of the first and second ply, at the joint edge at **B** (see Fig. 4.42 for the notation of joint edge **B**). In case of 3-D analysis the stress fields at the mid-plane at y/b = 0.0 (refer to Fig. 4.2) are considered so as to avoid the double-free edge or the corner effects. It may be noted that the closed-form solution BONJO is a quasi-2D analysis which does not model the joint corners and the free-edge effects.

The stress distributions for all the models are normalized by the far-field average axial stress (denoted as σ_0) value in the parent laminate of the respective model. These far-field average axial stress values are also used as input for applied loading in the BONJO program to analyze the four models.

4.3.2.1 Stress distributions in baseline Model 2-75

The distributions of normalized stresses along the bondline in the smeared layer SL1 at the parent/adhesive interface and at the centerline of the adhesive (refer to Fig. 4.55 for the coordinate system) in the baseline Model 2-75 as obtained from the BONJO and SAVE analyses are shown in Figs. 4.56-4.61. The distribution of the normalized stress σ_{xx} in the parent material at the parent/adhesive interface is shown in Fig. 4.56 from the two analyses. As shown in Fig. 4.56 the values for normal stress σ_{xx} predicted by the BONJO analysis do not compare well with those obtained from the SAVE analysis. The distribution of the normal stress σ_{yy} in the parent material at the parent/adhesive interface is shown in Fig. 4.57 from the SAVE analysis. The BONJO code does not account for this stress component in the analysis.

The distributions of transverse stress components σ_{zz} and τ_{xz} from the two analyses in the parent material layer SL1 at the adhesive/parent adherend interface are shown in Figs. 4.58 and 4.59. As shown in Figs. 4.58 and 4.59 the numerical values of these stress components compare well with each other from the two analyses except in the vicinity of the edge $x/L = 1.0$. Near the edge $x/L = 1.0$, the 3-D analysis SAVE predicts high gradient for the stress component σ_{zz} and a much higher peak value of the stress component τ_{xz} as compared to those obtained by the BONJO analysis. The edge $x/L = 1.0$ has been found to be the critical location of failure initiation between adhesive and lower adherend by many researchers during their experimental studies. The combination of high tensile value of the transverse normal stress component σ_{zz} (also called peel stress) and a higher magnitude of shear stress component τ_{xz} can cause failure initiation at the edge $x/L = 1.0$.

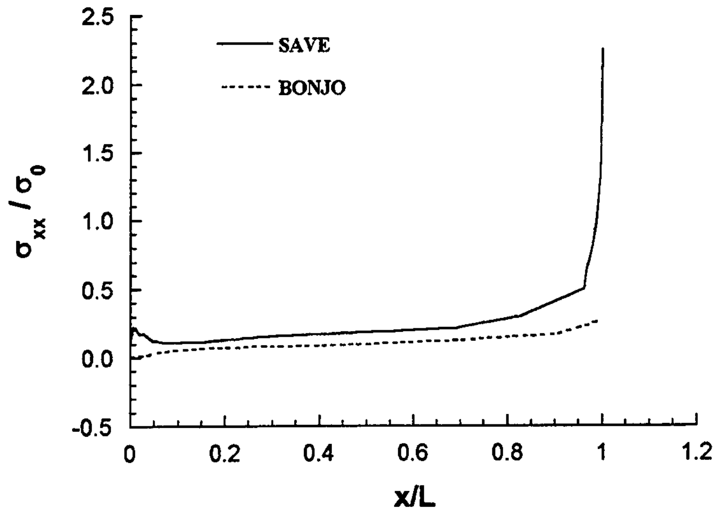

Fig. 4.56 Distributions of normal stress σ_{xx} in the parent laminate at the adhesive-parent laminate interface at $y/b = 0$.

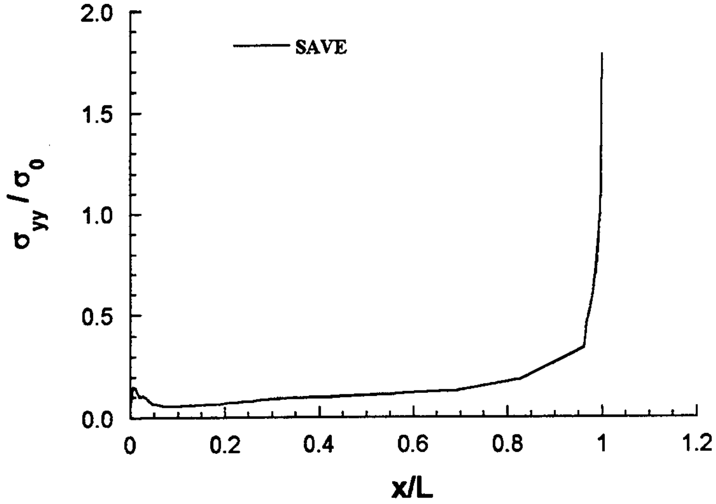

Fig. 4.57 Distributions of normal stress σ_{yy} in the parent laminate at the adhesive-parent laminate interface at $y/b = 0$.

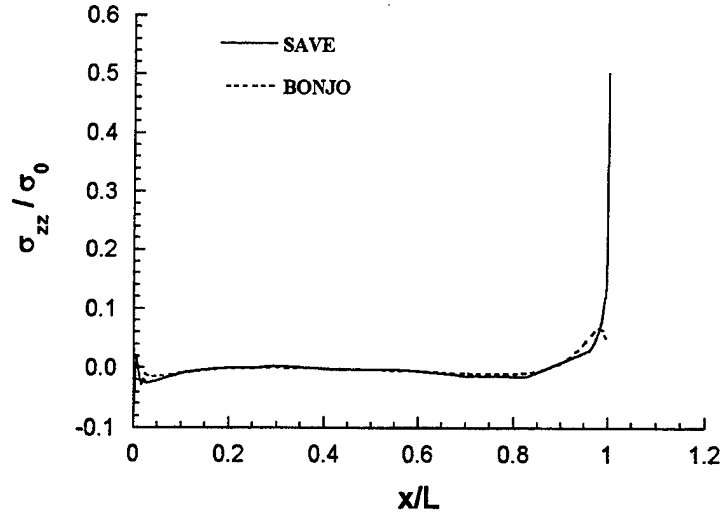

Fig. 4.58 Distributions of normal stress σ_{zz} in the parent laminate at the adhesive-parent laminate interface at *y/b* = 0.

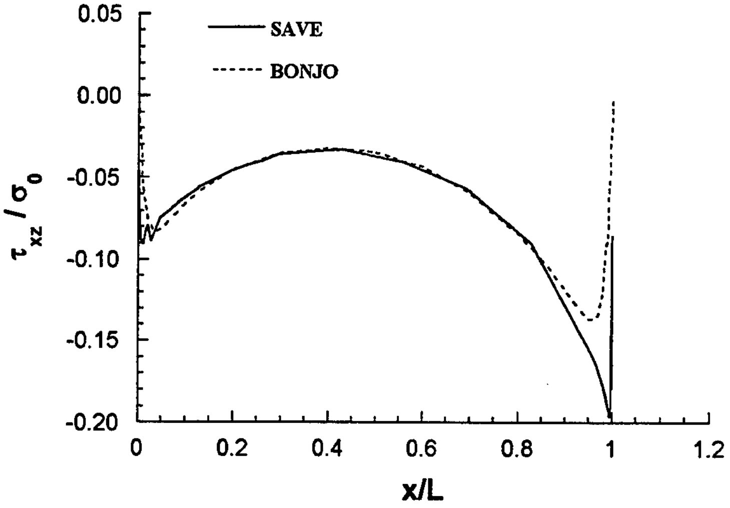

Fig. 4.59 Distributions of transverse shear stress τ_{xz} in the parent laminate at the adhesive- parent laminate interface at *y/b* = 0.

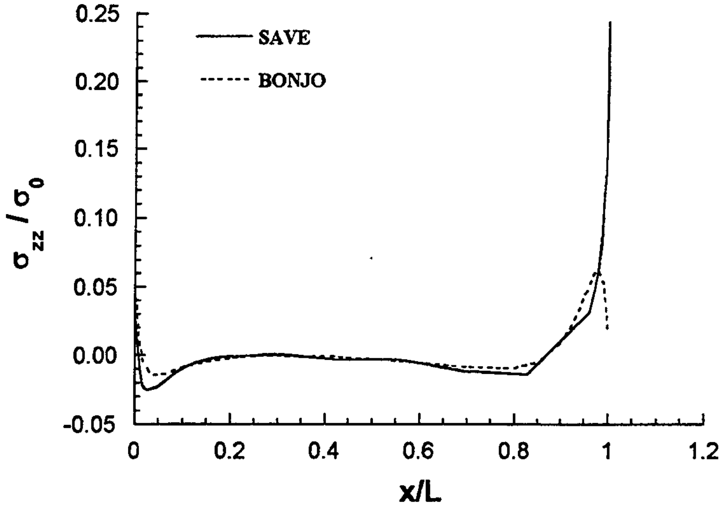

Fig. 4.60 Distributions of normal (peel) stress σ_{zz} in the adhesive at the adhesive centerline at *y/b* = 0.

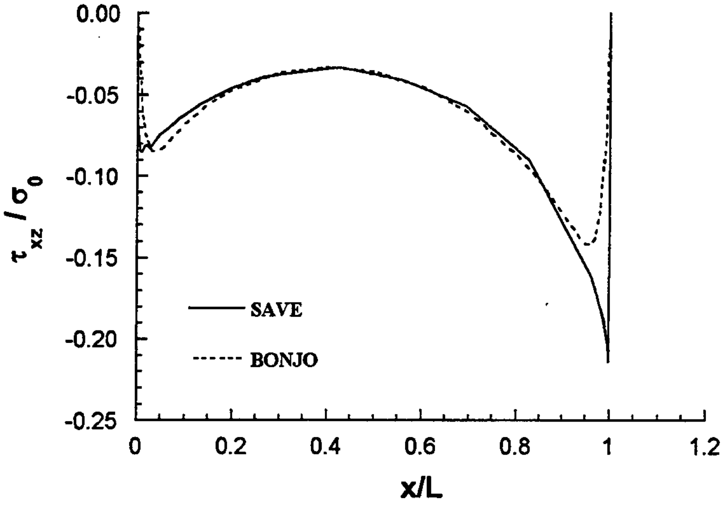

Fig. 4.61 Distributions of transverse shear stress τ_{xz} in the adhesive at the adhesive centerline at *y/b* = 0.

The distributions of the transverse normal stress σ_{zz} and transverse shear stress τ_{xz} at the centerline of the adhesive as obtained from the BONJO and SAVE analyses are shown in Figs. 4.60 and 4.61, respectively. Once again the numerical values of these stress components compare well from the two analyses except in the vicinity of the edge x/L = 1.0 as shown in Figs. 4.60 and 4.61. Near the vicinity of the edge x/L = 1.0, the 3-D analysis SAVE predicts high gradient for the stress component σ_{zz} and a much higher peak value of the stress component τ_{xz} compared to those obtained by the BONJO analysis.

Even modeling of the angle plies as a smeared sub-laminate (such as SL1 in the present numerical example) in the BONJO analysis does not yield correct values for in-plane stress components. Furthermore, the BONJO analysis is incapable of predicting the high gradient of the stress components in the vicinity of the edge $x/L = 1.0$ (see Figs. 4.56-4.61) where the 3-D analysis SAVE captured the stress variations in a more accurate manner. However, it has generally been noted that the distributions of the transverse normal stress σ_{zz} and shear stress τ_{xz} in the adhesive and the adhesive/adherend interfaces as obtained from the BONJO analysis compare reasonably well with those obtained from the other analytical techniques such as ABAQUS, *except* in the vicinity of the edge $x/L = 1.0$ (refer to Section 4.1). Since most of the earlier empirical design processes are based on the adhesive failure, the closed-form analysis technique BONJO seems to fulfill that objective by predicting the shear stress, and to some extent the peel stresses in the adhesive with reasonable accuracy.

4.3.2.2 Stress distributions in Model 2-65 vs. Model 2-75

Next, the effect of change of curing temperature on the stresses in a double-lap bonded joint is studied. The stress fields for the Model 2-65 and Model 2-75 as obtained from the SAVE analysis are compared. For the purpose of analysis, the material properties for the adherends and adhesive are used at -65°F for the Model 2-65, and at 75°F for the Model 2-75.

The distributions of stresses in the parent material along the bondline at the adhesive/parent material interface, and in the adhesive at the adhesive centerline as obtained from the SAVE analysis are shown in Figs. 4.62-4.67. As shown in Figs. 4.62-4.67, the peak values of all the stresses in Model 2-65, in the vicinity of the edge $x/L = 1.0$ are higher as compared to those obtained for the Model 2-75. (Note that the same element mesh design is used to analyze all the cases.) Except for the transverse shear stress component τ_{xz}, all other stress components have essentially the same numerical value from the two models away from the edge $x/L = 1.0$. The transverse shear stress component clearly attains a higher numerical value in the vicinity of the edge $x/L = 1.0$, both at the adhesive/parent material interface as well as at the centerline of the adhesive. The combination of higher shear and peel stresses near the edge $x/L = 1.0$, in all likelihood, would result in a lower failure load for the Model 2-65 as compared to Model 2-75. Also, the lower ultimate failure strain of the adhesive at -65° F ($\gamma = 0.16$ at -65° F as compared to $\gamma = 0.33$ at 75° F from the data supplied by McDonnell Douglas) also justifies a lower failure load for the Model 2-65.

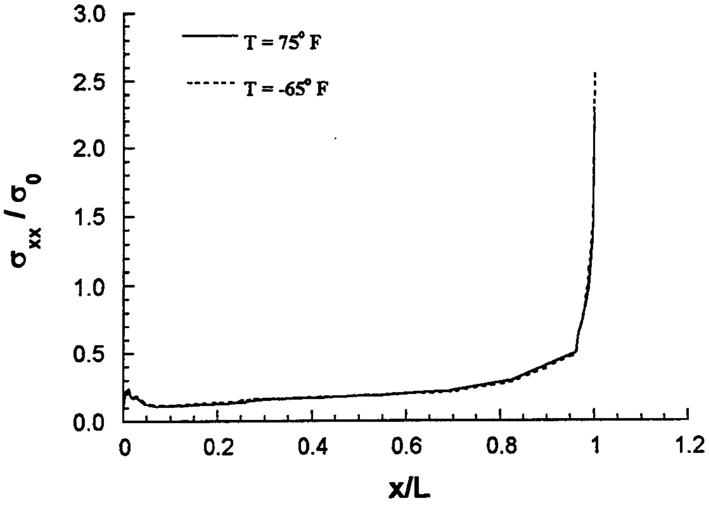

Fig. 4.62 Distributions of normal stress σ_{xx} in the parent laminate at the adhesive-parent laminate interface at $y/b = 0$.

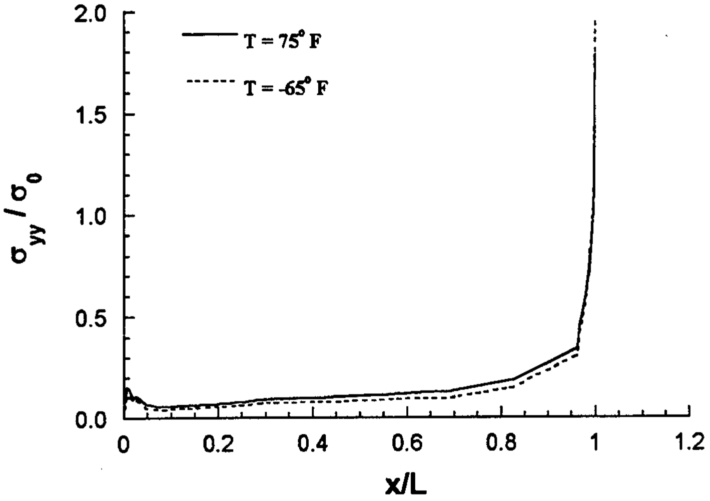

Fig. 4.63 Distributions of normal stress σ_{yy} in the parent laminate at the adhesive-parent laminate interface at $y/b = 0$.

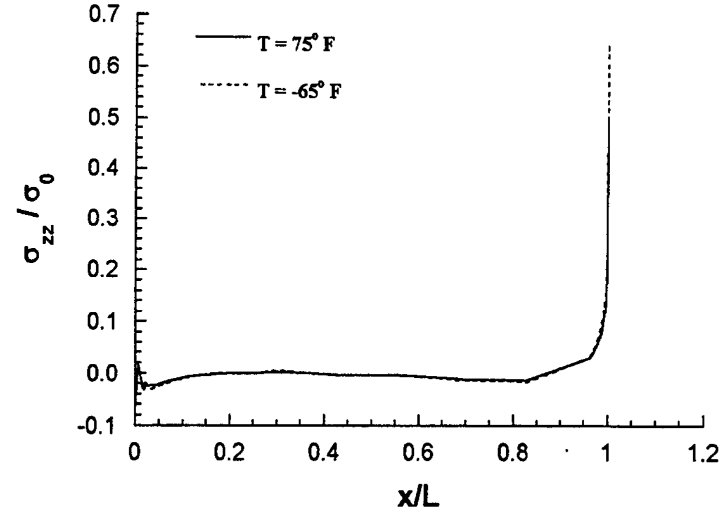

Fig. 4.64 Distributions of normal stress σ_{zz} in the parent laminate at the adhesive-parent laminate interface at $y/b = 0$.

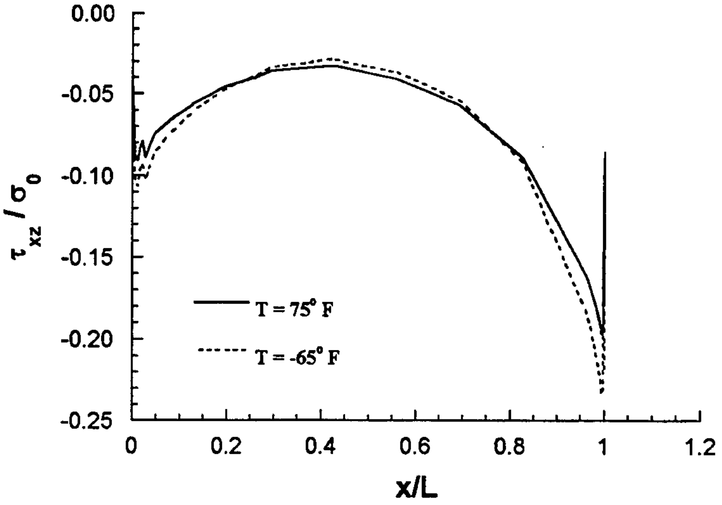

Fig. 4.65 Distributions of transverse shear stress τ_{xz} in the parent laminate at the adhesive- parent laminate interface at $y/b = 0$.

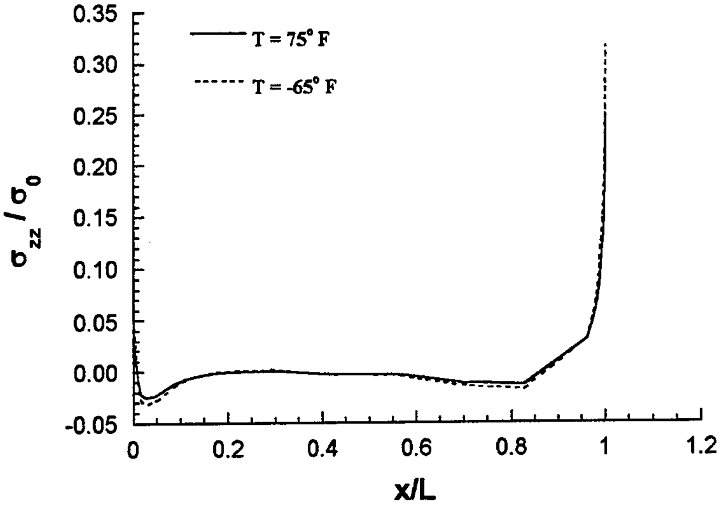

Fig. 4.66 Distributions of normal (peel) stress σ_{zz} in the adhesive at the adhesive centerline at $y/b = 0$.

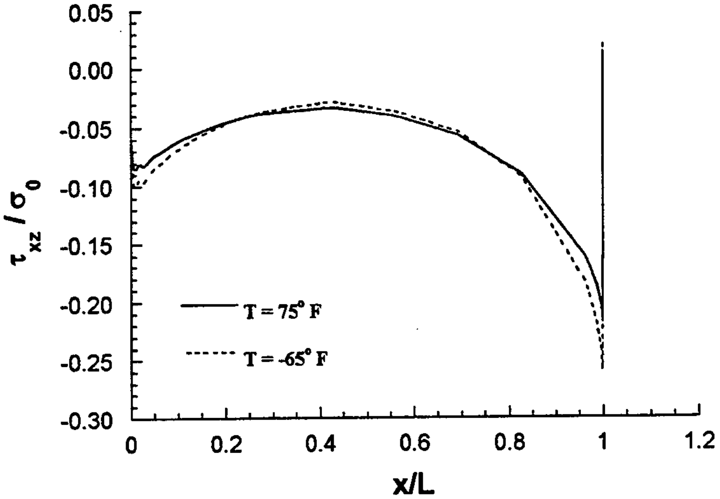

Fig. 4.67 Distributions of transverse shear stress τ_{xz} in the adhesive at the adhesive centerline at $y/b = 0$.

4.3.2.3 Stress distributions in Model 1-75 vs. Model 2-75

The stress fields for Model 1-75 and Model 2-75 as obtained from the SAVE analysis are compared to study the effect of change in the bond length in a double-lap bonded joint. As mentioned earlier Model 1-75 has the bond length L = 0.5 inches as compared to Model 2-75 which has the bond length L = 1.5 inches. For the purpose of analysis the material properties of adherends and adhesive at 75° F are used for both the models.

The distributions of stresses along the bondline at the adhesive/parent material interface and at the adhesive centerline as obtained from the SAVE analysis are shown in Figs. 4.68-4.73. As shown in Figs. 4.68-4.73, the numerical values of all the stresses along the bondline at the adhesive/parent material interface in Model 1-75 are considerably higher than those obtained for the Model 2-75. Specifically, the transverse normal stress σ_{zz} predicts a larger bending of the lower adherend for the Model 1-75 as compared to the Model 2-75 as shown in Fig. 4.70 Further , as shown in Fig. 4.71 the magnitude of the transverse shear stress τ_{xz} is nearly doubled for the Model 1-75 as compared to the Model 2-75. A similar conclusion can be reached about the stress distributions in the adhesive at the adhesive centerline (see Figs. 4.72 and 4.73). Thus, it is evident that the higher magnitude of the stresses would result in a lower failure load for the Model 1-75 as compared to Model 2-75.

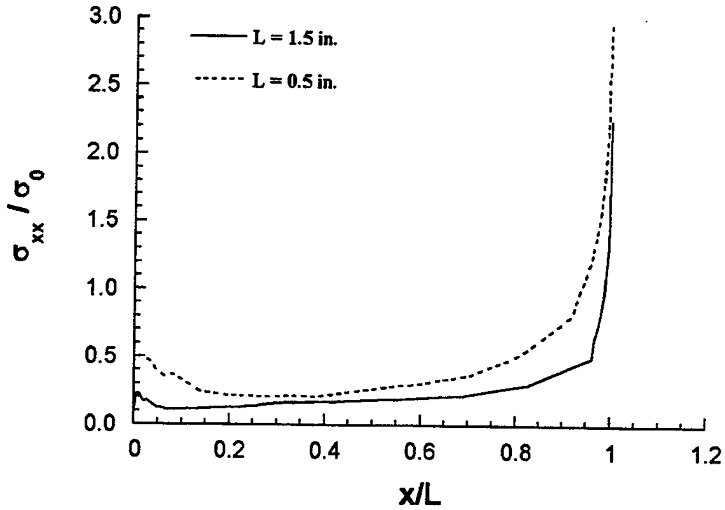

Fig. 4.68 Distributions of normal stress σ_{xx} in the parent laminate at the adhesive- parent laminate interface at $y/b = 0$.

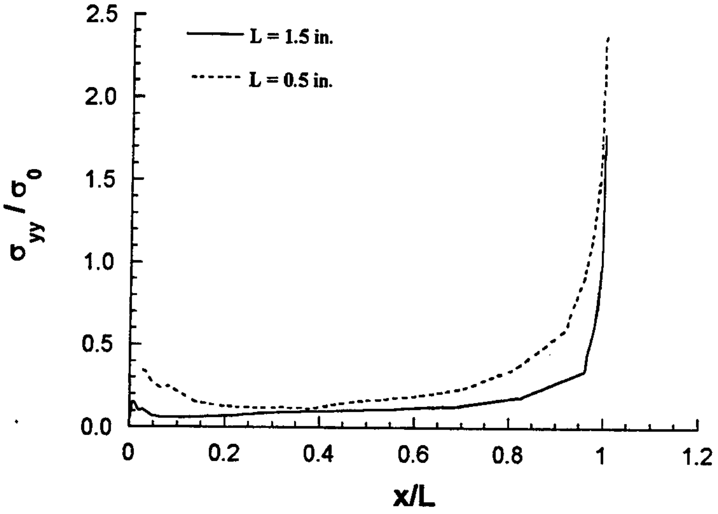

Fig. 4.69 Distributions of normal stress σ_{yy} in the parent laminate at the adhesive- parent laminate interface at *y/b* = 0.

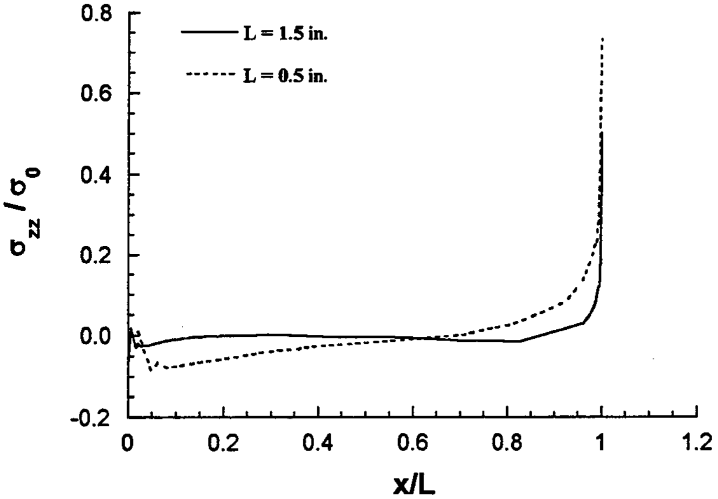

Fig. 4.70 Distributions of normal stress σ_{zz} in the parent laminate at the adhesive- parent laminate interface at *y/b* = 0.

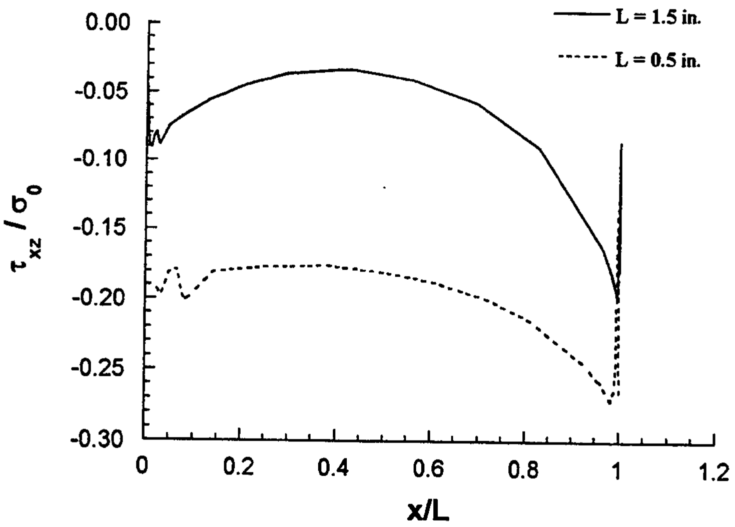

Fig. 4.71 Distributions of transverse shear stress τ_{xz} in the parent laminate at the adhesive- parent laminate interface at *y/b* = 0.

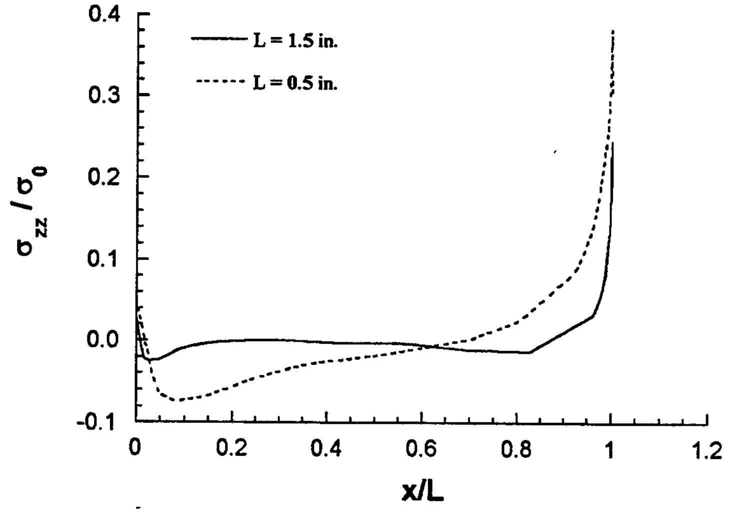

Fig. 4.72 Distributions of normal (peel) stress σ_{zz} in the adhesive at the adhesive centerline at *y/b* = 0.

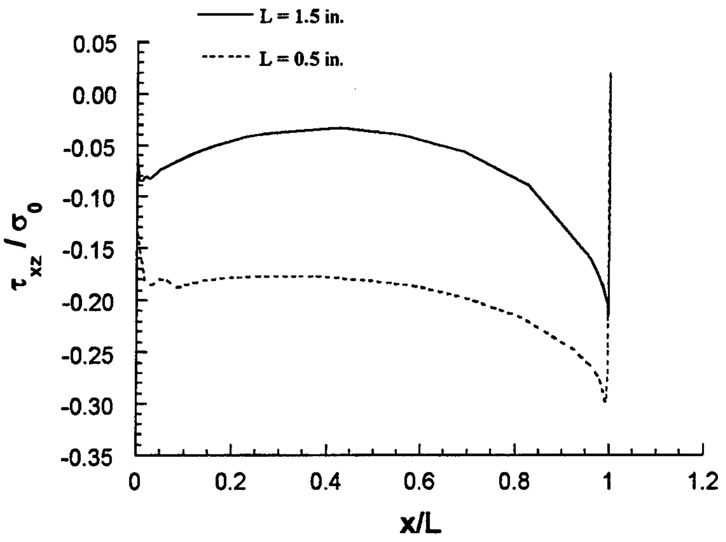

Fig. 4.73 Distributions of transverse shear stress τ_{xz} in the adhesive at the adhesive centerline at *y/b* = 0.

4.3.2.4 Stress distributions in Model 3-75 vs. Model 2-75

The effect of change in the bond thickness on the stresses in a double-lap bonded joint is studied by comparing the stress fields for the Model 3-75 and Model 2-75 as obtained from the SAVE analysis. The Model 3-75 has the bond thickness $t_b = 0.018$ inches as compared to the Model 2-75 which has the bond thickness $t_b = 0.006$ inches. The material properties of adherends and adhesive at 75° F are used for analyzing both the models.

The distributions of stresses along the bondline in the parent material at the adhesive/parent material interface and in the adhesive at the adhesive centerline as obtained from the SAVE analysis are shown in Figs. 4.74-4.79. As shown in Figs. 4.74 and 4.75, the magnitude of the stresses σ_{xx} and σ_{yy} in the Model 3-75 are slightly higher as compared to those obtained for the Model 2-75. The magnitude of the stress component σ_{zz} is essentially the same in the two models as shown in Fig. 4.76. However, the magnitude of the transverse shear stress component τ_{xz} is lower in the vicinity of the edge $x/L = 1.0$, and higher in the middle region of the bond for the Model 3-75 as compared to the Model 2-75 as shown in Fig. 4.77. A similar conclusion can also be reached for the distribution of shear stress τ_{xz} in the adhesive (see Fig. 4.79). In general, the shear stresses are more uniformly distributed in the bond area for the Model 3-75 as compared to the Model 2-75.

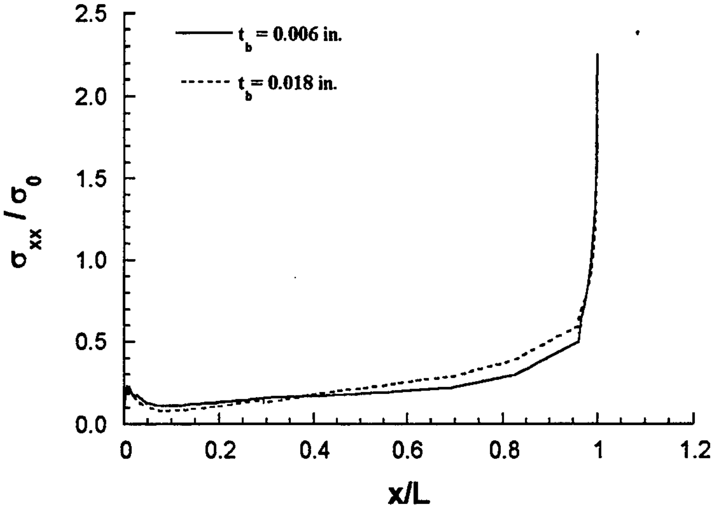

Fig. 4.74 Distributions of normal stress σ_{xx} in the parent laminate at the adhesive-parent laminate interface at $y/b = 0$.

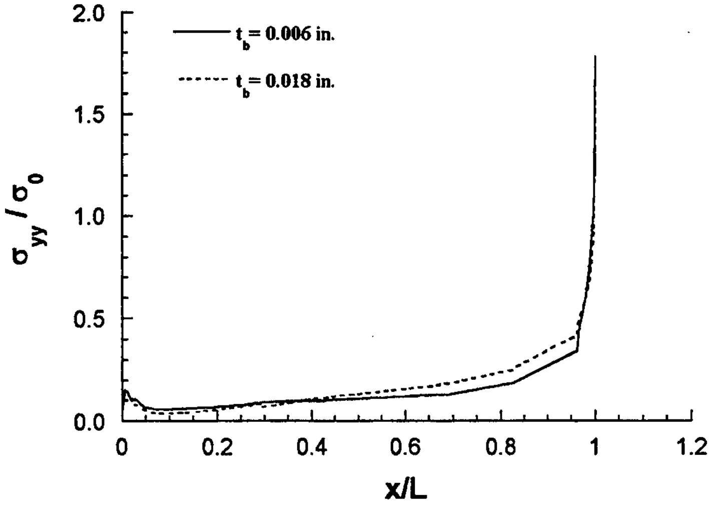

Fig. 4.75 Distributions of normal stress σ_{yy} in the parent laminate at the adhesive-parent laminate interface at $y/b = 0$.

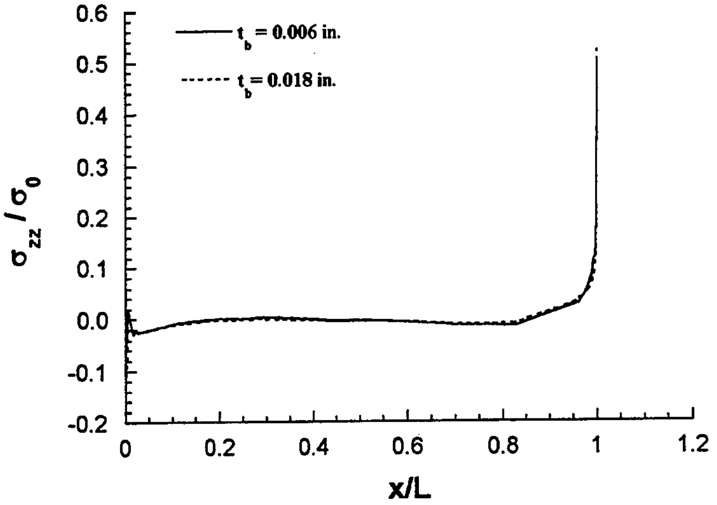

Fig. 4.76 Distributions of normal stress σ_{zz} in the parent laminate at the adhesive-parent laminate interface at *y/b* = 0.

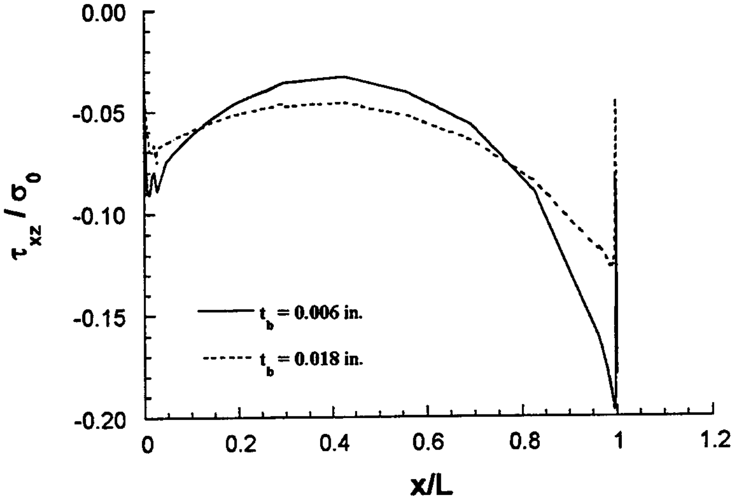

Fig. 4.77 Distributions of transverse shear stress τ_{xz} in the parent laminate at the adhesive- parent laminate interface at *y/b* = 0.

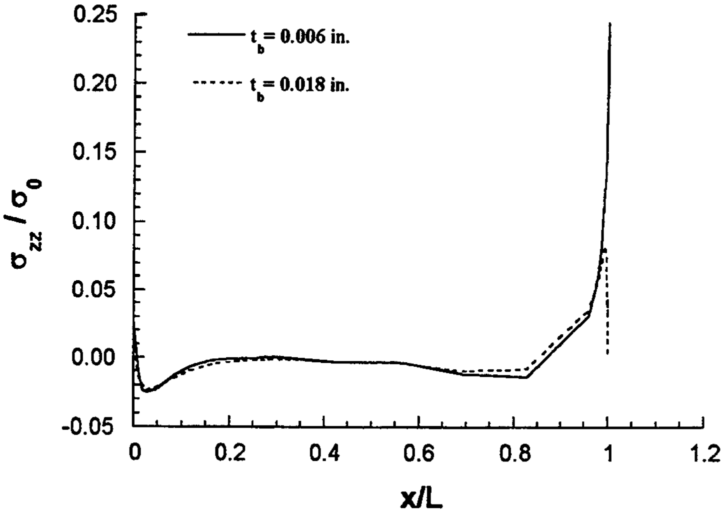

Fig. 4.78 Distributions of normal (peel) stress σ_{zz} in the adhesive at the adhesive centerline at $y/b = 0$.

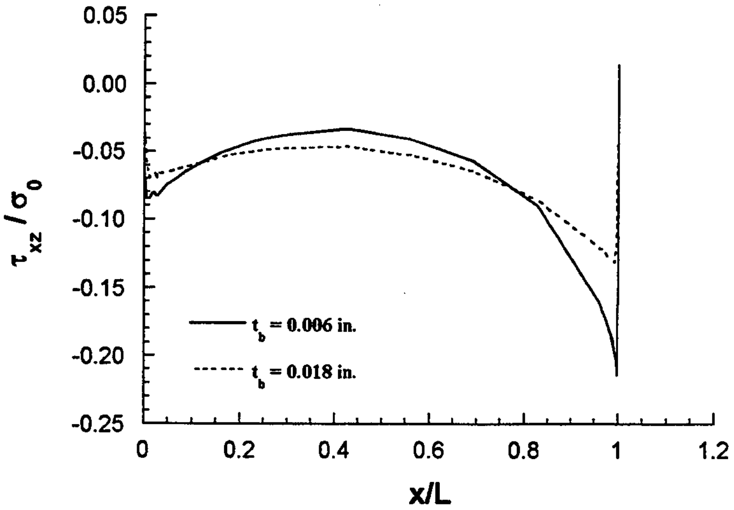

Fig. 4.79 Distributions of transverse shear stress τ_{xz} in the adhesive at the adhesive centerline at $y/b = 0$.

The lower magnitude of the transverse shear component in the vicinity of the edge $x/L = 1.0$ suggests a higher failure load for the Model 3-75 as compared to the Model 2-75. (The magnitude of transverse normal stress component σ_{zz} is essentially the same for the two models as shown in Figs. 4.76 and 4.78.) However, this statement is contradictory to what has been observed experimentally, i.e., the Model 6-75 and Model 6-65 have a lower failure load as compared to the Model 5-75 and Model 5-65. (see Table 4.3.) For the same reason, Model 3-75 would have a lower failure load as compared to the Model 2-75. This contradiction in predicting the failure load on the basis of adhesive shear stress behavior might be better understood in light of the work by Hart-smith[74] wherein he pointed out the importance of having the lower magnitude of the adhesive shear stress τ_{xz} in the middle region of the bond area. In his words "some part of the bond area must be so lightly stressed that the adhesive there will never creep; otherwise the bond will inevitably fail by accumulated damage under sustained load." Thus, in the middle region of the bond area, a lower magnitude of the adhesive shear is preferred over a more uniform distribution of the adhesive shear stress with higher magnitude so as to withstand sustained loading. In light of the aforementioned statement, the lower failure load for the Model 3-75 may be justified as compared to the Model 2-75. Moreover, higher normal stresses σ_{xx} and σ_{yy} in the parent material at the adhesive/parent material interface would also contribute to a lower failure load for Model 3-75 as compared to Model 2-75.

4.3.3 Summary

The stresses in a double-lap bonded joint are studied using a quasi-2D analysis BONJO and a 3-D discrete analysis SAVE. The effect of change in the design parameters such as bond length, bond thickness and curing temperature on the stress distributions and the failure loads in a double-lap bonded joint have been analyzed through a combined analytical and experimental study. The stress distributions obtained from the SAVE analysis provide an accurate qualitative correlation with the experimental observations for the various double-lap bonded joint configurations studied. The results of this study are summarized below:

1. A lower curing temperature results in higher magnitude of stresses in the vicinity of the critical edge location $x/L = 1.0$. The combination of high stresses and the lower ultimate failure strain of the adhesive at -65° F ($\gamma = 0.16$ at -65° F as compared to $\gamma = 0.33$ at 75° F) justifies a lower ultimate failure load at the lower curing temperature.
2. A smaller bond length results in higher magnitude of stresses in the joint along the bond length. Specifically, the joint undergoes higher bending resulting in considerably higher shear and peel stresses in the bonded region thereby resulting in a reduced joint strength.
3. An increase in the bond thickness results in lower shear stresses in the vicinity of the critical edge location $x/L = 1.0$, and higher and more uniform shear stress in the middle region of the bond. Furthermore, the increase in the bond thickness also results in higher normal stresses σ_{xx} and σ_{yy} in the parent material at the adhesive/parent material interface thereby suggesting a lower joint failure load.

4. The closed-form analysis technique BONJO does not accurately predict the in-plane normal stresses in the adherends (except when the adherends are either isotropic metallic plates or unidirectional composite laminates, see Section 4.2 for details) and as such fails to capture the true geometry and material property variations that give rise to high stress gradients in the vicinity of the joint corners.

5. The response of the transverse normal stress σ_{zz} (or peel stress) is more clearly predicted by the SAVE analysis as compared to the BONJO analysis. In most of the numerical examples studied, the BONJO analysis code provides a fairly accurate response of the adhesive transverse shear stress τ_{xz}. However, the magnitude of this stress component as predicted by the BONJO analysis code is lower than that predicted by the SAVE analysis code for all the cases studied.

In the absence of either a progressive damage analysis or a suitable failure criterion to predict the numerical value of ultimate joint failure load, the impact of the accuracy of numerical values of stresses obtained from the two analyses cannot be ascertained. The quantitative comparison of failure loads has always been an important issue that needs to be addressed fully justifying the need of 3-D analysis versus a 1-D or a 2-D simplified stress analysis. However, the importance of having a full 3-D analysis such as SAVE that utilizes the least amount of analytical simplifications as compared to any other analyses techniques cannot be undermined. A full 3-D analysis is necessary if one has to gain a complete insight into the stress response of a complex structural configuration such as an adhesively bonded joint.

4.4 SOFTWARE DEVELOPMENT

A *user friendly* PC based software package has been developed for the stress analysis of composite bonded joints. The bonded joint design software is based on BONJO I computer codes developed by Dickson et. al[49] at the Lockheed Cooperation. BONJO I incorporates analytical tools for determination of stress distribution in the overlap (bond) region of the adhesively bonded joints.

There are three design modules in the software package to analyze (i) a single-lap bonded joint with identical adherends, (ii) a single-lap bonded joint with different adherends, and (iii) a double-lap bonded joint. A common material database module links with all the three design modules for selecting material properties of the jointed plates and the adhesive. The design package is easy to acclimatize, and does not require prior knowledge of complex mathematical theories to work with it. Online help is available within the software which provides technical support on a variety of topics ranging from FAQs (Frequently Asked Questions) on how to create input/output, to more complex questions requiring explanations on mechanics of the analytical model. The **B**olted and **B**onded **J**oints **(BBJ)** software is distributed on four(4) 3.5" diskettes along with a *user's manual* explaining the steps involved in the use of these modules.

5.0 THREE-DIMENSIONAL FINITE ELEMENT ANALYSIS OF COMPOSITE-TO-METAL AND COMPOSITE-TO-COMPOSITE BONDED JOINTS

5.1. INTRODUCTION

Application of three-dimensional solid finite elements gains increasing interest in the numerical analysis of composite structures. Among the most popular types of solid elements is the family of rectangular hexahedra: 8-node (linear displacement) element with 24 d.o.f.; 20-node (quadratic displacement) "serendipity" element with 60 d.o.f.; 27-node "full Lagrange" type (quadratic displacement) element with 81 d.o.f.; 32-node (incomplete cubic displacement) element with 96 d.o.f.; 64-node (complete cubic displacement) element with 192 d.o.f.; 8-node (incomplete quintic displacement) element with 96 d.o.f.; "Hermite" type element with both displacements and displacement derivatives as d.o.f., etc.

Several types of 3-D numerical analyses have been applied to bonded joints in [75]-[78]. The finite difference analysis of double-lap joints presented in [75] have addressed specifics of the 3-D stress variations, double-edge effect at the corner points and inability of capturing it by a 2-D plane strain analysis, the effect of adhesive layer treated as distinct 3-D entity, and discussion on the failure criteria and fracture mechanics applicability. However, not all of the suggestions and conclusions (specifically, those regarding stress singularities) have been validated due to the difficulties with satisfying some of the boundary conditions and absence of the convergence study. An 8-node hexahedron finite element developed in [76] for bonded joint analysis contains substantial simplifications, which deprive many features of the full 3-D analysis. A 3-D finite element analysis of single-lap joints was presented in [77]. A quasi 3-D finite element analysis of double-lap composite-to-metal joints using the 27-node "full Lagrange" hexahedron has been applied in [78] using the "submodeling" technique available in ABAQUS [72]. This section briefly reports a comprehensive numerical study performed for composite-to-metal and composite-to-composite double-lap joints using the approach [78]. A 3-D stress analysis in the presence of initial debond crack, introduced along the line of singularity at the end of the overlap, is also presented.

5.2. THE CONCEPT OF SUBMODELING

The major difficulty faced when performing 3-D analysis of bonded joints is that there are several zones of high stress gradients, and also several *lines* of possible singularities. Obviously, an accurate stress characterization near the lines of singularity with the use of *uniform* element mesh would require extremely high refinement and, accordingly, be computationally expensive. On the other side, when using *nonuniform* element meshes (for example, by applying "parametric refinement" available in ABAQUS), the element aspect ratio may become very high and, thus, cause the indication of "zero or negative element volume error." Both these computational problems have been faced by the investigators when directly using C3D27 element in the analysis of double-lap joints. Particularly, the attempts to accurately compute stresses in relatively thick bonded joints with a thin adhesive layer (which was, indeed, modeled as distinct 3-D elastic entity) revealed severe limitations. Accuracy of the computed stresses was highly questionable. Thus, more sophisticated capabilities available in ABAQUS have been explored. The global-local type "submodeling" technique showed as a viable approach.

The idea how to apply the submodeling technique to the bonded joint problems can be explained using the specific example shown in Fig. 5.1a. Clearly, only those regions of the structure have to be analyzed in great detail (i.e., using fine element meshes), which are close to the corner lines AB and CD. Accordingly, the stress fields can be computed in several steps, by successively performing 3-D analysis for smaller and smaller local regions. When using such a multi-step approach, the computed nodal displacements from some "predecessor" local analysis are applied as the input geometric boundary conditions for the "successor" local analysis. If this methodology is implemented correctly, then each next step should provide increasingly accurate stresses in the zones of high stress gradients. Ultimately, if it is known that the stresses are finite everywhere in the structure, their values can be computed with any prescribed accuracy after a certain number of the submodeling steps. In principle, the number of consecutive local analyses is limited only by patience of the analyst and physical time allocated for the specific problem. An experienced analyst can easily optimize the submodeling strategy.

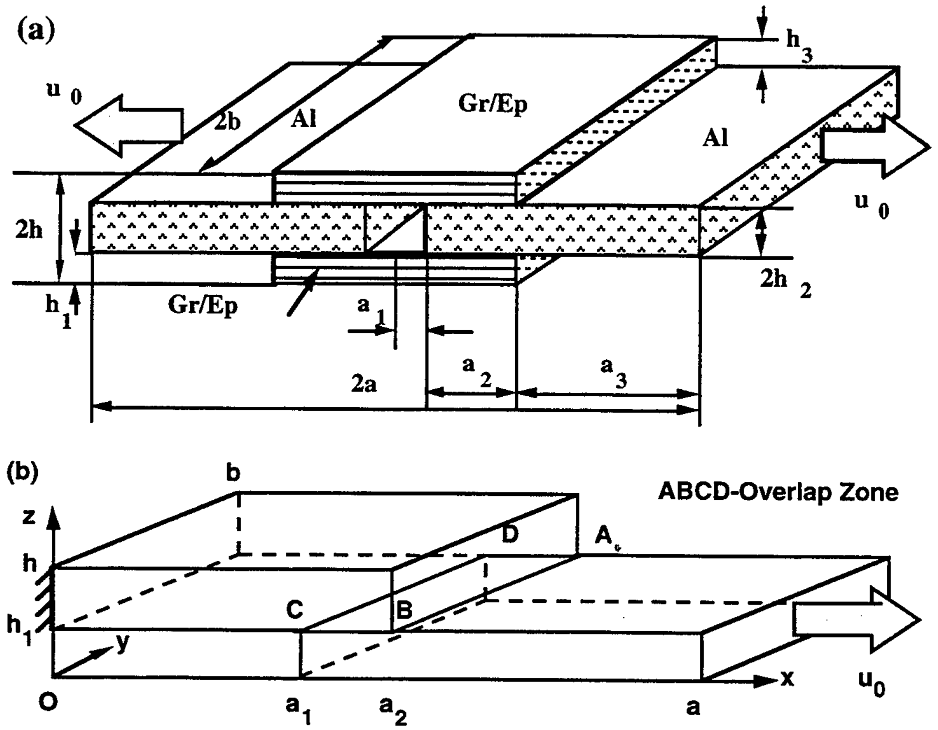
(a)
u 0
2b
Al
Gr/Ep
h 3
Al
u 0
2h
h 1
Gr/Ep
a 1
2h 2
2a
a 2
a 3
(b)
b
ABCD-Overlap Zone
z
h
D
A
h 1
C
B
y
O
a 1
a 2
a
x
u 0

Figure 5.1. Schematic of a double-lap joint (a) and its 1/8th part (b) solved.

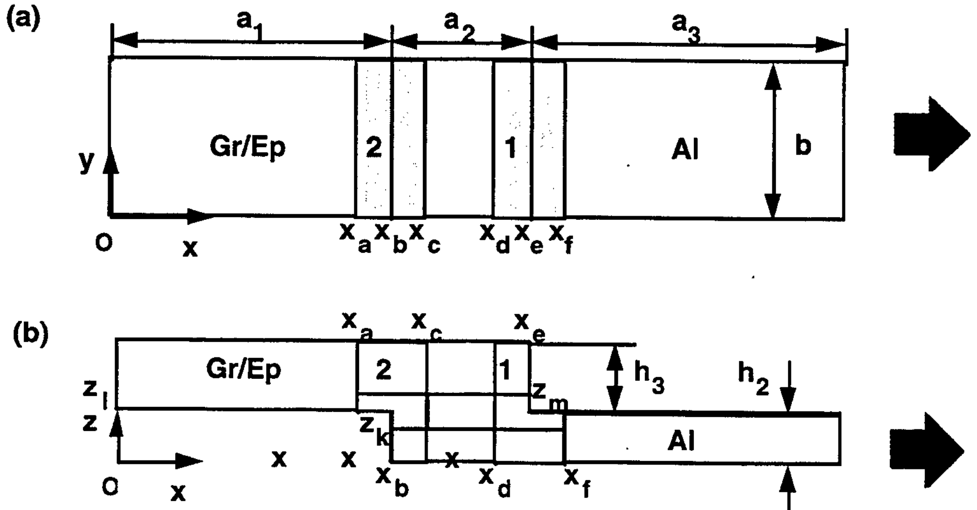
(a)
a 1
a 2
a 3
y
Gr/Ep
2
1
Al
b
O
x
x a x b x c
x d x e x f
(b)
x a
x c
x e
Gr/Ep
2
1
z m
h 3
h 2
z l
z
z k
Al
x
x
x
O
x
x b
x d
x f

Figure 5.2. Schematic of the global and local regions considered in the analysis.

Another important feature (which is, indeed, a common place for any global-local type analysis) is that after the initial step (i.e., global analysis) different local regions of the structure are analyzed *independently*. This is illustrated in Fig. 5.2, where the side view, *x-z*, and top view, *x-y*, of the structure are shown. In the local analyses, regions 1 and 2 are solved independently, and the number of d.o.f. used for the analysis of each local region may be even lower than in the initial global analysis. In other words, instead of performing stress analysis of the whole structure in one step, the analysis of its small portions is performed in several independent steps.

5.3. THREE-DIMENSIONAL STRESS ANALYSIS OF COMPOSITE-TO-METAL BONDED JOINT

A double-lap bonded joint shown in Fig. 5.1a is considered here. The structure is exposed to uniform uniaxial extension. The displacement u_x having some known value u_0 is applied uniformly at the right and left ends of the middle adherends. It is assumed that both the upper and lower adherends are made from the same material and have identical geometric characteristics. Also, it is assumed that both the right and left middle adherends are made from the same material, have identical geometric parameters and are placed symmetrically with respect to the plane perpendicular to the *x*-axis and passing through the center points of the upper and lower adherends. These assumptions allow one to apply symmetry conditions in all three coordinate directions and, accordingly, reduce the original structure to its 1/8th part, as shown in Fig. 5.1b. Accordingly, the full set of boundary conditions is as following:

$$u_x = 0 \text{ at } x = 0; \quad u_x = u_0 \text{ at } x = a; \quad u_y = 0 \text{ at } y = 0; \quad u_z = 0 \text{ at } z = 0 \tag{57}$$

The upper and lower adherends are made from unidirectional graphite/epoxy (Gr/Ep) composite with the following elastic properties:

$$\begin{aligned} &E_L = 164GPa \ (23.86Msi), \quad E_T = 9.82GPa \ (1.426Msi), \\ &G_L = 6.78GPa \, (0.9825Msi), \quad G_T = 3.66GPa \ (0.5306Msi), \quad \nu_{LT} = 0.24 \end{aligned} \tag{58}$$

Direction of the reinforcement in the composite adherends is along the *x*-axis. The middle adherends are made from aluminum (Al) with the following properties:

$$E = 73.7GPa \ (10.7Msi), \quad \nu = 0.25 \tag{59}$$

Geometric parameters used in the analysis are:

$$a / a_1 = a / a_2 = a / b = 4, \quad a / h_1 = a / h_2 = a / h_3 = 20 \tag{60}$$

It is further assumed that adhesive material provides perfect bonding, but due to a small thickness of adhesive layers those are not explicitly considered in this analysis.

The initial step is to perform global analysis of 1/8th part of the structure shown in Fig. 4.1b. For brevity of the element mesh description, the following notations of the number of elements in the *x*, *y* and *z*-directions are introduced:

$$\begin{aligned}
&N^x_{0a} \text{ for } 0 \le x/a \le x_a/a, \; N^x_{ab} \text{ for } x_a/a \le x/a \le x_b/a, \; N^x_{bc} \text{ for } x_b/a \le x/a \le x_c/a, \\
&N^x_{cd} \text{ for } x_c/a \le x/a \le x_d/a, \; N^x_{de} \text{ for } x_d/a \le x/a \le x_e/a, \\
&N^x_{ef} \text{ for } x_e/a \le x/a \le x_f/a, \; N^x_{f1} \text{ for } x_f/a \le x/a \le 1, \\
&N^y_{01} \text{ for } 0 \le y/b \le 1, \qquad (61) \\
&N^z_{0l} \text{ for } 0 \le z/h \le z_l/h, \; N^z_{l1} \text{ for } z_l/h \le z/h \le 1, \; N^z_{0k} \text{ for } 0 \le z/h \le z_k/h, \\
&N^z_{kl} \text{ for } z_k/h \le z/h \le z_l/h, \; N^z_{lm} \text{ for } z_l/h \le z/h \le z_m/h, \; N^z_{m1} \text{ for } z_m/h \le z/h \le 1
\end{aligned}$$

Values of x_b, x_e and z_l should be defined considering specific structural configurations. Coordinates x_a, x_c, x_d, x_f, z_k and z_m will be later on used for determining boundaries of the local regions. Their choice is dictated by the analyst's intuition. On one side, it is desirable to take them as close as possible to the corner lines AB and CD, because if solving smaller local regions the number of required steps of submodeling would be reduced. On the other side, the coordinate values should be at some reasonable distance away from the corner lines AB and CD, because if the local regions are too small, the global analysis has to be huge in order to provide converged displacements and stresses at the boundaries of the local regions. The following specific numerical values have been adopted in the analysis:

$$\begin{aligned}
&x_a/a=0.21, \; x_b/a=0.25, \; x_c/a=0.29, \; x_d/a=0.46, \; x_e/a=0.50, \; x_f/a=0.54, \\
&z_k/h=0.4, \; z_l/h=0.5, \; z_m/h=0.6 \qquad (62)
\end{aligned}$$

Table 5. describes global element meshes used in the global analysis. For the variants G.1-G.6, uniform meshes were applied inside each of the intervals in the *x*-direction. The nonuniform meshes were applied in the *y* and *z*-directions.

Table 5.1. Element meshes used in global analysis.

No. of mesh	N^x_{0a}	N^x_{ab}	N^x_{bc}	N^x_{cd}	N^x_{de}	N^x_{ef}	N^x_{f1}	N^y_{01}	N^z_{0l}	N^z_{l1}	Total d.o.f.
G.1	2	2	2	4	2	2	2	4	4	4	11,691
G.2	4	4	4	8	4	4	4	4	4	4	22,923
G.3	4	8	8	8	8	8	4	4	4	4	34,155
G.4	4	12	12	8	12	12	4	4	4	4	45,387
G.5	4	16	16	8	16	16	4	4	4	4	56,619
G.6	4	20	20	8	20	20	4	4	4	4	67,851
G.7	4	8	8	8	8	8	4	5	2	2	41,745
G.8	4	8	8	8	8	8	4	10	2	2	79,695
G.9	4	8	8	8	8	8	4	5	4	4	41,745
G.10	4	8	8	8	8	8	4	5	6	6	61,017
G.11	4	8	8	8	8	8	4	5	8	8	80,289

The element next to the mid-plane, $y=0$, was always chosen the largest of all elements in the *y*-direction. The element next to the free edge, $y=b$, was always chosen the smallest of all elements in the *y*-direction. The lengths' ratio of the largest to smallest elements in this direction was 40. In the *z*-direction, the largest element in Al adherend is next to the mid-plane, $z=0$, and the smallest element is next to the interface, $z=0.5h$. Their lengths' ratio in this direction was 8. Analogously, the largest element in the Gr/Ep adherend is next to the top surface, $z=h$, and the smallest element is next to the interface, $z=h_1$. Their lengths' ratio in the *z*-direction was 8. For the variants G.7

and G.8, uniform meshes were used inside each interval in the x and y-directions; nonuniform mesh with the element ratio 8 was used in the z-direction. For the variants G.9-G.11, uniform meshes were applied in all of the intervals and all of the coordinate directions.

The main objective of the global analysis is to obtain converged displacements at all points of the structure. It is expected *a priori* that the task would be most difficult for the corner lines AB and CD (shown in Fig. 5.1b). The convergence study performed for all three displacements is illustrated in Table 5.2 for one point of the line AB. If applying the simplest convergence criterion, namely, a monotonous decrease of the error factor with the mesh refinement, it can be concluded that convergence of u_x and u_y is very fast and can be achieved with a rather coarse element mesh, while in order to obtain converged u_z, a much finer element mesh is required.

In the next step, local regions 1 and 2 shown in Fig. 5.2 are solved separately using nodal displacement values calculated in the global analysis as the input data. The same 27-node element is used in all local analyses and for both local regions. In principle, any number of successive submodeling steps can be applied, using converged displacements computed in some preceding step for more accurate stress computation in the successive step. If applied correctly, this should consistently increase accuracy of the stress predictions for the local regions.

Table 5.2. Normalized displacements at $x=0.5a$, $y=0.8b$, $z=0.5h$ computed with the element meshes of Table 5.1.

Displacement	u_x / u_0	u_y / u_0	u_z / u_0
G.1	0.34079	-0.05446	0.00180
G.2	0.34100	-0.05445	0.00264
G.3	0.34107	-0.05447	0.00306
G.4	0.34110	-0.05447	0.00319
G.5	0.34111	-0.05448	0.00325
G.6	0.34112	-0.05448	0.00328
G.7	0.34108	-0.05445	0.00317
G.8	0.34102	-0.05446	0.00308
G.9	0.34069	-0.05444	0.00298
G.10	0.34111	-0.05445	0.00319
G.11	0.34135	-0.05446	0.00328

Mesh parameters used in the first step local analysis for the region 1 confined between the vertical planes $x_d / a = 0.46$ and $x_f / a = 0.54$ (this will be called "Submodel 1" analysis) are presented in

Table 5.3. All of the x-direction meshes are nonuniform with the ratio of the largest to smallest elements $l_x = L_x^{\max} / L_x^{\min} = 20$. The largest elements are next to the vertical planes passing through x_d and x_f, and the smallest elements are on both sides of the vertical plane passing through x_e. All meshes in the y and z-directions are uniform inside each of the intervals, i.e., $l_y = L_y^{\max} / L_y^{\min} = 1$ and $l_z = L_z^{\max} / L_z^{\min} = 1$.

Table 5.3. Various x-direction meshes used in Submodel 1 analysis.

No. of mesh	N^x_{de}	N^x_{ef}	N^y_{01}	N^z_{0k}	N^z_{kl}	N^z_{lm}	N^z_{m1}	Total d.o.f.
L1.1	4	4	10	4	4	4	4	27,279
L1.2	6	6	10	4	4	4	4	39,879
L1.3	8	8	10	4	4	4	4	52,479
L1.4	10	10	10	4	4	4	4	65,079
L1.5	12	12	10	4	4	4	4	77,679

Table 5.4. Stresses in Al and Gr/Ep adherends at $x=0.5a$, $y=b$, $z=0.5h$ computed with the element meshes of Table 5.3.

Adherend	Al			Gr/Ep		
Stress	σ_x/σ_0	σ_z/σ_0	τ_{xz}/σ_0	σ_x/σ_0	σ_z/σ_0	τ_{xz}/σ_0
L1.1	3.5386	1.6561	-1.3270	3.9617	2.0263	-1.1943
L1.2	3.6008	1.7096	-1.4071	3.9139	2.0412	-1.2072
L1.3	3.6276	1.7325	-1.4619	3.8834	2.0454	-1.2151
L1.4	3.6399	1.7431	-1.5003	3.8637	2.0468	-1.2205
L1.5	3.6482	1.7493	-1.5299	3.8499	2.0474	-1.2248

Results for the normalized stress components σ_x/σ_0, σ_z/σ_0 and τ_{xz}/σ_0 are presented in Table 5.4. The normalization factor $\sigma_0 = 0.961GPa$ $(0.1393Msi)$ is the nominal longitudinal stress calculated at $x = a$ from Hooke's law, assuming that the longitudinal strain value $\varepsilon_0 = 1\%$ at $x = a$ (this corresponds to the applied displacement $u_0 = 0.01a$). Again, if applying the convergence criterion of a monotonous decrease of the error factor, all three stress components under consideration show convergence in both adherends with the x-direction mesh refinement.

Next results illustrate the effect of different meshes in the y-direction. Most interesting here is to study stresses at the point $x=0.5a$, $y=b$, $z=0.5h$, which belongs simultaneously to the *interface* and *free edge*. In order to develop efficient computational strategies, the interval $0 \le y/b \le 1$ was first divided into two subintervals. The following notations of the number of elements have been introduced: N^y_{0g} for $0 \le y/b \le 0.8$ and N^y_{g1} for $0.8 \le y/b \le 1$. Uniform meshes were used for the interval $0 \le y/b \le 0.8$ and nonuniform meshes for the interval $0.8 \le y/b \le 1$. The mesh parameters are given in Table 5.5. It was taken $l_x = 20$, $l_z = 1$. Results for the stresses calculated with these meshes are presented in Table 5.6. It is seen that even at the point $x=0.5a$, $y=b$, $z=0.5h$ all three stress components show convergence.

Table 5.5. Element meshes in the y-direction used in Submodel 1 analysis.

No. of mesh	N_{0g}^{y}	N_{g1}^{y}	l_y for $0.8 \le y/b \le 1$
L1.6	4	4	1
L1.7	4	4	10
L1.8	4	4	20
L1.9	4	4	40
L1.10	4	4	80
L1.11	4	4	160

Table 5.6. Stresses in Al and Gr/Ep adherends at $x = 0.5a$, $y = b$, $z = 0.5h$ computed with the element meshes of Table 5.5.

Adherend	Al			Gr/Ep		
Stress	σ_x/σ_0	σ_z/σ_0	τ_{xz}/σ_0	σ_x/σ_0	σ_z/σ_0	τ_{xz}/σ_0
L1.6	3.5152	1.7037	-1.4388	3.8081	2.0097	-1.1954
L1.7	3.2098	1.6709	-1.4384	3.5948	1.9763	-1.1655
L1.8	3.0852	1.6560	-1.4500	3.4945	1.9687	-1.1594
L1.9	2.9824	1.6317	-1.4572	3.4096	1.9629	-1.1561
L1.10	2.9317	1.6141	-1.4593	3.3647	1.9603	-1.1554
L1.11	2.9249	1.6091	-1.4599	3.3535	1.9614	-1.1564

The next step is to study stress convergence with refining element mesh in the z-direction. To perform this more efficiently, the second step of submodeling is made. The local region having the same dimensions in the x and y-directions as before, but reduced in the z-direction (confined between horizontal planes $z_k/h = 0.4$ and $z_m/h = 0.6$) is considered. The displacement values obtained from the Submodel 1 analysis with mesh L1.10 have been used as the nodal displacement input.

The number of elements in the z-direction and mesh nonuniformity are described in Table 5.7. For meshes L2.5 and L2.6, $l_z = 2$ or 4 for each of the intervals, $0.4 \le z/h \le 0.5$ and $0.5 \le z/h \le 0.6$ (size of the elements decrease toward $z/h = 0.5$). The other parameters of meshes L2.1-L2.6 are: $N_{de}^{x} = 8$, $N_{ef}^{x} = 8$, $l_x = 20$ for both intervals $0.46 \le x/a \le 0.5$ and $0.5 \le x/a \le 0.54$; $N_{0g}^{y} = 4$, $l_y = 1$ for $0 \le y/b \le 0.8$; $N_{g1}^{y} = 4$, $l_y = 80$ for $0.8 \le y/b \le 1$.

Table 5.7. Element meshes used in Submodel 2 analysis.

No. of mesh	N_{kl}^{z}	N_{lm}^{z}	l_z	Total d.o.f.
L2.1	4	4	1	22,083
L2.2	6	6	1	32,283
L2.3	8	8	1	42,483
L2.4	10	10	1	52,683
L2.5	10	10	2	52,683
L2.6	10	10	4	52,683

Table 5.8. Stresses in Al and Gr/Ep adherends computed in Submodel 2 analysis.

Adherend	Al			Gr/Ep		
Stress	σ_x/σ_0	σ_z/σ_0	τ_{xz}/σ_0	σ_x/σ_0	σ_z/σ_0	τ_{xz}/σ_0
L2.1	2.9317	1.6141	-1.4593	3.3535	1.9614	-1.1564
L2.2	3.3443	1.9078	-1.6398	3.8974	2.3755	-1.3130
L2.3	3.6522	2.1184	-1.7543	4.3609	2.7049	-1.4336
L2.4	3.8874	2.2720	-1.8329	4.7726	2.9756	-1.5326
L2.5	4.2424	2.4822	-1.9371	5.5438	3.4378	-1.7123
L2.6	4.5522	2.6178	-2.0013	6.4947	3.9354	-1.9467

Numerical results for the normalized stresses at the point $x=0.5a,\ y=b,\ z=0.5h$ are presented in Table 5.8. In the case L2.6, a violation of the allowed smallness of the element aspect ratio has been indicated in ABAQUS, therefore the results for this variant are not reliable. However, even considering variants L2.1-L2.5 it is clear that the stresses *do not converge* at the point under consideration. Thus, mesh refinement in the z-direction indicates stress singularity.

A comparison between numerical results obtained in the global and local analyses is presented in Fig. 5.3. The global analysis results correspond to the mesh G.11 of Table 5.1 and the Submodel 2 analysis results correspond to the mesh L2.5 of Table 5.7. The advantages of using the submodeling technique can be summarized as following:

- Stress values at the peaks are considerably higher when using the local analysis (it should be kept in mind, however, that this statement has only a relative meaning, because the peak values tend to infinity with the mesh refinement).
- Stress variations are much smoother in the case of the local analysis.
- Local analysis provides practically zero values of σ_z and τ_{xz} everywhere at the traction-free surface of the middle adherend, with the exception of a narrow region near the end of the overlap, while global analysis does not satisfy these boundary conditions so accurately.

It has to be noted that, starting at some distance from the corner line $x/a=0.5$, the results obtained from the global and local analyses become practically indistinguishable. In particular, both the analyses provide practically identical stresses at the ends of the local region, $x/a=0.46$ and $x/a=0.54$. Note that σ_z is tensile and its values near the corner line AB are significantly higher than the nominal stress σ_0. Even the shear stress τ_{xz} exceeds σ_0 near the corner line. This confirms that the transverse stresses should be the primary concern as the cause of initial failure.

The problem under consideration is essentially *three-dimensional*. From this standpoint it is worthwhile illustrating that there is a considerable variation of the stresses in the *width* direction, which cannot be predicted by the two-dimensional (either plane strain or plane stress) analyses. Variations of σ_x, σ_z and τ_{xz} in the y-direction for $x/a=0.5,\ z/h=0.5$ (corner line AB) for half-width of the joint are shown in Fig. 5.4. The results correspond to the mesh L2.4 of Table 5.7. Total number of elements in the local region was 16, 8 and 20 in the x, y and z-directions, respectively. It is seen that for the main part (about 90%) of the joint width all three stress components are practically constant, however near the free edge there is a considerable stress variation. It is interesting that the stresses *decrease* toward the free edge. The results also show that σ_z and τ_{xz} computed from the sides of Al and Gr/Ep adherends have considerable jumps at the interface along the whole width of the joint. Ideally, these stress components should be continuous. The observed drawback cannot be fixed by simply refining finite element mesh.

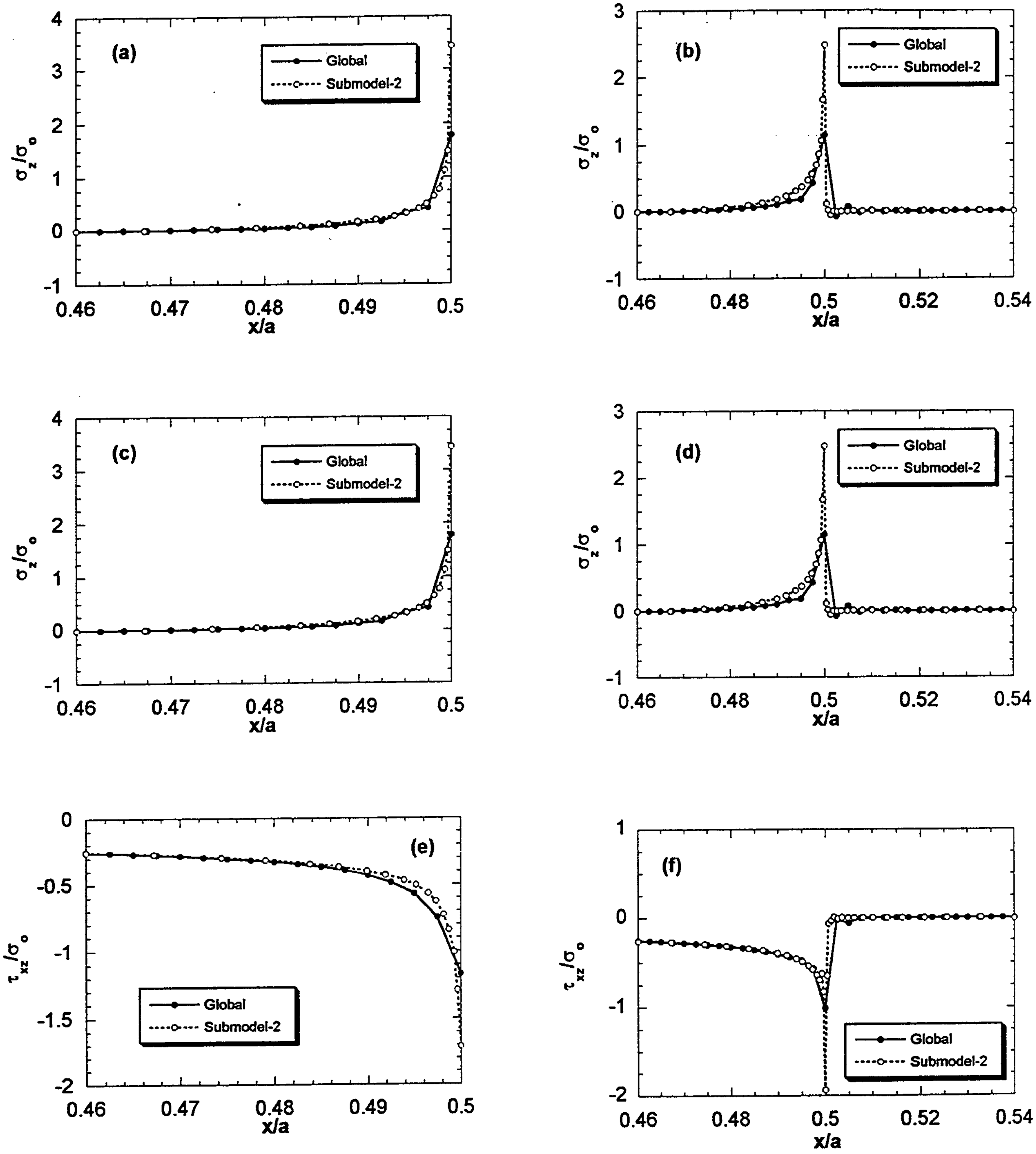

Figure 5.3. Variations of σ_x/σ_0, σ_z/σ_0 and τ_{xz}/σ_0 in Gr/Ep (a, c, e) and Al (b, d, f) adherends in local region 1 at $y/b=1$, $z/h=0.5$.

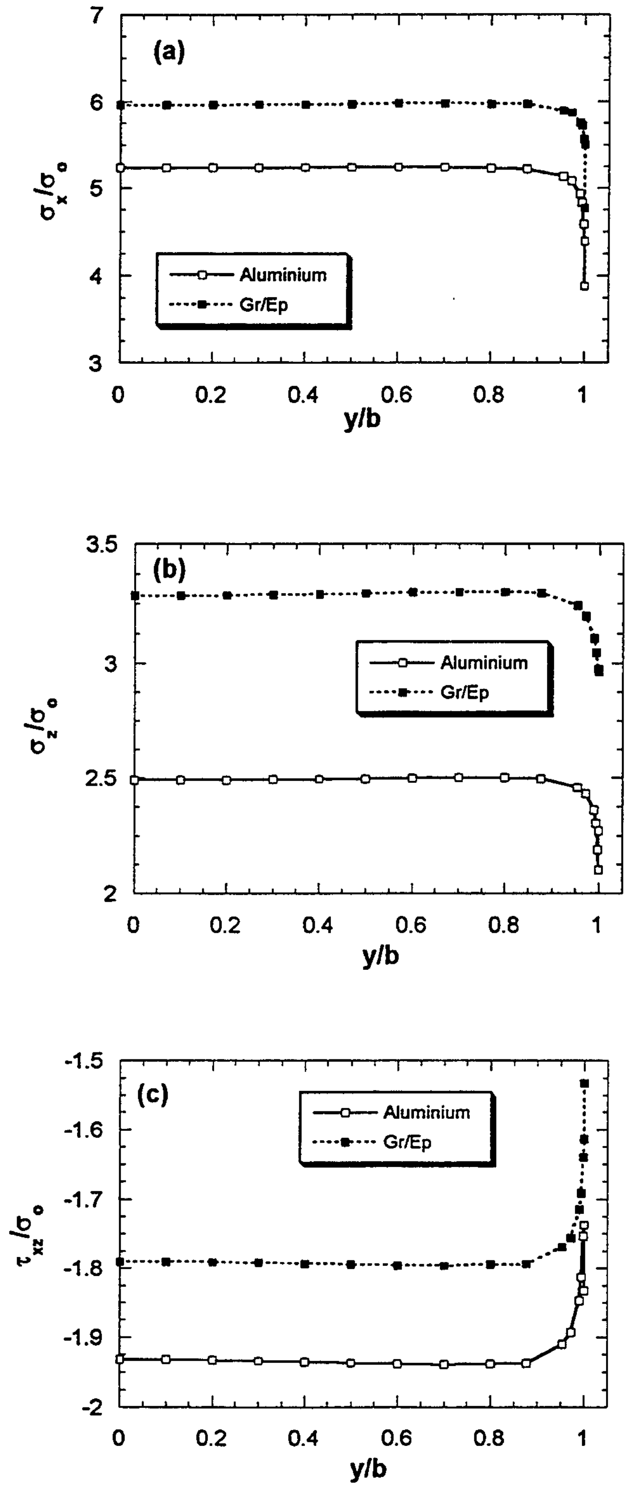

Figure 5.4. Variations of σ_x/σ_0 (a), σ_z/σ_0 (b) and τ_{xz}/σ_0 (c) in the width direction for Gr/Ep and Al adherends in local region 1 at $y/b=1$, $z/h=0.5$.

5.4. STRESS ANALYSIS IN THE PRESENCE OF INITIAL DEBOND CRACK

As indicated by the above stress convergence study, some stress components are singular at the corner line AB. This means that if considering failure as the phenomenon occurring at some *point* of the structure (which is physically unreasonable but commonly implied in the mathematical failure criteria), then *initial failure* must simultaneously occur at all points of the line AB even under an *infinitesimal* load. Accordingly, the initial failure in the form of debond crack starting at AB should be observed *immediately* after the load is applied. Thus, prediction of the failure initiation following the point-wise stress/strain failure criteria for the problem under consideration is impossible. The following two alternative approaches are visible to avoid this obstacle: (i) to compute *average* stresses along some finite width area near the line AB or (ii) to introduce an *initial* debond crack at the interface between Al and Gr/Ep adherends, starting at the end of the overlap and extending into the overlap. The latter approach could have been allowed to reformulate the boundary value problem and obtain solution in which singular stresses are relieved at the end of the overlap and appear at the crack tip.

An analysis with debond crack can be computationally performed using existing capabilities of 3-D ABAQUS elements: the debond crack of a given length can be introduced by detaching certain nodes which belong to the interface. Consequently, a number of double nodes would be created, one of them belonging to the Gr/Ep adherend and the other one to Al adherend. If this is performed only for that part of the interface where σ_z is tensile, then the adherends should separate along the whole area of detached nodes. This means that the debond crack, which configuration is defined by the area of detached nodes, would open, even under the *in-plane* tensile loading. Taking into consideration that the stresses are singular along the whole corner line AB, it is reasonable to detach the nodes along some area AA'B'B, as shown in Fig. 5.5. Length of the initial debond crack, denoted $\Delta x = x_e - x_{e'}$, can be chosen arbitrarily.

Two numerical examples are considered as an illustration of the described approach. They correspond to the cases of nodes detached along the area AA'B'B with $x_{e'}/a = 0.498$ (further referred as Crack 1) and $x_{e'}/a = 0.495$ (Crack 2); recall that $x_e/a = 0.5$. The nodal displacements obtained from the Submodel 2 analysis without debond crack (corresponding to the element mesh L2.5 of Table 5.7) were used as boundary conditions for the local analysis with the debond crack. Two local analysis variants were performed for the aforementioned crack lengths; they are further referred to as C.1 and C.2. The following number of elements have been taken: $N^x_{de'} = 8$, $N^x_{e'e} = 8$, $N^x_{ef} = 8$ for both cases C.1 and C.2. The value $l_x = 5$ has been applied for the intervals $0.49 \le x/a \le 0.498$ and $0.498 \le x/a \le 0.5$ in the case C.1 and for the intervals $0.49 \le x/a \le 0.495$ and $0.495 \le x/a \le 0.5$ in the case C.2. In both cases, the highest mesh refinement was applied near the crack tip, $x/a = 0.498$ for C.1 and $x/a = 0.495$ for C.2. The uniform *x*-direction mesh was used for the interval $0.5 \le x/a \le 0.51$. Other mesh parameters are the same as in variant L2.5 of Table 5.7. Results obtained from the Submodel 2 analysis with the mesh L2.5 have been used for a comparison.

Variations of σ_x, σ_z and τ_{xz} in the *x*-direction computed without crack, with Crack 1 and with Crack 2 are shown in Fig. 5.6. It is seen in Figs. 5.6a that a variation of σ_x in Gr/Ep adherend radically changes in the presence of debond crack. In addition to the tensile peak there is also a compressive peak. When the crack length increases, the compressive peak is growing, while tensile peak is decreasing. Note that σ_x is practically zero at the location $x/a = 0.5$ when using analysis with debond crack, while that was significantly nonzero in the analysis without crack (compare to Fig. 5.3a). Thus, σ_x at the right edge of the upper adherend is relieved by a debond

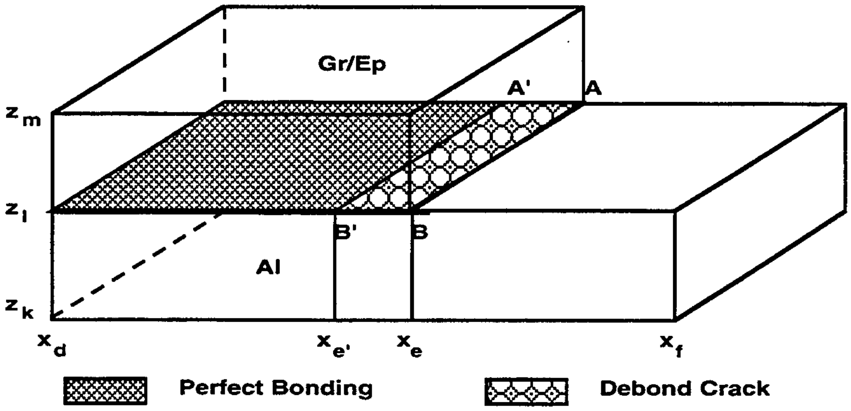

Figure 5.5. Initial debond crack at the and of the overlap zone.

crack. When considering σ_x in Al adherend shown in Fig. 5.6b, it is seen that the stress is tensile along the whole interval. The stress peak (which now takes place at the crack tip) is considerably higher than in the case without crack. Note that the peak grows when increasing the crack length.

Variations of σ_z in the x-direction are shown in Figs. 5.6c and 5.6d. For both the Gr/Ep and Al adherends, this stress component is tensile in all three cases. Its peak monotonously decreases in the upper adherend with the increasing length of the crack. However, in the lower adherent the trend is quite different: there is some crack length which provides the highest peak. It is worth mentioning that for both the crack length cases, σ_z in both the adherends is very small along the whole crack length, so the stress has been relieved from the end of the overlap.

Variations of τ_{xz} in the x-direction are shown in Figs. 5.6e and 5.6f. In the upper adherend these variations are radically different for the cases with and without debond crack. There are both positive and negative peaks, while only one peak with a monotonous stress variation was obtained in the analysis without debond crack. For the middle adherend, the highest peak is observed in the case of Crack 1, similarly to the trend for σ_z (compare to Fig. 5.6c). It is also seen that τ_{xz} values at the traction-free crack surface are very close to zero in the upper adherend and slightly deviate from zero in the middle adherend.

Presented results reveal some basic features of the stress variations in perfectly bonded double-lap joints having small initial debond crack. The results seem reasonable and reflect the expected trend: high peaks of the transverse stresses are relieved from the end of the overlap zone and shifted to the debond crack tip. Accordingly, another analytical problem emerges: to analyze debond crack propagation. A number of analytical and numerical fracture mechanics approaches are known for analyzing crack growth conditions (for example, a critical energy release rate or stress intensity factor approaches), however the revealed specifics of the stress fields in bonded joints, e.g., presence of at least *three* significant stress components (σ_x, σ_z and τ_{xz}), while each of them are substantially contributing in the crack propagation process, as well as extremely high stress gradients, will make fracture analysis of bonded joints a rather complex problem.

5.5. ANALYSIS OF COMPOSITE-TO-COMPOSITE ADHESIVE BONDED JOINT

In the previous example it was assumed that the structure shown in Fig. 5.1 is perfectly bonded, but adhesive layers have zero thickness and, therefore, are not included in the analysis as physical

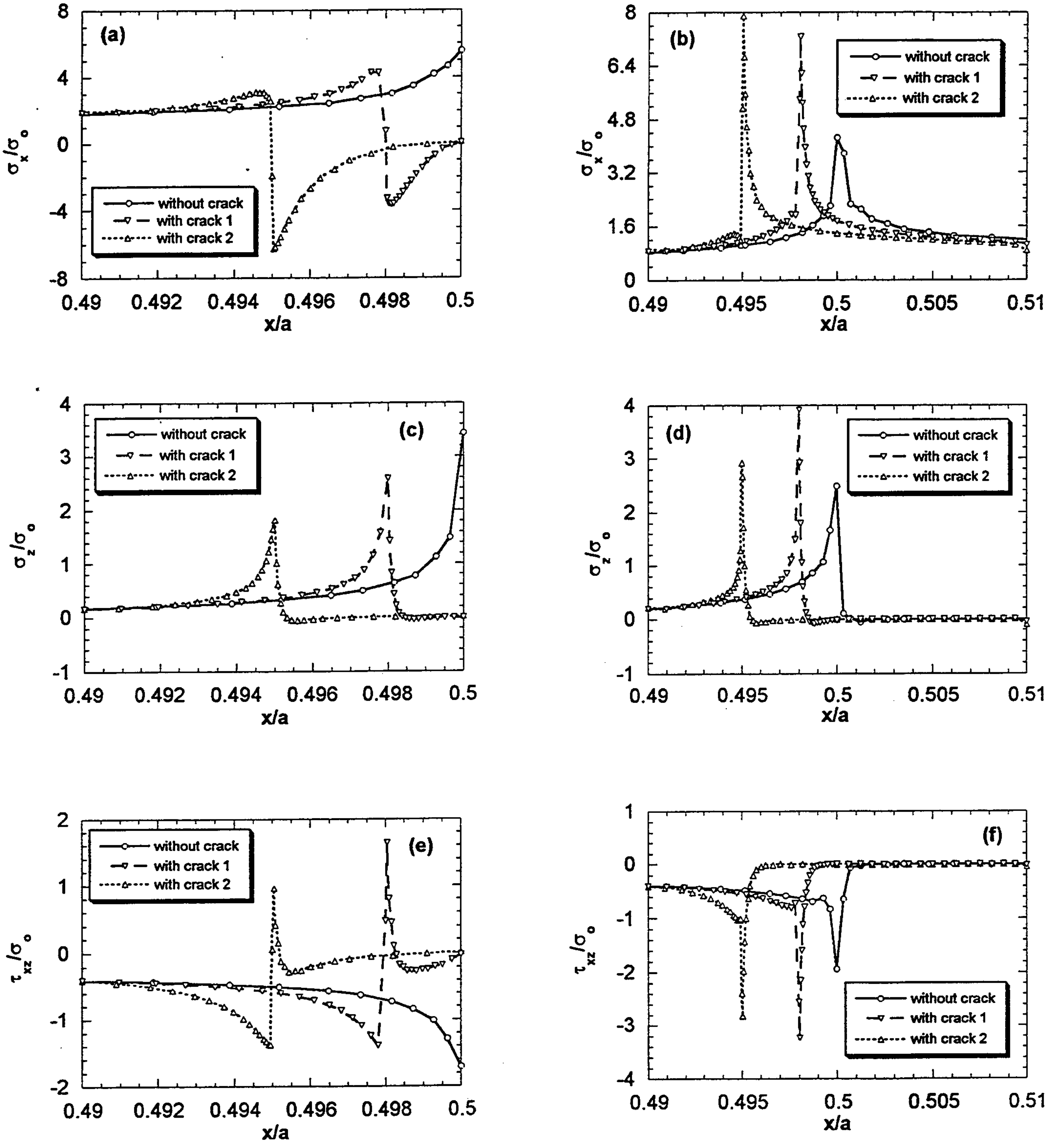

Figure 5.6. Variations of σ_x/σ_0, σ_z/σ_0 and τ_{xz}/σ_0 in Gr/Ep (a, c, e) and Al (b, d, f) adherends at $y/b=1$, $z/h=0.5$ without crack and with initial debond crack of two different lengths.

entities. Here we will illustrate the effect of a finite-thickness adhesive layer in the analogous double-lap joint problem. Schematic of a structural element under consideration is shown in Fig. 5.7a. As before, the structure is exposed to uniform uniaxial extension. The applied displacement u_0 is uniformly distributed along the right and left ends of the middle adherends. All four composite adherends are made from the same material and have equal thickness. Also, both the right and left middle adherends have equal length and are placed symmetrically with respect to the plane perpendicular to the x-axis and passing through the center points of the upper and lower adherends. It is also assumed that all four adhesive layers have identical elastic properties and geometric parameters. The above assumptions are allowing to apply symmetry conditions in all three coordinate directions and, accordingly, to reduce the analysis to 1/8th part of the joint, as shown in Fig. 5.7b. The full set of geometric boundary conditions is exactly the same as in (5.1).

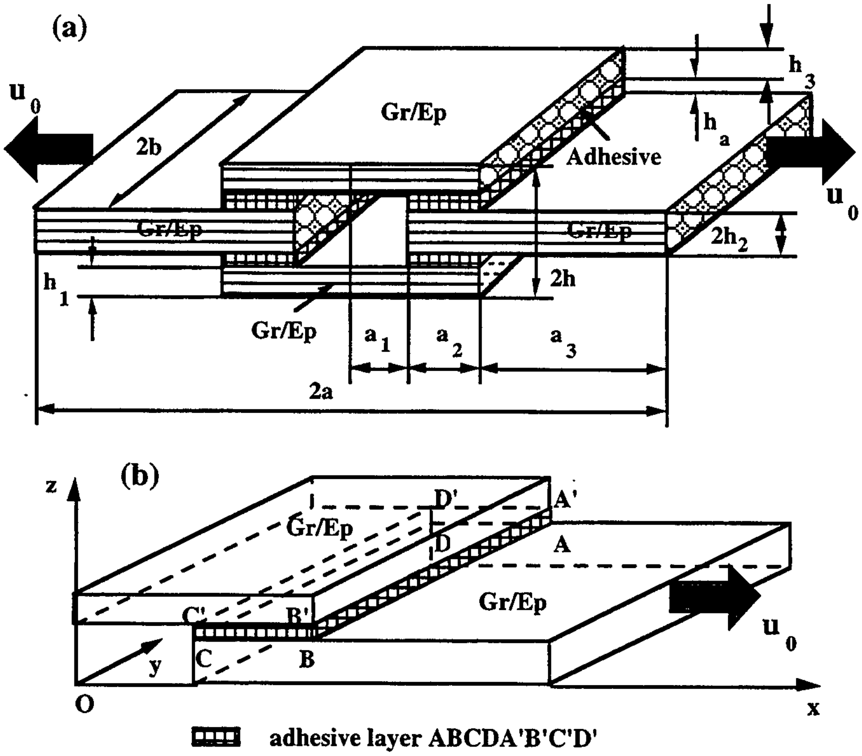

Figure 5.7. Schematic of a composite-to-composite adhesive bonded joint (a) and its 1/8th part (b) considered in the analysis.

All of the adherends are made from 16 layers (all layers are placed in the x-direction) of unidirectional graphite/epoxy Hercules AS4/3501-6 tape having the following elastic properties:

$$E_L = 137GPa\ (20.0Msi),\quad E_T = 10.57GPa\ (1.54Msi),\quad \nu_{LT} = 0.30,$$
$$G_L = 5.15GPa\ (0.750Msi),\quad G_T = 3.47GPa\ (0.506Msi) \tag{63}$$

The bonding adhesive is Cytec FM300-2K film with the following elastic characteristics:

$$E = 3.43GPa\ (0.50Msi),\quad \nu = 0.30 \tag{64}$$

The following geometric parameters are considered in the analysis:

$$a = 45.72cm\ (18.0in),\ a_1 = a_3 = 20.32cm\ (8.0in),\ a_2 = 5.08cm\ (2.0in),\ b = 1.27cm\ (0.5in),$$
$$h = 0.3556cm\ (0.14in),\ h_1 = h_3 = 0.2286cm\ (0.09in),\ h_2 = 0.1143cm\ (0.045in), \tag{65}$$
$$h_a = 0.0127cm\ (0.005in)$$

Mechanical tests of experimental double-lap joint specimens with the above material properties and geometric characteristics have been reported in [79].

It is recognized from the above geometric characteristics that the aspect ratios are $a/h = 129$ for the overall joint and $a_2/h_a = 400$ for the adhesive layers. An accurate direct 3-D stress analysis of the structure with this kind of geometric configuration would be a very computationally expensive task. Indeed, if utilizing uniform element meshes, a huge number of elements will be required. On the other side, if using nonuniform element meshes, the *element aspect ratio* may become too high before the required accuracy is achieved. Actually, both the uniform and nonuniform types of element meshes have been tried by the investigators, and the aforementioned difficulties were faced. It was concluded that the best one can hope when using a direct global analysis is to accurately predict 3-D displacement fields. In order to obtain sufficiently accurate stresses, a global-local type analysis should be used. The submodeling technique described in Section 5.2 has thus been applied to the example of 3-D stress analysis of thin composite-to-composite adhesive bonded joints.

Like in the previous example, an initial step is to perform global analysis of the structure shown in Fig. 5.7b, using successively refined meshes of elements. The objective is to obtain converged displacements everywhere in the structure. After that, the local regions are selected and solved separately with the corresponding nodal displacement taken from the global analysis as the boundary conditions. Schematic of the global and local regions is shown in Fig. 5.8.

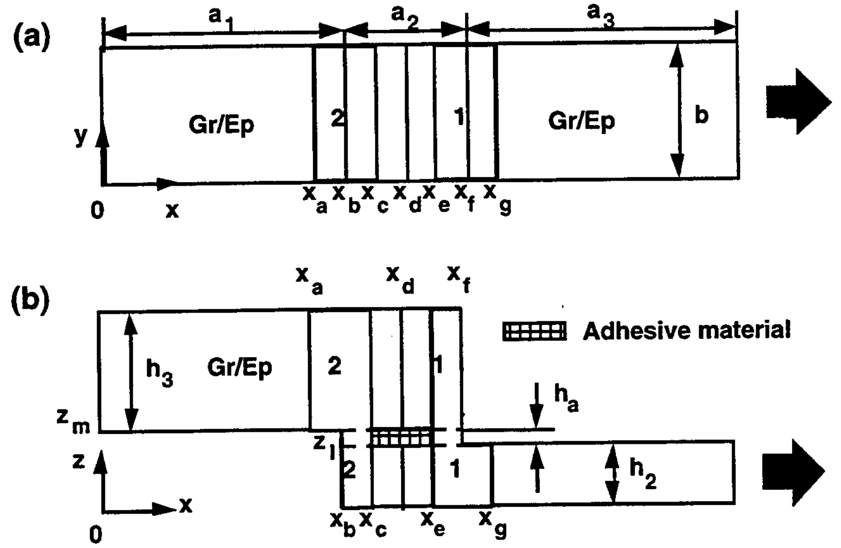

Figure 5.8. A view of global and local regions in the planes x-y (a) and x-z (b).

Without further dwelling into computational details, we present illustrations of the stress variations computed from the global and local analyses. Consider local Region 1 shown in Fig. 5.8. Variations of the normalized stresses σ_x/σ_0, σ_z/σ_0 and τ_{xz}/σ_0 in the x-direction obtained from the global and submodel analysis are shown in Fig. 5.9 for the lower interface and Fig. 5.10 for the upper interface. As seen in Fig. 5.9a, in the adhesive the difference between results near the corner point is considerable: the submodel analysis provides smooth stress variation and much higher peak value. On the contrary, results for the adherend in Fig. 5.9b are very close. Note that at the right end, σ_x in adherend tends to σ_0, and at the left end it tends to $\sigma_0/2$. It has to be pointed out that the region of high stress gradients is very small compared to the length of the overlap zone. Analogous trends are seen in Figs. 5.9c and 5.9d for the stress σ_z / σ_0: in the adhesive there is a significant difference between the results, while in the adherend they are very close. It has only to be added that, as seen in Fig. 5.9d, the submodel analysis is satisfying the free-surface boundary condition with much higher accuracy. The τ_{xz} / σ_0 variations in the adhesive shown in Fig. 5.9e are rather close; the minor difference is near the corner point: the submodel analysis provides smoother variation of the stress and higher peak value. At the same time, Fig. 5.9f shows that the variations of τ_{xz} / σ_0 in the adherend are very different near the corner point: a characteristic "double peak" is barely seen in the global analysis results, while this is very obvious in the submodel results.

The results presented in Fig. 5.10 for the upper interface at some very small distance from the corner point, show that the difference between the global and submodel solutions for all three stress components is only quantitative. In each case the submodel analysis shows smoother stress variation near the corner point and higher peak value. However, there are some problems in both the analysis approaches. Namely, Fig. 5.10a indicates that the very right point of the σ_x variation in the adhesive does not tend to be zero, as is required by the free surface boundary condition. Though, as is seen in Fig. 5.10b, the very right point of the σ_x variation in the adherend is close to zero (this may be occasional). Where will this point move with further mesh refinement? Possibly, to increasingly higher negative value. The same questions arise when analyzing results in Fig. 5.10c and 5.10d. Ideally, the stress component τ_{xz} should be zero at the very right points of the stress variations in the adhesive and adherend. However, it seems that their trend is to take some negative values which will probably grow with further mesh refinement.

A general conclusion is that the explored submodeling technique showed significant accuracy improvement of the stress computation near the ends of the overlap in composite-to-metal and composite-to-composite bonded joints.

The obtained results show that even at a small distance from the line of singularity, the stresses computed with the global analysis and with the submodeling technique are practically indistinguishable. The difference appears only in a small vicinity of the line of singularity, where submodeling definitely improves the stress computation. However, even by using more and more localized stress analyses, it seems impossible to numerically satisfy all of the required stress boundary conditions at the end of the overlap. It can be argued that the problem is of a purely academic interest, because *exactly* at the end of the overlap the stresses are *singular* anyway, so mathematical failure criteria does not apply there and, accordingly, *failure initiation* prediction is impossible. On the other hand, if applying *averaging* of the computed stresses along some finite length zone near the end of the overlap, obtaining *exact* stress values at the points close to the line of singularity may be unnecessary.

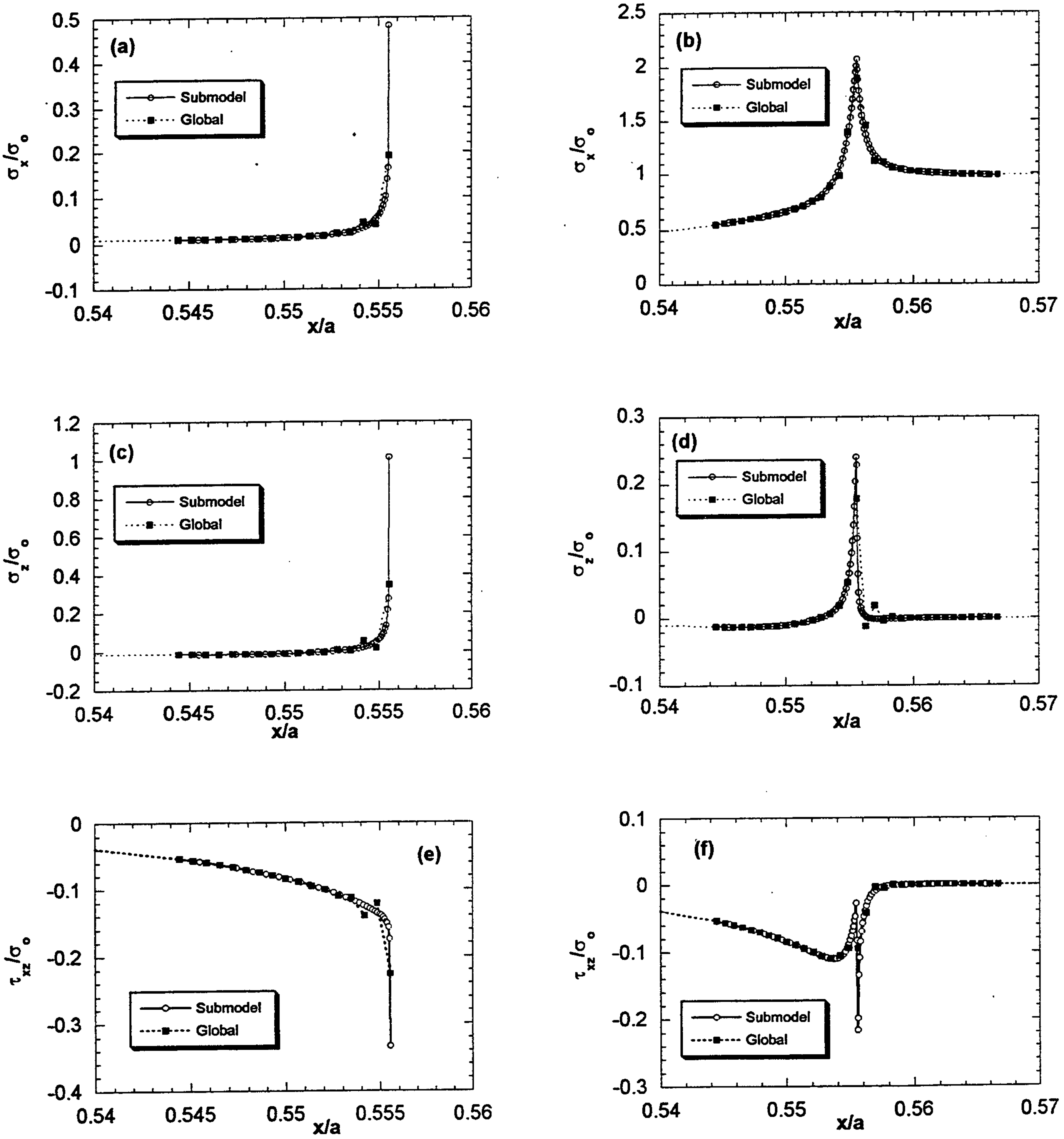

Figure 5.9. Variations of σ_x/σ_0, σ_z/σ_0 and τ_{xz}/σ_0 in the adhesive layer (a, c, e) and middle adherend (b, d, f) along the interface at $y/b=1$, $z/h=0.3214$.

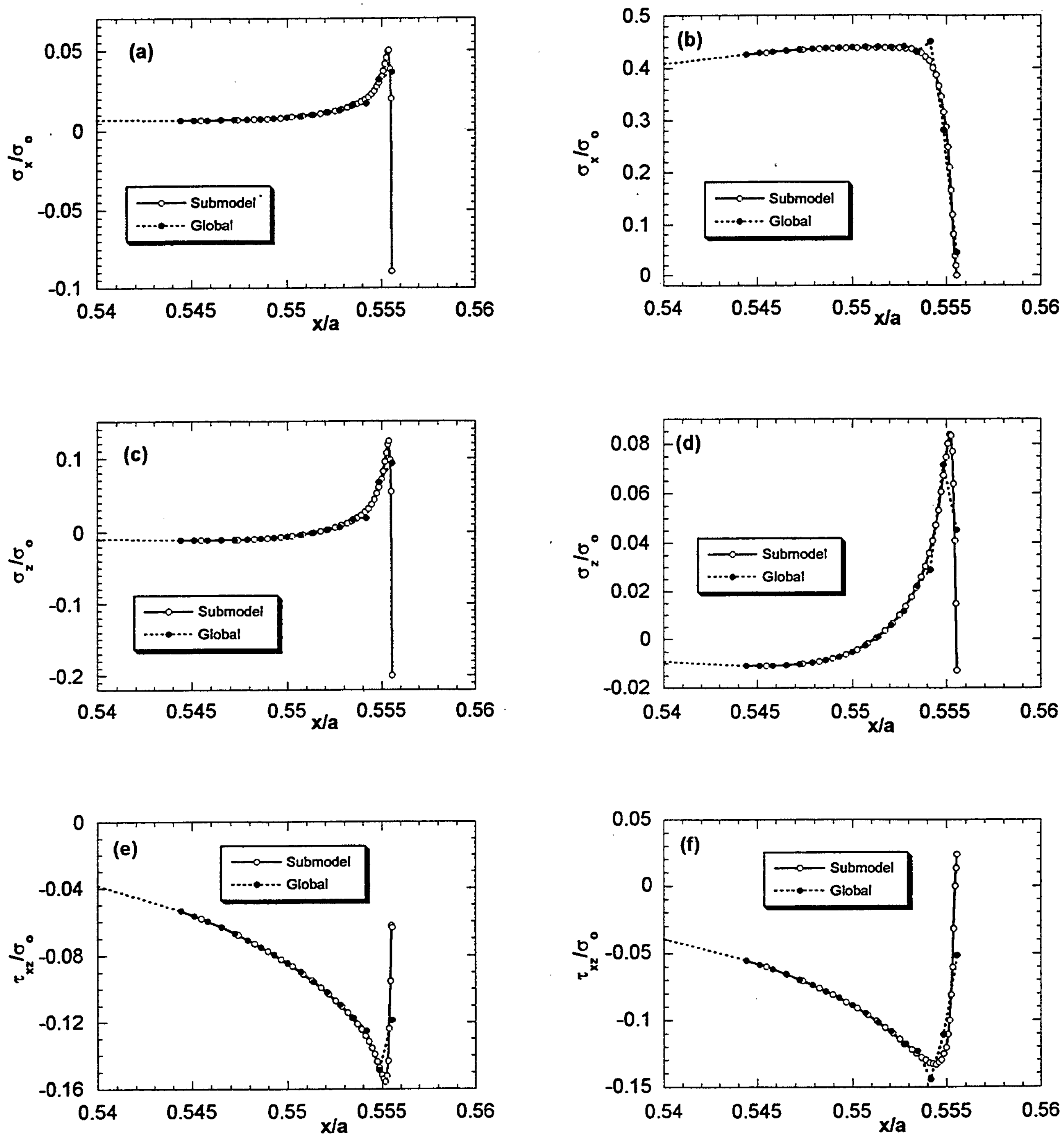

Figure 5.10. Variations of σ_x/σ_0, σ_z/σ_0 and τ_{xz}/σ_0 in the adhesive layer (a, c, e) and upper adherend (b, d, f) along the interface at $y/b = 1$, $z/h = 0.3571$.

6.0 CONCLUSIONS AND RECOMMENDATIONS

6.1 SUMMARY AND CONCLUSIONS

During the SBIR Phase II work on the strength and life prediction of adhesively bonded composite joints, the following tasks were undertaken:

1. A comprehensive literature survey on the state of the art in the strength and life prediction of composite bonded joints.
2. Development of a versatile three-dimensional hygrothermomechanical analysis of structures using variable-order (similar to p-type) rectangular and cylindrical solid elements.
3. Comparison of various 2-D and 3-D analytical tools available for the stress analysis and/or strength prediction of bonded composite joints, and outline their capabilities and limitations.
4. A combined analytical and experimental study of the effect of design parameters such as bond length, bond thickness and adhesive curing temperature on the failure loads of a double-lap adhesively bonded joint.
5. Application of a submodeling technique available in commercial finite element package ABAQUS to study the stress field in the vicinity of free-edges and debond cracks.
6. Development of a PC-based design methodology for composite bonded joints.

The outcome of this work is discussed in the following paragraphs.

In the last three decades extensive work has been performed in the area of stress analysis and strength prediction of composite bonded joints. This has resulted in a number of analytical models and computer packages developed for the purpose of bonded joint analysis and design. Most of the analyses approach consider one dimensional or quasi-two-dimensional state-of-stress in the vicinity of the joint corners thereby neglecting the double-free edge effects, and hence, the influence of interlaminar transverse normal and shear stresses on the failure mechanisms. Nonetheless, the design and analysis software based on the these approaches have proven themselves to be effective tools in the design of bonded composite joints. However, the development of an analysis and/or design capability that accounts for a three-dimensional state-of-stress in the adherends in the vicinity of the double free-edge formed by the joint corners, and that incorporates a failure criterion based on interaction of interlaminar normal and/or transverse shear stress components is imperative for the timely enhancement of the technology in the area of bonded joints utilizing advanced composite materials.

Mathematical formulations for the displacement-based variable-order solid elements are presented for the three-dimensional linear elastic, hygrothermomechanical analysis of structures. The computational algorithm SAVE using variable-order rectangular and cylindrical solid elements has been developed in FORTRAN. The computer code is currently based on the displacement field being approximated by Bernstein polynomials in the three coordinate directions. The SAVE program is subsequently utilized to analyze a number of benchmark problems and compare the numerical results. Based on the results obtained from the displacement-based analyses using variable-order rectangular and cylindrical solid elements, the following conclusions are drawn:

(i) The continuity of stresses at the interface(s) of the elements of the same material or of different materials is achieved with a very high accuracy without enforcing it a priori.

(ii) The static (or natural) boundary conditions at the external surfaces are satisfied with a very high accuracy.

(iii) In most cases the analysis using variable-order elements requires less degrees of freedom to solve the problem and achieve the same or even higher accuracy of the solution.

(iv) There is always an optimum level of order M of the variable-order elements beyond which there is not much significant improvement in the accuracy of the solution. Thus, it is preferable to achieve an optimum combination of the order M and the number of variable-order elements to analyze a given structural problem.

Subsequently, the comparisons among 2-D analysis code BONJO and 3-D analyses codes SAVE and ABAQUS were performed by analyzing a number of double-lap composite bonded joints subjected to thermomechanical loading. A combined analytical and experimental study of the effect of design parameters such as bond length, bond thickness and adhesive curing temperature on the failure loads of a double-lap adhesively bonded joint was also undertaken. The results obtained from these studies lead to the conclusion that the BONJO solution approach provides reasonably accurate stress distributions in the adhesive and adherends when the adherends are either unidirectional, cross-ply or balanced laminates. However, in the case of balanced laminates the axial stress in the angle plies may not be correctly predicted by the BONJO solution approach due to the neglect of extension-shear coupling effects in the lamina constitutive law. Furthermore, the closed-form analysis technique BONJO fails to capture the true geometry and material property variations that give rise to high stress gradients in the vicinity of the joint corners. In the absence of either a progressive damage analysis or a suitable failure criterion to predict the numerical value of ultimate joint failure load, the impact of the accuracy of numerical values of stresses obtained from these analyses could not be ascertained. The quantitative comparison of failure loads has always been an important issue that needs to be addressed in fully justifying the need of 3-D analysis versus a 1-D or a 2-D simplified stress analysis. However, the importance of having a full 3-D analysis such as SAVE or ABAQUS that utilizes the least amount of analytical simplifications as compared to any other analyses techniques cannot be undermined. A full 3-D analysis is necessary if one has to gain a complete insight into the stress response of a complex structural configuration such as an adhesively bonded joint.

The submodeling technique available in the commercial finite element package ABAQUS was explored to study the stress field in the vicinity of free-edges and debond cracks in the bond region. A general conclusion is that the explored submodeling technique showed significant accuracy improvement of the stress computation near the ends of the overlap in composite-to-metal and composite-to-composite bonded joints. The obtained results show that even at a small distance from the line of singularity, the stresses computed with the global analysis and with the submodeling technique are practically indistinguishable. The difference appears only in a small vicinity of the line of singularity, where submodeling definitely improves the stress computation. However, even by using more and more localized stress analyses, it seems impossible to numerically satisfy all of the required stress boundary conditions at the end of the overlap. It can be argued that the problem is of a purely academic interest, because *exactly* at the end of the overlap the stresses are *singular* anyway, so mathematical failure criteria does not apply there and, accordingly, *failure initiation* prediction is impossible. On the other hand, if applying *averaging* of the computed stresses along some finite length zone near the end of the overlap, obtaining *exact* stress values at the points close to the line of singularity may be unnecessary.

Finally, the bonded joint analyses codes BONJO series developed by the Lockheed Corporation under a contract from WL/FIBE, Wright-Patterson Air Force Base, OH, were incorporated into a PC based bonded design methodology. The bonded joint design tool is made more informative and user-friendly through the use of Windows 95TM based Graphic User Interfaces (GUIs) fully integrated with a material database and online help. This design tool would be useful for DoD, aerospace and other industries such as automotive, sporting goods, etc.

6.2 RECOMMENDATIONS FOR FUTURE WORK

The work performed on this SBIR Phase II activity can be readily extended by the AdTech. It is felt that the accomplishment of following works would enhance the composite bonded joint technology immensely.

- Use of singular elements to model the regions of stress singularities either at the joint corners or at the tip of the debond cracks;

- Incorporation of either a failure criterion based on the interaction of interlaminar normal and/or transverse shear stress components or a fracture mechanics based progressive failure methodology to get estimates of the failure initiation load and/or ultimate failure load in composite bonded joints;
- Incorporation of a life prediction methodology under fatigue loading;
- Elaborate experimental study of bonded joint specimens to generate sufficient data to validate the analytical models.

7.0 REFERENCES

1. Goland, M. and Reissner, E., "The Stress in Cemented Joints," Journal of Applied Mechanics, 1944, pp. A17-A26.

2. Hart-Smith, L. J., "An Engineer's View Point on Design and Analysis of Aircraft Structural Joints," Journal of Aerospace Engineering, Vol. 209, No. 2, 1995, pp. 105-129.

3. Hart-Smith, L. J., "The Key to Designing Durable Adhesively Bonded Joints," Composites, Vol. 25, No. 9, October 1994, pp. 895-898.

4. Hart-Smith, L. J., "Designing to Minimize Peel Stresses in Adhesive-Bonded Joints," Proceedings of the International Symposium: Delamination and Debonding of Materials, ASTM Meeting, Philadelphia, PA, 1985, pp. 238-266.

5. Hart-Smith, L. J., "Adhesive-Bonded Joints for Composites - Phenomenological Considerations," Proceedings of the Conference on Advanced Composite Technology, El Segundo, CA, March 1978, pp. 163-180.

6. Hart-Smith, L. J., "Adhesive Layer Thickness and Porosity Criteria for Bonded Joints - Final Report," AFWAL-TR-82-4172, McDonnell-Douglas Corporation, Long Beach, CA, December 1982.

7. Vinson, J. R., "Adhesive Bonding of Polymer Composites," Polym. Engng Sci., Vol. 29, 1989, pp. 1325-1331.

8. Renton, W. J. and Vinson, J. R., "Analysis of Adhesive Bonded Joints between Panels of Composite Materials," Journal of Applied Mechanics, March 1977, pp. 101-106.

9. Wetherhold, R. C. and Vinson, J. R., "An Analytical Model for Bonded Joint Analyses in Composite Structures including Hygrothermal Effects," AFOSR-TR-78-1337, July 1978.

10. Vinson, J. R. and Zumsteg, J. R., "Analysis of Bonded Joints in Composite Material Structures including Hygrothermal Effects," Proceedings of the AIAA/ASME/ASCE/AHS/ASC 20th Structures, Structural Dynamics and Materials Conference, AIAA, Washington, D. C., April 1979, pp. 291-302.

11. Vinson, J. R., "On the State of Technology in Adhesively Bonded Joints in Composite Material Structures," Proceedings of the Aerospace Conference: Emerging Technologies in Aerospace, Structures, Design, Structural Dynamic and Materials, San Francisco, CA, August 1980, pp. 67-85.

12. Renton, W. J., Flaggs, D. L. and Vinson, J. R., "The Analysis and Design of Composite Material Bonded Joints," AFOSR-TR-78-1371, July 1978.

13. Adams, R. D. and Peppiatt, N. A., "Stress Analysis of Adhesively-Bonded Lap Joints," Journal of Strain Analysis, Vol. 9, No. 3, 1974, pp. 185-196.

14. Adams, R. D., 1989, "Strength Predictions for Lap Joints Especially With Composite Adherends: A Review," J. Adhesion, Vol. 30, pp. 219-242.

15. Adams, R. D., "The Mechanics of Bonded Joints," Proceedings of the International Conference on Structural Adhesives in Engineering, Mechanical Engineering Publications Ltd., Bristol, England, 1986, pp. 17-24.

16. Adams, R. D. and Wake, W. C., "Structural Adhesive Joints in Engineering," Elsevier Applied Science Publishers, 1984.

17. Kutscha, D., "Mechanics of Adhesive-Bonded Lap-type Joints: Survey and Review," AFML-TDR-64-298, December 1964, Air Force Materials Laboratory, Wright-Patterson AFB, OH-45433.

18. Kutscha, D. and Hofer, K. E., Jr., "Feasibility of Joining Advanced Composite Flight Vehicles: Survey and Review," AFML-TR-68-391, January 1969, Air Force Materials Laboratory, Wright-Patterson AFB, OH-45433.

19. Schliekelmann, Robert J., "Bonded Joints and Preparation for Bonding," AGARD Lecture Series, AGARD-LS-102, April 1979.

20. Mall, S., Liechti, K. M., and Vinson, J. R., Proceedings of the Symposium: Advances in Adhesively Bonded Joints, ASME Winter Annual Meeting, Chicago, IL, November 1988.

21. Johnson, W. S., Proceedings of the International Symposium: Adhesively Bonded Joints: Testing, Analysis, and Design, ASTM Special Technical Publication, No. 981, Baltimore, MD, September 1986.

22. Delale, F., Erdogan, F. and Aydinoglu, M. N., "Stresses in Adhesively Bonded Joints: A Closed Form Solution," NASA-CR-165638, August 1980.

23. Groth, H. L., "Calculation of Stresses in Bonded Joints using the Substructuring Technique," International Journal of Adhesion and Adhesives, Vol. 6, January 1986, pp. 31-35.

24. An-Ton Liu, "Linear Elastic and Elasto-plastic Stress Analysis for Adhesive Lap Joints," UILU-ENG 76 6005, University of Illinois, Urbana, Illinois, July 1976 .

25. Pahoja, M. H., "Stress Analysis of an Adhesive Lap Joint Subjected to Tension, Shear Force and Bending Moments," Report No. 361, Department of Theoretical and Applied Mechanics, University of Illinois, Urbana, Illinois, 1972 .

26. Srinivas, S., "Analysis of Bonded Joints," NASA-TN-D-7855, May 1975.

27. Amijima, S., Fujii, T. and Yoshida, A., "Two Dimensional Stress Analysis on Adhesive Bonded Joints," Proceedings of the 20th Japan Congress on Materials Research, Society of Materials and Science, Kyoto, Japan, September 1976, pp. 276-281.

28. Amijima, S. and Fujii, T., "A Simple Stress Analysis Method for Adhesive Bonded Tapered Joints," International Journal of Adhesion and Adhesives, Vol. 9, No. 3, July 1989, pp. 155-160.

29. Roy, S. and Reddy, J. N., "A Finite Element Analysis of Adhesively Bonded Composite Joints including Geometric Nonlinearity, Nonlinear Viscoelasticity, Moisture Diffusion and Delayed Failure-Interim Report," VPI-E-87-21, Virginia Polytechnic Institute and State University, Blacksburg, Virginia, October 1984.

30. Sable, William W., and Sharifi, Parviz, "Structural Analysis of Bonded Joints Using the Finite Element Method," Proceedings of the 8th International Conference on Composite Materials (ICCM/8), Honolulu, HI, July 15-19, 1991. Section 1-11 (A92-32535 13-39). Covina, CA, Society for the Advancement of Material and Process Engineering, 1991, pp. 9-F-1 - 9-F-11.

31. Humphreys, E. A. and Herakovich, C. T., "Nonlinear Analysis of Bonded Joints with Thermal Effects-Interim Report," VPI-E-77-19, Virginia Polytechnic Institute and State University, Blacksburg, Virginia, June 1977.

32. Barthelemy, B. M., Kamat, M. P. and Brinson, H. F., "Finite Element Analysis of Bonded Joints," M. S. Thesis, Virginia Polytechnic Institute and State University, Blacksburg, Virginia, May 1984.

33. Barker, R. M. and Hatt, F., "Analysis of Bonded Joints in Vehicular Structures," Proceedings of the AIAA/ASME/SAE 14th Structures, Structural Dynamics and Materials Conference, AIAA, Washington, D. C., March 1973, AIAA paper no. 73-371.

34. Chamis, C. C., and Murthy, P. L. N., "Simplified Procedures for Designing Adhesively Bonded Composite Joints," NASA-TM-102120, February 1989.

35. Shyprykevich, P., "Design and Fabrication of Realistic Adhesively Bonded Joints," NASA-CR-166099, 1983.

36. Findlater D., "A Preliminary Design Approach for Adhesively Bonded Joints," International Journal of Adhesion and Adhesives, Vol. 7, No. 3, July 1987, pp. 129-134.

37. Kelly, P. A., Hills, D. A. and Nowell, D., "The Design of Joints between Elastically Dissimilar Components," Journal of Strain Analysis for Engineering Design, Vol. 27, January 1992, pp. 15-20.

38. Tsai, M., and Morton, J., 1994, "An Evaluation of Analytical and Numerical Solutions to the Single-Lap Joint," Int. J. Solids and Structures, Vol. 31, No. 18, pp. 2537-2563.

39. Negaard, G. R. 1994. "Guide to ASIAC computer programs," WL-TR-94-3127, Air Force Flight Dynamics Laboratory, Wright-Patterson AFB, OH-45433.

40. Smith, M. K., Hart-Smith, L. J. and Dietz, C. G., "Interactive Composite Joint Design," AFFDL-TR-78-38, Part 1-3, Air Force Flight Dynamics Laboratory, Wright-Patterson AFB, OH-45433, 1978.

41. Hart-Smith, L. J., "Adhesive Bonded Double-lap Joints,", NASA-CR-112235, January 1973.

42. Hart-Smith, L. J., "Adhesive Bonded Single-lap Joints," NASA-CR-112236, January 1973.

43. Hart-Smith, L. J., "Adhesive Bonded Scarf and Stepped Joints," NASA-CR-112237, January 1973.

44. Grimes, G. C., Greimann, L. F., Wah, T., Commerford, G. E., Blackstone, W. R., and Wolfe, G. K., "The Development of Nonlinear Analysis Methods for Bonded Joints in Advanced Filamentary Composite Structures," AFFDL-TR-72-97, September 1972, Air Force Flight Dynamics Laboratory, Wright-Patterson AFB, OH-45433.

45. Ramberg, W. and Osgood, W. R., "Description of Stress-Strain Curves by Three Parameters," NACA TN 902, July 1943.

46. Sharpe, Wiilliam N., Jr. and Muha, Theodore J., Jr., "Comparison of Theoretical and Experimental Shear Stress in the Adhesive Layer of a Lap Joint Model," AMMRC-MS-74-9, Army Materials and Mechanics Research Center, Watertown, MA, 1974, pp. 23-41.

47. Renton, James, W. and Vinson, Jack R., "The Analysis and Design of Composite Material Bonded Joints Under Static and Fatigue Loading," AFOSR-TR-73-1627, August 1973, Air Force Office of Scientific Research, Arlington, VA 22209.

48. Renton, James, W. and Vinson, Jack R., "The Analysis and Design of Anisotropic Bonded Joints," AFOSR-TR-75-0125, Report No. 2, August 1974, Air Force Office of Scientific Research, Arlington, VA 22209.

49. Dickson, J. N., Hsu, T. M., and McKinney, J. M., "Development of an Understanding of the Fatigue Phenomena of Bonded and Bolted Joints in Advanced Filamentary Composite Materials," AFFDL-TR-72-64, Vol. I and II, 1972, Air Force Flight Dynamics Laboratory, Wright-Patterson AFB, OH-45433.

50. Hart-Smith, L. J., "Design Methodology for Bonded-Bolted Composite Joints," AFWAL-TR-81-3154, Vol. 1 and 2, Air Force Flight Dynamics Laboratory, Wright-Patterson AFB, OH-45433, 1982.

51. Fogarty, J. H. and Saff, C. R., "PGLUE User's Manual - Rev. A," MDC Report No. B0288, McDonnell Aircraft Company, Saint Louis, MO-63166, August 1987.

52. Bathe, K. J. and Wilson, E. L., Numerical Methods in Finite Element Analysis, Prentice Hall, Inc., New Jersey, 1987.

53. Zeinkiewicz, O. C., De, J. P., Gago, S. R. and Kelly, D. W., The hierarchical concept in finite element analysis, Computers and Structures, 1983, 16, 53-65.

54. Babuska, I., Szabo, B. A. and Katz, I. N., The p-version of the finite element method, SIAM Journal of Numerical Analysis, 1981, 18, 515-545.

55. Szabo, B. A., Mesh design for the p-version of the finite element method, Computer Methods in Applied Mechanics and Engineering, 1986, 55, 181-197.

56. Zeinkiewicz, O. C., Zhu, J. Z. and Gong, N. G., Effective and practical h-p version adaptive analysis procedures for the finite element method, International Journal for Numerical Methods in Engineering, 1989, 28, 879-891.

57. Babuska, I. and Guo, B. Q., The h-p version of the finite element method for domains with curved boundaries, SIAM Journal of Numerical Analysis, 1988, 25, 837-861.

58. Farin, Gerald E., NURB Curves and Surfaces: From Projective Geometry to Practical Use, A. K. Peters, Ltd., Wellesley, MA, 1995, 98.

59. Singh, A. V., "On vibrations of shells of revolution using Bezier polynomials," Journal of Pressure Vessel Technology, 1991, 113, 579-584.

60. Kumar, V. and Singh, A. V., "Vibration analysis of non-circular cylindrical shells using Bezier functions," Journal of Sound and Vibration, 1993, 161, 333-354.

61. Bogdanovich, A. E. , Pastore, C. M. and Deepak, B. P., "A comparison of various 3-D approaches for the analysis of laminated composite structures," Composite Engineering, 1995, 5, 1105-1126.

62. Bogdanovich, A. E. and Deepak, B. P., "Three-dimensional analysis of thick composite plates with multiple layers," Composites: Part B, 1997, 28, 345-357.

63. Bogdanovich, A. E. and Rastogi, Naveen, “3-D variational analysis of bonded composite plates,” Proc. of the ASME Aerospace Division: Structures and Materials for Aerospace Vehicles, 1996, AD-Vol. 52, The ASME, New York, NY 100172, 123-143.

64. Bogdanovich, A. E., “3-D analysis of anisotropic spatially reinforced structures,” Composites Manufacturing, 1993, 4, 173-186.

65. Taylor, R. L., “On completeness of shape functions for finite element analysis,” International Journal of Numerical Methods in Engineering, 1972, 4, 17-22.

66. Pagano, N. J., "Exact solutions for bi-directional composites and sandwich plates," Journal of Composite Materials, 1970, 4, 20-34.

67. Pagano, N. J., "On the calculation of interlaminar stresses in composite laminate," Journal of Composite Materials, 1974, 8, 65-xx.

68. Pagano, N. J. and Soni S. R., "Models for studying free-edge effects," in: Interlaminar Response of Composite Materials, Composite Materials Series, 5, ed: N. J. Pagano, Elsevier Science Publishing Company, Inc., New York, NY 10010, USA, 1989, 1-68.

69. Ren, J. G., "Analysis of simply-supported laminated circular cylindrical shell roofs," Composite Structures, 1989, 11, 277-292.

70. I-DEAS model solutionTM verification manual, Report No. P-40049, SDRC, Milford, OH 45150, 1996, 307-310.

71. Srinath, L. S., Advanced Mechanics of Solids, Tata McGraw-Hill Publishing Company Ltd., New Delhi, 1980, 266-275.

72. The ABAQUS User’s Manual: Version 5.6, Hibbit, Karlsson & Sorensen, Inc., Pawtucket, Rhode Island, U. S. A., 1996.

73. Johnson, Eric R. and Rastogi, Naveen, “Effective Hygrothermal Expansion Coefficients for Thick Multilayer Bodies,” Proc. of the 39th AIAA/ASME/ASCE/AHS/ASC Structures, Structural Dynamics and Materials Conference, Long Beach, CA, April 20-23, 1998, AIAA-98-1814.

74. Hart-Smith, L. J., “The Key to Designing Durable Adhesively Bonded Joints,” Composites, Vol. 25, No. 9, 1994, pp. 895-898.

75. E. Altus, “Three-Dimensional Singularities in Double Lap Joints,” *Engineering Fracture Mechanics*, 1985, Vol. 21, pp. 1097-1112.

76. W. W. Sable and P. Sharifi, “Structural Analysis of Bonded Joints Using the Finite Element Method,” *Proceedings of ICCM-8, Honolulu, HI*, July 15-19, 1991. SAMPE, Covina, CA, pp. 9-F-1 - 9-F-11.

77. M. Y. Tsai and J. Morton, “Three-Dimensional Deformations in a Single-Lap Joint,” *Journ. of Strain Analysis*, 1994, Vol. 29, pp. 137-145.

78. A. E. Bogdanovich and I. Kizhakkethara, “Three-Dimensional Finite Element Analysis of Adhesively Bonded Plates,” *Collection of Techn. Pap. 38th AIAA/ASME/ASCE/AHS/ASC Conf. and Exhibit*, April 7-10, 1997, Kissimmee, FL. AIAA-97-1120, Pt. 3, pp. 1984-1993.

79. S. L. Donaldson and A. K. Roy, “Experimental Studies on Composite Bonded Joints,” *Proceedings of ICCM-11*, Gold Coast, Australia, 14-18 July, 1997, Vol. V: Textile Composites and Characterization, pp. 444-455.

Appendix-A

Consider a brick element composed of an orthotropic lamina oriented at an angle θ_{ply} w.r.t to the x-axis. The angle θ_{ply} is also known as the ply orientation angle, and is measured positive anti-clockwise w.r.t to the x-axis. Thus, the transformed stiffness coefficients Q_{ij} of the $\{Q\}$ matrix appearing in the material law of the brick element in Eqs. (5) and (6) (see Section 3.1) are given by

$$
\begin{aligned}
Q_{11} &= C_{11}m^4 + 2(C_{12} + 2C_{66})m^2n^2 + C_{22}n^4 \\
Q_{12} &= (C_{11} + C_{22} - 4C_{66})m^2n^2 + C_{12}(m^4 + n^4) \\
Q_{13} &= C_{13}m^2 + C_{23}n^2 \\
Q_{16} &= [(C_{11}m^2 - C_{22}n^2 - (C_{12} + 2C_{66})(m^2 - n^2)]mn \\
Q_{22} &= C_{11}n^4 + 2(C_{12} + 2C_{66})m^2n^2 + C_{22}m^4 \\
Q_{23} &= C_{13}n^2 + C_{23}m^2 \\
Q_{26} &= [(C_{11}n^2 - C_{22}m^2 + (C_{12} + 2C_{66})(m^2 - n^2)]mn \qquad \text{(A-1)} \\
Q_{33} &= C_{33} \\
Q_{36} &= (C_{13} - C_{23})mn \\
Q_{44} &= C_{44}m^2 + C_{55}n^2 \\
Q_{45} &= (C_{55} - C_{44})mn \\
Q_{55} &= C_{44}n^2 + C_{55}m^2
\end{aligned}
$$

$$Q_{66} = (C_{11} + C_{22} - 2C_{12})m^2n^2 + + C_{66}(m^2 - n^2)^2$$

where

$$C_{11} = \frac{E_{11}(1 - \upsilon_{23}\upsilon_{32})}{D},\ C_{12} = \frac{E_{22}(\upsilon_{12} + \upsilon_{13}\upsilon_{32})}{D},\ C_{13} = \frac{E_{33}(\upsilon_{13} + \upsilon_{12}\upsilon_{23})}{D}$$

$$C_{22} = \frac{E_{22}(1 - \upsilon_{13}\upsilon_{31})}{D},\ C_{23} = \frac{E_{33}(\upsilon_{23} + \upsilon_{21}\upsilon_{13})}{D},\ C_{33} = \frac{E_{33}(1 - \upsilon_{12}\upsilon_{21})}{D}$$

$C_{44} = G_{23}$, $C_{55} = G_{13}$, $C_{66} = G_{12}$ and $D = 1 - \upsilon_{12}\upsilon_{21} - \upsilon_{13}\upsilon_{31} - \upsilon_{32}\upsilon_{23} - 2\upsilon_{12}\upsilon_{23}\upsilon_{31}$.

The coefficients R^i_j, $i = \alpha, \beta$ and $j = 1,2..6$ represent the contributions of hygrothermal stresses into the material law of the brick element. These coefficients as appearing in Eqs. (5) and (7) are given as

$$R^i_1 = (C_{11}i_1 + C_{12}i_2 + C_{13}i_3)m^2 + (C_{12}i_1 + C_{22}i_2 + C_{23}i_3)n^2$$

$$R^i_2 = (C_{11}i_1 + C_{12}i_2 + C_{13}i_3)n^2 + (C_{12}i_1 + C_{22}i_2 + C_{23}i_3)m^2$$

$$R^i_3 = C_{13}i_1 + C_{23}i_2 + C_{33}i_3 \qquad \text{(A-2)}$$

$$R^i_4 = R^i_5 = 0$$

$$R^i_6 = [(C_{11} - C_{12})i_1 + (C_{12} - C_{22})i_2 + (C_{13} - C_{33})i_3]mn,\ i = \alpha, \beta.$$

The Eq. (A-2) computes the thermal stress coefficients $\vec{R}^{\alpha}$ for $i = \alpha$, and the stress coefficients due to moisture content $\vec{R}^{\beta}$ for $i = \beta$. In Eqs. (A-1) and (A-2), $m = Cos\theta_{ply}$ and $n = Sin\theta_{ply}$.

Appendix-B

In general the stiffness matrix $\overline{\overline{A}}_{nm}$ of the brick element, Eq. (22) (see Section 3.1), can be written in the partitioned form as

$$\overline{\overline{A}}_{nm} = \begin{bmatrix} A_{nm}^{uu} & A_{nm}^{uv} & A_{nm}^{uw} \\ A_{nm}^{uv} & A_{nm}^{vv} & A_{nm}^{vw} \\ A_{nm}^{uv} & A_{nm}^{vw} & A_{nm}^{ww} \end{bmatrix} \tag{B-1}$$

The symmetric sub-elements of the stiffness matrix appearing in Eq. (B-1) for a rectangular brick element are given by

$$A_{nm}^{uu} = \frac{bhQ_{11}\Phi_2^{u\xi}\Phi_1^{u\eta}\Phi_1^{u\zeta}}{a} + \frac{ahQ_{66}\Phi_1^{u\xi}\Phi_2^{u\eta}\Phi_1^{u\zeta}}{b} + \frac{abQ_{55}\Phi_1^{u\xi}\Phi_1^{u\eta}\Phi_2^{u\zeta}}{h} + 2hQ_{16}\Phi_3^{u\xi}\Phi_3^{u\eta}\Phi_1^{u\zeta}$$

$$\begin{aligned} A_{nm}^{uv} = {} & \frac{bhQ_{16}\Phi_2^{uv\xi}\Phi_1^{uv\eta}\Phi_1^{uv\zeta}}{a} + \frac{ahQ_{26}\Phi_1^{uv\xi}\Phi_2^{uv\eta}\Phi_1^{uv\zeta}}{b} + \frac{abQ_{45}\Phi_1^{uv\xi}\Phi_1^{uv\eta}\Phi_2^{uv\zeta}}{h} \\ & + h(Q_{12} + Q_{66})\Phi_3^{uv\xi}\Phi_3^{uv\eta}\Phi_1^{uv\zeta} \end{aligned}$$

$$A_{nm}^{uw} = b(Q_{13} + Q_{55})\Phi_3^{uw\xi}\Phi_1^{uw\eta}\Phi_3^{uw\zeta} + a(Q_{36} + Q_{45})\Phi_1^{uw\xi}\Phi_3^{uw\eta}\Phi_3^{uw\zeta} \tag{B-2}$$

$$A_{nm}^{vv} = \frac{bhQ_{66}\Phi_2^{v\xi}\Phi_1^{v\eta}\Phi_1^{v\zeta}}{a} + \frac{ahQ_{22}\Phi_1^{v\xi}\Phi_2^{v\eta}\Phi_1^{v\zeta}}{b} + \frac{abQ_{44}\Phi_1^{v\xi}\Phi_1^{v\eta}\Phi_2^{v\zeta}}{h} + 2hQ_{26}\Phi_3^{v\xi}\Phi_3^{v\eta}\Phi_1^{v\zeta}$$

$$A_{nm}^{vw} = b(Q_{36} + Q_{45})\Phi_3^{vw\xi}\Phi_1^{vw\eta}\Phi_3^{vw\zeta} + a(Q_{23} + Q_{44})\Phi_1^{vw\xi}\Phi_3^{vw\eta}\Phi_3^{vw\zeta}$$

$$\begin{aligned} A_{nm}^{ww} = {} & \frac{bhQ_{55}\Phi_2^{w\xi}\Phi_1^{w\eta}\Phi_1^{w\zeta}}{a} + \frac{ahQ_{44}\Phi_1^{w\xi}\Phi_2^{w\eta}\Phi_1^{w\zeta}}{b} + \frac{abQ_{33}\Phi_1^{w\xi}\Phi_1^{w\eta}\Phi_2^{w\zeta}}{h} \\ & + 2hQ_{45}\Phi_3^{w\xi}\Phi_3^{w\eta}\Phi_1^{w\zeta} \end{aligned}$$

where

$$\Phi_1^{u\xi} = \int_0^1 F_i^u(\xi)F_p^u(\xi)d\xi\,,\ \Phi_1^{u\eta} = \int_0^1 G_j^u(\eta)G_q^u(\eta)d\eta,\ \Phi_1^{u\zeta} = \int_0^1 H_k^u(\zeta)H_r^u(\zeta)d\zeta$$

$$\Phi_2^{u\xi} = \int_0^1 \frac{\partial F_i^u(\xi)}{\partial\xi}\frac{\partial F_p^u(\xi)}{\partial\xi}d\xi\,,\ \Phi_2^{u\eta} = \int_0^1 \frac{\partial G_j^u(\eta)}{\partial\eta}\frac{\partial G_q^u(\eta)}{\partial\eta}d\eta,\ \Phi_2^{u\zeta} = \int_0^1 \frac{\partial H_k^u(\zeta)}{\partial\zeta}\frac{\partial H_r^u(\zeta)}{\partial\zeta}d\zeta$$

$$\Phi_3^{u\xi} = \int_0^1 F_i^u(\xi)\frac{\partial F_p^u(\xi)}{\partial\xi}d\xi = \int_0^1 F_p^u(\xi)\frac{\partial F_i^u(\xi)}{\partial\xi}d\xi \tag{B-3}$$

$$\Phi_3^{u\eta} = \int_0^1 G_j^u(\eta)\frac{\partial G_q^u(\eta)}{\partial\eta}d\eta = \int_0^1 G_q^u(\eta)\frac{\partial G_j^u(\eta)}{\partial\eta}d\eta\,,$$

$$\Phi_3^{u\zeta} = \int_0^1 H_j^u(\zeta)\frac{\partial H_q^u(\zeta)}{\partial\zeta}d\zeta = \int_0^1 H_q^u(\zeta)\frac{\partial H_j^u(\zeta)}{\partial\zeta}d\zeta$$

and

$$\Phi_1^{uv\xi} = \int_0^1 F_i^v(\xi)F_p^u(\xi)d\xi\,,\ \Phi_1^{uv\eta} = \int_0^1 G_j^v(\eta)G_q^u(\eta)d\eta,\ \Phi_1^{uv\zeta} = \int_0^1 H_k^v(\zeta)H_r^u(\zeta)d\zeta$$

$$\Phi_2^{uv\xi} = \int_0^1 \frac{\partial F_i^v(\xi)}{\partial\xi}\frac{\partial F_p^u(\xi)}{\partial\xi}d\xi\,, \Phi_2^{uv\eta} = \int_0^1 \frac{\partial G_j^v(\eta)}{\partial\eta}\frac{\partial G_q^u(\eta)}{\partial\eta}d\eta,\ \Phi_2^{uv\zeta} = \int_0^1 \frac{\partial H_k^v(\zeta)}{\partial\zeta}\frac{\partial H_r^u(\zeta)}{\partial\zeta}d\zeta$$

$$\Phi_3^{uv\xi} = \int_0^1 F_i^v(\xi)\frac{\partial F_p^u(\xi)}{\partial\xi}d\xi = \int_0^1 F_p^u(\xi)\frac{\partial F_i^v(\xi)}{\partial\xi}d\xi \tag{B-4}$$

$$\Phi_3^{uv\eta} = \int_0^1 G_j^v(\eta)\frac{\partial G_q^u(\eta)}{\partial\eta}d\eta = \int_0^1 G_q^u(\eta)\frac{\partial G_j^v(\eta)}{\partial\eta}d\eta$$

$$\Phi_3^{uv\zeta} = \int_0^1 H_k^v(\zeta) \frac{\partial H_r^u(\zeta)}{\partial \zeta} d\zeta = \int_0^1 H_r^u(\zeta) \frac{\partial H_k^v(\zeta)}{\partial \zeta} d\zeta$$

Other forms of integrals such as $\Phi_1^{v\xi}$, $\Phi_1^{v\eta}$, $\Phi_1^{v\zeta}$, etc., appearing in Eqs. (B-2) are obtained by simply replacing superscript '*u*' by '*v*' in the expressions for the integrals $\Phi_1^{u\xi}$, $\Phi_1^{u\eta}$, $\Phi_1^{u\zeta}$, etc., given by the Eqs. (B-3). Similarly, the integrals such as $\Phi_1^{w\xi}$, $\Phi_1^{w\eta}$, $\Phi_1^{w\zeta}$, etc., appearing in Eqs. (B-2) are obtained by replacing superscript '*u*' by '*w*' in the expressions for the integrals $\Phi_1^{u\xi}$, $\Phi_1^{u\eta}$, $\Phi_1^{u\zeta}$, etc., given by Eqs. (B-3). Furthermore, the integrals such as $\Phi_1^{uw\xi}$, $\Phi_1^{uw\eta}$, $\Phi_3^{uw\zeta}$, etc., appearing in Eqs. (B-2) are obtained by replacing superscript '*u*' by '*w*' in the expressions for the integrals $\Phi_1^{uv\xi}$, $\Phi_1^{uv\eta}$, $\Phi_3^{uv\zeta}$, etc., given by Eqs. (B-4). Similarly, the integrals such as $\Phi_1^{vw\xi}$, $\Phi_1^{vw\eta}$, $\Phi_3^{vw\xi}$, etc., appearing in Eqs. (B-2) are obtained by replacing superscripts '*u*' by '*v*' and '*v*' by '*w*' in the expressions for the integrals $\Phi_1^{uv\xi}$, $\Phi_1^{uv\eta}$, $\Phi_3^{uv\zeta}$, etc., given by Eqs. (B-4).

It is common to use the same polynomial approximations for all the three displacement components. This results in reduced computational efforts and book-keeping. For this special case the actual and virtual displacement fields for the rectangular brick element are written as

$$\bar{u} = \sum_{i=1}^{I} \sum_{j=1}^{J} \sum_{k=1}^{K} \bar{U}_m F_i\ (\xi) G_j(\eta) H_k(\zeta)$$

$$\delta\bar{u} \in \{\delta\bar{U}_n F_p(\xi) G_q(\eta) H_r(\zeta)\} \tag{B-5}$$

where, $\bar{U}_m = \{U_m, V_m, W_m\}$ and $\delta\bar{U}_n = \{\delta U_n, \delta V_n, \delta W_n\}$.

Thus, the integrals given by Eqs. (B-4) assume the same form as those given by Eqs. (B-3). The symmetric sub-elements of the stiffness matrix $\overline{\overline{A}}_{nm}$, Eq. (B-2), get simplified, and are now given by

$$A_{nm}^{uu} = \frac{bhQ_{11}\Phi_2^{\xi}\Phi_1^{\eta}\Phi_1^{\zeta}}{a} + \frac{ahQ_{66}\Phi_1^{\xi}\Phi_2^{\eta}\Phi_1^{\zeta}}{b} + \frac{abQ_{55}\Phi_1^{\xi}\Phi_1^{\eta}\Phi_2^{\zeta}}{h} + 2hQ_{16}\Phi_3^{\xi}\Phi_3^{\eta}\Phi_1^{\zeta}$$

$$A_{nm}^{uv} = \frac{bhQ_{16}\Phi_2^{\xi}\Phi_1^{\eta}\Phi_1^{\zeta}}{a} + \frac{ahQ_{26}\Phi_1^{\xi}\Phi_2^{\eta}\Phi_1^{\zeta}}{b} + \frac{abQ_{45}\Phi_1^{\xi}\Phi_1^{\eta}\Phi_2^{\zeta}}{h} + h(Q_{12} + Q_{66})\Phi_3^{\xi}\Phi_3^{\eta}\Phi_1^{\zeta}$$

$$A_{nm}^{uw} = b(Q_{13} + Q_{55})\Phi_3^{\xi}\Phi_1^{\eta}\Phi_3^{\zeta} + a(Q_{36} + Q_{45})\Phi_1^{\xi}\Phi_3^{\eta}\Phi_3^{\zeta} \tag{B-6}$$

$$A_{nm}^{vv} = \frac{bhQ_{66}\Phi_2^{\xi}\Phi_1^{\eta}\Phi_1^{\zeta}}{a} + \frac{ahQ_{22}\Phi_1^{\xi}\Phi_2^{\eta}\Phi_1^{\zeta}}{b} + \frac{abQ_{44}\Phi_1^{\xi}\Phi_1^{\eta}\Phi_2^{\zeta}}{h} + 2hQ_{26}\Phi_3^{\xi}\Phi_3^{\eta}\Phi_1^{\zeta}$$

$$A_{nm}^{vw} = b(Q_{36} + Q_{45})\Phi_3^{\xi}\Phi_1^{\eta}\Phi_3^{\zeta} + a(Q_{23} + Q_{44})\Phi_1^{\xi}\Phi_3^{\eta}\Phi_3^{\zeta}$$

$$A_{nm}^{ww} = \frac{bhQ_{55}\Phi_2^{\xi}\Phi_1^{\eta}\Phi_1^{\zeta}}{a} + \frac{ahQ_{44}\Phi_1^{\xi}\Phi_2^{\eta}\Phi_1^{\zeta}}{b} + \frac{abQ_{33}\Phi_1^{\xi}\Phi_1^{\eta}\Phi_2^{\zeta}}{h} + 2hQ_{45}\Phi_3^{\xi}\Phi_3^{\eta}\Phi_1^{\zeta}$$

Further, the superscripts used in the functions $F_i^{\nu}(\xi)$, etc., in the integrals given by Eqs. (B-3) are no more required. Thus, the integrals of Eqs. (B-3) can now be written in simplified form as

$$\Phi_1^{\xi}=\int_0^1 F_i(\xi)F_p(\xi)d\xi\,,\ \Phi_1^{\eta}=\int_0^1 G_j(\eta)G_q(\eta)d\eta,\ \Phi_1^{\zeta}=\int_0^1 H_k(\zeta)H_r(\zeta)d\zeta$$

$$\Phi_2^{\xi}=\int_0^1 \frac{\partial F_i(\xi)}{\partial\xi}\frac{\partial F_p(\xi)}{\partial\xi}d\xi,\ \Phi_2^{\eta}=\int_0^1 \frac{\partial G_j(\eta)}{\partial\eta}\frac{\partial G_q(\eta)}{\partial\eta}d\eta,\ \Phi_2^{\zeta}=\int_0^1 \frac{\partial H_k(\zeta)}{\partial\zeta}\frac{\partial H_r(\zeta)}{\partial\zeta}d\zeta$$

$$\Phi_3^{\xi}=\int_0^1 F_i(\xi)\frac{\partial F_p(\xi)}{\partial\xi}d\xi=\int_0^1 F_p(\xi)\frac{\partial F_i(\xi)}{\partial\xi}d\xi \tag{B-7}$$

$$\Phi_3^{\eta}=\int_0^1 G_j(\eta)\frac{\partial G_q(\eta)}{\partial\eta}d\eta=\int_0^1 G_q(\eta)\frac{\partial G_j(\eta)}{\partial\eta}d\eta,$$

$$\Phi_3^{\zeta}=\int_0^1 H_j(\zeta)\frac{\partial H_q(\zeta)}{\partial\zeta}d\zeta=\int_0^1 H_q(\zeta)\frac{\partial H_j(\zeta)}{\partial\zeta}d\zeta$$

Appendix-C

The symmetric sub-elements of the stiffness matrix appearing in Eq. (B-1) for a cylindrical brick element are given by

$$A_{nm}^{uu}=\frac{h\Theta Q_{11}\Phi_2^{u\xi}\Phi_1^{u\eta}\Phi_4^{u\zeta}}{a}+\frac{ahQ_{66}\Phi_1^{u\xi}\Phi_2^{u\eta}\Phi_5^{u\zeta}}{\Theta}+\frac{a\Theta Q_{55}\Phi_1^{u\xi}\Phi_1^{u\eta}\Phi_6^{u\zeta}}{h}+2hQ_{16}\Phi_3^{u\xi}\Phi_3^{u\eta}\Phi_1^{u\zeta}$$

$$\begin{aligned}A_{nm}^{uv}=&\frac{h\Theta Q_{16}\Phi_2^{uv\xi}\Phi_1^{uv\eta}\Phi_4^{uv\zeta}}{a}+\frac{ahQ_{26}\Phi_1^{uv\xi}\Phi_2^{uv\eta}\Phi_5^{uv\zeta}}{\Theta}+\frac{a\Theta Q_{45}\Phi_1^{uv\xi}\Phi_1^{uv\eta}\Phi_6^{uv\zeta}}{h}\\&+h(Q_{12}+Q_{66})\Phi_3^{uv\xi}\Phi_3^{uv\eta}\Phi_1^{uv\zeta}-a\Theta Q_{45}\Phi_1^{uv\xi}\Phi_1^{uv\eta}\Phi_3^{uv\zeta}\end{aligned}$$

$$\begin{aligned}A_{nm}^{uw}=&\Theta(Q_{13}+Q_{55})\Phi_3^{uw\xi}\Phi_1^{uw\eta}\Phi_7^{uw\zeta}+a(Q_{36}+Q_{45})\Phi_1^{uw\xi}\Phi_3^{uw\eta}\Phi_3^{uw\zeta}\\&+h\Theta Q_{12}\Phi_3^{uw\xi}\Phi_1^{uw\eta}\Phi_1^{uw\zeta}+ahQ_{26}\Phi_1^{uw\xi}\Phi_3^{uw\eta}\Phi_5^{uw\zeta}\end{aligned} \qquad \text{(C-1)}$$

$$\begin{aligned}A_{nm}^{vv}=&\frac{\Theta hQ_{66}\Phi_2^{v\xi}\Phi_1^{v\eta}\Phi_4^{v\zeta}}{a}+\frac{ahQ_{22}\Phi_1^{v\xi}\Phi_2^{v\eta}\Phi_5^{v\zeta}}{\Theta}+\frac{a\Theta Q_{44}\Phi_1^{v\xi}\Phi_1^{v\eta}\Phi_6^{v\zeta}}{h}+2hQ_{26}\Phi_3^{v\xi}\Phi_3^{v\eta}\Phi_1^{v\zeta}\\&+ah\Theta Q_{44}\Phi_1^{v\xi}\Phi_1^{v\eta}\Phi_5^{v\zeta}-2a\Theta Q_{44}\Phi_1^{v\xi}\Phi_1^{v\eta}\Phi_3^{v\zeta}\end{aligned}$$

$$\begin{aligned}A_{nm}^{vw}=&\Theta(Q_{36}+Q_{45})\Phi_3^{vw\xi}\Phi_1^{vw\eta}\Phi_7^{vw\zeta}+a(Q_{23}+Q_{44})\Phi_1^{vw\xi}\Phi_3^{vw\eta}\Phi_3^{vw\zeta}\\&+ah(Q_{22}-Q_{44})\Phi_1^{vw\xi}\Phi_3^{vw\eta}\Phi_5^{vw\zeta}+h\Theta(Q_{26}-Q_{45})\Phi_3^{vw\xi}\Phi_1^{vw\eta}\Phi_1^{vw\zeta}\end{aligned}$$

$$\begin{aligned}A_{nm}^{ww}=&\frac{h\Theta Q_{55}\Phi_2^{w\xi}\Phi_1^{w\eta}\Phi_4^{w\zeta}}{a}+\frac{ahQ_{44}\Phi_1^{w\xi}\Phi_2^{w\eta}\Phi_5^{w\zeta}}{\Theta}+\frac{a\Theta Q_{33}\Phi_1^{w\xi}\Phi_1^{w\eta}\Phi_6^{w\zeta}}{h}\\&+2hQ_{45}\Phi_3^{w\xi}\Phi_3^{w\eta}\Phi_1^{w\zeta}+2a\Theta Q_{23}\Phi_1^{w\xi}\Phi_1^{w\eta}\Phi_3^{w\zeta}+ah\Theta Q_{22}\Phi_1^{w\xi}\Phi_1^{w\eta}\Phi_5^{w\zeta}\end{aligned}$$

where

$$\Phi_4^{u\zeta}=\int_0^1 H_k^u(\zeta)H_r^u(\zeta)(R+h\zeta)d\zeta$$

$$\Phi_5^{u\zeta} = \int_0^1 H_k^u(\zeta) H_r^u(\zeta) \frac{d\zeta}{(R+h\zeta)}$$

$$\Phi_6^{u\zeta} = \int_0^1 \frac{\partial H_k^u(\zeta)}{\partial\zeta} \frac{\partial H_r^u(\zeta)}{\partial\zeta} (R+h\zeta) d\zeta$$

$$\Phi_4^{uv\zeta} = \int_0^1 H_k^v(\zeta) H_r^u(\zeta)(R+h\zeta) d\zeta \qquad \text{(C-2)}$$

$$\Phi_5^{uv\zeta} = \int_0^1 H_k^v(\zeta) H_r^u(\zeta) \frac{d\zeta}{(R+h\zeta)}$$

$$\Phi_6^{uv\zeta} = \int_0^1 \frac{\partial H_k^v(\zeta)}{\partial\zeta} \frac{\partial H_r^u(\zeta)}{\partial\zeta} \frac{d\zeta}{(R+h\zeta)}$$

$$\Phi_7^{uv\zeta} = \int_0^1 H_k^v(\zeta) \frac{\partial H_r^u(\zeta)}{\partial\zeta} (R+h\zeta) d\zeta = \int_0^1 H_r^u(\zeta) \frac{\partial H_k^v(\zeta)}{\partial\zeta} (R+h\zeta) d\zeta$$

The common integrals appearing in Eqs. (B-2) and (C-1) are given by Eqs. (B-3) and (B-4), and are not repeated again. As explained earlier, the other forms of integrals appearing in Eqs. (C-1) are obtained by simply replacing superscript '*u*' by '*v*' and '*u*' by '*w*' in the expressions for the integrals $\Phi_1^{u\xi}$, $\Phi_1^{u\eta}$, $\Phi_1^{u\zeta}$, $\Phi_1^{uw\xi}$, $\Phi_3^{uw\zeta}$, etc given by the Eqs. (C-2).

For the case of same polynomial approximations employed for all the three displacement components, the symmetric sub-elements of the stiffness matrix $\overline{\overline{A}}_{nm}$, Eq. (C-1), for the cylindrical brick element are given in simplified form as

$$
\begin{aligned}
A_{nm}^{uu} &= \frac{h\Theta Q_{11}\Phi_2^{\xi}\Phi_1^{\eta}\Phi_4^{\zeta}}{a} + \frac{ahQ_{66}\Phi_1^{\xi}\Phi_2^{\eta}\Phi_5^{\zeta}}{\Theta} + \frac{a\Theta Q_{55}\Phi_1^{\xi}\Phi_1^{\eta}\Phi_6^{\zeta}}{h} + 2hQ_{16}\Phi_3^{\xi}\Phi_3^{\eta}\Phi_1^{\zeta} \\
A_{nm}^{uv} &= \frac{h\Theta Q_{16}\Phi_2^{\xi}\Phi_1^{\eta}\Phi_4^{\zeta}}{a} + \frac{ahQ_{26}\Phi_1^{\xi}\Phi_2^{\eta}\Phi_5^{\zeta}}{\Theta} + \frac{a\Theta Q_{45}\Phi_1^{\xi}\Phi_1^{\eta}\Phi_6^{\zeta}}{h} + h(Q_{12}+Q_{66})\Phi_3^{\xi}\Phi_3^{\eta}\Phi_1^{\zeta} \\
&\quad - a\Theta Q_{45}\Phi_1^{\xi}\Phi_1^{\eta}\Phi_3^{\zeta} \\
A_{nm}^{uw} &= \Theta(Q_{13}+Q_{55})\Phi_3^{\xi}\Phi_1^{\eta}\Phi_7^{\zeta} + a(Q_{36}+Q_{45})\Phi_1^{\xi}\Phi_3^{\eta}\Phi_3^{\zeta} + h\Theta Q_{12}\Phi_3^{\xi}\Phi_1^{\eta}\Phi_1^{\zeta} \\
&\quad + ahQ_{26}\Phi_1^{\xi}\Phi_3^{\eta}\Phi_5^{\zeta} \\
A_{nm}^{vv} &= \frac{\Theta hQ_{66}\Phi_2^{\xi}\Phi_1^{\eta}\Phi_4^{\zeta}}{a} + \frac{ahQ_{22}\Phi_1^{\xi}\Phi_2^{\eta}\Phi_5^{\zeta}}{\Theta} + \frac{a\Theta Q_{44}\Phi_1^{\xi}\Phi_1^{\eta}\Phi_6^{\zeta}}{h} + 2hQ_{26}\Phi_3^{\xi}\Phi_3^{\eta}\Phi_1^{\zeta} \\
&\quad + ah\Theta Q_{44}\Phi_1^{\xi}\Phi_1^{\eta}\Phi_5^{\zeta} - 2a\Theta Q_{44}\Phi_1^{\xi}\Phi_1^{\eta}\Phi_3^{\zeta} \\
A_{nm}^{vw} &= \Theta(Q_{36}+Q_{45})\Phi_3^{\xi}\Phi_1^{\eta}\Phi_7^{\zeta} + a(Q_{23}+Q_{44})\Phi_1^{\xi}\Phi_3^{\eta}\Phi_3^{\zeta} + ah(Q_{22}-Q_{44})\Phi_1^{\xi}\Phi_3^{\eta}\Phi_5^{\zeta} \\
&\quad + h\Theta(Q_{26}-Q_{45})\Phi_3^{\xi}\Phi_1^{\eta}\Phi_1^{\zeta} \\
A_{nm}^{ww} &= \frac{h\Theta Q_{55}\Phi_2^{\xi}\Phi_1^{\eta}\Phi_4^{\zeta}}{a} + \frac{ahQ_{44}\Phi_1^{\xi}\Phi_2^{\eta}\Phi_5^{\zeta}}{\Theta} + \frac{a\Theta Q_{33}\Phi_1^{\xi}\Phi_1^{\eta}\Phi_6^{\zeta}}{h} + 2hQ_{45}\Phi_3^{\xi}\Phi_3^{\eta}\Phi_1^{\zeta} \\
&\quad + 2a\Theta Q_{23}\Phi_1^{\xi}\Phi_1^{\eta}\Phi_3^{\zeta} + ah\Theta Q_{22}\Phi_1^{\xi}\Phi_1^{\eta}\Phi_5^{\zeta}
\end{aligned}
\tag{C-3}
$$

where

$$
\begin{aligned}
\Phi_4^{\zeta} &= \int_0^1 H_k(\zeta)H_r(\zeta)(R+h\zeta)d\zeta \\
\Phi_5^{\zeta} &= \int_0^1 H_k(\zeta)H_r(\zeta)\frac{d\zeta}{(R+h\zeta)} \\
\Phi_6^{\zeta} &= \int_0^1 \frac{\partial H_k(\zeta)}{\partial\zeta}\frac{\partial H_r(\zeta)}{\partial\zeta}(R+h\zeta)d\zeta
\end{aligned}
\tag{C-4}
$$

$$\Phi_7^{\zeta} = \int_0^1 H_k(\zeta)\frac{\partial H_r(\zeta)}{\partial \zeta}(R + h\zeta)d\zeta = \int_0^1 H_r(\zeta)\frac{\partial H_k(\zeta)}{\partial \zeta}(R + h\zeta)d\zeta$$

The common integrals appearing in Eq. (B-6) and (C-3) are given by Eqs. (B-7) and hence, are not repeated here.

Appendix-D

The stiffness matrix $\overline{\overline{A}}_{nm}$ for the solid wedge element is derived only for the special case of same polynomial functions being used to approximate all the three displacement components. For the solid wedge element oriented in *x-y* plane the actual and virtual displacement field for the can be written as

$$\vec{u} = \sum_{i=1}^{I} \sum_{j=1}^{J} \sum_{k=1}^{K} \vec{U}_m F_{ij}(\xi, \eta) H_k(\zeta)$$

$$\delta\vec{u} \in \{\delta\vec{U}_n F_{pq}(\xi, \eta) H_r(\zeta)\} \tag{D-1}$$

Various quantities appearing in Eq. (D-1) have been defined elsewhere in this work. The symmetric sub-elements of the stiffness matrix $\overline{\overline{A}}_{nm}$ as described in Eq. (B-1) for a wedge element oriented in *x-y* plane are given by

$$A_{nm}^{uu} = \frac{bhQ_{11}\Phi_2^{\xi\eta}\Phi_1^{\zeta}}{a} + \frac{ahQ_{66}\Phi_3^{\xi\eta}\Phi_1^{\zeta}}{b} + \frac{abQ_{55}\Phi_1^{\xi\eta}\Phi_2^{\zeta}}{h} + 2hQ_{16}\Phi_6^{\xi\eta}\Phi_1^{\zeta}$$

$$A_{nm}^{uv} = \frac{bhQ_{16}\Phi_2^{\xi\eta}\Phi_1^{\zeta}}{a} + \frac{ahQ_{26}\Phi_3^{\xi\eta}\Phi_1^{\zeta}}{b} + \frac{abQ_{45}\Phi_1^{\xi\eta}\Phi_2^{\zeta}}{h} + h(Q_{12} + Q_{66})\Phi_6^{\xi\eta}\Phi_1^{\zeta}$$

$$A_{nm}^{uw} = b(Q_{13} + Q_{55})\Phi_4^{\xi\eta}\Phi_3^{\zeta} + a(Q_{36} + Q_{45})\Phi_5^{\xi\eta}\Phi_3^{\zeta} \tag{D-2}$$

$$A_{nm}^{vv} = \frac{bhQ_{66}\Phi_2^{\xi\eta}\Phi_1^{\zeta}}{a} + \frac{ahQ_{22}\Phi_3^{\xi\eta}\Phi_1^{\zeta}}{b} + \frac{abQ_{44}\Phi_1^{\xi\eta}\Phi_2^{\zeta}}{h} + 2hQ_{26}\Phi_6^{\xi\eta}\Phi_1^{\zeta}$$

$$A_{nm}^{vw} = b(Q_{36} + Q_{45})\Phi_4^{\xi\eta}\Phi_3^{\zeta} + a(Q_{23} + Q_{44})\Phi_5^{\xi\eta}\Phi_3^{\zeta}$$

$$A_{nm}^{ww}=\frac{bhQ_{55}\Phi_2^{\xi\eta}\Phi_1^{\zeta}}{a}+\frac{ahQ_{44}\Phi_3^{\xi\eta}\Phi_1^{\zeta}}{b}+\frac{abQ_{33}\Phi_1^{\xi\eta}\Phi_2^{\zeta}}{h}+2hQ_{45}\Phi_6^{\xi\eta}\Phi_1^{\zeta}$$

The integrals $\Phi_i^{\zeta}, i=1,2,3$ are given by Eqs. (B-7). The remaining integrals are given by the following expressions:

$$\Phi_1^{\xi\eta}=\int_0^1\left[\int_0^{1-\xi}F_{ij}(\xi,\eta)F_{pq}(\xi,\eta)d\eta\right]d\xi,\ \Phi_2^{\xi\eta}=\int_0^1\left[\int_0^{1-\xi}\frac{\partial F_{ij}(\xi,\eta)}{\partial\xi}\frac{\partial F_{pq}(\xi,\eta)}{\partial\xi}d\eta\right]d\xi,$$

$$\Phi_3^{\xi\eta}=\int_0^1\left[\int_0^{1-\xi}\frac{\partial F_{ij}(\xi,\eta)}{\partial\eta}\frac{\partial F_{pq}(\xi,\eta)}{\partial\eta}d\eta\right]d\xi, \tag{D-3}$$

$$\Phi_4^{\xi\eta}=\int_0^1\left[\int_0^{1-\xi}F_{ij}(\xi,\eta)\frac{\partial F_{pq}(\xi,\eta)}{\partial\xi}d\eta\right]d\xi=\int_0^1\left[\int_0^{1-\xi}\frac{\partial F_{ij}(\xi,\eta)}{\partial\xi}F_{pq}(\xi,\eta)d\eta\right]d\xi$$

$$\Phi_5^{\xi\eta}=\int_0^1\left[\int_0^{1-\xi}F_{ij}(\xi,\eta)\frac{\partial F_{pq}(\xi,\eta)}{\partial\eta}d\eta\right]d\xi=\int_0^1\left[\int_0^{1-\xi}\frac{\partial F_{ij}(\xi,\eta)}{\partial\eta}F_{pq}(\xi,\eta)d\eta\right]d\xi$$

$$\Phi_6^{\xi\eta}=\int_0^1\left[\int_0^{1-\xi}\frac{\partial F_{ij}(\xi,\eta)}{\partial\xi}\frac{\partial F_{pq}(\xi,\eta)}{\partial\eta}d\eta\right]d\xi=\int_0^1\left[\int_0^{1-\xi}\frac{\partial F_{ij}(\xi,\eta)}{\partial\eta}\frac{\partial F_{pq}(\xi,\eta)}{\partial\xi}d\eta\right]d\xi$$

Similarly, the symmetric sub-elements of the stiffness matrix for a wedge element oriented in *y-z* plane are given by

$$A_{nm}^{uu}=\frac{bhQ_{11}\Phi_2^{\xi}\Phi_1^{\eta\zeta}}{a}+\frac{ahQ_{66}\Phi_1^{\xi}\Phi_2^{\eta\zeta}}{b}+\frac{abQ_{55}\Phi_1^{\xi}\Phi_3^{\eta\zeta}}{h}+2hQ_{16}\Phi_3^{\xi}\Phi_4^{\eta\zeta}$$

$$A_{nm}^{uv}=\frac{bhQ_{16}\Phi_2^{\xi}\Phi_1^{\eta\zeta}}{a}+\frac{ahQ_{26}\Phi_1^{\xi}\Phi_2^{\eta\zeta}}{b}+\frac{abQ_{45}\Phi_1^{\xi}\Phi_3^{\eta\zeta}}{h}+h(Q_{12}+Q_{66})\Phi_3^{\xi}\Phi_4^{\eta\zeta}$$

$$A^{uw}_{nm} = b(Q_{13} + Q_{55})\Phi_3^{\xi}\Phi_5^{\eta\zeta} + a(Q_{36} + Q_{45})\Phi_1^{\xi}\Phi_6^{\eta\zeta} \tag{D-4}$$

$$A^{vv}_{nm} = \frac{bhQ_{66}\Phi_2^{\xi}\Phi_1^{\eta\zeta}}{a} + \frac{ahQ_{22}\Phi_1^{\xi}\Phi_2^{\eta\zeta}}{b} + \frac{abQ_{44}\Phi_1^{\xi}\Phi_3^{\eta\zeta}}{h} + 2hQ_{26}\Phi_3^{\xi}\Phi_4^{\eta\zeta}$$

$$A^{vw}_{nm} = b(Q_{36} + Q_{45})\Phi_3^{\xi}\Phi_5^{\eta\zeta} + a(Q_{23} + Q_{44})\Phi_1^{\xi}\Phi_6^{\eta\zeta}$$

$$A^{ww}_{nm} = \frac{bhQ_{55}\Phi_2^{\xi}\Phi_1^{\eta\zeta}}{a} + \frac{ahQ_{44}\Phi_1^{\xi}\Phi_2^{\eta\zeta}}{b} + \frac{abQ_{33}\Phi_1^{\xi}\Phi_3^{\eta\zeta}}{h} + 2hQ_{45}\Phi_3^{\xi}\Phi_4^{\eta\zeta}$$

The integrals $\Phi_i^{\xi}, i = 1,2,3$ appearing in Eqs. (D-4) are given by Eqs. (B-7), and the remaining integrals are obtained by replacing ξ by η and η by ζ in Eqs. (D-3). Proceeding on the similar lines, the symmetric sub-elements of the stiffness matrix for a wedge element oriented in *x*-*z* plane (see Fig. 3) are given by

$$A^{uu}_{nm} = \frac{bhQ_{11}\Phi_2^{\xi\zeta}\Phi_1^{\eta}}{a} + \frac{ahQ_{66}\Phi_1^{\xi\zeta}\Phi_2^{\eta}}{b} + \frac{abQ_{55}\Phi_3^{\xi\zeta}\Phi_1^{\eta}}{h} + 2hQ_{16}\Phi_4^{\xi\zeta}\Phi_3^{\eta}$$

$$A^{uv}_{nm} = \frac{bhQ_{16}\Phi_2^{\xi\zeta}\Phi_1^{\eta}}{a} + \frac{ahQ_{26}\Phi_1^{\xi\zeta}\Phi_2^{\eta}}{b} + \frac{abQ_{45}\Phi_3^{\xi\zeta}\Phi_1^{\eta}}{h} + h(Q_{12} + Q_{66})\Phi_4^{\xi\zeta}\Phi_3^{\eta}$$

$$A^{uw}_{nm} = b(Q_{13} + Q_{55})\Phi_6^{\xi\zeta}\Phi_1^{\eta} + a(Q_{36} + Q_{45})\Phi_5^{\xi\zeta}\Phi_3^{\eta} \tag{D-5}$$

$$A^{vv}_{nm} = \frac{bhQ_{66}\Phi_2^{\xi\zeta}\Phi_1^{\eta}}{a} + \frac{ahQ_{22}\Phi_1^{\xi\zeta}\Phi_2^{\eta}}{b} + \frac{abQ_{44}\Phi_3^{\xi\zeta}\Phi_1^{\eta}}{h} + 2hQ_{26}\Phi_4^{\xi\zeta}\Phi_3^{\eta}$$

$$A^{vw}_{nm} = b(Q_{36} + Q_{45})\Phi_6^{\xi\zeta}\Phi_1^{\eta} + a(Q_{23} + Q_{44})\Phi_5^{\xi\zeta}\Phi_3^{\eta}$$

$$A^{ww}_{nm} = \frac{bhQ_{55}\Phi_2^{\xi\zeta}\Phi_1^{\eta}}{a} + \frac{ahQ_{44}\Phi_1^{\xi\zeta}\Phi_2^{\eta}}{b} + \frac{abQ_{33}\Phi_3^{\xi\zeta}\Phi_1^{\eta}}{h} + 2hQ_{45}\Phi_4^{\xi\zeta}\Phi_3^{\eta}$$

The integrals $\Phi_i^{\eta}, i = 1,2,3$ appearing in Eqs. (D-5) are given by Eqs. (B-7), and the remaining integrals are obtained by simply replacing and η by ζ in Eqs. (D-3).